U.PORTO

DOUTORAMENTO
MEDICINA DENTÁRIA

Immunomodulation of periodontal disease through a repurposed tetracycline released from antimicrobial bimetallic-oxide nanoparticles

Victor Zacharias Martin

D

2023

VICTOR ZACHARIAS MARTIN

Immunomodulation of periodontal disease through a repurposed tetracycline released from antimicrobial bimetallic-oxide nanoparticles

Tese apresentada na Faculdade de Medicina Dentária da Universidade do Porto para obtenção do grau de Doutor em Medicina Dentária

Orientador:

Doutor Pedro de Sousa Gomes

Professor Catedrático da Faculdade de Medicina Dentária da Universidade do Porto

Coorientadoras:

Doutora Ana Francisca Campos Simão Bettencourt

Professora Auxiliar com Agregação da Faculdade de Farmácia da Universidade de Lisboa

Doutora Catarina Ferreira dos Santos

Professora Adjunta do Instituto Politécnico de Setúbal da Escola Superior de Tecnologia de Setúbal

Financiamento:

A presente tese teve o apoio financeiro da Fundação para a Ciência e a Tecnologia através da bolsa de doutoramento (Ref.2020.04935.BD).

Resumo

A periodontite é uma doença imuno-inflamatória multifatorial causada pela presença de biofilmes disbióticos, dominados pelo crescimento excessivo de bactérias do complexo vermelho. A carga inflamatória adicional resultante da progressão da periodontite está associada a doenças sistémicas que podem comprometer a qualidade de vida dos pacientes afetados, contribuindo, eventualmente, para uma mortalidade prematura. A administração sistémica de antibióticos pode ser usada como uma terapia adjuvante da remoção mecânica de cálculos e do biofilme. No entanto, devido à sua eficácia questionável, os efeitos adversos existentes, e o risco de desenvolvimento de resistência bacteriana, há uma crescente tendência de substituir esta abordagem por uma alternativa, baseada em estratégias de administração local. Além da atividade bactericida desejável, as estratégias de libertação local, para esta aplicação, devem incluir propriedades imunomoduladoras e terem a capacidade de eliminar bactérias intracelulares, visando evitar a destruição do tecido periodontal e recidivas. Portanto, para abordar adequadamente a periodontite, torna-se essencial o desenvolvimento de um periocêutico à escala nanométrica, biocompatível, estável em condições fisiológicas e de inflamação, e com capacidade de libertar antibióticos por períodos prolongados, além de apresentar efeitos antioxidantes e anti-inflamatórios.

O presente estudo teve como objetivo o desenvolvimento e a caracterização de um periocêutico, desenhado para ser aplicado localmente, que pudesse cumprir todos os requisitos mencionados. Para atingir este objetivo, as tetraciclinas (TCs) - uma classe de antibióticos que possui efeitos pleiotrópicos, incluindo atividade antioxidante e anti-inflamatória - foram selecionadas como agentes bioativos.

Nesse contexto, foi realizada uma revisão da literatura, focada na análise de micropartículas e nanopartículas contendo TCs. Inspirados pelo conhecimento adquirido na revisão, foi projetado o desenvolvimento de um veículo inorgânico - nanopartículas compostas por camadas de hidróxido de zinco-magnésio (Zn-Mg LH NPs) - devido à sua potencial biocompatibilidade, bioatividade, estabilidade e elevada capacidade de ser carregado com fármacos.

Primeiramente foram produzidas nanopartículas (Zn-Mg LH NPs) utilizando água destilada ou extrato de roseira brava (RH). As NPs foram sintetizadas por um método rápido e escalonável, livre de solventes orgânicos, mantendo uma baixa temperatura, permitindo a incorporação de fármacos e fitoquímicos durante sua síntese. A

caracterização físico-química mostrou que as NPs desenvolvidas são compostas por folhas ultrafinas de hidróxido de zinco, contendo aniões e água entre as suas camadas. Os compostos polifenólicos provenientes do extrato de RH foram identificados e quantificados nas NPs. As Zn-Mg LH NPs mostraram-se citocompatíveis e apresentaram elevada atividade antioxidante e anti-inflamatória, A presença de extratos de RH na composição potenciou estes efeitos, posicionando as Zn-Mg LH NPs como uma alternativa terapêutica promissora para distúrbios inflamatórios não infeciosos.

Concomitantemente, quatro TCs foram avaliadas, incluindo uma molécula da última geração (sareciclina), quanto à citocompatibilidade e potencial osteogénico, em culturas de células estaminais mesenquimais humanas. Pela primeira vez, o potencial osteogénico da sareciclina foi avaliado e validado. Embora todas as TCs testadas tenham induzido o processo de diferenciação osteogénica, a tetraciclina e a doxiciclina exerceram os seus efeitos através do aumento da sinalização Wnt, enquanto a minociclina e a sareciclina parecem atuar através da modulação da via sinalização Hedgehog. A doxiciclina (DX) foi selecionada para ser incorporada nas NPs desenvolvidas, devido à sua solubilidade, atividade contra bactérias gram-negativas e perfil de biossegurança.

Por fim, avaliou-se a capacidade das Zn-Mg LH NPs atuarem como veículos transportadores do fármaco para o tratamento da periodontite. A DX foi incorporada nas NPs durante a etapa de síntese, permitindo assim, a produção num único passo de NPs com fármaco incorporado. As DX Zn-Mg LH NPs apresentaram citocompatibilidade e mantiveram a bioatividade do veículo, como evidenciado pelos efeitos antioxidantes e anti-inflamatórios. Aproximadamente 80% da DX carregada foi libertada das NPs durante 14 dias. Adicionalmente, as NPs carregadas apresentaram uma atividade antibacteriana efetiva contra bactérias gram-positivas e gram-negativas. Adicionalmente, observou-se um potencial efeito sinérgico antibacteriano entre a DX e NPs. As imagens de microscopia eletrónica de transmissão indicaram que as Zn-Mg LH NPs possivelmente foram internalizadas por fibroblastos via macropinocitose, o que poderá ser de utilidade terapêutica na eliminação de bactérias internalizadas, responsáveis pela recorrência da doença.

Em suma, as Zn-Mg LH NPs contendo DX ou extratos de RH foram desenvolvidas com sucesso e mostraram potencial para serem utilizadas como tratamento adjuvante para periodontite e outros distúrbios inflamatórios.

Abstract

Periodontitis is a widespread multifactorial immuno-inflammatory disease caused by the presence of dysbiotic biofilms. The consequential periodontal inflammatory burden is further associated with the increase of systemic inflammation, that greatly undermines the quality of life and may contribute to anticipated death of affected patients.

Antibiotics administered systemically can be employed as adjutant therapy to the mechanical removal of calculi and biofilm. However, due to the questionable efficacy, adverse side effects, and a propensity to foster antibacterial resistance, there is a growing tendency towards local treatment strategies, fostering on local drug delivery systems.

Beyond the desirable bactericidal activity, these delivery systems shall provide active immuno-modulatory activity and target internalized bacteria, aiming the avoidance of further tissue destruction and recurrences. Therefore, to properly tackle periodontitis, the innovative development of a perioceutic at the nanoscale becomes essential, demanding adequate biocompatibility, stability under physiological/inflamed conditions, and the ability to release antibacterial drugs during prolonged periods, besides providing antioxidant and anti-inflammatory activity.

The present study aimed the development and characterization of a perioceutic, devised to be applied locally, which could meet all the mentioned requirements. To accomplish this, tetracyclines (TCs) - a class of antibiotic drugs that possesses useful pleiotropic effects, including antioxidant and anti-inflammatory activity – were chosen as a bioactive agent. In this context, a review of the literature was carried out, focused on micro and nanoparticles loaded with TCs, which provided valuable insights. Inspired by the knowledge gathered in the review, an inorganic nanocarrier - layered zinc-magnesium hydroxide nanoparticles (Zn-Mg LH NPs) – was conceptualized and produced, aiming for a granted biocompatibility, bioactivity, stability, and high drug loading capacity.

The NPs were synthesized via a green synthesis method, that is rapid, organic solvent-free, occurring at a low-temperature and scalable method that allows the incorporation of drugs and phytochemicals during synthesis. Two approaches were subsequently employed for the synthesis: one using distilled water and the other incorporating rosehip (RH) extract, to introduce phytochemical compounds.

Physicochemical characterization showed that the developed materials were organized as ultrathin zinc hydroxide sheets, containing anions and water between layers. Notably,

polyphenols were quantified in NPs synthesized with RH extract. Developed Zn-Mg LH NPs, from either synthesis process, were found to be cytocompatible and presented robust antioxidant and anti-inflammatory properties. The presence of RH extracts in the formulation further enhanced these effects, positioning Zn-Mg LH NPs as a promising innovative therapy for noninfectious inflammatory disorders.

Concomitantly, four TCs, including one molecule from the most recent generation (sarecycline), were assessed for cytocompatibility and potential to enhance the osteogenic differentiation using human mesenchymal stromal cells. For the first time, the osteogenic potential of sarecycline was assessed and validated. Although all assayed TCs induced an osteogenic differentiation, tetracycline and doxycycline exert their effects through increased Wnt signaling, while minocycline and sarecycline seem to act via Hedgehog signaling. Doxycycline (DX) was selected for loading in the developed perioceutic due to its improved solubility, sustained activity against gram-negative bacteria and biosafety profile.

Lastly, the capability of Zn-Mg LH NPs to function as a drug carrier for periodontitis was evaluated. Doxycycline was loaded into the carrier during the synthesis step, simplifying the production. DX Zn-Mg LH NPs were cytocompatible and maintained the bioactivity of the carrier, noted by their antioxidant and anti-inflammatory effects. Approx. 80% of the loaded DX was continuously released from the NPs for 14 days. Moreover, loaded NPs displayed a clear antibacterial activity against gram-positive and gram-negative bacteria. A potential synergetic antibacterial effect between DX and the carrier was noted. Transmission electron microscopy images indicated that Zn-Mg LH NPs were internalized by fibroblasts via macropinocytosis, which could engage internalized bacteria, accountable for disease's recurrence.

All in all, Zn-Mg LH NPs containing DX or RH extracts were successfully developed and have the potential to be employed as adjutant treatment for periodontitis and other inflammatory disorders.

Agradecimentos

Começo por expressar a minha profunda gratidão ao meu orientador, Professor Pedro de Sousa Gomes, pela generosidade, conhecimentos e a total disponibilidade nesses 4 anos de doutoramento. Minha admiração pelo professor Pedro antecede o programa doutoral – começou durante o mestrado, com as colaborações iniciais nos artigos e a arguição, e desde então, só veio a aumentar. Além de todo conhecimento partilhado da medicina dentária, docência, investigação e orientação, também tive o privilégio da partilha sobre tópicos menos formais, como carros, juros monetários, viagens e música. Agradeço também pelas oportunidades dadas, tanto na docência quanto nos vários projetos de investigação alheios à tese, as quais consideraria inimagináveis há alguns anos.

Agradeço à Professora Ana Francisca Bettencourt, coorientadora da tese de doutoramento. No entanto, a importância da professora Ana é bastante mais significativa do que esse estatuto. Tenho a professora Ana como uma "mãe" acadêmica, pois toda a vontade de realmente seguir nessa área iniciou-se durante a unidade curricular do projeto 2, no mestrado, onde tive sua primeira ajuda e orientação. Todo o mérito desses últimos anos passa, sem dúvidas ou exageros, pelas suas mãos.

À Professora Catarina Ferreira dos Santos, também na qualidade de coorientadora da presente tese. Conhecemo-nos através de colaborações em 2017, e desde então, já foram mais do que algumas á lista de publicações. Admiro a energia de trabalho da Professora Catarina, além do conhecimento e da criatividade na área dos biomateriais. Lembro-me, com carinho, dos nossos *brainstorms* que abrangem desde a coordenação octaédrica do zinco até perfis de *pets* no Instagram.

À Professora Maria Helena Fernandes, que, apesar de não constar oficialmente como orientadora, tem um papel fundamental não só no contexto da tese, mas também em minha formação profissional. Agradeço imenso, desde a calorosa receção no BoneLab, as inúmeras oportunidades e desafios colocados ao longo desses anos. Sinto-me privilegiado de ter participado na escrita de alguns artigos, na montagem e ministração de aulas e frequências consigo, além das boas e descontraídas conversas que tivemos ao longo desses anos.

Agradeço à Professora Isabel Ribeiro e à Professora Lídia Gonçalves por todos esses anos de ensinamentos e cooperações. Em especial, por me receberem tão bem em vossos laboratórios após o término do mestrado. Senti-me em casa todas as vezes que estive de volta à FFUL.

À Doutora Marta Alves, por me receber no CQE e pela incansável ajuda nas caracterizações dos materiais no IST.

Ao investigador Miguel Rodrigues e à Professora Maria Ascensão Lopes por toda ajuda com as partículas na FEUP.

Agradeço à Professora Liliana Grenho, grande responsável pela minha integração ao grupo do BoneLab e desempenho nos ensaios laboratoriais. Por tornar exequível importantes experiências no laboratório, seja pelos seus infindáveis protocolos, seja por "importar" materiais e compostos do i3s (através da Doutora Joana Barros e Doutora Ângela Carvalho, as quais também tenho muito a agradecer). E muito além disso, por dedicar uma parte do seu dia em fazer a rotina do laboratório ser mais leve e divertida e por tanto se importar com todos os integrantes do BoneLab.

Às pessoas do BoneLab - Lorena, Sanjana, Carla, Rita, Laura, Maria – Pelo conhecimento partilhado e os incontáveis momentos de descontração, incluindo as jantaradas, finos, dicas de culinária e viagens, memes do JJ, rockadas, visitas a longínquos estádios e repetidas coletas de água ao i3s. You will never walk (or laugh) alone!

Aos amigos, de ambos os lados do Atlântico, pelas mensagens de carinho e suporte ao longo dos anos e, principalmente, pelas visitas. Bernardo, espero-te para a obrigatória e bimestral francesinha e Nuno, que oxalá poderei chamar de "vizinho de cima" em breve. Ao meu colega de profissão e amigo sino-brasileiro Wladimir, por toda a alegria que trouxe ao laboratório em sua estadia, o posterior suporte remoto e os *case reports* que foram e os que virão.

À família. Tenho o privilégio de partilhar o amor pela área da saúde com meus pais, através de diferentes prismas. Obrigado pelo incondicional suporte, particularmente nos últimos anos, apesar da drástica mudança produzida por uma decisão, que inicialmente, não pareceu das mais lógicas. Luísa, pelas conversas fáceis e difíceis que acompanharam as nossas jornadas ultramarinas e pelos esforços das visitas aqui e em Itália. Avó Bete, por todas as orações, videochamadas e visitas, que ajudam nas saudades. Eliane e Carlos,

pelo suporte irrestrito e todo o carinho para com o vosso genro, que vos espera ansiosamente aqui. Aos tios e primos por todo apoio e atenção.

À minha querida Fernanda, que apesar de possuir múltiplos pseudônimos, deixarei registada como tal. Seu nome vem sendo escrito nas páginas de agradecimento desde a minha especialização, em 2013. No entanto, marco, sem qualquer hesitação, que seu apoio teve um peso muito maior no doutoramento do que em qualquer outro momento profissional que já vivi. Agradeço por toda a compreensão, amor e a (quase) infindável paciência nesse último ano de escritas. Espero sempre conseguir prover a si o apoio, amor e a parceria necessários para qualquer desafio pessoal e profissional.

Agradeço as plataformas do i3s Bioimaging (Doutora María Lázaro), HEMS (Doutor Rui Fernandes e Doutora Rossana Correia) e CCGen (Doutora Paula Magalhães e Doutora Tânia Meireles) pela colaboração nos trabalhos.

Agradeço a Fundação para a Ciência e a Tecnologia pelo financiamento através da bolsa de doutoramento (Ref. 2020.04935.BD).

Agradeço a Faculdade de Medicina Dentária da Universidade do Porto (FMDUP) e seus colaboradores, por permitirem que o trabalho fosse sempre realizado da melhor maneira possível. Estendo os agradecimentos ao Instituto de Investigação do Medicamento (iMed, FFUL), ao Centro de Química Estrutural (CQE, ISTUL) e ao Instituto Politécnico de Setúbal (IPS) que possibilitaram a realização do trabalho.

Membros do Conselho Científico em Vigor

Prof. Doutor Américo dos Santos Afonso

Prof. Doutora Ana Paula Coelho de Macedo Augusto

Prof. Doutora Ana Paula Mendes Alves Peixoto Norton

Prof. Doutor César Fernando Coelho Leal da Silva

Prof. Doutora Cristina Maria Ferreira Guimarães Pereira Areias

Prof. Doutor Filipe Poças de Almeida Coimbra

Prof. Doutora Inês Alexandra Costa Morais Caldas

Prof. Doutora Irene Graça Azevedo Pina Vaz

Prof. Doutor João Carlos Antunes Sampaio Fernandes

Prof. Doutor Jorge Manuel de Carvalho Dias Lopes

Prof. Doutor José António Ferreira Lobo Pereira

Prof. Doutor José Carlos Reis Campos

Prof. Doutora Maria Benedita Almeida Garrett de Sampaio Maia Marques

Prof. Doutora Maria Cristina Pinto Coelho Mendonça de Figueiredo Pollmann

Prof. Doutora Maria de Lurdes Ferreira Lobo Pereira

Prof. Doutora Maria Helena Guimarães Figueiral da Silva

Prof. Doutora Maria Helena Raposo Fernandes

Prof. Doutora Maria João Feio Ponces Ramalhão

Prof. Doutor Mário Ramalho de Vasconcelos

Prof. Doutor Miguel Fernando da Silva Gonçalves Pinto

Prof. Doutora Paula Cristina dos Santos Vaz Fernandes

Prof. Doutor Paulo Rui Galrão Ribeiro de Melo

Prof. Doutor Pedro de Sousa Gomes

Prof. Doutor Pedro Manuel Vasconcelos Mesquita

Prof. Doutor Ricardo Manuel Casaleiro Lobo de Faria e Almeida

List of Abbreviations

3D Three-dimensional

α-MEM α-Minimal Essential Medium

AA Ascorbic acid

AB Alcian blue

ALP Alkaline phosphatase

ANOVA One-way analysis of variance

ATCC American Type Culture Collection

ATR Attenuated total reflectance

AXIN2 Axis Inhibition Protein 2

BBB Blood-brain-barrier

BCP Biphasic calcium phosphate

BG Bioactive glass

BGLAP Osteocalcin

BHI Brain-Heart Infusion media

BMD Bone mineral density

BMP Bone Morphogenetic Protein

BS Bone surface

BSA Bovine serum albumin

BspA Leucine-rich-repeat protein

β-TCP β-tricalcium phosphate

BV Bone volume

C-BAS Basal control

CD Cluster of differentiation

cDNA Complementary DNA

CFU Colony-forming unit

CHX Chlorhexidine

CLSI Clinical and Laboratory Standards Institute

CNS Central nervous system

COL1A1 Collagen Type I Alpha 1

COX Cyclooxygenase

CT threshold cycle

DCFDA 2′,7′-dichlorofluorescin diacetate

DL% Drug loading percentage

DMEM Dulbecco's Modified Eagle Medium

DMSO Dimethyl sulfoxide

DNA Deoxyribonucleic acid

DOXY/DX Doxycycline hydrochloride

DPPH 2,2-diphenyl-1-picrylhydrazyl

EM Emission

ER Endoplasmic-reticulum

EX Excitation

FBS Fetal bovine serum

FDA Food and Drug Administration

FTIR Fourier transformed infrared spectroscopy

GABA Gamma-aminobutyric acid

GAPDH Glyceraldehyde-3-Phosphate Dehydrogenase

GLI2 Glioma-Associated Oncogene Family Zinc Finger 2

HA Hydroxyapatite

hBMSCs Human bone marrow-derived mesenchymal stromal cells

H&E Hematoxylin and eosin

HES Hes Family BHLH Transcription Factor 1

HEY1 HES-Related Repressor Protein 1

HFs Human fibroblasts

HGFs Human gingival fibroblasts

HH Hedgehog

HIV Human immunodeficiency virus

HNF1A Hepatocyte nuclear factor 1-alpha

ICP Inductively coupled plasma spectroscopy

Ig Immunoglobulin

Igf2 insulin-like growth factor 2

IKK blocking IkB kinase

IL Interleukin

LDDS Local drug delivery systems

LDH Layered double hydroxide

LDL Low density lipoproteins

LH Layered hydroxide

LPS Lipopolysaccharides

LZH Layered zinc hydroxide

µCT Micro-computed tomograph

MHA Mueller–Hinton Agar

MHB Mueller–Hinton broth

MIC Minimum inhibitory concentration

MINO Minocycline hydrochloride

MMPs Matrix metalloproteinases

MTT Tetrazolium dye

NAC N-Acetylcysteine

NFkB Nuclear factor kappa-light-chain-enhancer of activated B cells

NIR Near-infrared

NPs Nanoparticles

NSAIDs Nonsteroidal anti-inflammatory drugs

OST osteogenic

p P-value

P. gingivalis Porphyromonas gingivalis

PBS Phosphate buffered saline

PCL polycaprolactone

PDI Polydispersity index

PDs Periodontal diseases

PEG Polyethylene glycol

pH Potential of hydrogen

PLA polylactide acid

PLGA Polylactic-co-glycolic acid

PMNs polymorphonuclear neutrophils

PTCH1 Protein Patched Homolog 1

PVA Polyvinyl alcohol

qPCR Quantitative Polymerase chain reaction

RANKL Receptor activator of nuclear factor κB-Ligand

RGD Arginylglycylaspartic acid

RH Rosehip

RNA Ribonucleic acid

ROS Reactive oxygen species

RPM Revolutions per minute

RUNX2 Runt-Related Transcription Factor 2

S. aureus Staphylococcus aureus

SA/SARE Sarecycline hydrochloride

SAED Selected area electron diffraction

SARS-CoV-2 Severe acute respiratory syndrome coronavirus 2

SD standard deviation

SMO Smoothened

SP7 Osterix

SPARC Osteonectin

SPSS Statistical Package for Social Sciences

SR Sirius red

T. denticola Treponema denticola

T. forsythia Tannerella forsythia

TA Tannic acid

TCF/LEF T-cell factor/lymphoid enhancer factor

TCs Tetracyclines

TEM Transmission electron microscopy

TETRA Tetracycline hydrochloride

TLR2/4 Toll-Like receptors 2/4

TNF Tumor Necrosis Factor.

TPP Tripolyphosphate

TV Tissue volume

TWIST1 Twist Family BHLH Transcription Factor 1

XPS X-ray photoelectron spectroscopy

XRD X-ray diffraction

Index of Figures

Figure 11. (A) Relative expression of osteogenesis-related genes of hBMSCs cultured with SA at 1 µg/mL, for 7 days. Values were normalized by the gene expression values at the control culture. (B) Quantitative ALP activity of HBMSCs cultured with sarecycline at 1 µg/mL, for 14 days. (*) Significantly different to control (n=5, $p<0.05$).

Figure 12. Relative expression of genes associated with relevant signaling pathways (Hedgehog, Notch and Wnt) of hBMSCs cultured with SA at 1 µg/mL, for 7 days. Values were normalized by the gene expression values at the control culture. (*) Significantly different to control (n=5, $p<0.05$).

Figure 13. (A) Variation of the bone length of the femurs grown with SA. (B) Representative macroscopic images of control, SA at 1 and 10 µg/mL, respectively. Scale bar corresponds to 5 mm (n=5, $p<0.05$). No statistical differences among groups were attained.

Figure 14. Representative images of µCT analysis. (A) C-BAS; (B) SA 1 µg/mL; (C) SA 10 µg/mL. Images were created setting the defined volume of interest, using the maximum intensity and attenuated projection respectively. Scale bar corresponds to 500 µm. (D) Quantitative histomorphometric 3D-analysis of the femurs cultured with SA. (*) significantly different to control. (#) significantly different to SA 10 µg/mL (n=5, $p<0.05$). BV - bone volume; BS - bone surface; TV - tissue volume.

Figure 15. (A) Representative images of histochemical staining using Alcian Blue and Sirius Red (AB/SR) staining. Proteoglycans of the cartilage tissue are labeled in blue, while collagen matrix is labeled in red. (B) Representative images of von Kossa staining, with calcium deposits evidenced in black, in addition to a pinkish staining of the cells. (C) Quantitative analysis of the percentage of collagen area using the (AB/SR) stained images. (D) Quantitative analysis of the percentage of mineralized area using von Kossa dyed images. Scale bar corresponds to 100 µm. (*) significantly different to control. (n=5, $p<0.05$).

Figure 16. Metabolic activity/cell viability of HBMSC cultures incubated with tetracyclines at different concentrations - MTT assay. TETRA corresponds to tetracycline; DOXY to doxycycline; MINO to minocycline; SARE to sarecycline; and OST to osteogenic-induced cultures. The color scale corresponds to the tetracycline/drug and concentrations of 0.1, 1, and 10 µg/mL. Experimental group values were normalized by the basal control (C) for each timepoint, set as 1.0. (#) different from C; (z) different from DOXY at 10 µg/mL, (a) different from MINO at 10 µg/mL. (n=5, $p\leq0.05$).

Figure 17. Representative fluorescent images of cellular morphology of HBMSC cultures at day 7 and day 14, incubated with tetracyclines at different concentrations. The cellular actin cytoskeleton was stained in green; nuclei were counter-stained in blue, and mitochondria were dyed in red. The scale bar corresponds to 100 µm. TETRA corresponds to tetracycline; DOXY to doxycycline; MINO to minocycline; SARE to sarecycline; C-BAS to basal control; and OST to osteogenic-induced cultures.

Figure 18. Osteogenic activity of HBMSCs cultured with TCs at 1.0 µg/mL. Quantitative analysis and representative histochemical staining of ALP activity displayed as a normalized percentage as compared to the basal control (C-BAS) set as 1.0. TETRA

corresponds to tetracycline; DOXY to doxycycline; MINO to minocycline; SARE to sarecycline; C-BAS to basal control; and OST to osteogenic-induced cultures. The scale bar corresponds to 100 μm. (#) different from control; (*) different from TETRA and DOXY. n=5, $p \leq 0.05$.

Figure 19. Relative gene expression of osteogenesis-related genes using quantitative PCR assessment. Values were normalized via the $2^{-\Delta\Delta Ct}$ method. TETRA corresponds to tetracycline; DOXY to doxycycline; MINO to minocycline; SARE to sarecycline; C-BAS to basal control; and OST to osteogenic-induced cultures. (#) different from control; (z) different from TETRA and DOXY; (a) different from MINO and SARE. n=5, $p \leq 0.05$.

Figure 20. Relative gene expression of relevant osteogenic pathways of cultures using qPCR technique. Values were normalized via the $2^{-\Delta\Delta Ct}$ method. (#) different from control; (z) different from TETRA and DOXY; (a) different from MINO and SARE; (b) different from OST. n=5, $p \leq 0.05$.

Figure 21. Schematics of the inflamed organotypic mucosal model, comprising a mesenchymal constituent (i.e., fibroblasts embedded into a collagen matrix) and a stratified epithelial outer layer of keratinocytes. *P. gingivalis*' LPS was used to trigger an inflammatory response, inducing the expression of cytokines (IL-1b, IL-6, TNF), chemokines (CXCL-8) and related transcription factors (NFKB) (data not shown).

Figure 22. Physicochemical characterization of Zn-Mg LH NPs, encompassing the (a) X-ray diffraction (XRD), (b) ICP, (c) structural scheme of the LH structure, (d) FTIR/ATR, (e and f) XPS, and (g) Zeta potential analyses measured in distilled water. (hi-hiii) TEM/SEM representative images of Zn-Mg LH and (hiv-hvi) of RH-Zn-Mg LH NPs.

Figure 23. (a): Metabolic activity of HFs incubated with Zn-Mg LH NPs normalized by the control, represented as 100% in the graphs. (b): Representative images of the cellular morphology of HFs grown in the absence (control) or the presence of 10 μg/mL of NPs, at day 1 (upper panel) and day 7 (lower panel). Cells were stained for F-actin cytoskeleton in green and counterstained for nuclei in blue. Scale bar: 100 μm. (*) Statistically significant from control, set as 100%. $p \leq 0.05$.

Figure 24. NPs' zeta potential measurement in an isotonic saline solution (Hepes buffer) at different pH values.

Figure 25. Representative TEM images of HF cultures incubated with Zn-Mg LH and RH-Zn-Mg LH NPs. (a) Early-stage incubation (3h), with the scale bar set at 1 μm. (b) Late-stage incubation (24h). Red squares: endosomes; Blue squares: lysosomes; Yellow squares: amphisomes. Dashed images correspond to magnified areas. Scale bar of frameless images was set at 1 μm, while the scale bar of framed images was set at 250 nm.

Figure 26. Reactive oxygen species (ROS) assays, using ZN-Mg LH and RH-Zn-Mg LH NPs at different concentrations. (a) Measurement of ROS generated by NPs and (b) Antioxidant activity of NPs in HF cultures. (c) ROS scavenging activity of NPs in the presence of peroxides. # significant different from other experimental samples. * Significantly different from control. * Significantly different from positive control. # Significantly different from Zn-Mg LH NPs. $p < 0.005$. **** Significantly different from

positive control, $p < 0.0001$. AA corresponds to ascorbic acid; NAC corresponds to N-Acetylcysteine.

Figure 27. (a): Representative histological section of the organotypic mucosal model stained with H&E. (b): Anti-inflammatory activity of LH NPs assessed by QPCR analysis. The organotypic model was incubated with 1.0 µg/mL of LPS prior incubation with 10 µg/mL of NPs. Values were normalized by the housekeeping gene (GAPDH), set as 1.0. * Significant different from Zn-Mg LH NPs. # Significant different from negative control. (a) Significant different from C+. $p < 0.005$.

Figure 28. Physicochemical characterization of LH NPs. A - TEM Images of Zn-Mg LH NPs and DX-Zn-Mg LH NPs. Scale bar corresponds to 200 nm. B – XRD analysis, assessing the crystallinity degree of NPs. C – FTIR/ATR results, qualitatively evaluating the composition of the NPs. D – XPS analysis and E - ICP analysis, corresponding to the quantitative analysis of NPs' composition. F – Zeta potential of NPs assessed by light scattering, using distilled water and HEPES buffer. The pH of HEPES was adjusted to 7.0.

Figure 29. Concentrations of DX released from the DX-Zn-Mg LH NPs for 14 days in Hepes buffer, displayed by concentration (left graph) and percentage, using the DL% as reference for 100% (right graph).

Figure 30. Antibacterial activity of Zn-Mg LH NPs and DX-Zn-Mg LH NPs against *S. aureus* (A and B) and *P. gingivalis* (C). A – Representative images of the Kirby Bauer assay. B – Inhibition zone measurements and minimum inhibitory concentration (MIC) assay of NPs against *S. aureus*. C – CFU counting of *P. gingivalis*, after 24h incubation with NPs, at 10 µg/mL. (*) Statistically different to Control. (#) Statistically different to other experimental samples.

Figure 31. Upper part: Metabolic activity of HGFs incubated with and without NPs. (*) Statistically different to Control. (#) Statistically different to other experimental samples. Lower part: Representative images of cellular morphology of HGFs grown in the presence of 10 µg/mL of NPs, at day 1 and day 7. Cells were stained for F-actin cytoskeleton in green and counterstained for nuclei in blue. Scale bar: 100 µm.

Figure 32. A - Measurement of ROS generated by Zn-Mg LH and DX-Zn-Mg LH NPs after 1 h of incubation. B - Anti-ROS activity of NPs. (#) significantly different from cells treated with N-Acetylcysteine. (*) significantly different from C+. * $p < 0.05$. **** $p < 0.0001$.

Figure 33. Representative images of NPs' uptake by HGFs after 3 h of incubation, addressed by TEM. Upper scale bar: 0.5 µm. Lower scale bar: 1 µm. Blue squares highlight membrane's protrusions and general perturbations, while blue arrows indicate areas of vacuole formations. NPs' concentration of 10 µg/mL.

Figure 34. Representative TEM images of NPs' intracellular trafficking after 24 h of incubation. Scale bars: 0.5 µm. Yellow square: Golgi apparatus. Orange arrow: phagosomes. Red arrow: autophagosomes. Green arrow: amphisomes. Blue arrow: autolysosomes. Red asterisk: healthy mitochondria. Yellow asterisk: Damaged mitochondria. NPs' concentration of 10 µg/mL.

Figure 35. (A) Representative histological section of the organotypic mucosal model stained with H&E. Scale bar: 250 µm. (B) Anti-inflammatory activity of NPs assessed by QPCR. Cells were incubated with 1.0 µg/mL of LPS prior incubation with 10 µg/mL of NPs. Values were normalized by the housekeeping gene (GAPDH), set as 1.0. (*) Significantly different from C+. (#) Significantly different from C-.

Index of Tables

TABLE OF CONTENTS

Preamble

Periodontal diseases are the most prevalent oral condition in human population worldwide, responsible for significant economic impacts and aggravation of systemic chronic inflammatory conditions. The main etiologic factor of these diseases is the existence of a dysbiotic bacterial setting at the gingival crevice, with a continuously growing presence of key periopathogens, as *Porphyromonas gingivalis, Treponema denticola, Tannerella forsythia.*

Among periodontal diseases, periodontitis is characterized by tissue destruction and tooth loss, due to an exacerbated host inflammatory response triggered by these bacteria. This immune response is set on the overproduction of reactive oxygen species, proinflammatory interleukins, matrix metalloproteinases and immunoglobulins. Despite this realization, current therapies are mainly focused on the decontamination of compromised sites, overlooking the immune-inflammatory character of the disease, which lead to a persistent tissue destruction. Moreover, systemic antibiotic use as auxiliary therapy has a contested efficacy against periopathogens, further being associated with potential adverse effects as the promotion of antibacterial resistance.

Facing these issues, innovative adjutant therapies have been proposed relying on different local drug delivery strategies. In this respect, tetracycline antibiotics are vastly employed as auxiliary therapy, administrated locally or systemically, showcasing useful pleiotropic effects besides their bacteriostatic activity.

In the present study, the current knowledge about periodontitis, local drug delivery systems and tetracyclines are explored in the chapter 1, detailing the pathogenic mechanisms of the periodontitis, and discussing the vast options of drug carriers, their synthesis, advantages, and limitations. Chapter 2 details the objectives of this thesis.

Further, chapter 3 and 4 describe the assessment of the *in vitro* cytocompatibility and osteogenic potential of four tetracyclines, comprising different generations - tetracycline (1^{st} gen.), doxycycline and minocycline (2^{nd} gen.), and sarecycline (3^{rd} gen.), conducted to select the most suitable candidate to be part of the perioceutic formulation.

Finally, chapter 5 and 6 encompass the development and characterization of inorganic nanoparticles, based on the layered zinc-magnesium hydroxide construction, to be used as local drug delivery systems. Polyphenols were incorporated to zinc-based nanoparticles by adding rosehip extract during their production, relying on a straightforward and scalable green synthesis process. Alternatively, zinc-based

nanoparticles were loaded with doxycycline using a co-precipitation method, targeting a satisfactory drug release profile for periodontitis treatment. Both nanoparticle' types were comprehensively characterized for physicochemical and biological aspects. The *in vitro* characterization of the nanoparticles demonstrated their potential as promising adjutant therapies to tackle inflammatory conditions and periodontitis.

CHAPTER 1

General Introduction

1.1.Periodontal disease: Current understanding of the disease.

Periodontal diseases (PDs) encompass a group of multifactorial immuno-inflammatory diseases caused by a host reaction to the presence of polymicrobial biofilms on dental surfaces. [1,2]. PDs are regarded as the most frequent oral condition of the human population, with a global prevalence between 20 to 50% [3], responsible for an economic impact of hundreds of billions annually [4].

Among PDs and conditions, periodontitis is distinguished by the progressive destruction of bone and connective tissues, currently classified in stages (severity) and grades (progression rate) [5]. Locally, periodontitis is characterized by the reduction of clinical attachment of periodontal ligament fibers and the destruction of surrounding alveolar bone that can lead to tooth loss, affecting the masticatory function and esthetics of the patients [4,6]. Additionally, inflammation is a hallmark of this condition, evident in the affected gingival region, and associated with edema, erythema, and bleeding [6].

Systemically, periodontitis increases the organism inflammatory burden [7]. Bacteria, bacterial products, and inflammatory mediators from the periodontal tissue can enter the blood circulation through oral micro-wounds (caused by mastication and brushing) and increased local transepithelial and endothelial permeability [8]. Consequently, PDs can incite and aggravate other chronic inflammatory conditions as cardiovascular, neurodegenerative and metabolic disorders, being also associated with adverse pregnancy outcomes [3,8]. Moreover, connections between oral squamous cell carcinoma and periopathogens have been proposed recently [9,10]. Conjoining these local and systemic effects, it becomes evident that PDs greatly lessen the quality of life and may contribute to anticipated death of affected patients.

Being an infectious-inflammatory disease, the presence of periodontal pathogens at the gingival crevice is the main etiologic factor in periodontitis [10]. The persistence of supra- and subgingival biofilm instigates an *in situ* dysbiotic change by the colonization and outgrowth of bacteria – frequently from the red complex, uplifting the virulence and, therefore, the inflammation [10,11]. The red complex comprises three anaerobic and gram-negative bacteria, *Porphyromonas gingivalis, Treponema denticola, Tannerella forsythia* [12]. These periopathogens are considered late colonizers that present several virulence factors, including proteolytic, proinflammatory, immunosuppressive and evasive factors [9,12]. As a result, periodontal pathogens can manipulate the host

inflammatory response by promoting inflammation and simultaneously, evading such responses via immunosuppressive maneuvers [10].

For instance, *P. gingivalis*' lipopolysaccharides (LPS), vesicles, fimbriae and pili induce a potent inflammatory reaction by binding to Toll-Like receptors 2/4 (TLR2/4) of the host cells, which further induce the production of proinflammatory cytokines via Nuclear factor kappa-light-chain-enhancer of activated B cells (NFκB) and p38 pathways [8,13]. Additionally, gingipains – proteases of outer membrane of *P. gingivalis* – degrade immunomodulatory proteins as IL-1β and TNF-α, decreasing the inflammatory response that ultimately facilitate the bacteria to escape from the immune system [8,13].

Similarly, *T. denticola* exhibits an outer membrane that contains sheath proteins and lipooligosaccharide, which are also recognized by TLR2 receptors [8]. This bacterium produces proteases such as dentilisin, which degrades collagen, IL-1β and IL-6, besides activating polymorphonuclear neutrophils (PMNs) via the complement C3 pathway [8,14]. Regarding *T. forsythia*, this specimen presents LPS and leucine-rich-repeat protein (BspA) in its surface that bind to TLR2 receptors [15]. As a distinctive feature, *T. forsythia* has a surface layer formed of glycosylated proteins that prevent immune recognition [8].

Despite the role of these bacteria in periodontitis onset and their ability to induce damage to the periodontium via the expression of collagenases and other proteases, it is the host's inflammatory response that primarily contributes to tissue destruction [10]. Initially, neutrophils, macrophages and T lymphocytes are the most prevalent defensive cells, while advanced lesions display augmented number of B lymphocytes and the detection of immunoglobulins [10].

Activated PMNs produce reactive oxygen species (ROS) in the attempt to eliminate pathogenic microorganisms [16]. However, the overproduction of ROS causes intracellular damage (e.g., DNA, cell membrane) in periodontal cells and direct breakage of extracellular matrixes, as collagen. This process triggers the secretion of proinflammatory cytokines and promotes osteoclastogenesis. Furthermore, it impairs the synthesis of extracellular matrix and, at the same time, increases the levels of matrix metalloproteinases (MMPs) at the infected site [16], key proteases involved in the degradation of extracellular matrix of the periodontium [17]. Furthermore, chronic DNA damage induces a senescent phenotype in mammal cells, which are accounted for an additional upregulation of proinflammatory cytokines and the overproduction of MMPs, including MMP-1, -3, -12, and -13 [10].

The augmented levels of proinflammatory interleukins (IL-1β, IL-6, IL-23) and the stimulation of antigen presenting cells by bacteria promote the differentiation of naive CD^{4+} T cells into distinct helper T cells subtypes, including Th1, Th2 and Th17, known for their proinflammatory cytokine production. Th17 cells, in particular, secrete high levels of IL-17 [18]. This interleukin, in turn, recruits more neutrophils and monocytes, exacerbating the inflammatory burden [18]. In addition, IL-17 activates B cells that produce immunoglobulins (IgG and IgM) against recognized bacterial components [18,19]. Nevertheless, B cells also produce the receptor activator of nuclear factor κB-Ligand (RANKL) and may synthetize autoantibodies against extracellular matrix components (i.e., collagen, fibronectin, laminin), resulting in stimulated osteoclastogenesis and further tissue destruction [10,19].

In established periodontitis, a positive feedback loop is observed between the inflammatory burden and periopathogens' overgrowth – the inflammatory scenario makes available byproducts from the tissue destruction, as amino acids, iron and heme, which further promotes the growth of periopathogens, resulting in additional inflammation [10]. Moreover, the host's immune response fosters microbial dysbiosis, perpetuating the progression of the disease [9,10]. Considered as an additional aggravating factor, red complex bacteria have the ability to invade and survive within periodontal cells, evading the host immune system, perpetuating their multiplication and dissemination [8,20–22].

Despite all considerations, the standard therapeutic approach for periodontitis relies on mechanical scaling and root planning, aiming the reduction of the pathogenic load, allowing an improved plaque biofilm control by the patient [23]. Being a bacterial-triggered disease, antibiotic regimens were extensively evaluated for PDs. As observed in systematic reviews, there is a tendency of clinical improvements (i.e., probing depth reduction and clinical attachment gain) when systemic antibiotics are employed as auxiliary therapy in comparison to mechanical scaling alone, with significant gains when considering aggressive periodontitis (administrating amoxicillin + metronidazole) [24–27]. However, it is pointed out that this tendency wanes over time and adverse effects are frequently perceived in clinical trials [27]. In addition, these pharmaceutic regimens are not specifically devised for immuno-modulation [28]. Likewise, they may not be effective against internalized bacteria, which can incite diseases' recurrence [29,30]. Compounding these challenges is the increasing antimicrobial resistance against regularly used

antibiotics, including amoxicillin/clavulanic acid, clindamycin, and metronidazole, hampering the usefulness of the already questioned adjutant therapy [31].

Taking together the widespread prevalence, the crippling consequences associated to the progression of periodontitis and the lack of efficacy of current adjutant therapies, an alternative approach is urgent to tackle periodontitis.

1.2. Reviewing The In-Situ Delivery Strategies of Repurposed Tetracyclines – From Micro to Nanoparticles

The review article of this section was published as Martin V, Bettencourt AF, Santos CF, Gomes PS. Reviewing particulate delivery systems loaded with repurposed tetracyclines – From micro to nanoparticles. Int. J. Pharm 2024.

DOI: 10.1016/j.ijpharm.2023.123642

1.2.1. Tetracyclines

Tetracyclines (TCs) are a class of broad-spectrum antibacterial drugs that exert their antimicrobial effects by binding to the bacterial 30S ribosomal subunit, thereby inhibiting the protein synthesis. This allows the effective targeting of aerobic, anaerobic, gram-positive, and gram-negative bacteria [32]. Additionally, it has been reported that TCs also possess activity against other microorganisms, as fungi (e.g., mycoplasmas, *Candida albicans*), viruses (e.g., HIV, SARS-COV2), and protozoan parasites (e.g., *Entamoeba histolytica*, *Leishmania major*) [33–35]. The origin of tetracyclines began with the discovery of chlortetracycline (Aureomycin®) and oxytetracycline (Terramycin®), the first and second compounds isolated from *Streptomyces spp.* bacteria [36]. The third antibiotic of the group, tetracycline, was developed by submitting chlortetracycline to catalytic hydrogenation, generating the first semi-synthetic antibiotic approved by the Food and Drug Administration (FDA), in 1954, for clinical use [36]. In comparison to its predecessors, tetracycline presented higher potency and a more favorable solubility profile, resulting in improved pharmacological activity. Throughout the 1960's, several attempts to enhance the structural features of TCs resulted in the second generation of TCs - doxycycline (1967) and minocycline (1971). These drugs presented improved solubility in water, extended half-life, and increased plasma protein binding, contributing to enhanced pharmacological profile and antibacterial activity [37,38] (Figure 1).

For decades, TCs were widely prescribed for their broad-spectrum antibacterial activity. However, their effectiveness has significantly reduced due to a rapid evolution and spread

of bacterial resistance across several species [38]. To address this issue, the third generation of TCs was introduced, starting with tigecycline, the first tetracycline designed to overcome bacterial resistance, approved in 2006. It was followed by omadacycline and eravacycline (2018) [39]. This newer generation of TCs features chemical alterations, mainly in the R9 position (Figure 1), rendering the capability to overcome bacterial resistance mechanisms. This is achieved by inhibiting tetracycline efflux proteins and preventing the dislodgement of the antibiotic from the bacterial ribosome by protective proteins [38–40].

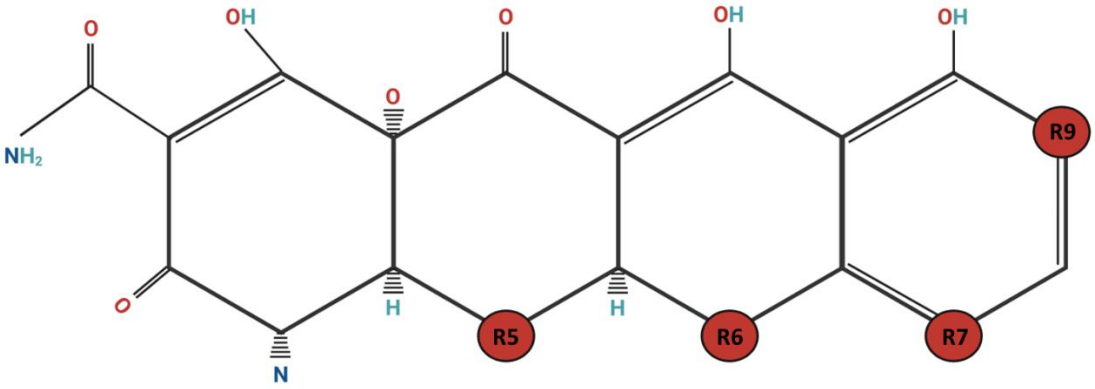

Figure 1. Chemical structure of tetracyclines, featuring the characteristic four tetracyclic naphthacene carboxamide ring system. Red spheres indicate typical segments for modifications. In relation to tetracycline, doxycycline has R5 and R6 alterations; minocycline has R6 and R7 changes; and tigecycline, omadacycline, and eravacycline have modifications at R6, R7 and R9 positions.

Notably, besides their antimicrobial activity, TCs' pleiotropic effects in eukaryotic cells have been described since 1983, following their ability to modulate extracellular enzymes activity [36]. Presently, TCs are acknowledged by their potent anti-inflammatory and antioxidant activities, inhibitory effects on collagenases and distinct matrix metalloproteinases (MMPs), and stimulation of osteogenesis [32,41]. Moreover, it has been reported that TCs exhibit anticancer activity, by inhibiting the mitochondrial biogenesis in cancer stem cells, besides preventing metastatic invasion [42,43].

Despite these promising pleiotropic effects, utilizing TCs for alternative clinical applications often requires high doses in extended posological regimens, leading to adverse effects including significant hepatotoxicity [44,45]. Additionally, administering TCs systemically may lead to varying and unpredictable levels of drug concentration across tissues, which can result in inconsistent therapeutic effects [46]. As a result, the repositioning of TCs has been limited to conditions such as acne and periodontitis, relying on the use of low dose formulations (e.g., Doryx®, Ximino®, MinoLira®, Periostat®)

[47]. In contrast, local drug delivery strategies aim to maximize the targeted delivery of therapeutics to specific sites, minimizing off-target accumulation and associated systemic adverse effects [28,48]. To achieve this goal, drug carrier systems - biocompatible devices as hydrogels, fibers, and particulates, have been developed to effectively transport and release drugs at targeted locations [49]. These systems have been developed for a myriad of clinical applications, varying from dermal wound healing to aortic aneurysms [50,51]. Local drug delivery also enables the repositioning of several drugs that have already been approved by regulatory agencies, including TCs [52]. Repurposing a drug for new applications outside its original scope offers some advantages over developing a new medication. Since pre-clinical and safety assays have already been performed for these drugs, the repurposing strategy reduces the time frame, financial investment, and risk of failure associated with drug development [52]. In the case of TCs, *in situ* drug delivery systems loaded with these agents were assessed pre-clinically for novel clinical applications (Figure 2), such as bone regeneration [53], osteoarthritis [54], psychosis [44], central analgesia [55], depression [56], spinal cord injury [57], abdominal aortic aneurysm [58], and cancer [43]. Moreover, due to their cost-effectiveness and widespread availability, TCs have also been used as hydrophilic drug models for the development of drug release platforms for unspecific indications [59,60].

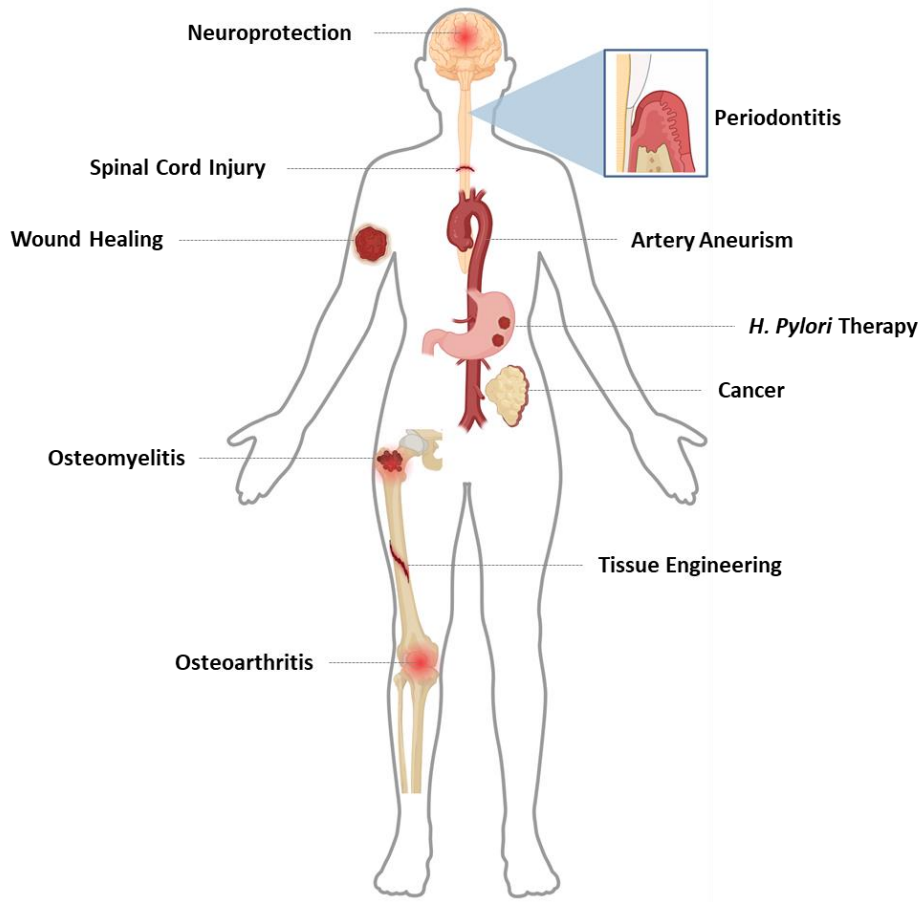

Figure 2. Alternative clinical applications that tetracyclines have been repurposed for in pre-clinical settings, enabled by local drug-delivery systems.

Entrapped drugs within these carriers can be protected from external factors as pH fluctuations, enzymatic degradation, and oxidation. In addition, this approach creates a local drug reservoir, extending drug bioavailability and half-life, addressing the main shortfalls of using free drugs [61–63]. Consequently, posological regimens can be established with fewer administrations, increasing patient convenience and compliance [64]. In this regard, the sales of drug delivery systems generated more than 200 billion USD in 2020, with an estimation of surpassing 300 billion USD, by 2025 [49].

Among all drug-delivery systems, micro and nanoparticles stand out as versatile and promising tools, being directly employed into living tissues or incorporated into other carrier system, improving drug release profiles and mechanical characteristics [65,66]. These particles can have either a homogenous matrix, where the carrier material and the drug are mixed resulting in an indistinguishable core and outer layer; or a core-shell structure, with the drug usually confined to the core with a protective layer surrounding it [63,64]. Figure 3 displays the main types of micro and nanoparticles, as well as their drug-loading alternatives.

Currently, studies exploring TCs' loading onto micro and nanoparticles for local delivery tend to focus on specific clinical applications, which precludes the comparison of different platforms' developmental aspects, loading strategies, and ability to avoid off-target effects in a broader context. Additionally, a comprehensive analysis of the induced biological responses is lacking.

Therefore, the present review aimed to assess and critically discuss the current literature on TCs-loaded micro/nanoparticles for biomedical applications. The exploration encompasses different materials, drug loading methods, and the achievement of different drug release profiles through the manipulation of their composition, formulation, and properties. For a comparative analysis, studies were categorized by their scale, distinguishing between micro and nano particles, reflecting the historical development of these technologies. By examining these aspects, this review seeks to shed light on influential formulation characteristics of TCs-loaded micro/nanoparticles, identify their limitations, and highlight prospects. Ultimately, it offers guidance for an upcoming rational development of these systems, underlining important aspects that need to be considered in their clinical translation.

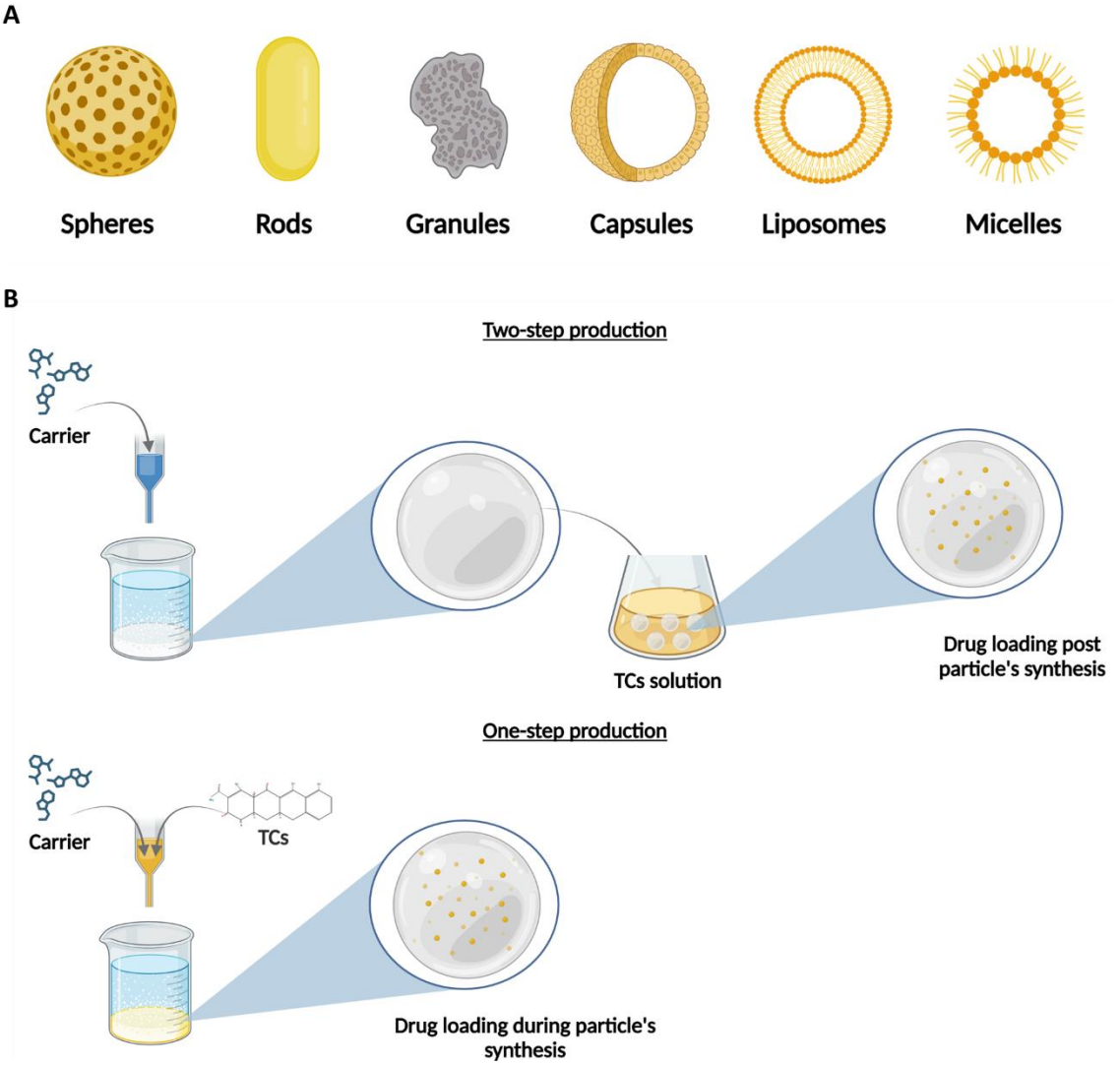

Figure 3. (A) Schematics depicting the main types and shapes of micro/nanoparticulate platforms conjugated with TCs. Spheres, rods, and granules usually exhibit a homogenous matrix, while capsules, liposomes, and micelles broadly feature distinct layers. (B) Schematics illustrating the preparation methods, where vehicles can be loaded either during or after their synthesis.

1.2.2. Microparticles

In the present review, microparticles and microspheres were defined as biocompatible and bioactive particles with a diameter greater than 1000 nm [67]. Compared to nanoparticles (Figure 4), micro-scale materials present certain characteristics that can be advantageous for specific scenarios. Due to their larger particle size, microparticles tend to have a slower release rate due to the smaller surface area to volume ratio, and also a slower clearance, as they are unlikely to cross biological barriers [64]. Likewise, microparticles are less readily taken up by most type of cells, except for macrophages, neutrophils, and dendritic cells, enabling a targeted delivery to these phagocytic cells, which can be exploited in the development of vaccines [68]. Additionally, the conjugation

of large-size biological molecules as proteins and nucleic acids is simpler in micro-scale materials in comparison to nanoparticles [63,64].

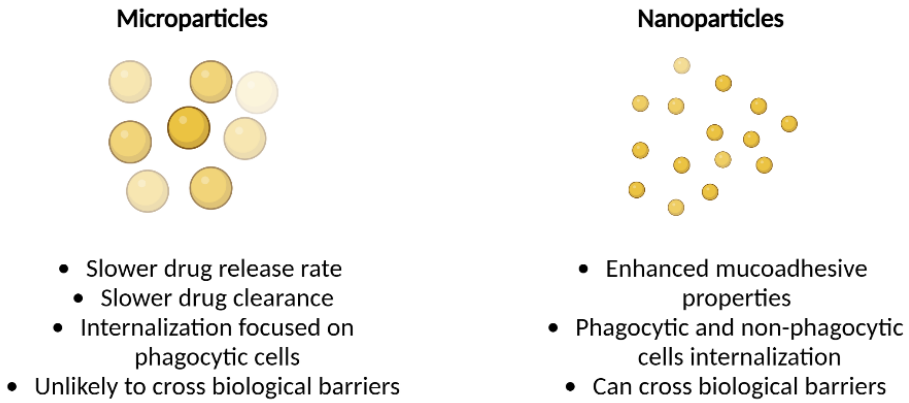

Figure 4. Comparison between micro and nanoparticles, highlighting their main advantages.

TCs loading into microparticles was vastly explored for local drug delivery, with some studies focused on technical feasibility, physicochemical characteristics assessment and drug release profiles [69–72]. However, most of TC-loaded microparticles' systems were developed for periodontal diseases' treatment (Table 1).

The conventional periodontal therapy encompasses the mechanical removal of the dental plaque and calculus, reducing the bacterial load, aiming for the disease control [73]. However, in challenging anatomical environments (as deep periodontal pockets and furcation areas), an adjunctive drug therapy can be necessary to improve the treatment outcome. In this context, local TC delivery is a promising adjunct therapy to the mechanical debridement, preventing infectious relapses through its antimicrobial activity, and further modulating the host inflammatory response to reduce the destruction of periodontal tissues [74].

Microparticles carrying TCs have been available in the market, since the 2000s, for periodontitis treatment - ARESTIN® - poly(lactic-co-glycolic acid) (PLGA) microspheres loaded with 1 mg of minocycline. Randomized clinical trials documented significant benefits in clinical parameters, as reduced pocket depth, in patients that received the adjuvant therapy [75]. Since then, alternative microparticulate systems were developed to further improve the treatment outcomes. These systems often rely on the functionalization of synthetic polymers or bioactive platforms, as chitosan and biphasic calcium phosphate (BCP) [76–81]. For instance, the incorporation of other synthetic polymers, as polycaprolactone (PCL), into PLGA matrixes resulted in a higher initial burst release and a gradual continuous discharge up to 10 days, in comparison to PLGA-only particles, since PCL facilitates water penetration into the amorphous regions of the

matrix [77,78]. Clinical trials were performed with these developed materials, however comparison took place with scaling and root planning and commercial gels containing TCs, preluding a direct comparison with previous microparticles-based systems [77,78].
Setting on another approach, alginate-coated PLGA-chitosan microspheres containing tetracycline were developed, taking advantage of the alginate's anti-inflammatory effects and its ability to reduce protein adsorption over the microspheres' surface [79]. Alginate-coated microspheres presented a higher load efficiency and a higher cumulative release, resulting in a higher total discharge in comparison to uncoated materials [79]. No cytocompatibility nor antibacterial effects of these coated particles were assessed, preventing further conclusions.
Regarding chitosan-based platforms, loading TCs is relatively straightforward, relying on simple and more ecologic techniques that avoid organic solvents, as dichloromethane or chloroform [82]. However, the obtention of an optimal encapsulation efficiency and drug release for water-soluble drugs as TCs can be challenging and may require further adjustments or additives in the formulations. For instance, adding tetracycline to chitosan solution prior to the ionic gelation with tripolyphosphate (TPP) presented significantly higher tetracycline entrapment, in comparison to the addition of the antibiotic into the TPP before the ionic gelation with chitosan solution [83]. Other studies have incorporated additives as calcium alginate or ethyl cellulose in the attempt to overcome the limitations of chitosan platforms [80,84]. These approaches seem to improve the drug release kinetics of TCs from chitosan microparticles, while maintaining their cytocompatibility and antibacterial activity [80,84]. Nevertheless, it is worth noting that currently, no chitosan-based microparticle are available in the market. Alternatively, TCs-loaded methylcellulose particles were also evaluated for periodontitis treatment, and randomized clinical trials presented promising results compared to scaling and root planning alone, though a comparison with other material-based approaches is still to be performed [85,86].
Furthermore, modifying the shape of microparticulate can confer improved adhesive properties. In the oral environment, while microspheres can be quickly removed from the crevicular region by the drainage of its fluid and high saliva turnover, concave alginate-based microparticles were found to exhibit better attachment to teeth roots even under water washing, performing significantly better than their sphere-shaped counterparts [87]. Additionally, the drug release from this microparticulate system was triggered by near-

infrared (NIR) irradiation, due to the presence of a photothermal activator in the formulation (i.e., black phosphorous), offering greater control to the operator [87].

Ceramic microparticles containing TCs have also been evaluated for periodontitis treatment. However, unfavorable TC release profiles and inadequate degradation profiles may limit their usage in the crevicular microenvironment [81]. Nevertheless, this class of vehicle can be considered appropriate for bone regeneration and osteomyelitis-related therapies, due to their ability to chemically anchor to the natural osseous matrix, leveraging their similarities [88]. In this frame, modified bioactive glass (BG) and hydroxyapatite (HA) particles were developed focusing on extending the drug loading and TCs-release period for bone applications [53,88,89]. As TCs-loaded HA and HA microspheres were assessed in experimental alveolar sockets defects. Despite that no statistical differences were observed in new bone formation between the control and the TCs-HA microspheres group, these materials demonstrated antibacterial activity for up to 7 days, which can be particularly useful for infected sites [90].

TCs-loaded microparticles were also employed for gastrointestinal applications. By exploring their mucoadhesive properties, chitosan microspheres were developed to target *Helicobacter pylori*. Given the inherent instability of free antibiotics in the low pH of gastric fluids and their inability to reach bacteria beneath the mucosa at effective concentrations, this approach holds potential [91,92]. In initial attempts using an *in vivo* gerbil model, TCs-loaded microspheres failed to provide significant benefits. However, when chitosan was crosslinked with glyoxal, attained microparticles were able to adhere to the stomach mucosa, extending the detection time in the stomach from 2 to 10 h after the administration, providing a local tetracycline release of 6 h [93,94]. The alternative crosslinking enhanced the microspheres' stability under acidic conditions and facilitated electrostatic interactions between chitosan and gastric mucosa.

Table 1 comprehensively summarizes the included studies on TCs-loaded microparticles, showcasing distinct applications of these innovative drug delivery systems across various therapeutic domains.

Table 1. Included studies of microparticles conjugated with TCs, grouped by clinical applications.

Authors / Reference	Tetracycline	Material	Indication	Other added substances	Drug Loading Method	Mean size (µm)
Torshabi et al. [74]	Minocycline	PLGA	Periodontitis	Metronidazole, and Ciprofloxacin	During synthesis	10
Liu et al. [79]	Tetracycline	PLGA + Chitosan coated with alginate	Periodontitis	–	During synthesis	60 to 100

Srirangarajan et al. [78]	Doxycycline	PLGA + PCL	Periodontitis	–	During synthesis	90 to 200
Mundargi et al. [77]	Doxycycline	PLGA + PCL	Periodontitis	–	During synthesis	90 to 200
Gjoseva et al. [80]	Minocycline	Chitosan	Periodontitis	–	During synthesis	3.7 to 7.8
Victor and Kumar [81]	Doxycycline	BCP	Periodontitis	–	Post synthesis	1
Yadav et al. [84]	Doxycycline	Chitosan + Calcium alginate	Periodontitis	Ornidazole	During synthesis - TC into calcium alginate sol	74 to 461
Wang et al. [76]	Doxycycline	PLGA	Periodontitis	–	During synthesis	1
Govender et al. [83]	Tetracycline	Chitosan	Periodontitis	–	During synthesis	1000 to 2000
Moura et al. [95]	Doxycycline	PLGA	Periodontitis	–	During synthesis	1 to 5
Rao et al. [86]	Doxycycline	Methylcellulose	Periodontitis	–	During synthesis	--
Zhao et al. [96]	Minocycline	PLGA	Periodontitis	–	During synthesis	11.4
Song et al. [87]	Minocycline	Photo-curing Alginate + PEG diacrylate	Periodontitis	Black phosphorus	During synthesis	200
Chiappe et al. [85]	Minocycline	Methylcellulose	Periodontitis	–	During synthesis	800
Zheng et al. [53]	Tetracycline	Pollen-templated bioactive glass	Bone regeneration	–	Post synthesis	44
Murugan and Ramakrishna [88]	Tetracycline	Coralline HA + glycidylmethacrylate	Bone regeneration	–	Post synthesis	> 50
Soriano-Souza et al. [90]	Doxycycline	HA	Bone regeneration	–	Post synthesis	400
Aydin et al. [54]	Doxycycline	PCL	Osteoarthritis	Chondroitin	During synthesis	12 to 75
Calasans- Maia et al. [89]	Minocycline	Alginate + HA	Bone infection	–	Post synthesis - Adsorption into HA	400
Hejazi and Amiji [92]	Tetracycline	Chitosan	Stomach-specific delivery	–	During OR Post synthesis	3
Hejazi and Amiji [93]	Tetracycline	Chitosan	Stomach-specific delivery	–	During synthesis	3
Hejazi and Amiji [94]	Tetracycline	Chitosan	Stomach-specific delivery	–	Post synthesis	3
Cruz et al. [91]	Oxytetracycline	Alginate + Chitosan + PEG	Stomach-specific delivery	–	During synthesis - Into alginate sol	600 to 800
Fwu-Long et al. [97]	Oxytetracycline	Chitosan	Oral and Intramuscular administration	–	During synthesis	5 to 710
Patel et al. [98]	Minocycline	PLGA	General Drug release	–	During synthesis	14 to 18
Kim et al. [69]	Tetracycline	PLGA	General Drug release	–	During synthesis	88
Fundueanu et al. [70]	Tetracycline	Sulfopropylated dextran + Cellulose acetate	General Drug release	–	During synthesis	130 to 416
Gillissen et al. [71]	Doxycycline	PVA	General Drug release	–	During synthesis	10 to 60
Caroni et al. [72]	Tetracycline	Chitosan	General Drug release	–	Post synthesis	69
Sousa et al. [99]	Tetracycline	PLGA + Zein	General Drug release	–	During synthesis	--

Bittner et al. [100]	Tetracycline	PLGA	General Drug release	–	During synthesis	1.2 to 600
Garg et al. [101]	Tetracycline	Bioactive glass	General Drug release	–	During synthesis	5
Trofin et al. [102]	Tetracycline	Glycidyl methacrylate OR monochloroacetate	General Drug Release	–	Post synthesis	400

Abbreviations: PVA - Poly(vinyl alcohol). HA - Hydroxyapatite. PCL - Polycaprolactone. BCP - Biphasic calcium phosphate. PLGA - Poly(lactic-co-glycolic acid). PEG - Polyethylene glycol.

1.2.3. Nanoparticles

From a regulatory perspective, nanoparticles (NPs) are defined as solid materials with at least one dimension ranging between 1–100 nm, a size range that facilitates the passage through biological barriers, expanding the potential for biological modulation [67,103]. However, particulate materials with a size between 1.0 and 1000 nm are also considered as nano-scale materials by industry standards, which is the definition applied in this review [67,104].

The smaller size of NPs enables challenging clinical applications that are often unachievable by microparticulate platforms. For instance, NPs have been used in gene therapy (aiming the manipulation of nucleic acids of defective genes) and in targeted drug delivery to sheltered structures as the central nervous system (CNS), lymphatic system and solid tumors, using minimally invasive techniques such as the intravenous administration [57,67,105]. Due to their smaller size and increased surface area, NPs possess enhanced mucoadhesive properties and tend to exhibit higher drug release rates [106]. Moreover, alternative administration routes can also be envisaged by their reduced size. For instance, subcutaneous injection of NPs (ranging from 10 to 100 nm) can directly reach lymphatic vessels, avoiding their retention within the administration site and the systemic circulation, which could be more effective than the systemic administration of antifilarial drugs against lymphatic filarial parasites [107].

Unlike microparticles, NPs can also be taken up by non-phagocytic cells by endocytosis and transcytosis (Figure 5), allowing for drug and gene delivery in several types of cells, including osteoblasts, epithelial cells, and neurons [108]. While larger NPs (mean size over 200 nm) are mainly internalized through macropinocytosis (i.e., non-selective process that involves the engulfment of fluids and particles nearby the plasma membrane, without a specific size or shape) [109], smaller NPs can also be uptaken via clathrin- and caveolae-mediated endocytosis, selective processes limited by particle's size (≤ 200 nm) [109,110]. However, these extended possibilities add another layer of complexity in the development of NPs. For instance, depending on the type of endocytosis induced by the

nanoparticulate, they must be resistant to the lysosomal environment to reach the cytosol intact, or escape from endosomes prior to their fusion with lysosomes [67].

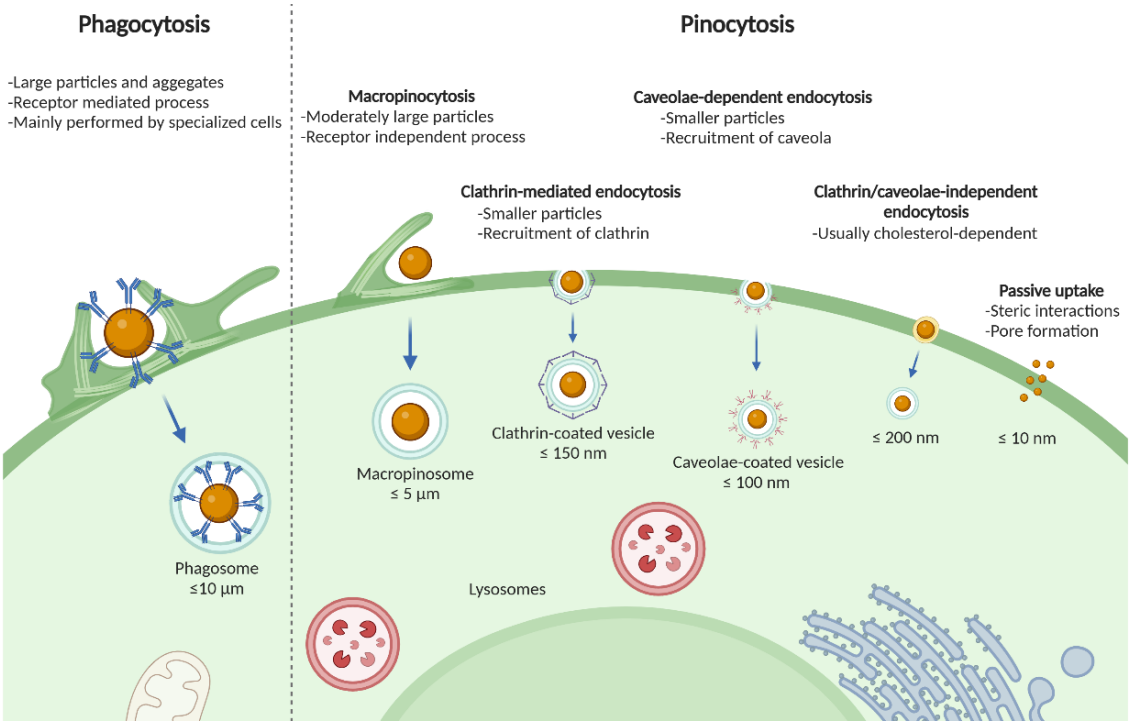

Figure 5. Particle's endocytic pathways. Microparticles, NPs > 200 nm and NP's clusters are mainly internalized via actin-dependent processes, as phagocytosis and macropinocytosis. Alternatively, smaller particles can be internalized through specific routes that are actin-independent processes, as clathrin and caveolae mediated endocytosis, clathrin/caveolae independent endocytosis and passive uptake. Clathrin/caveolae independent endocytosis requires specific NP's lipidic composition, while passive uptake relies on van der Waals forces or adhesive interactions between NPs and the cell membrane.

Moreover, the electric charge of NPs can modulate their clearance rate from the blood circulation, as well as their accumulation in the liver, which can potentially result in hepatotoxicity and reduce effectiveness in the targeted tissues [67,105,111]. Despite these emerging challenges, NPs are considered promising platforms for potent and less toxic therapies, with more than 30 nanodrugs approved by the FDA in the recent decades [67]. In fact, in addition to improving the outcome of medications for their established therapeutical objectives, nanoparticle conjugation has also enabled the innovative use of existing drugs for distinct clinical applications, including TCs.

For instance, it has been demonstrated that doxycycline and minocycline have neuroprotective activity, being beneficial for a variety of neurological disorders including Parkinson's disease, multiple sclerosis, spinal cord injury, and depression [56,112]. However, high doses must be administered systemically due to their relatively short half-life and restricted passage through the blood-brain-barrier (BBB). This results in adverse

effects, morbidity, and significant liver toxicity, preventing a feasible employment of TCs to treat these conditions [44,45]. In this context, loading these drugs into NPs has the potential to repurpose them for neurological disorders, aiming a targeted and controlled drug delivery to the CNS, thereby reducing or avoiding the systemic adverse effects observed with free drug administration [44,45,105]. Their neuroprotective effects are set on their anti-inflammatory, anti-MMPs, and anti-oxidative properties, as well as the ability to increase monoamine levels in the brain by inhibiting MAO-A activity [56].

In this frame, chitosan NPs were loaded with minocycline to tackle depression, provide memory enhancement and central analgesic activity in *in vivo* models, through intraperitoneal or intravenous administration [55,56,105]. Interestingly, two distinct vehicle formulations were synthesized and compared, chitosan only and chitosan with Tween®80, a non-ionic surfactant that can improve the penetration of NPs into the BBB. This is achieved by its ability to bind to plasma Apo-E lipoprotein, mimicking low density lipoproteins (LDL) and further attaching to LDL receptors of endothelial cells of the cerebral micro vasculature [44]. Therefore, the presence of the surfactant (Tween®80) could enable NPs' transcytosis across the endothelium, increasing the subsequent uptake by neuronal cells [55]. It was noted that chitosan NPs without Tween®80 failed to induce a clear activity in the CNS, while the administration of NPs with the surfactant resulted in significant improvements for all neurological disorders assessed. In addition, the inclusion of surfactant led to a decreased accumulation of minocycline in the liver, spleen, and kidney, suggesting enhanced brain uptake and improved drug safety by decreasing the systemic toxicity. Regarding physicochemical characteristics, the addition of the surfactant resulted in smaller particle size (approximately 200 nm) and lower polydispersity index (PDI), without altering the positive zeta potential of the NPs or their drug release profile [105]. Similarly, chitosan and Tween®80 were used to encapsulate doxycycline for antipsychotic therapy and assessed upon oral administration within an *in vivo* model. The surfactant provided protection to the drug against first-pass effect, facilitating the entrance of the NPs into the systemic circulation and, further, the brain uptake via absorptive transcytosis. Results showed increased levels of gamma-aminobutyric acid (GABA) and diminished levels of dopamine, presenting analogous clinical outcomes as observed with olanzapine administration (an antipsychotic drug) [44]. However, all analyzed chitosan-based nanoparticles presented a relatively short drug release ability, lasting no longer than 24 h.

In addition to chitosan, synthetic polymeric NPs have also been developed for CNS delivery of minocycline. However, these materials may face opsonization by the reticuloendothelial system, requiring a surface modification with hydrophilic substances to avoid premature degradation and their phagocytosis by immune cells [67,113]. A PLGA/chitosan NPs system containing albumin was developed, relying on its moistening properties and capability to bind to gp60 receptors (albondin), widely distributed at inflammatory and neoplastic sites [57]. This facilitated NPs internalization through transcytosis in targeted areas. Albumin-coated NPs presented a controlled release of minocycline for 7 days, improving all functional outcomes and mitigating the inflammatory condition by preventing an inflammatory profile of glia cells in a spinal cord injury *in vivo* model [57,114,115].

It is worth noting that the free form of minocycline presents a higher liposolubility in comparison to doxycycline, allowing it to cross the BBB more efficiently, resulting in 2.2-fold higher brain levels than doxycycline after IV administrations in a pre-clinical model [55,116]. However, it remains unclear whether their nano-conjugated forms exhibit a similar trend.

Regarding antimicrobial activity, NPs loaded with TCs can provide enhanced penetration and antibacterial efficacy, demonstrating effectiveness against tetracycline-resistant strains, and potentially attenuating the burden of the current antibiotic resistance scenario [117–119]. To achieve a synergetic antibacterial effect, TCs have been conjugated with metallic and metallic oxide particles, as gold (Au), silver (Ag), and magnesium oxide (MgO) NPs. These nanoconjugates harness their bactericidal activity by inducing intracellular ROS generation and disturbing bacterial cell walls [119,120]. In fact, studies observed that TC-AgNPs presented greater inhibition of bacterial growth compared to the individual use of tetracycline or unloaded AgNPs [119]. By forming TC-AgNPs complexes, the linkage to bacteria cell wall is enhanced, resulting in increased Ag^{2+} activity. Moreover, the presence of tetracycline in the formulation doubled the release of Ag^{2+} from the NPs. Similarly, TC-AuNPs, significantly reduced the minimal inhibitory concentration of unloaded AuNPs against TC-resistant Gram-positive and Gram-negative bacteria [118,119]. Furthermore, TC-ZnO NPs were found to be effective against multi-drug resistant bacteria, even at concentrations where free tetracycline showed minimal antibacterial activity [120]. These findings highlight the potential of TC-conjugated metallic/metallic oxide NPs as promising strategies to combat antibiotic-resistant bacterial infections.

Recent studies have highlighted the potential of carbon NPs (C-NPs) as promising drug delivery systems given their excellent biocompatibility [121]. In addition, C-NPs were shown the ability to inhibit bacterial drug extrusion from efflux pumps, overcoming tetracycline resistance in bacteria [117]. It has been demonstrated that unloaded C-NPs lacked antibacterial activity, while TC-C-NPs significantly reduced the minimal inhibitory concentration of TCs, up to tenfold against some Gram-negative bacteria, as *Klebsiella* and *Acinetobacter spp.* [117].

Aside from localized and extended-release benefits provided by microparticles and other platforms, nano-scale materials have shown additional effectiveness against intracellular pathogens, a feat not easily achieved by microparticulate or most free antimicrobial drugs. Traditional antimicrobial drugs broadly fail to actively penetrate cellular membranes, hindering their ability to impede the replication of internalized pathogens [29,30,110,122]. These intracellular bacteria reservoirs can ultimately lead to disease persistence, recurrence, and dissemination to adjacent tissues, exacerbating the infection progression [123]. For instance, *S. aureus*, responsible for 80% of all diagnosed osteomyelitis cases, can form small colonies that grow inside nonprofessional phagocyte cells, evading the immune system and contributing to the chronicity of the disease [122,123]. Intracellular infections play a pivotal role in osteomyelitis recurrences and intensified bone loss, due to the induction of inflammatory mediators in the host cells [123]. Analogously, *P. gingivalis* – a keystone periodontal pathogen – can invade oral keratinocytes and gingival fibroblasts, with studies documenting the presence of *P. gingivalis* in epithelial cells collected from patients who underwent systemic antibiotic therapy [124].

Unsurprisingly, several studies have described the production and characterization of NPs loaded with TCs for both osteomyelitis and periodontal conditions, using chitosan, poly-lactide acid (PLA), PLGA and ceramics as carrier systems [110,125,134–136,126–133]. Despite presenting favorable outcomes as increased bone formation, reduced probing depth, and diminished levels of inflammatory markers, most studies did not specifically evaluate the intracellular antibacterial activity of the developed systems, preventing definitive conclusions about their efficacy against internalized bacteria and, therefore, their ability to reduce recurrences in the long term [110,117,127,128,135,136]. In reality, the treatment of intracellular infections remains a complex challenge, and the lack of standardized models or guidelines to assess these conditions hinders effective progress in this matter [122]. Nonetheless, TCs-loaded NPs hold potential as a viable alternative

for treating intracellular infections and even overcome bacterial resistance to free TCs [117].

Lastly, groundbreaking approaches strive for the development of carrier-free nanoantibiotics. Relying on high frequency ultra-sound (at 490 kHz, 9.6 W cm^{-3}), it was documented the transformation of a doxycycline solution into doxycycline NPs [137]. The characterization of the system suggested that NPs formation was achieved by a partial oxidation of the molecule that resulted in doxycycline dimerization (C-C coupling). While carrier-free NPs presented an enhanced radical scavenging activity in comparison to the doxycycline solution, the antibacterial activity was found to be significantly reduced, particularly against Gram-negative strains. Despite the drawbacks reported and the absence of drug release and cytocompatibility evaluation, this approach is promising in simplifying the NPs' production [137]. Table 2 summarizes the included studies of NPs loaded with TCs.

Table 2. Included studies about TCs loaded to nanoparticles, grouped by clinical applications.

Authors / Reference	Tetracycline	Material	Indication	Other added substances	Drug Loading Method	Mean size (nm)
Madhumathi et al. [134]	Tetracycline	Calcium-deficient HA	Periodontitis	Ibuprofen	Post synthesis	≤ 100
Madhumathi and Sampath Kumar [136]	Tetracycline	Calcium-deficient HA	Periodontitis	–	Post synthesis	30 to 40
Liang et al. [125]	Minocycline	Chitosan	Periodontitis	–	During synthesis	100
Lecio et al. [129]	Doxycycline	PLGA	Periodontitis	–	During synthesis	≤ 1000
Martin et al. [110]	Minocycline	Chitosan	Periodontitis	–	During synthesis	50
Yao et al. [127]	Minocycline	PEG/PLA	Periodontitis	RGD peptide	During synthesis	90 to 110
Yao et al. [130]	Minocycline	PEG/PLA	Periodontitis	–	During synthesis	100
Kashi et al. [131]	Minocycline	PEG/PLGA	Periodontitis	Lecithin	During synthesis	85 to 424
Tong et al. [138]	Minocycline	Magnetic FeO coated with dopamine	Periodontitis	–	During synthesis	217 to 273
Lee et al. [126]	Tetracycline	PLGA + Chitosan	Periodontitis	Lovastatin	During synthesis	105 to 111
Marycz et al. [139]	Tetracycline	Nanocrystalline Calcium phosphate	Bone regeneration	–	During synthesis	22 to 79
Venkatesan et al. [135]	Tetracycline	HA and Calcium-deficient HA	Bone regeneration	–	Post synthesis	50 to 400
Cazalbou et al. [140]	Tetracycline	Nanocrystalline apatite	Bone regeneration	–	Post synthesis	--
Cortés et al. [141]	Tetracycline	BG particles	Bone regeneration	Cyclodextrin	During synthesis	100
Lee et al. [142]	Tetracycline	Ag-doped mesoporous BG	Bone and Dental regeneration	–	Post synthesis	60
Ignjatovic et al. [132]	Tigecycline	CaP + Poly(DL-lactide-co-glycolide)	Bone regeneration	–	During synthesis - into PLGA	65 to 95

Ignjatovic et al. [143]	Tigecycline	CaP + Poly(DL-lactide-co-glycolide)	Bone regeneration	–	During synthesis - into PLGA	65 to 95
Wang et al. [128]	Tetracycline	PLGA	Bone regeneration	Simvastatin	During synthesis	220
Tham et al. [144]	Minocycline	Polycaprolactone + Silk fibroin + Hyaluronic acid	Bone regeneration	–	During synthesis	540
Nagpal et al. [105]	Minocycline	Chitosan	CNS drug delivery	–	During synthesis	155 to 636
Nagpal et al. [55]	Minocycline	Chitosan	CNS drug delivery - Anti-nociceptive	–	During synthesis	165
Nagpal et al. [56]	Minocycline	Chitosan	CNS drug delivery - Depression	–	During synthesis	155
Holmkvist et al. [45]	Minocycline	PLGA + Bis(2-ethylhexyl) sulfosuccinate + Ca	CNS drug delivery	–	During synthesis	220
Yadav et al. [44]	Doxycycline	Chitosan	CNS drug delivery - Psychosis	–	During synthesis	237
Zhang et al. [112]	Minocycline	Dextran + $CaCl_2$ or $MgCl_2$	CNS drug delivery - Neuroprotective	–	During synthesis	50 to 100
Xiao-Feng et al. [57]	Minocycline	PLGA + Chitosan + Albumin	Spinal cord injury	Prednisolone	During synthesis - into PLGA	153 to 188
Papa et al. [114]	Minocycline	Poly-ε-caprolactone	Spinal cord injury	–	During synthesis	102 to 108
Papa et al. [115]	Minocycline	Poly-ε-caprolactone + PEG	Spinal cord injury	–	During synthesis	102 to 108
Lin et al. [145]	Minocycline	Poly-A-Lipoic acid	Spinal cord injury	Methylprednisolone	During synthesis	60
Dhanalakshmi et al. [51]	Tigecycline	Chitosan	Wound healing	Lecithin	During synthesis	85 to 235
Marto et al. [146]	Minocycline	Starch	Cutaneous delivery	–	During synthesis	498
Cover et al. [147]	Doxycycline	Chitosan	Uterine infection	–	During synthesis	30 to 320
Wang et al. [148]	Tigecycline	Tocopheryl PEG succinate + CaP S-thanatin peptide	Pulmonary infection	–	During synthesis - TG into CaP + PEG	25 to 28
Seleem et al. [30]	Doxycycline	A-methoxy-x-bromoisobutyrate poly(ethylene oxide)	Liver infection	Streptomycin	Post synthesis	110
Singh et al. [107]	Doxycycline	PLGA	Lymphatic Parasites	–	During synthesis	95
Sivaraman and Ramamurthi [58]	Doxycycline	PLGA	Abdominal aortic aneurysms	–	During synthesis	100 to 500
Das et al. [120]	Tetracycline	Magnesium Oxide	Antibiotic enhancement	–	Post synthesis	5
Ye et al. [149]	Tetracycline	Mesoporous Silica	Antibiotic enhancement	–	Post synthesis	30 to 90
Alavi and Karimi [150]	Tetracycline	Ag NPs	Antibiotic enhancement	–	Post synthesis	≤ 70
Taghizadeh et al. [151]	Tetracycline	Chitosan	General Drug release	Betamethasone	Post synthesis	≤ 5
Zhang et al. [152]	Tetracycline	CaP with and WO poly(acrylic acid)	General Drug release	–	Post synthesis	40
Lima et al. [153]	Tetracycline	Chitosan + Poly(sodium 4-styrenesulfonate)	General Drug release	Cromoglycate	Post synthesis	200
Deng et al. [119]	Tetracycline	Ag NPs	General Drug release	–	Post synthesis	30

Naimi-Shamel et al. [118]	Tetracycline	Au NPs	General Drug release	–	Post synthesis	50
Giammarco et al. [121]	Tetracycline	Nanodiamond	General Drug release	–	Post synthesis	5 to 8
Kim et al. [117]	Tetracycline	Carbon	General Drug release	–	Post synthesis	5 to 10
Wu et al. [154]	Tetracycline	Fe_3O_4 NPs + BSA	General Drug release	–	During synthesis - Into Fe sol	300
Zhu et al. [137]	Doxycycline	Carrier free - DX sol was sonicated to become NPs	General Drug Release	–	Carrier free NP	100 to 200

Abbreviation: Fe_3O_4/FeO - Iron oxide. BSA - Bovine serum albumin. CaP - Calcium phosphate. PLGA - Poly(lactic-co-glycolic acid). PEG - Polyethylene glycol. $CaCL_2$ - Calcium chloride. $MgCl_2$ - Magnesium chloride. CNS - Central nervous system. BG - Bioactive glass. HA - Hydroxyapatite. RGD - Arginylglycylaspartic acid. DX - Doxycycline.

1.2.4. Current limitations and emerging approaches of TCs carriers

As verified in the present review, TCs have been extensively conjugated with micro and nanoparticles, charting their wide-ranging purpose. Within antibacterial applications, most studies reported the usage of tetracycline, followed by minocycline and doxycycline, with other TCs less frequently used for local delivery (Figure 6-A). Despite their pharmacokinetic profile characterized by a short half-life and low protein binding ability [36–38], early generation tetracyclines serve as benchmark drugs to validate synthesis process and assess the drug release capability from carriers, due to their accessibility and suitability for general applications [34]. Oppositely, the limited use of the third-generation TCs (glycylcyclines and aminomethylcyclines) can be attributed to their restricted indications - which is limited for the treatment of severe infections [155], harsher adverse effects [156], as well as their current limited obtainability.

While TCs are well-known for their pleiotropic effects, most clinical applications discussed in this review focused on their antibacterial activity, periodontal diseases' modulation, general drug release, bone tissue applications, CNS/spinal cord-related therapies, and stomach delivery being the more prevalent indications (Figure 6-B). However, only microparticles devised for periodontitis treatment are currently commercial formulations, demonstrating the complexity in the validation of these carriers, as well as in the translation of laboratorial processes to an industrial production.

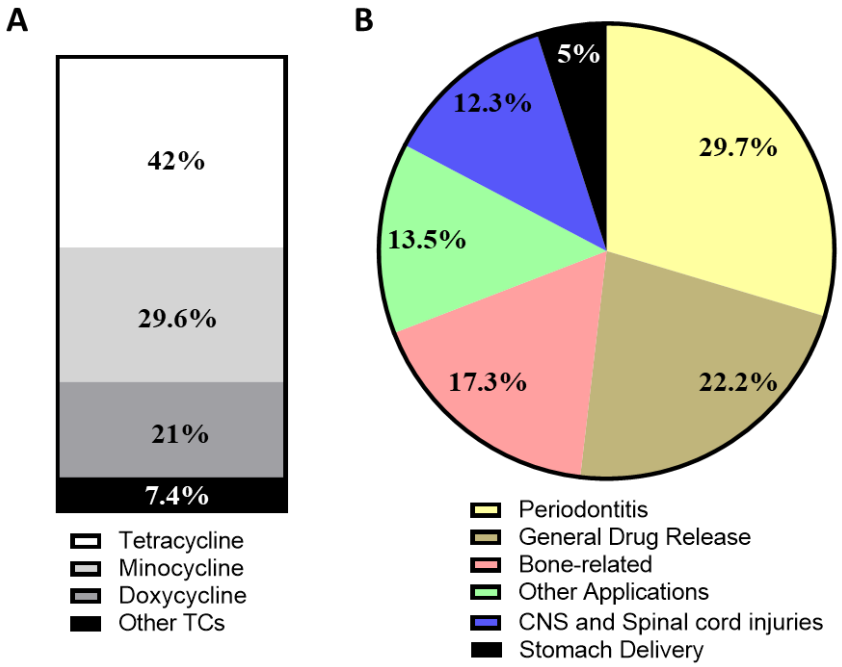

Figure 6. The distribution of (A) tetracycline antibiotics employed and (B) devised clinical applications in the included studies in the review. In total, 81 research articles were included, being 33 grouped as microparticles and 48 as nanoparticles.

Over the last three decades, one of the most important innovations regarding local TCs delivery has been set on drug micro/nano carriers [64,67]. Micro and nanoparticles frequently share the material and techniques of production, with particle size distribution being a controllable feature during synthesis [64,67,131,157]. Particle size directly affects the application of a material, as the possible routes of delivery (e.g., large particles are not suitable for intravenous injection), the delivery approach (e.g., large particles are prone to clog needles), and intended vehicle clearance and systemic distribution (Figure 3) [63,64]. In addition, particle morphology and several physicochemical characteristics (e.g., composition, crystallinity, zeta potential) also play a key role in particle uptake and drug loading [157].

Regarding synthetic polymeric particles, their production relies mostly on the emulsification–solvent evaporation method, and double or multiple emulsions are necessary to encapsulate hydrophilic drugs as TCs, as they tend to partition into the external aqueous phase when a single emulsion is used [157]. TCs' drug release rate from these particles is associated with their matrix degradation and swelling, which can be modulated during production by adjusting the polymer's molecular weight (MW), crystallinity, and porosity (e.g., lower MW/crystallinity accelerates degradation by increasing water diffusion; while pores increase drug mobility and contact surface area) [157,158].

Comparing to synthetic polymers, natural-based materials possess improved bioactivity due to their similarity to natural ECM and can be produced through eco-friendly processes [82]. Chitosan, extensively used for drug encapsulation, provides antibacterial, anti-inflammatory and mucoadhesive capabilities [84]. To synthesize chitosan-based particles, ionic gelation – a physicochemical procedure that is set on the ionic interactions between the positively charged chitosan and a polyanion (e.g., TPP) – is commonly used for encapsulating hydrophilic drugs as TCs, which can be adsorbed onto chitosan through protonation [103,159]. Particle size is influenced by the molecular weight of chitosan, with high molecular weight yielding larger particles, and low molecular weight recommended for obtaining NPs [106]. Moreover, the ratio of chitosan and polyanion solution directly affects particle size and PDI [106]. This method extends to other natural polymers as alginate, cellulose, and collagen, and allows incorporation of metallic salts (e.g., copper, magnesium, and zinc nitrates or sulphates) within the particles [160,161].

Ceramic particles, as HA and β-tricalcium phosphate (β-TCP), can also function as TCs micro/nano-carriers, finding application in hard tissues due to their analogous composition with the mineral constituents [135,139]. However, their TCs' loading ability is frequently limited to post-production methods, as adsorption, as their synthesis mostly relies on very-high temperatures (500 to 1100 °C) for the sintering process [90]. This limitation often results in an acute initial burst release followed by an inability to release the remaining TCs from the platform, as oxygen atoms of TCs can bond with calcium atoms from HA, producing an anchorage between molecules known as chelation [90,135,152]. In fact, TCs are known to chelate divalent cations as Mg^{2+} and Ca^{2+}, forming stable TCs-Ca^{2+} chelates that can provide a stable reservoir of TCs, without affecting their biological activity [112,162]. Moreover, burst TCs release is believed to correspond to unchelated molecules on the surface of ceramic-based materials, while the exceedingly slow release is attributed to the chelated antibiotics [163]. However, lowered pH environments can weaken the link between TCs and Ca^{2+}, accelerating the antibiotic release, which can be beneficial in inflammatory and infectious conditions [112].

All in all, micro and nanoparticles are promising TCs' carrier systems that cover a wide range of clinical applications. Nonetheless, the sparse number of marketed systems suggests that the repositioning of TCs associated with innovative delivery systems is still in an early stage, and highlights the complexity involved in the development of drug carrier systems in a reproduceable and scalable way.

Although microparticles possess interesting characteristics and some advantages compared to nanoparticles, the future points towards the development of nano-scaled systems. Upcoming evaluations should focus on comprehensive physicochemical characterization, as biodegradation time, long-term stability, and shelf-life, facilitating their translation into advanced clinical trials and eventual commercialization. Additionally, future carrier systems should prioritize delivery mechanisms, relying on specific receptors of a targeted tissue (e.g., plasma Apo-E lipoprotein and albondin) and employ smart materials to enable switch control over TCs' release. These approaches hold the potential to reduce off-target effects and accumulation, enhancing the prospective therapeutic efficacy.

Moreover, embracing the concept of personalized medicine will be crucial, tailoring TCs-carrier formulations to meet the individual needs of patients, considering personalized factors, such as patient-specific requirements and medical conditions. By addressing these future perspectives, the field of TCs-carrier systems can advance further, bringing us closer to the realization of their full therapeutic potential in clinical applications.

1.3. Inorganic nanoparticles and layered hydroxide materials as drug delivery systems.

As described before, NPs are promising materials for diverse biomedical applications, including diagnosis and treatment of diseases [164]. Their composition is highly variable, including lipidic- and polymeric-based NPs as organic specimens, as well as metallic- and ceramic-based NPs, regarded as inorganic materials.

Recently, inorganic NPs have gained attention in the biomedical field due to their good biocompatibility, stability in physiological conditions and distinct physical and electrical properties, derived from the base material itself [165]. These properties allow the management of their physicochemical properties including their size and geometry (spheres, rods, stars, layered, etc.), enabling their application for precision medicine [165,166]. Additionally, inorganic NPs are stable for long-term storage, resulting in prolonged shelf-life [167]. In fact, some specimens are commercially available for contrast imaging (Resovist®) and iron deficiency treatment (Feraheme®, Injectafer®) [166].

In the context of local drug delivery, anionic clay nanoparticulate, as layered hydroxide (LH) salts and layered double hydroxide (LDH) grabbed attention due to their favorable biocompatibility, slow degradation rates [164], easy obtainability [168], rich surface functionality, pH-sensitivity response [169] and high drug loading capacity [170,171]. These nanosystems consist in interconnected two-dimensional metallic (cationic) layers with anionic biomolecules and water within the interlayer space, bonded by weak electrostatic interactions [172,173]. As their structure (Figure 7), LH elements are set on divalent cations (e.g., magnesium, zinc, copper, manganese) combined with hydroxide groups, water, and exchangeable anions (e.g., chloride, carbonate, nitrate, hydroxide, and sulfate), while LDH must possess a trivalent cation (iron, aluminum, chromium) in addition to the other elements to be established [174,175].

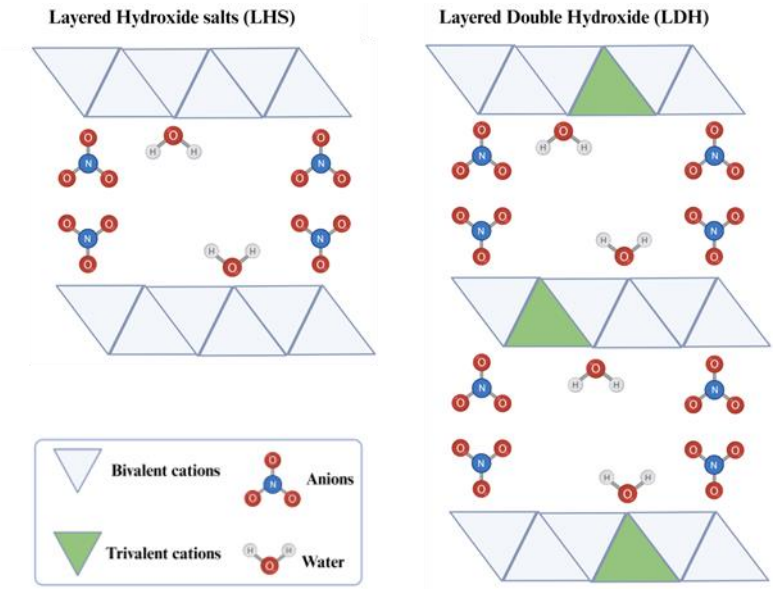

Figure 7. Schematics of layered hydroxide systems, encompassing interconnected cationic layers with anionic molecules and water within the interlayer spaces.

For biomedical applications, LH structures are most frequently based on magnesium cations (Mg^{2+}) to form the hydroxide-like structures [176], followed by zinc (Zn^{2+}) [173]. These essential elements for human homeostasis are known by their biodegradability [177], key role in enzymatic activity and immunological functions, being also related to anti-inflammatory and antioxidant effects [178–180]. Thus, these elements can confer bioactivity to LH drug carrier systems.

Interactions between LH nanostructures and physiological environments are set on ionic exchanges, leading to a slow and steady drug release [169]. Alternatively, in acidic

microenvironments (e.g., inflamed and infected sites) LH NPs are readily degraded, which leads to a burst drug and ionic release [169].

Moreover, their positively charged surface is favorable to interact with eukaryotic cells (negatively charged), allowing their uptake [169,181]. Intracellularly, LH NPs are likely to be confined into endosomes [109]. Due to the acidic characteristics of these vesicles, LHs can be partially dissolved, discharging high amounts of cations, resulting in an osmotic disbalance between the endosome and the cytoplasm [169]. This phenomenon can lead to the rupture of these vesicles, releasing the LH NPs to the cytoplasm, allowing a drug release in the perinuclear region, enabling the employment of these structures to gene therapy [181].

Exploring these advantages, LH and LDH NPs were vastly employed as local delivery systems, being loaded with several different drug categories, including NSAIDs, anticancer agents, phytochemicals, and antibiotics [170,173]. As displayed in figure 8, anionic drugs can substitute the interlayer anions of the LH systems during their synthesis (e.g., co-precipitation technique) or post synthesis, by anionic exchange [171,173]. Moreover, the distance between the cationic layers can be modified along the basal axis without changing the general structure, favoring the drug loading [174].

Regarding antibiotics, LH NPs were found to be effective to treat tuberculosis (loaded with 4-amino salicylic acid) [182], wound healing (amoxicillin) [183] and middle ear infections (ciprofloxacin) [184] in pre-clinical settings. Furthermore, in infectious scenarios, bactericidal synergetic effects between LH NPs and antibiotics have been reported [183,185], reinforcing their position as attractive antibacterial drug carriers.

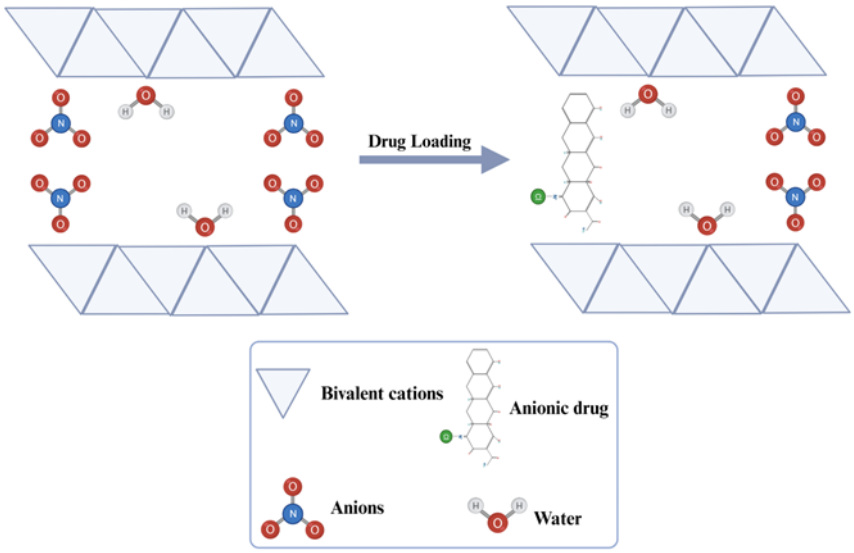

Figure 8. Schematics of the drug loading in layered hydroxide systems, where anionic drugs can substitute the interlayer anions, as nitrate and chloride.

Focusing on TCs, LH NPs were first employed as efficient absorbent materials to remove these antibiotics from the aqueous environment [186,187]. Since LH NPs possess the capability to exchange anions, high charge density among layers, and high surface area, TCs can easily be adsorbed by them [186,187]. However, recent studies demonstrated that LH could also function as local TCs delivery systems [183,188], exploiting their advantages as optimal stability, slow and pH-sensitivity degradation, and high drug loading capacity [164,168,169]. Therefore, given the outstanding properties of LH NPs for TC local delivery and their relevance in clinical applications, this topic will be further developed in chapters 5 and 6 of this thesis.

CHAPTER 2

Objectives

This thesis aims the production, characterization, and biological validation of two variations of layered hydroxide nanoparticles, devised to be a therapeutic approach for periodontal diseases and other inflammatory conditions.
This premise is set on the conjoining activity of: a) antibiotic-loaded LH nanoparticles, able to be internalized into periodontal cells and exert an effective antibacterial activity against periopathogens; b) modulation of the immuno-inflammatory activation in targeted tissues.

With this overarching aim in mind, the following proposal outputs are expected to be achieved:

• Selection of the most appropriate tetracycline for periodontitis management, through a detailed screening using *in vitro* cell culture systems, as well as *ex vivo* organotypic models. This screening will encompass various tetracyclines from different generations, and distinct concentrations, aiming their repurposing for periodontitis immunomodulation and prospective enhanced tissue healing.

• Development of cytocompatible layered hydroxide nanoparticles that can serve as effective drug carriers. These nanoparticles will be synthesized using both chemical and green synthesis methods, providing versatility and eco-friendliness.

• Bio-conjugation of the selected tetracycline with the LH nanoparticles by straightforward and cost-effective methodologies.

• Validation of the *in vitro* effectiveness of the developed systems within an advanced organotypic 3D-cellular model of the oral environment, addressing the inflammatory modulation capabilities.

By addressing these specific objectives, this research endeavors to make a meaningful contribution to the field of periodontal disease management and the broader realm of inflammatory condition treatment.

CHAPTER 3

Repurposing Sarecycline for Osteoinductive Therapies: An *in Vitro* And *ex Vivo* Assessment

The original article in this chapter was published as Martin V, Grenho L, Fernandes MH, Gomes PS. Repurposing sarecycline for osteoinductive therapies: an *in vitro* and *ex vivo* assessment. J Bone Miner Metab 2023.

DOI: 10.1007/s00774-023-01428-9

3.1. Introduction

Tetracyclines (TCs) embrace a class of broad-spectrum bacteriostatic antibiotics that inhibit the bacterial protein synthesis by binding to the 30S ribosomal subunit, being effective against a wide range of bacteria, including aerobic, anaerobic, gram-positive and gram-negative pathobionts [189].

Of additional relevance, non-antimicrobial effects of TCs with potential clinical application were described, including anti-inflammatory properties, inhibition of matrix metalloproteinases (MMPs) and stimulation of osteogenesis, found to be effective at sub-antimicrobial concentrations [32]. This opened a window of opportunity for their repurposing, leading to their clinical application for different indications, as dermatoses, diabetes-related complications, periodontal disease, rheumatoid arthritis, bowel disease, Parkinson's disease and enhanced bone healing, among others [32,52].

Regarding the osteogenic capability of TCs, controversial results can be found in the literature. For instance, some *in vitro* studies reported that low TC concentrations induce the osteoblastic proliferation rate, enhance alkaline phosphatase (ALP) activity and calcium deposition and upregulated the osteogenic gene program, without impairing phenotypic or functional activity [190,191]. However, other studies reported no increase in cell proliferation neither any induction of the osteogenic program by low TCs concentrations [192,193]. Nevertheless, using *in vivo* models, either independently or conjugated with different bone-related biomaterials, studies tend to report overall positive results. In addition, substantial outcomes in clinical trials were obtained by the conjugation of TCs with biomaterials targeting bone healing in periodontal disease [129].

Most recently, a new generation of synthetic TCs (e.g. tigecycline, eravacycline and omadacycline) has been developed, with its use largely restricted to community-acquired bacterial pneumonia and intra-abdominal infections, due to their retained activity against tetracycline-resistance organisms as methicillin-resistant *Staphylococcus aureus* [40]. Additionally, Sarecycline (SA), also a new generation molecule with a narrower spectrum of antimicrobial activity, has been approved for acne vulgaris' treatment, due to its anti-inflammatory profile and absence of adverse side-effects associated with prolonged administrations - as gastrointestinal disorders, mycotic infections and increased potential of bacterial resistance [194,195].

SA antimicrobial profile was already characterized *in vitro* and *in vivo* - SA presents a similar activity against Gram-positive bacteria, being much less effective against Gram-negative

bacteria, when compared to early generation TCs [195]. Further, SA demonstrated a comparable anti-inflammatory activity within an *in vivo* paw edema model, further presenting a significant reduction of inflammatory acne lesions in clinical trials [196]. However, little is known about SA osteogenic potential, as to the best of the authors' knowledge, the effects of SA on bone tissue or related cell populations have not been addressed previously, either *in vitro*, *ex vivo* or *in vivo*.

Accordingly, the present study is focused on the assessment of the *in vitro* response of osteoblastic precursor cells to SA, at different concentrations, addressing distinct functional parameters as metabolic activity, morphology, and osteoblastic differentiation at the molecular level, further uncovering the potential modulation of Wnt, Hedgehog and Notch signaling pathways. In addition, to provide an in-depth analysis of the bone tissue to this new generation TC, an *ex vivo* femoral organotypic system was further established, developed and characterized in the presence of SA.

3.2. Methods

3.2.1. Materials

α-MEM culture medium, fetal bovine serum (FBS), penicillin, streptomycin, amphotericin B and TrypLE (all Gibco); Tetrazolium salt (3-(4,5-dimethylthiazol-2-yl)-2,5-diphenyltetrazolium bromide) (MTT kit, Sigma-Aldrich), Triton-X, p-nitrophenyl phosphate (ALP kit, Sigma-Aldrich), Albumin Bovine, Alcian blue/Sirius red/von Kossa reagents (all Sigma Aldrich); iTaq Universal SYBR green Supermix PCR Kit and primers (all Bio-Rad), Trizol reagent (Ambion Life technologies), NZY first-strand cDNA synthesis kit (NZYTECH), phalloidin-conjugated Alexa Fluor 488 (Molecular Probes), MitoSpy™ Red FM (Biolegend), Hoechst 33342 (Enzo) and Quant-iT™ PicoGreen® ds-DNA kit (Invitrogen). Sarecycline hydrochloride (SA) was kindly donate by Adooq Bioscience.

3.2.2. In vitro assessment of sarecycline osteogenic potential – osteoblastic cell cultures

Sarecycline activity was characterized *in vitro* using human bone marrow-derived mesenchymal stromal cells (hBMSCs - Human Mesenchymal Stem Cells, Lonza, Catalog #: PT-2501). Cells were characterized by flow cytometry and found to be positive for CD105, CD73 and CD90, and negative for CD45, CD34 and CD14 markers. Cells from the 4th passage were used in the present experiment. hBMSCs cultures were expanded in α-MEM culture

medium, containing 10% FBS, 100 IU/mL penicillin, 100 µg/mL streptomycin, and 2.5 µg/mL amphotericin B, and were incubated at 37 °C and 5% CO_2. At a confluence of approximately 70%, grown cells were detached and sub-cultured at 10^4 cells.cm^{-2}. After 24 hours, cultures were incubated with complete culture medium supplemented with 10% SA solutions (V/V), reaching final concentrations of 0.1, 1 and 10 µg/mL, in accordance with experimental conditions. For the gene expression and ALP activity analysis, hBMSCs cultures were incubated with SA at 1 µg/mL. Cultures grown in complete culture media devoid of SA were used as basal control condition (C-BAS).

3.2.2.1.Metabolic activity and DNA content

Metabolic activity of the cell cultures was determined by MTT assay. At selected time-points, MTT solution (5 mg/mL) was added, and cultures were incubated for 3 h. Following, the supernatant was removed, crystals were dissolved with dimethyl sulfoxide, and the absorbance of the colored solution was determined at 550 nm with a microplate reader (Synergy-HT; BioTek). In addition, DNA quantification was performed as previously described[197]. Briefly, at the same selected timepoints, cultures were treated with 0.1% Triton X-100 for 15 min, and then, a Quant-iT™ PicoGreen® ds-DNA kit was employed according to manufacturer's instructions. Fluorescence was determined at 480/520 nm (excitation/emission) using the same microplate reader. Five independent experiments were performed.

3.2.2.2.Cell morphology

Cell morphology was assessed by fluorescence microscopy, upon staining of F-actin cytoskeleton and mitochondria, using phalloidin-conjugated Alexa Fluor 488 and MitoSpy™ Red FM, respectively, followed by a nucleus counterstaining with Hoechst 33342. Representative images were captured using a Celena S digital imaging system (Logos Biosystems). Briefly, at 24 and 120 h of culture, cells were incubated for 30 min with MitoSpy™ Red FM, at 37 °C and 5% CO_2. Cells were then fixed with paraformaldehyde 3.7%, following their permeabilization with Triton-X 0.1% and incubation with bovine serum albumin at room temperature. Finally, cells were stained with phalloidin-conjugated Alexa Fluor 488 and Hoechst 33342, for F-actin and nucleus staining, respectively, and proceeded to microscopic analysis. Images were treated using the ImageJ software v.1.53k. Five independent experiments were performed.

3.2.2.3.Gene expression analysis

Total RNA was isolated from hBMSCs cultures grown for 7 days using Trizol reagent, in accordance with the standard manufacturer's protocol. RNA concentration and quality were assessed by absorbance reading (A260/A280) with NanoDrop (NanoDrop Technologies). Samples with A260/A280 ratio of approx. 2.0 were proceeded to cDNA conversion.

The conversion to cDNA was conducted with a reverse transcription system, normalizing the RNA' concentration to 500 ng/µL, reaching a final volume of 20 µL for each sample. Conversion' cycle was set as 10 min at 25 °C, 30 min at 50 °C and 5 min at 85 °C. Then, 1 µL of RNAse was added to each sample prior incubation at 37 °C for 20 min.

Quantitative PCR (qPCR) was performed with a CFX384 real-time PCR system (Bio-Rad), using 5 µL of iTaq Universal SYBR green Supermix PCR Kit, 3.5 µL of DEPC water, 0.5 µL of the primer and 1 µL of cDNA in each well. The Bio-Rad cycling protocol was applied (activation – 2 min at 95 °C; 40 cycles of denaturation/annealing, 5 sec at 95 °C and 30 sec at 60 °C; melt curve, 65 – 95 °C). DEPC water was used as negative control for each primer.

Quality control was checked using Bio-Rad CFX Maestro 1.1, v.4.1.24. Samples with amplification efficiency greater than 110 and less than 90 were excluded, as well as samples with a linear standard curve (R^2) less than 0.98. The relative quantification of each target gene was normalized using the housekeeping gene (GAPDH) levels and final values were calculated via the $2^{-\Delta\Delta Ct}$ method. The references of the used primers are presented on Table 3. Five independent experiments were performed.

Table 3. The assay ID of the used primers. Primers were purchased from Bio-Rad

Gene	Assay ID	Gene	Assay ID
GAPDH	qHsaCED0038674	SPARC	qHsaCID0010332
RUNX2	qHsaCED0044067	PTCH1	qHsaCEP0055042
SP7	qHsaCED0003759	GLI2	qHsaCEP0057630
COL1A1	qHsaCED0043248	HEY1	qHsaCEP0053501
BGLAP	qHsaCED0038437	HES1	qHsaCED0006922
ALP	qHsaCED0045991	AXIN2	qHsaCID0017930
BMP2	qHsaCID0015400	HNF1A	qHsaCEP0024214
TWIST1	qHsaCED0003856		

Abbreviations: GAPDH: Glyceraldehyde-3-Phosphate Dehydrogenase, RUNX2: Runt-Related Transcription Factor 2, SP7: Osterix, COL1A1: Collagen Type I Alpha 1, BGLAP: Osteocalcin, ALPL: Alkaline Phosphatase, BMP2: Bone Morphogenetic Protein 2, TWIST1: Twist Family BHLH Transcription Factor 1, SPARC: Osteonectin, PTCH1 - Protein Patched Homolog 1, GLI2 - Glioma-Associated Oncogene Family Zinc Finger 2, HEY1: HES-Related Repressor Protein 1, HES1: Hes Family BHLH Transcription Factor 1, AXIN2: Axis Inhibition Protein 2, HNF1A: Hepatocyte nuclear factor 1-alpha.

3.2.2.4.Alkaline phosphatase (ALP) activity

ALP activity from 14-days cultures was determined in cell lysates after the treatment with Triton-X 0.1%. Quantitative analysis was performed following the dissolution of p-nitrophenyl phosphate in an alkaline buffer solution (pH 10.3) and the colorimetric determination of the p-nitrophenol product was measured at 405 nm using a microplate reader (Synergy HT, BioTek). Hydrolysis was established for 30 min, at 37 °C. ALP levels were normalized for the levels of total protein, assayed by the method of Lowry, using a DC protein kit (Bio-Rad), and the same microplate reader, at 750 nm. Results were expressed in nanomoles of p-nitrophenol produced per min per μg of protein (nmol/min/μg protein). Five independent experiments were performed.

3.2.3. Ex vivo assessment of sarecycline osteogenic functionality - organotypic cultures of embryonic chick femora

The influence of SA on bone tissue development was assayed within an *ex vivo* model – the embryonic chick femora organotypic culture. The experimental use for research of avian fetal forms within the first two-thirds of development is not encompassed by current European (Directive 2010/63/EU) or National (Decreto-Lei n. º 113/2013) legislation, precluding the need for regulatory approval of the experimental procedures.

Briefly, fertilized chick eggs (*Gallus domesticus*), acquired from a certified vendor were incubated in an automatic egg incubator (Octagon Advance, Brinsea) until the 11th day of development. Then, chick embryos were euthanized, and the femurs were dissected and carefully placed into Netwell® inserts (Costar 3480, 440 μm of pore diameter) in six-well-plates. Femurs were maintained for 24h in α-MEM culture medium supplemented with ascorbic acid (50 μg/mL), penicillin (100 U/mL)/streptomycin (100 μg/mL) and 2.5 μg/mL amphotericin-B, at liquid/gas interface, in a humidified atmosphere of 5% CO_2 in air, and 37°C. After, the medium was replaced by the previously described medium, further supplemented with SA, at 1 or 10 μg/mL. Control femurs were grown in the absence of SA, with daily changes of the culture media, for an 11-day period. Femora were following characterized by microtomographic evaluation and histochemical analysis, as following detailed.

3.2.3.1.Morphometric analysis by micro-computed tomography (μCT)

At the end of the experimental period, selected femurs were scanned at 40 Kv, 100 μA and an isotropic resolution of 4.5 μm, using a Skyscan 1276 Microtomographic System (Bruker, Belgium). The obtained projection images were reconstructed with NRecon software (Bruker,

version 1.7.4.2). Morphological analysis of the bone was set on the region of interest (ROI), obtained by the separation of femur samples from the background noise and the Eppendorf. The quantitative analysis was carried out in 900 slices at the diaphysis region (450 slices above and 450 below the mid-diaphysis) with CTAnalyser software (Bruker, version 1.0.11), contemplating the following parameters: bone volume (BV), bone surface (BS) and tissue volume (TV), and associated ratios BV/TV, BS/BV and BS/TV. Three-dimensional images were generated using CTVox software (Bruker, version 3.3.0). Five independent experiments were performed.

3.2.3.2.Histochemical Staining

At the end of the experimental period, selected femurs were fixed in 4% paraformaldehyde, embedded in paraffin blocks, and cut in 5 µm-thick sections. Then, sections were marked with Alcian blue/Sirius red (AB/SR) for the staining of glycosaminoglycans and collagenous matrix, respectively. In addition, femurs' sections were also stained using von Kossa's dyeing for calcified tissue visualization, relying on the replacement of calcium by silver and ultraviolet light exposure, producing dark metallic areas[198]. Images were captured using a Zeiss Axiolab 5 microscope coupled with an Axiocam 5 Color Camera. The percentage of collagen and mineralized areas of AB/SR and von Kossa's obtained images, respectively, were calculated using ImageJ software (version 1.53k), after setting the thresholding of images with Huang algorithm[199]. Three independent experiments were performed.

3.2.4. Statistical analysis

Statistical analysis and graphics were performed using the IBM SPSS v.26 software. The data normality was determined by the Shapiro-Wilk test. For normal datasets, one-way ANOVA was performed, followed by multiple comparisons using Tukey's test. For non-parametric datasets, Kruskal-Wallis test was performed, followed by multiple comparisons using Dunn's tests. p values < 0.05 were considered significant. Data were presented as mean ± standard deviation (SD).

3.3. Results

3.3.1. In vitro assessment of sarecycline osteogenic functionality

In vitro hBMSCs cultures were established and grown in the presence and absence of selected concentrations of SA. In control cultures, both MTT reduction values and total DNA content

were found to increase until day 21, a trend followed by cultures grown in the presence of SA 0.1 µg/mL, found to be significant increased from day 7 onwards regarding the MTT assay (Figure 9-A). Total DNA levels for cultures grown in the presence of SA 0.1 µg/mL were found to be significantly higher at day 14 (Figure 9-B). Cultures grown in the presence of SA 1 and 10 µg/mL also presented a trend for higher metabolic activity up to day 14 – being significantly higher than control at day 7 and 14. Similar growth curve can be observed in figure 9-B by the quantification of total DNA, confirming an active proliferation of hBMSCs cultures in control and experimental groups. It is noted that SA at 1 µg/mL presented the highest DNA amount at day 14.

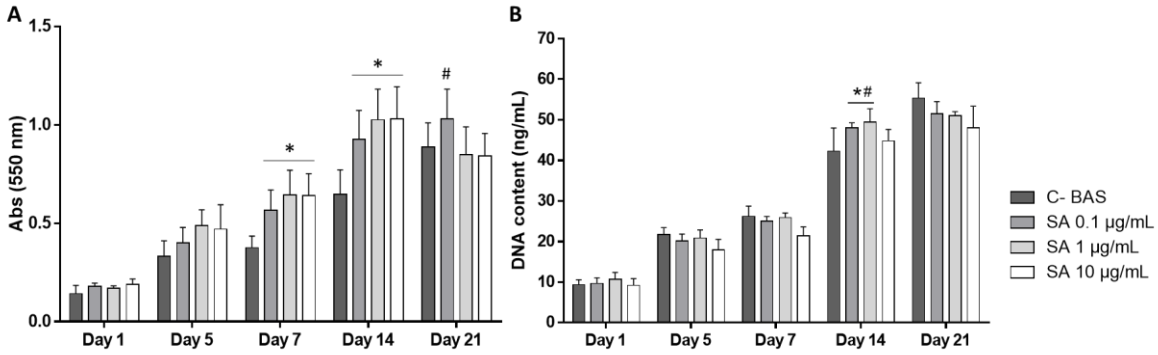

Figure 9. (A) Metabolic activity/cell viability – MTT assay; and cell proliferation – total DNA (B) of hBMSCs cultured with different concentrations of sarecycline, up to 21 days. (*) Significantly different to control; (#) significantly different to experimental groups. (n=5, $p<0.05$).

Regarding the assessment of cell morphology at day 1 (Figure 10-A), hBMSCs control cultures presented a morphologically homogeneous phenotype, with well-organized F-actin filamentous fibers, an elongated morphology, prominent nucleus, and a feeble mitochondrial staining. In addition, a polygonal morphology is observed, as an evident cytoplasmic spreading, with filopodial protrusions and spikes, extending and establishing direct contact with adjacent cells. A strong similarity is noted in cells exposed to SA, with mitochondrial staining mostly concentrating at the perinuclear area, being suggestive of a healthy cellular functionality.

At day 5 (Figure 10-B), hBMSCs cultures presented higher cellular density areas - confirming an active proliferation - with abundant intercellular contacts, as well as an increased mitochondria presence around the nucleus, for control and experimental cultures. No differences were observed between the control cultures and experimental groups.

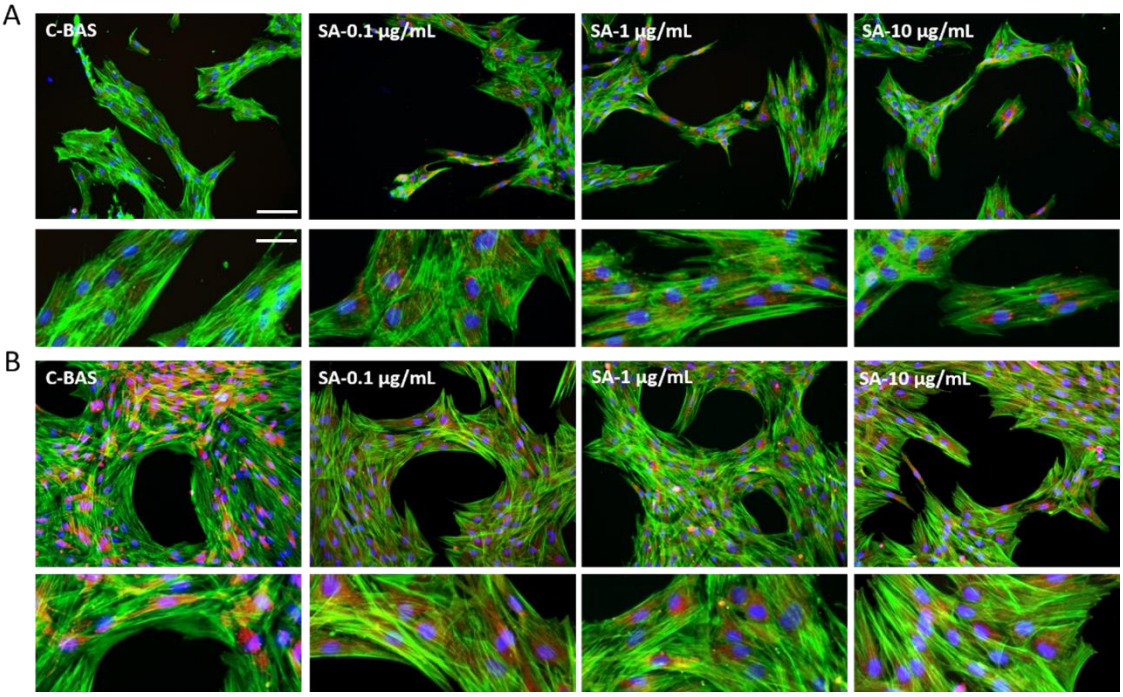

Figure 10. Representative fluorescent images of hBMSCs exposed to sarecycline, stained for cytoskeleton (F-actin, green) and mitochondria (red), counterstained for nucleus (blue). Images representative of 24h (A) and 5 days (B) of culture. Scale bars corresponds to 100 µm on first and third line of figures and 25 µm on the second and fourth line of figures, respectively. n=5.

The osteoblastic differentiation of hBMSCs was evaluated through qPCR (Figure 11 and 12), contemplating distinct osteogenic markers and relevant osteogenic signaling pathways. hBMSCs exposed to SA presented significant differences regarding the osteogenic gene expression in comparison to control. For instance, RUNX2 was upregulated 2.5-folds and it's-downstream genes, COL1A1 and osteonectin (SPARC) were slightly upregulated. Importantly, ALP expression was 7-fold increased, which is supported by a significant increase of the enzyme's activity (Figure 11-B). However, the experimental group presented some downregulation of BMP2, an important inducer of osteogenic differentiation and bone formation.

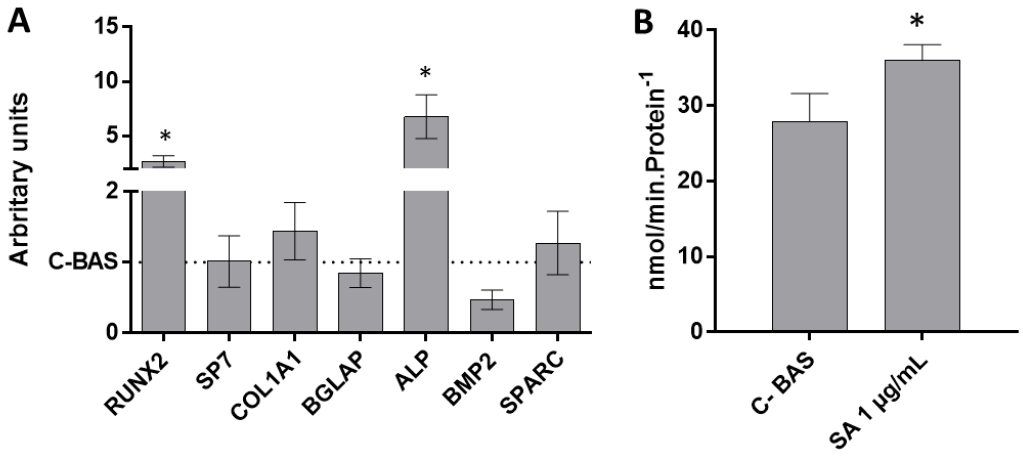

Figure 11. (A) Relative expression of osteogenesis-related genes of hBMSCs cultured with SA at 1 µg/mL, for 7 days. Values were normalized by the gene expression values at the control culture. (B) Quantitative ALP activity of HBMSCs cultured with sarecycline at 1 µg/mL, for 14 days. (*) Significantly different to control (n=5, $p<0.05$).

Further, the activation of relevant signaling pathways on the osteogenic differentiation (Figure 12) - Hedgehog, Notch and Wnt - were also assessed in the presence of SA. Hedgehog signaling was found to be stimulated, once GLI expression was significantly upregulated (9.5-fold), while PTCH1 - a surface receptor that activates GLI transcription factor expression – also presented some increased expression.

Substantial changes were also verified in the gene expression of Notch signaling - HES1 was unaltered by SA's exposure; however, HEY1 was strongly downregulated by SA. Finally, the Wnt signaling was assessed by TWIST1, AXIN2 and HNF1A expression. AXIN2 and TWIST1 levels were similar to control, while HNF1A/TCF1 were massively downregulated.

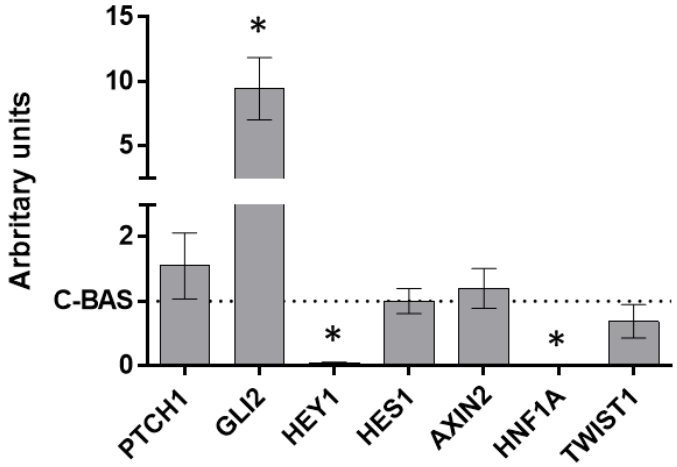

Figure 12. Relative expression of genes associated with relevant signaling pathways (Hedgehog, Notch and Wnt) of hBMSCs cultured with SA at 1 µg/mL, for 7 days. Values were normalized by the gene expression values at the control culture. (*) Significantly different to control (n=5, $p<0.05$).

3.3.2. Ex vivo assessment of sarecycline osteogenic functionality - organotypic cultures of embryonic chick femora

The biological response to SA was further addressed in an *ex vivo* model of the embryonic chick femora development, in order to provide an in-depth analysis of cell differentiation, mineralization stages and developmental growth patterns, maintaining the relationship of the cells within their extracellular matrix [200].

The first parameter analyzed was the length of the femurs exposed to two concentrations of SA, for 11 days (Figure 13). The incubation with SA marginally increased the femurs' length in comparison to control. Moreover, femurs incubated with SA markedly enlarged the cartilage of the epiphyseal region.

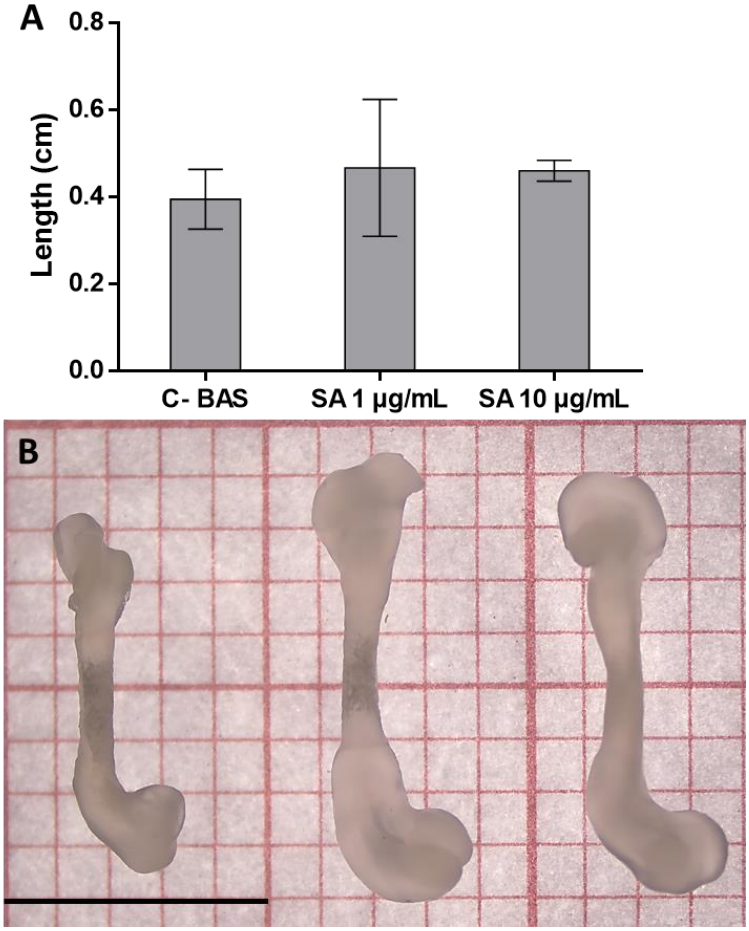

Figure 13. (A) Variation of the bone length of the femurs grown with SA. (B) Representative macroscopic images of control, SA at 1 and 10 µg/mL, respectively. Scale bar corresponds to 5 mm (n=5, $p<0.05$). No statistical differences among groups were attained.

Secondly, the bone morphometric analysis was set on the correlation of µCT results and the histological/histochemical evaluation of the corresponding femurs. µCT results showed that the addition of SA to E11 femur cultures resulted in a significant increase in mineralized content, as verified by a higher BV/TV ratio (Figure 14-D). In addition, bone surface density (BS/TV)

was found to be significantly higher in the presence of SA. Comparing experimental groups, SA at 1 µg/mL presented a stronger osteogenic potential in relation to SA at 10 µg/mL, presenting a significant increase in the BS/BV ratio, as well as in the bone surface density (BS/TV).

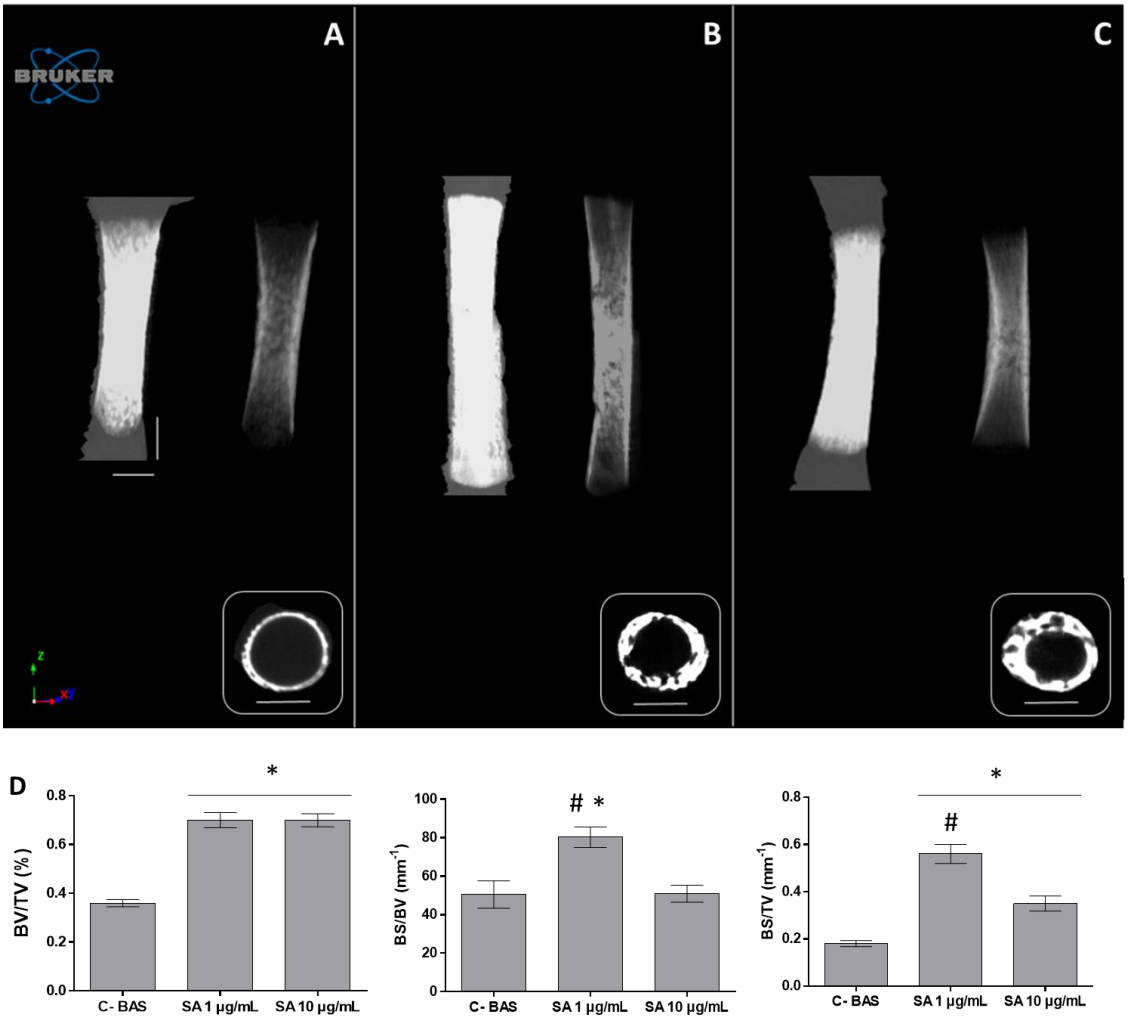

Figure 14. Representative images of µCT analysis. (A) C-BAS; (B) SA 1 µg/mL; (C) SA 10 µg/mL. Images were created setting the defined volume of interest, using the maximum intensity and attenuated projection respectively. Scale bar corresponds to 500 µm. (D) Quantitative histomorphometric 3D-analysis of the femurs cultured with SA. (*) significantly different to control. (#) significantly different to SA 10 µg/mL. (n=5, $p<0.05$). BV - bone volume; BS - bone surface; TV - tissue volume.

Regarding the histochemical analysis, the diaphysis region of control femora presented an exterior collar of collagen-rich matrix stained by Sirius red, and an interior filled with a proteoglycan-rich matrix, dyed by Alcian blue (Figure 15-A). In addition, a mild reddish accent can be observed within the interior cartilage matrix, as well as empty spaces, suggesting some cell migration and the initiation of the trabecular organization, characteristic of the expected phenotypic development. Experimental groups presented more extended cellular migration

areas within the internal diaphysis, in addition to a significant increase in collagen thickness over the marginal region for both SA concentrations, verified by the quantification of collagen' areas (Figure 15-C). Moreover, the von Kossa staining evidenced a mineral deposition within the collagen outer layer at the mid-diaphysis (Figure 15-B). Among samples, noticeable differences can be observed. Femurs exposed to SA presented abundant mineralized areas, with significant stronger staining, as well as thicker and more developed mineralized trabeculae, corroborated by the quantitative analysis (Figure 15-D). In fact, the significant increase in bone volume (BV/TV) observed within µCT analysis correlates with the increased collagen and mineral deposition observed within the diaphyseal section.

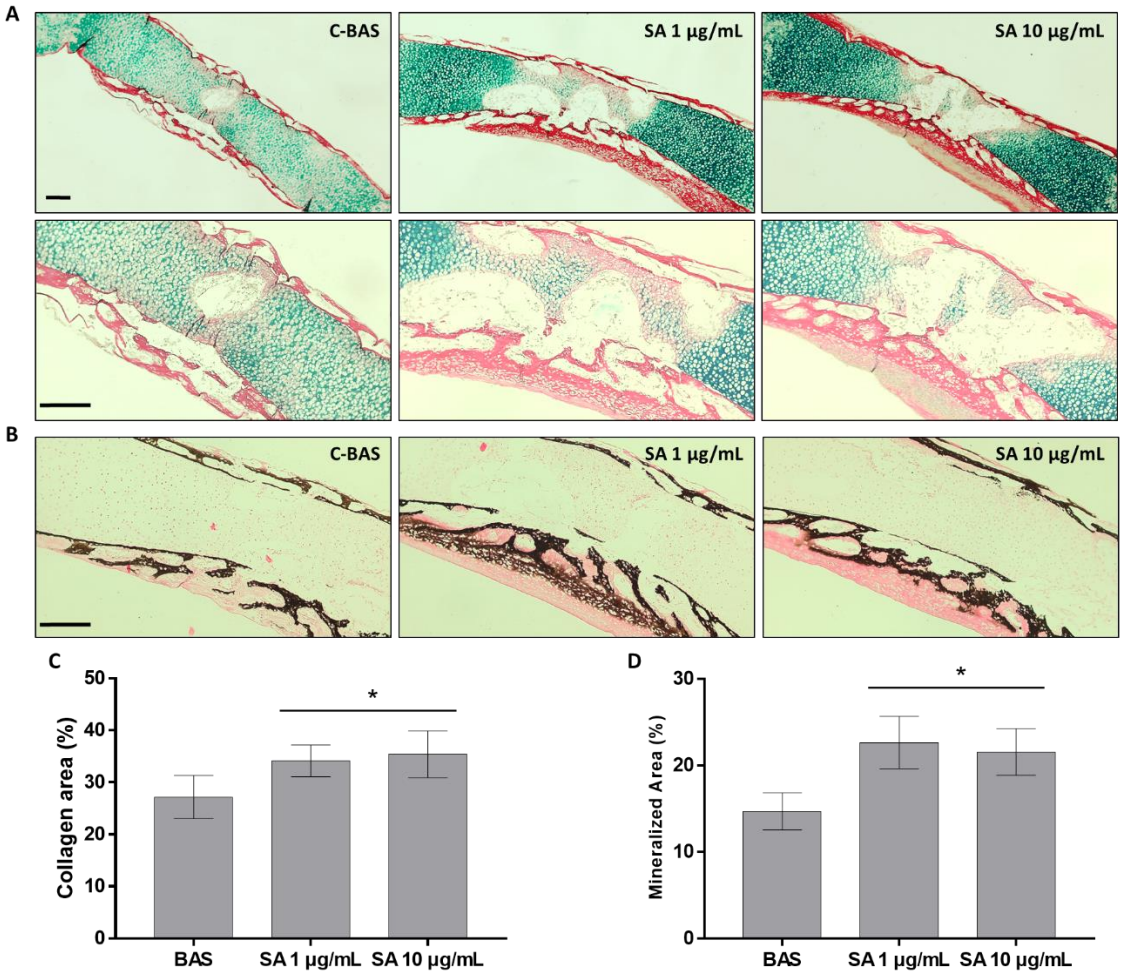

Figure 15. (A) Representative images of histochemical staining using Alcian Blue and Sirius Red (AB/SR) staining. Proteoglycans of the cartilage tissue are labeled in blue, while collagen matrix is labeled in red. (B) Representative images of von Kossa staining, with calcium deposits evidenced in black, in addition to a pinkish staining of the cells. (C) Quantitative analysis of the percentage of collagen area using the (AB/SR) stained images. (D) Quantitative analysis of the percentage of mineralized area using von Kossa dyed images. Scale bar corresponds to 100 µm. (*) significantly different to control. (n=5, $p<0.05$).

3.4. Discussion

3.4.1. In vitro assessment of sarecycline osteogenic functionality

In the present study, hBMSCs were selected as precursor cells to address the osteogenic differentiation potential of SA, given their multilineage differentiation capability, depending partially on external stimuli and condition of culture [201].

Comparing the metabolic activity and cell proliferation of hBMSCs cultures grown in the presence of SA, with those grown in the presence of early-generation TCs, it is noticeable that SA, even at higher concentrations (10 µg/mL), did not present any impairment or initial dose-dependent inhibitory effects, as previously verified, suggesting an enhanced cytocompatibility [190,202]. For instance, in the study of Gomes and Fernandes (2007), the metabolic activity of hBMSCs cultured with doxycycline and minocycline was assessed and an initial inhibitory effect was observed even at low concentrations (1 µg/mL) - despite the improvement with longer culture times, and a significant impairment attained with higher concentrations [190]. Similar results were obtained with different cell lines, demonstrating the inhibitory effects of TCs at concentrations higher than 10 µg/mL [202,203]. This enhancement of the metabolic activity may be related to the improvement of the status of energy coupling in mitochondria, triggered by several factors, as the possibility to modify the membrane potential, modulating the mitochondrial respiratory chain and ATP synthase activity [204]. In addition, selected second generation TCs' concentrations also seem to decrease the expression of caspases and inhibit cytochrome-c release through specific signaling of Bcl-2 and XIAP, thus modulating both the intrinsic and extrinsic apoptotic pathways into an increased cell viability [205,206].

Regarding the morphology of hBMSCs cultures, some studies associate a rounded-shape with adipogenic differentiation and a slower proliferative profile, while a polygonal-shape and the presence of a high density of filopodia-like protrusions are usually correlated with an enhanced osteogenic differentiation of precursor populations [207,208]. In addition, our findings diverge from other studies with previous generation TCs - in the study of Park (2011), osteoprecursor cells cultured with TCs presented a reduction of the number of the cells at 10 µM and a more rounded shape and reduced attachment at 100 µM [192]. A similar pattern was observed in the study of Almazin et al. (2009) – primary osteoblasts cultured with minocycline presented a rounded morphology and a decreased number of the cells [209]. Gathering the information, our results suggest that hBMSCs cultures incubated with SA presented a morphology associated with a proliferative profile and the priming of the osteogenic activation.

The gene expression pattern of osteoblastic-related genes reported in the literature is similar to the one of the present study - RUNX2 and ALP were found to be upregulated when cells were cultured with low-dosage TCs [191,210,211]. RUNX2 is considered the master osteogenic transcription factor [212], while ALP is a known early osteoblastic marker, essential to catalyze the liberation of phosphate from various substrates allowing the formation of hydroxyapatite and the consequently maturation the bone matrix [213]. Besides, COL1A1, SPARC and BGLAP genes that encode collagen type I - the main protein component of the osteoid -, osteonectin and osteocalcin, respectively - were slightly upregulated or preserved, suggesting the maintenance of the bone matrix production and mineralization, at gene expression level, of cells exposed to SA [214,215]. The maintenance of osteonectin levels can be observed in other studies with doxycycline [191]. Furthermore, the downregulation of BMP2 by TCs is documented in the literature, as in the study of Muthukuru and Sun (2013), in which the combination of doxycycline and BMP2 hampered osteogenesis in periodontal ligament cells and in the study of Park (2011), wherein three different TCs reduced the expression of BMP2 in osteoprecursor cells [191,192]. One possible reason for this downregulation may lie on the BMPs' regulation – these glycoproteins are members of the TGF-β superfamily, known to play an important role regarding inflammation and MMPs upregulation, via SMADs or other intracellular signals. TCs present anti-inflammatory and a potent anti-MMP activity - therefore, they seem to be able to indirectly decrease BMPs expression by downregulating the TGF-β signaling and the MMP production [216].

Additionally, SA upregulated the Hedgehog signaling, a key pathway to drive undifferentiated cells to the osteoblast lineage, assessed by GLI2 and PTCH1 gene expression. GLI2 seems to function as a transcriptional activator when the Hedgehog signaling is active [217], being an essential factor for the endochondral ossification process as, in its absence, a decreased bone formation is attained [218]. Its increased expression seems to upregulate RUNX2, and subsequently the osteogenic activity via a direct physical interaction with the transcription factor [219]. In accordance, RUNX2 expression was found to be significantly increased, relating to the SA-mediated increase of GLI2.

Notch signaling (assessed via HES and HEY gene expression) is known to be active at early stages of osteoblast differentiation, relying on RUNX2-dependent signaling and known to play a significant role in bone development and repair [212,220]. HES1 transcription factor is related to an increase of protein stability and transcriptional activity of RUNX2 resulting in the stimulation of osteoblast differentiation [220,221]. However, the literature seems to be controversial about the timing of HES1 upregulation during osteogenesis, varying from a very

early stage of osteoblast differentiation, to a later one [220,221]. HEY1, on the other hand, seems to inhibit RUNX2 transcriptional activity as well as bone matrix mineralization, suggesting that HEY1 counteracts RUNX2 and osteoblastic differentiation, at least at early differentiation stages [222]. On the contrary, other studies pointed out that HEY1 is associated to an increased osteogenic differentiation at a late stage, presenting significant increases at day-28 in osteoblastic-precursor cell cultures [220]. In addition, BMP2 is needed for the induction of HEY1 and, as described before, its expression was found to be decreased by SA at the 7-day time point, which could result in the indirect HEY1 downregulation [220,222].

Lastly, little is known about the effects of TCs on Wnt signaling pathway – literature is focused on its carcinogenic potential. The study of Qin et al. (2015) doxycycline suppressed the expression of TWIST1 in several cancer cell lines, while tigecycline did not altered AXIN2 expression in cervical squamous cell carcinoma [223]. Moreover, the absence of HNF1A/TCF1 levels is probably due to the downregulation of the BMP2 gene as previously described, once HNF1A is also related to the BMP/TGF-β signaling pathway and may exist some degree of interdependency between BMPs and HNF1A/TCF1 activity [224]. TWIST1 is a critical modulator of mesenchymal cell fate that induces osteogenic differentiation, while AXIN2 provides a negative feedback on the pathway by promoting the degradation of β-catenin, retarding the osteogenic differentiation [225].

Overall, results suggest that the exposure of hBMSCs to SA enhanced the metabolic activity and the osteogenic differentiation, demonstrated by cell morphology, ALP activity and gene expression pattern, which showcased the multitude of regulatory pathways that seems to modulate the osteogenic differentiation process [212].

3.4.2. Ex vivo assessment of sarecycline osteogenic functionality - organotypic cultures of embryonic chick femora

The e*x vivo* embryonic chick femora model was chosen to evaluate the effects of SA on the developmental bone growth and mineralization in a more complex biological system. This organotypic culture provides multiple cell types, with a similar organization that is found in *in vivo* models, allowing the assessment of some intercellular and cell-matrix processes without systemic interferences, easier manipulation and more ethically acceptable [226].

To the best of our knowledge, it is the first time that a bone development *ex vivo* system using an air/liquid interface was tested with TCs. However, other types of experiments were performed, as in the study of Cole et al. (1994) in which avian tibias were submerged in the presence of doxycycline, and an increase in the length was observed, at 20 and 40 μg/mL [227],

in line with the attained data. Additionally, TCs are usually associated with an improvement in mineralization and bone formation, as presently verified within assessed tissue sections, given the increased collagenous matrix deposition and trabecular mineralization at the mid-diaphysis. For instance, considering *in vitro* cell models, in the study of Tham et al. (2016) the quantification of mineral deposition in BMSCs significantly increased when cells were incubated with nanoparticles loaded with minocycline [144]. Similar results were observed in the study of Muthukuru and Sun (2013) – cultures incubated with 1 μg/mL doxycycline presented a significant increase in calcium deposition when compared to control or BMP2 exposure, as in the study of Gomes et al. (2008), in which cells treated with 1 μg/mL doxycycline or minocycline increased the extent of matrix mineralization in human osteoblast cultures growing on biomaterials [191,228]. Regarding *in vivo* characterization, in the study of Silva et al. (2018), a bone cement loaded with minocycline induced a significant higher formation of mineralized tissue, increasing bone outgrown over the surface of the cement and bone-cement contact [229]. As other examples, nanoparticles loaded with tetracycline aiming osteoporosis treatment, a significant increase of the bone mineral density of femurs from ovariectomized rats, as well as nanoparticles loaded with tetracycline conceived to periodontitis treatment significantly increased the percentage of new bone formation in dogs [126].

3.5. Conclusions

In the present study, sarecycline stimulated the proliferation and osteogenic differentiation of hBMSCs within *in vitro* cultures. In addition, for the first time, the relationship of the activation of relevant signaling pathways (i.e., Hedgehog and Notch) and a tetracycline was characterized. Further, an *ex vivo* embryonic chick femora development model exposed to sarecycline presented an increased collagenous deposition and mineral content, validating the enhanced osteogenesis. These results suggest that sarecycline might be suitable to other medical indications than dermatosis and is a promising candidate to repurposing for bone tissue-related applications, promoting osteoinduction in a wider concentration' range, in comparison to early generation TCs.

CHAPTER 4

Unveiling The Osteogenic Potential of Tetracyclines: A Comparative Study in Human Mesenchymal Stromal Cells

The original article in this chapter was published as Martin V, Bettencourt AF, Santos C, Fernandes MH, Gomes PS. Unveiling the Osteogenic Potential of Tetracyclines: A Comparative Study in Human Mesenchymal Stem Cells. Cells 2023;12:2244.

DOI: 10.3390/cells12182244.

4.1. Introduction

Tetracyclines (TCs) are a class of broad-spectrum bacteriostatic antibiotics characterized by a four-ring carbocyclic structure. Chemically, TCs differ from one another due to the varying functional groups attached to the core structure [38,211]. The therapeutic effectiveness of TCs has been extensively demonstrated in the management of various infectious conditions caused by Gram-positive and Gram-negative bacteria, rickettsia, and mycoplasma, comprehensively reviewed in previous studies [230,231]. The primary antibacterial mechanism of action for TCs relies on their ability to bind to multiple target sites within the bacterial ribosomal structure. This binding interferes with tRNA binding and disrupts protein synthesis, resulting in the inhibition of cell growth in a bacteriostatic way [232]. Additional mechanisms, relying for instance on membrane perturbation, have been described [232]. These findings provide further evidence of the chemical and biological versatility of TCs, as they can adapt and modify their conformation in an environment-dependent manner [233], further highlighting the dynamic nature of TCs and their ability to exert multiple effects on bacterial cells [38].

In addition to their well-established chemotherapeutic effectiveness, TCs have been associated with distinct pleiotropic effects that outreach into eukaryotic cells and tissues [38]. These effects include anti-inflammatory, anti-metalloproteinase, antitumor, neuroprotective, antioxidant, and cation chelation activities [234]. As a result, TCs have been investigated and tested for a range of diseases, such as osteoporosis, neuropathies, acne, rheumatoid arthritis, periodontitis, certain types of carcinomas, and recently, COVID-19, endorsing its repurposing by the pharmaceutical industry [32,196,223,234–237]. In this frame, TCs have garnered attention for bone-tissue-related applications due to their high affinity and remarkable retention in the bone matrix, as well as their ability to modulate the functionality of bone cells [238,239]. This realization has prompted the development of distinctive drug-carrier platforms (e.g., nanoparticles, microparticles, cements, 3D printing scaffolds, coatings, and fibers), which have been conjugated with TCs using various approaches [110,240]. The goal of these carrier systems was to enable the targeted release of TCs to the bone, capitalizing on their antibacterial and/or non-antibacterial effects in situ [229,241].

TCs possess the ability to chelate metallic ions, including calcium, resulting in a high affinity for binding to the hydroxyapatite-rich inorganic matrix of the bone tissue [112]. In addition to their bone-targeting capability, TCs also appear to modulate the bone

formation and bone resorption processes [209,211]. They seem to contribute to the inhibition of bone resorption by blocking the metal-dependent matrix metalloproteinases (MMPs)—namely gelatinase and collagenases [242]. Furthermore, TCs were shown to inhibit osteoclastogenesis by inducing the apoptosis of osteoclasts [243], and by blocking the NFATc1 signaling pathway upon RANK-RANKL signaling modulation, as demonstrated *in vitro* and *in vivo* [211,244,245]. Preliminary evidence suggests that TCs may also induce the osteogenic program [190,209,228]. However, the specific signaling pathways through which TCs modulate osteogenic commitment in physiological conditions have not been previously investigated. Furthermore, although some individual TC molecules have been reported to have potential bone-modulatory effects, there is currently a lack of comprehensive comparative assessments between different drugs.

The primary objective of this study was to assess the *in vitro* osteogenic potential of four TCs, representing all three generations, to understand their ability to influence the osteogenic commitment of human mesenchymal stem cells. The tested TCs were tetracycline (TETRA, 1st gen.), doxycycline (DOXY 2nd, gen.), minocycline (MINO, 2nd gen.), and sarecycline (SARE 3rd gen.), assayed at different concentrations. The evaluation of the biological response encompassed a comprehensive analysis of various aspects in the established cell cultures. These included evaluating the metabolic activity, observing cell morphology and organization, determining the expression and activity of osteogenic markers, and investigating the activation of relevant signaling pathways.

4.2. Methods

The response to different concentrations (0.1, 1.0, and 10 µg/mL) of selected tetracyclines (TETRA, DOXY, MINO, and SARE) (Table 4) was evaluated *in vitro*, using precursor osteoblastic populations - human bone marrow stromal cells (HBMSCs, Lonza, Catalog #: PT-2501). Before the biological evaluation, HBMSCs were characterized by flow cytometry and found to be positive for CD105, CD73, and CD90, while negative for CD45, CD34, and CD31 markers. Cells from the 4^{th} passage were used in this study. The HBMSCs were expanded in α-Minimal Essential Medium (α-MEM) culture medium, supplemented with 10% fetal bovine serum (FBS), 100 IU/mL penicillin, 100 µg/mL streptomycin, and 2.5 µg/mL amphotericin B (all from Gibco). The cultures were maintained at 37 °C with 5% CO_2 in air. Once the cultures reached approximately 70% confluence, they were detached and sub-cultured at a density of 10,000 cells/cm^2 in the defined culture medium. After 24 hours, the culture medium was removed, and the cells

were incubated with a complete culture medium supplemented with 10% PBS-antibiotic solution, containing the designated concentrations of the tetracyclines, for up to 21 days. Control cultures were grown in basal culture medium supplemented with 10% PBS without any tetracyclines (C-BAS), while osteogenic-induced cultures were grown in 10 mM β-glycerophosphate, 50 μg/mL ascorbic acid and 10 nM dexamethasone (all from Sigma-Aldrich). The culture medium was changed twice a week.

Table 4. The chemical structure, characteristics, and source of the assessed TCs.

	Tetracycline-HCl	Doxycycline-HCl	Minocycline-HCl	Sarecycline-HCl
Chemical Structure	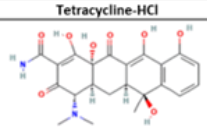	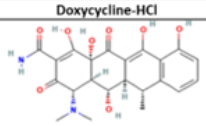		
Generation	1st Generation	2nd Generation		3rd Generation
Modification (to TC)	—	C5 (R4) addition of OH C6 (R2) removal of OH	C7 (R1) addition of $N(CH_3)_2$ C6 (R2 and R3) removal of OH and CH_3	C7 (R1) addition of methoxy-methyl-amino-methyl group C6 (R2 and R3) removal of OH and CH_3
Obtained from / Batch	Sigma-Aldrich / T8032	Sigma-Aldrich / D3447	Sigma-Aldrich / M9511	Adooq Bioscience / P005672

From National Center for Biotechnology Information (2023). PubChem Compound Summary for CID 54675776 (tetracycline), CID 54671203 (doxycycline), CID 54675783 (minocycline) and CID 54681908 (sarecycline). Accessed on 9 September 9, 2023, https://pubchem.ncbi.nlm.nih.gov

4.2.1. Metabolic activity assay

The metabolic activity of the cell cultures was assessed using the tetrazolium dye (MTT). At selected periods, a 10% MTT solution (5 mg/mL, Sigma-Aldrich) was added to cultured cells, and incubated for 3 h. Afterwards, the supernatant was removed, and the formed crystals were dissolved with dimethyl sulfoxide (DMSO). The absorbance of the resulting-colored solution was measured at 550 nm using a microplate reader (Synergy HT; BioTek). The obtained data were normalized to the values of the control group (C-BAS), set as 1.0. The assay was performed in quintuplicates.

4.2.2. Cell morphology

Cell morphology was assessed using fluorescence microscopy, upon F-actin and mitochondria staining, using phalloidin-conjugated Alexa Fluor 488 (Molecular Probes) and MitoSpy™ Red FM (Biolegend), respectively. Nuclei were counterstained with Hoechst 33342 (Enzo). Stained cells were visualized using a Celena S digital imaging system (Logos Biosystems). To perform the staining, at selected time points, the cultures were incubated with MitoSpy™ Red FM, for 30 minutes at 37 °C. Subsequently, the cells were fixed with 3.7% paraformaldehyde, permeabilized with 0.1% Triton-X, and blocked with bovine serum albumin (Sigma–Aldrich) to prevent non-specific interactions, at room

temperature. The cells were then stained with phalloidin-conjugated Alexa Fluor 488 and Hoechst 33342, for F-actin and nucleus staining, respectively. Stained cells were subjected to microscopic analysis. Images were treated using the ImageJ software v.1.53k. The assay was conducted in triplicates.

4.2.3. Assessment of gene expression by quantitative PCR (qPCR)

Total RNA was isolated from cell cultures, at selected timepoint, with Trizol reagent (Invitrogen, Carlsbad, USA) following the manufacturer's protocol. RNA concentration and quality were assessed by absorbance reading (260/280 nm) using a Take3 module (Gen5, BioTek) and a microplate reader (Synergy HT; BioTek), and samples with A260/A280 ratio of approx. 2.0 proceeded to cDNA conversion. The conversion to cDNA was achieved using a two-step reverse transcription quantitative NZY Kit (NZYTECH), normalizing the RNA concentration to 300 ng/µL, followed by the addition of RNAse (NZY). The qPCR reaction was performed in a CFX384 real-time PCR system (Bio-Rad) with the iTaq Universal SYBR green Supermix (Bio-Rad), accordingly to the Bio-Rad cycling protocol (activation – 2 min at 95 °C; 40 cycles of denaturation/annealing, 5 sec at 95 °C and 30 sec at 60 °C; melt curve, 65 – 95 °C). Selected primers were purchased from Bio-Rad (Table 3, chapter 3) and the negative control was set using DEPC for each primer. Finally, Bio-Rad CFX Maestro 1.1 (v.4.1.24) was used to collect data and check the reaction's quality control, where only samples with amplification efficiency between 90 – 100 were used, with a linear standard curve (R2) greater than 0.98. The relative quantification of each target gene was normalized to beta-actin levels (housekeeping gene) and calculated via the $2^{-\Delta\Delta Ct}$ method. The assay was conducted in quintuplicates.

4.2.4. Alkaline phosphatase (ALP) histochemical staining

At defined time points, HBMSCs were fixed in 1.5% glutaraldehyde for 10 min. Then, cells were stained with α-naphthyl acid phosphate (2 mg/mL) and Fast Blue R (2 mg/mL) solutions, incubated for 1 h protected from the light. The presence of ALP was noticed by brown-to-black staining according to the relative amount of the enzyme. Images were taken using a Zeiss Axiolab 5 microscope coupled with an Axiocam 5 Color Camera. The percentage of the ALP-stained area of obtained images was calculated using ImageJ software (v.1.53k) using the Otsu algorithm to set the threshold. The assay was conducted in triplicates.

4.2.5. Statistical analysis

Statistical analysis was conducted using the SPSS software (IBM, v.27). The normality of the datasets was assessed using the Shapiro-Wilk test. For datasets that followed a normal distribution, one-way ANOVA was performed, followed by Tukey's multiple comparisons test. Non-parametric datasets were analyzed using the Kruskal-Wallis test, followed by Dunn's multiple comparison tests. The significance level was set at $p \leq 0.05$. The data were presented as mean ± standard deviation (SD) to provide a measure of the central tendency and variability of the results.

4.3. Results

Throughout the culture period, both the basal control and the experimental conditions exhibit a gradual increase in the metabolic activity/cell viability, from day 1 to day 21. When a comparative assessment was conducted for each time point (Figure 16), regarding days 1 and 7, no significant differences were observed between conditions, regardless of the tested TCs or concentrations. However, a tendency for decreased values could be seen in the TETRA group at a concentration of 10 µg/mL, at day 1; while the DOXY group presented this trend across all concentrations at day 7. Moreover, TETRA at 0.1 µg/mL and the SARE group at all concentrations showed a trend for increased MTT reduction values, compared to the basal control (C-BAS), also at day 7. No significant differences were found regarding the comparison to the osteogenic-induced condition (OST) at early time points. At day 14, significant differences were observed, with the MINO and DOXY groups showing significantly lower metabolic activity, particularly at a concentration of 10 µg/mL. In contrast, the TETRA and SARE groups exhibited similar metabolic activity to the basal control (C-BAS). The OST condition showed a trend for reduced metabolic activity values. Finally, at day 21, all experimental groups had MTT reduction levels lower than those of the basal control, with significant differences observed at concentrations of 1 and 10 µg/mL for all TCs, except for DOXY at 1 µg/mL. The OST cultures maintained the trend of reduced metabolic activity values. Lower concentrations (0.1 µg/mL) of all TCs showed no significant differences compared to the control.

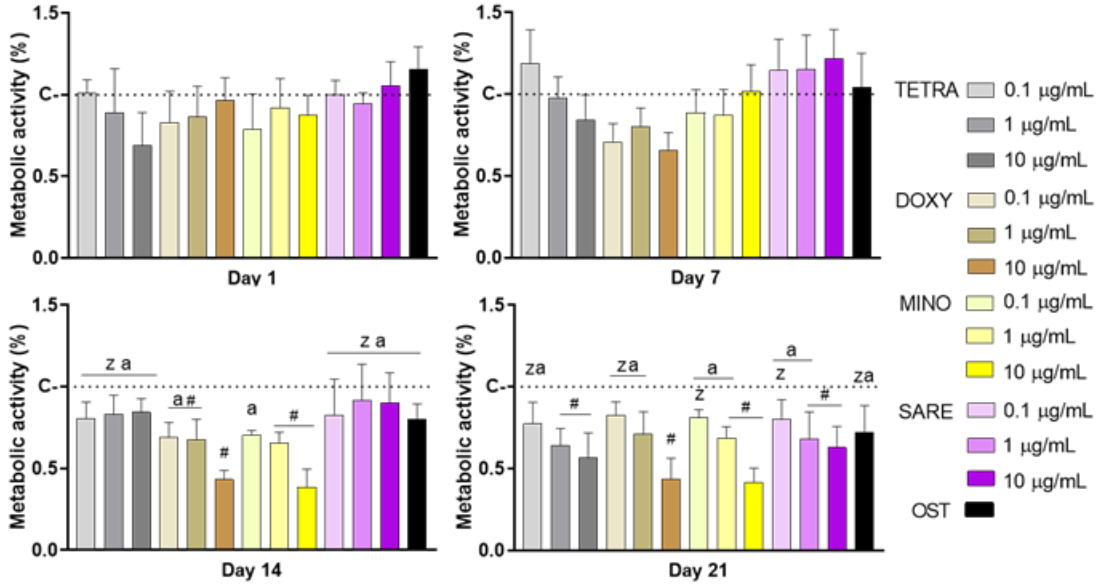

Figure 16. Metabolic activity/cell viability of HBMSC cultures incubated with tetracyclines at different concentrations - MTT assay. TETRA corresponds to tetracycline; DOXY to doxycycline; MINO to minocycline; SARE to sarecycline; and OST to osteogenic-induced cultures. The color scale corresponds to the tetracycline/drug and concentrations of 0.1, 1, and 10 µg/mL. Experimental group values were normalized by the basal control (C) for each timepoint, set as 1.0. (#) different from C; (z) different from DOXY at 10 µg/mL, (a) different from MINO at 10 µg/mL. (n=5, $p \leq 0.05$).

HBMSCs' morphology was observed and documented after 7 and 14 days of culture (Figure 17). On day 7, the control group (C-BAS) exhibited a dispersed distribution of cells with a uniform elongated morphology. Actin stress fibers extended across the scattered cytoplasm in a parallel fashion, accompanied by filopodial projections indicating an attempt to establish direct contact with nearby cells. Nuclei were prominently stained, while mitochondrial staining was faint, and concentrated at the perinuclear region. Osteogenic-induced cells (OST) presented a similar pattern of culture organization, although some cells exhibited a more polygonal shape. Cultures exposed to tetracyclines, at different concentrations, displayed a comparable culture organization and morphological pattern. By day 14, an increased cellular density was observed in all conditions, although there were some variations in the overall cell number. Cells were arranged in a trabecular-like organization, and there was a more intense reddish perinuclear accent due to stronger mitochondrial staining. Compared to the control (C-BAS), the TCs-exposed conditions and OST showed rearrangement of the actin cytoskeleton, with thicker actin filament bundles observed at the cell periphery.

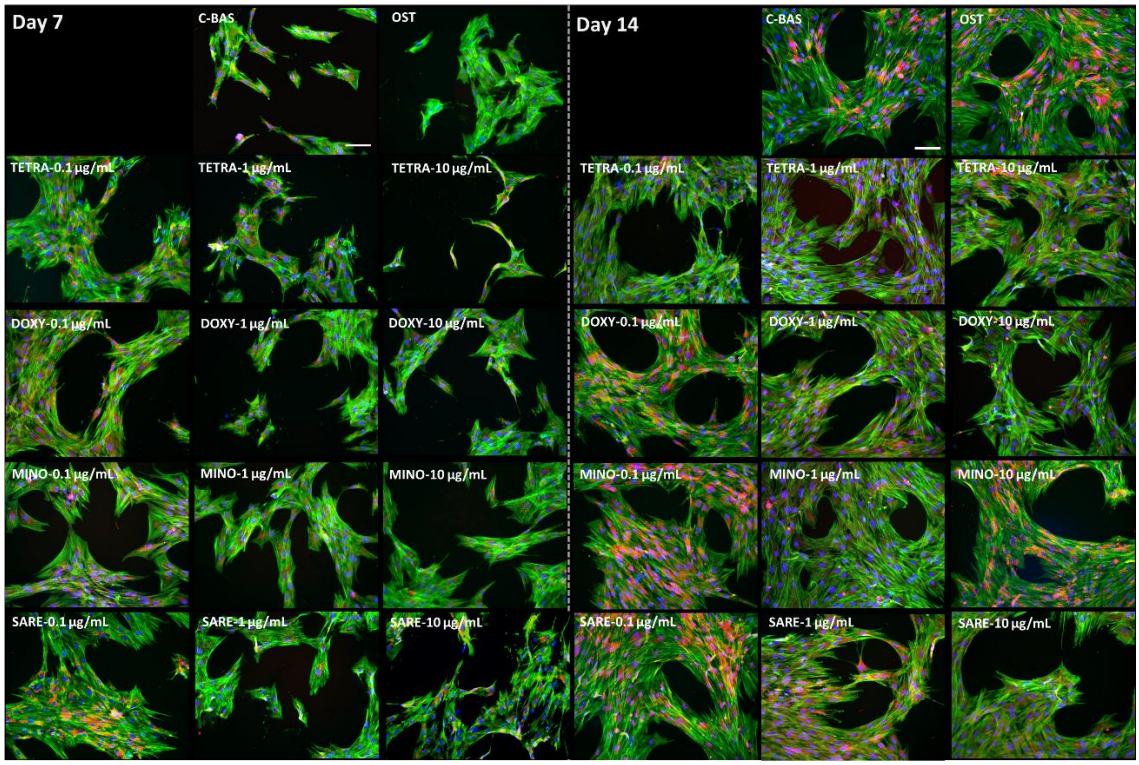

Figure 17. Representative fluorescent images of cellular morphology of HBMSC cultures at day 7 and day 14, incubated with tetracyclines at different concentrations. The cellular actin cytoskeleton was stained in green; nuclei were counter-stained in blue, and mitochondria were dyed in red. The scale bar corresponds to 100 µm. TETRA corresponds to tetracycline; DOXY to doxycycline; MINO to minocycline; SARE to sarecycline; C-BAS to basal control; and OST to osteogenic-induced cultures.

To evaluate and compare the ability of TCs to modulate the osteogenic program in precursor populations, 14-day HBMSCs cultures incubated with TCs at 1.0 µg/mL were assessed for alkaline phosphatase (ALP) activity (Figure 3) and osteogenic gene expression (Figure 18). In terms of the ALP histochemical staining, the control cultures (C-BAS) displayed a light-brownish accent, indicating baseline ALP activity. In contrast, the osteogenic-induced cultures (OST) exhibited significantly increased dark staining, indicating a higher level of ALP activity. The experimental groups treated with TCs exhibited an intensified color accent and the presence of focalized areas of darker staining, demonstrating regions of increased enzyme activity, compared to the control (C-BAS). This observation was confirmed by the quantitative analysis, where all experimental groups showed significantly higher levels of ALP compared to the control (C-BAS), with MINO and SARE reaching levels like those observed in the OST group.

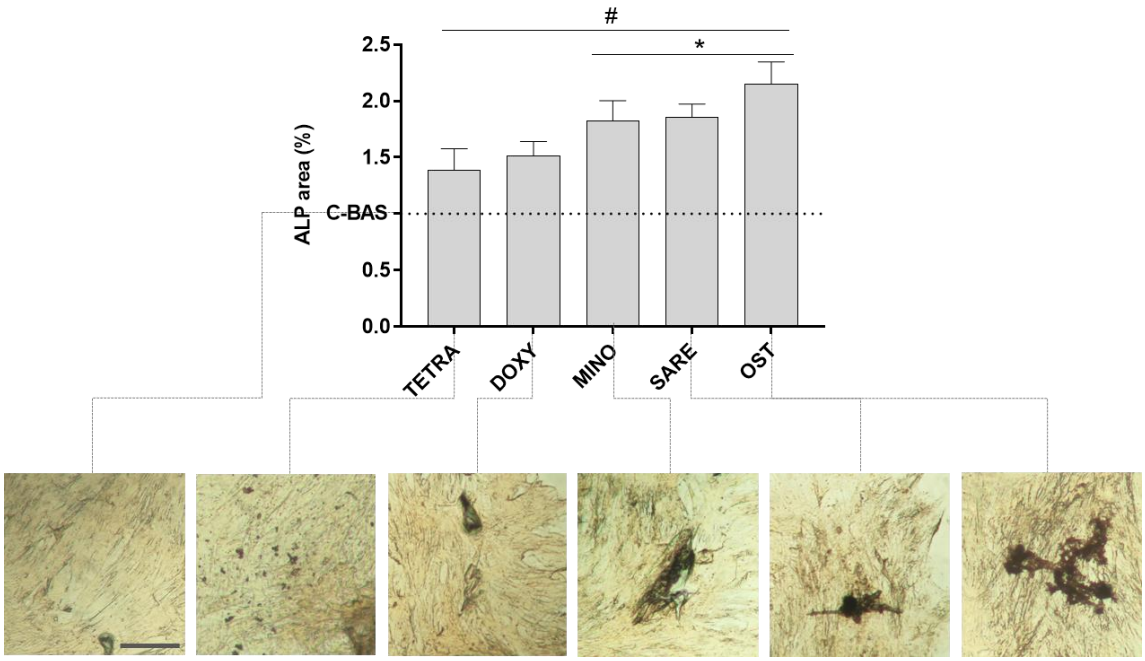

Figure 18. Osteogenic activity of HBMSCs cultured with TCs at 1.0 µg/mL. Quantitative analysis and representative histochemical staining of ALP activity displayed as a normalized percentage as compared to the basal control (C-BAS) set as 1.0. TETRA corresponds to tetracycline; DOXY to doxycycline; MINO to minocycline; SARE to sarecycline; C-BAS to basal control; and OST to osteogenic-induced cultures. The scale bar corresponds to 100 µm. (#) different from control; (*) different from TETRA and DOXY. n=5, p≤0.05.

In Figure 19, significant differences can be observed among TCs' exposed cultures, in terms of osteogenic gene expression. The genes RUNX2, SP7, COL1A1 and SPARC were significantly upregulated in all experimental groups in comparison to control (C-BAS). Among these, MINO and SARE groups induced the highest overall upregulation to levels like those of OST with RUNX2 and SP7.

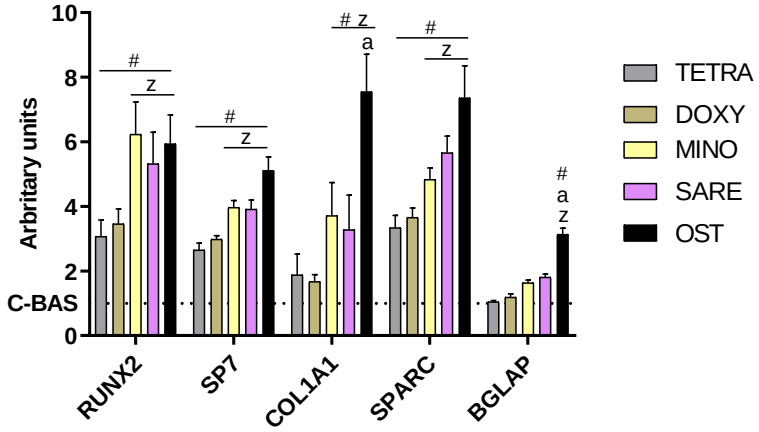

Figure 19. Relative gene expression of osteogenesis-related genes using quantitative PCR assessment. Values were normalized via the $2^{-\Delta\Delta Ct}$ method. TETRA corresponds to tetracycline; DOXY to doxycycline; MINO to minocycline; SARE to sarecycline; C-BAS to basal control; and OST to osteogenic-induced cultures. (#) different from control; (z) different from TETRA and DOXY; (a) different from MINO and SARE. n=5, p≤0.05.

Further, the potential modulation of relevant signaling pathways was evaluated via the assessment of target genes: HES1 and HEY, for the Notch pathway; AXIN2 and TWIST for the Wnt/β-catenin pathway; and PTCH1 and GLI2 for the Hedgehog (HH) pathway (Figure 20). No significant differences were reported in HES1 and HEY expression in the presence of TCs or OST. DOXY and TETRA were found to significantly upregulate AXIN2 expression, further inducing a trend for increased TWIST expression. PTCH1 and GLI2 expression were upregulated by all TCs, with MINO and SARE inducing the expression to levels like or higher than those attained with OST.

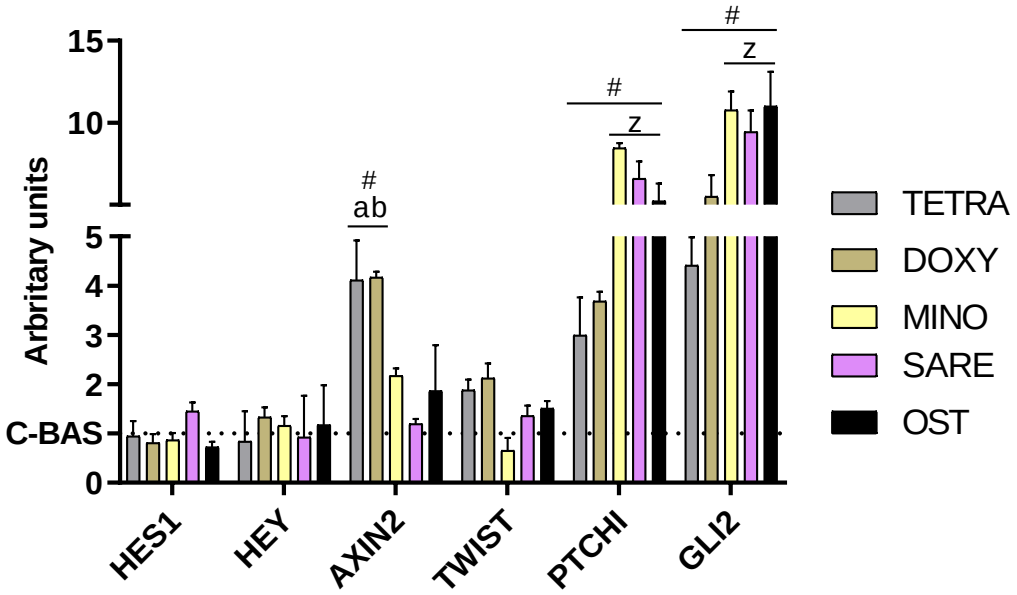

Figure 20. Relative gene expression of relevant osteogenic pathways of cultures using qPCR technique. Values were normalized via the $2^{-\Delta\Delta Ct}$ method. (#) different from control; (z) different from TETRA and DOXY; (a) different from MINO and SARE; (b) different from OST. n=5, $p \leq 0.05$.

4.4. Discussion

Tetracyclines (TCs) are broad-spectrum antibacterial agents widely used for the treatment of bacterial infections. Tetracycline, doxycycline, and minocycline are the most frequently used molecules in this class [36,246]. TCs have also demonstrated clinical efficacy in managing dermatological conditions, specifically acne vulgaris and rosacea, with a particular focus on the application of sarecycline [247]. In dermatological and related therapies, both antimicrobial and sub-antimicrobial dosages have proven effective, harnessing the pleiotropic effects of TCs while minimizing potential dose-related adverse side effects [248]. Furthermore, sub-antimicrobial therapies have also

been expanded to address other local and systemic conditions, such as periodontal diseases, given their immunomodulatory capabilities [236,249], emphasizing the potential for repurposing the TCs family in various therapeutic areas.

Tetracyclines (TCs) have shown a remarkable affinity for the bone matrix, potentially attributed to their ability to chelate calcium ions [112]. Consequently, the investigation of TCs' potential modulatory effects on bone tissue has gained attention. While some studies have explored the potential effects of individual TCs on osteogenic differentiation - such as minocycline, doxycycline [190], and sarecycline [41] - a comparative evaluation within the same experimental settings is still lacking. Additionally, the characterization of the underlying signaling pathways responsible for the observed effects remains unexplored. Therefore, this study aimed to comparatively evaluate the *in vitro* osteogenic capabilities of the most used TCs (i.e., TETRA, DOXY, MINO, and SARE) at distinct concentrations, representing the three generations of TCs. Furthermore, this research focused on the assessment of relevant signaling pathways activation that may contribute to the modulation of the osteogenic differentiation process. By shedding light on the differential osteogenic potential and underlying signaling mechanisms of these TCs, this research intended to provide valuable insights into their potential therapeutic applications in bone tissue-related conditions.

Human mesenchymal stem cells (HMSCs) were selected as osteoblastic precursors in this study, with consideration given to their origin in the bone marrow. Bone marrow-derived HMSCs possess an epigenetic memory for the osteogenic lineage and exhibit an enhanced capability for osteogenic differentiation, as compared to cells originating from other tissues [250,251]. To induce osteogenic differentiation as a positive control, cultures were grown in the presence of dexamethasone, ascorbic acid, and β-glycerophosphate, which are well-established *in vitro* inducers of the osteogenic program [252,253]. Dexamethasone is known to induce and enhance the activity of RUNX2, the master transcription factor of the osteoblastic differentiation [252]. Ascorbic acid stimulates collagen type I secretion and subsequent collagen/integrin-mediated signaling, while β-glycerophosphate serves as a source of phosphate for the mineralization of the extracellular matrix, further augmenting the osteogenic signaling [254]. The established cultures were characterized regarding metabolic activity/viability, morphological organization, ALP expression, and gene expression analysis to assess the activation of the osteogenic program and relevant signaling pathways.

The evaluation of the metabolic activity in the TCs-exposed cultures revealed no significant differences at early time points (days 1 and 7). However, a trend of reduced values was observed at later time points (day 14, for DOXY and MINO groups; and day 21, regarding all TCs), similarly to the attained in the osteogenic group (OST). Previous studies have indicated that different TCs do not impair the viability/metabolic activity of osteoblastic and precursor populations, particularly at low concentrations [190]. Moreover, TCs have demonstrated cell-specific anti-apoptotic effects [255,256], particularly in mesenchymal-derived populations [257], while also selectively increasing apoptosis in osteoclastic-related populations [243,257]. Additionally, a decrease in metabolic activity is expected in osteogenic differentiating populations, at longer culture timepoints. This reduction can be attributed to the increased differentiation commitment within the osteogenic program, as more differentiated cells have a reduced ability to divide compared to less mature cells [258], in line with the well-established inverse relationship between proliferation and differentiation kinetics [259,260]. It is also essential to consider that higher TCs concentrations may induce cytotoxicity, as evidenced by the significant reduction in the metabolic activity observed with the 10 μg/mL concentration, at later time points. Reported TCs' IC50 values, typically falling within the 3-10 μg/mL range, as observed in different cell populations, suggest a potential negative impact of higher concentrations on cellular behavior [190,261].

Despite some variations in the cell number that correlate with differences in the metabolic activity, HBMSCs exposed to TCs displayed a consistent morphology across all groups, resembling the morphology observed in the osteogenic-induced group (OST). This similarity suggests that TCs may contribute to the ongoing osteogenic differentiation of HBMSCs and help to elude senescent and adipogenic profiles, which are typically associated with a rounder cell morphology [207]. Notably, during the osteogenic differentiation, cells undergo modifications in their cell shape, adopting a spread and polygonal morphology, and forming thick actin bundles. These alterations are attributable to changes in the actin polymerization status, triggered by the physical and chemical signaling transduction elicited by the osteogenic inducers (i.e., dexamethasone, ascorbic acid, and β-glycerophosphate used within the OST group) [262], and similar to the changes observed in TCs-exposed populations. These findings suggest that TCs may stimulate similar actin remodeling processes as the established osteogenic inducers, further supporting their potential role in promoting osteogenic differentiation of HBMSCs.

The activation of the osteogenic program was further validated by assessing the expression of relevant osteogenic genes and ALP activity, upon exposure to TCs at 1.0 μg/mL. Osteogenic-induced cells (OST) exhibited a significant increase in the ALP activity and expression of key transcription factors, RUNX2 and SP7 – coding respectively for Runt-related transcription factor 2 and osterix. RUNX2, a major transcription factor for osteoblastogenesis, plays a crucial role in regulating the transcription program of lineage-specific genes essential for bone formation through genetic and epigenetic mechanisms [263]. SP7, an equally important transcription factor for bone formation and bone matrix deposition, modulates the osteoblastic commitment downstream of RUNX2 [264]. All TCs demonstrated a significant increase in the activity of ALP and expression of both transcription factors compared to the control group (C-BAS), indicating their potential to enhance osteogenic differentiation. Notably, MINO and SARE groups exhibited ALP activity and gene expression levels like those achieved with OST, reaching 4-6 times higher expression levels than the basal control. Furthermore, MINO and SARE also upregulated the expression of downstream osteogenic genes, including COL1A1, which encodes the pro-alpha1 chain of type I collagen, the major protein of the extracellular matrix; and SPARC, which encodes osteonectin, a non-collagenous protein with collagen- and hydroxyapatite-binding domains that modulate collagen deposition and influence osteoblastic/osteoclastic differentiation [214]. The expression levels of these genes in the presence of MINO and SARE were like those observed in the OST group, indicating that these TCs effectively promote osteogenic differentiation. Additionally, there was a trend towards increased expression of BGLAP, which encodes osteocalcin – the most abundant non-collagenous protein involved in modulating the mineralization process, and an acknowledged late marker of osteogenic differentiation [265]. This tendency was particularly evident in MINO and SARE groups. Overall, while all TCs were able to induce the osteogenic gene expression program, MINO and SARE exhibited the highest induction levels, comparable to those achieved with OST. These differences in gene expression patterns attained with different TCs may be attributed to their selective ability to activate specific signaling pathways involved in the osteogenic differentiation, which were following addressed.

The impact of TCs exposure on Notch signaling was evaluated by the assessment of classical canonical target genes, and interestingly, neither TCs exposure nor OST induction significantly altered their expression. HES1 (coding for hairy enhancer of the split-1) and HEY (coding for hairy ears, Y-linked), showed no significant changes in their

expression levels in response to either OST or TCs treatment. Notch signaling has been reported to play a role in the regulation of osteogenic differentiation, albeit with conflicting findings [266,267]. It has been suggested that Notch signaling may enhance late-stage osteogenesis, particularly during the matrix mineralization process; whether an inhibitory activity has been described at early osteogenic stages by suppression of the Wnt pathway [266,267]. Given that the assessment of the target genes was conducted on day 14 – a transition period between the early and late *in vitro* osteogenic differentiation, the absence of significant modifications in Notch signaling is apprehensible [267].

Regarding the Wnt pathway, the expression of AXIN2 and TWIST - target genes known to regulate the pathways' activity, was assessed. AXIN2, encoding the axis inhibition proteins 2, is an endogenous inhibitor providing negative feedback to regulate the pathways' signaling [268]; whilst TWIST encodes the Twist Family BHLH Transcription Factor 1, an early transcription factor able to inhibit chondrogenic development in favor of osteogenesis [269]. The Wnt signal transduction pathway, particularly the canonical pathway initiated by distinct Wnt ligands, plays a crucial role in bone formation and the commitment of precursor populations to osteogenesis [270]. The activation of this pathway involves the stabilization β-catenin by inhibiting its phosphorylation, which leads to cytoplasmic accumulation and subsequent nuclear translocation. Once in the nucleus, β-catenin binds to T-cell factor/lymphoid enhancer factor (TCF/LEF) transcription factors, thereby activating the transcription of downstream genes associated with the osteogenic differentiation [270]. In this study, exposure to TETRA and DOXY significantly upregulated the expression of AXIN2, further inducing a positive trend for TWIST expression, substantiating the activation of Wnt signaling during the verified osteogenic induction of HBMSCs. These findings are in line with previous research demonstrating the ability of DOXY to enhance osteogenic commitment via an increased Wnt signaling, both *in vitro* - in osteogenic-compromised bone marrow mesenchymal stromal cells [271], and *in vivo* by promoting alveolar bone repair [272]. MINO and SARE were found not to significantly influence the expression of Wnt targets, suggesting that the attained osteogenic induction was majorly attained via a distinct signaling.

Indeed, MINO and SARE exposure exhibited a notable association with increased Hedgehog (HH) signaling, as supported by the upregulation of the target genes PTCH1 and GLI2. The expression levels of these genes in the MINO and SARE groups were comparable to, or even higher than, those observed in the OST group. In the HH pathway, signaling is initiated by the activation of Smoothened (SMO) receptor, leading to the

activation of GLI transcription factors, and subsequent upregulation of target genes, including PTCH1 (a negative regulator of the pathway) and the GLI transcription factors, such as GLI2 [273]. Previous research has linked HH signaling to the promotion of the osteogenic differentiation of HMSCs through the increased expression of key transcription factors, including RUNX2 and SP7 [274,275]. Specifically, the upregulation of GLI2 has been correlated with increased RUNX2 activity, as these two factors physically interact and synergistically enhance the osteogenic induction [276]. Moreover, a positive feedback loop has been described, involving the GLI2 signaling and the induction of the insulin-like growth factor 2 (Igf2), an established inducer of osteogenesis [277]. While evidence on TCs-mediated HH signaling in bone-related cells/tissues is limited, previous studies have associated MINO with elevated HH signaling in various cellular populations, speculating on its potential effectiveness in neuromodulation [278]. The differentiated biological outcomes and signal modulation observed with the distinct TCs may find origin in chemical dissimilarities. This divergence could be potentially attributed to differences in their chemical structure, particularly at the critical C7 position of the D ring. Interestingly, both SARE and MINO share modifications in in this very C7 position of the D ring, with the addition of distinct amino derivative groups (Table 4). Alterations in the C7 position are considered a major structural optimization, being constantly exploited in the development of new TC molecules [155,156]. In fact, key functional traits as antibacterial potency and spectrum, interactions between TCs and bacterial mRNA, as well as calcium chelation rate can be directly manipulated by the addition of functional groups at C7 position [156]. This highlights the potential relevance of this specific alteration in shaping the interaction and functional modulation of eukaryotic cells, despite further studies are needed to fully uncover the implications of this issue.

4.5. Conclusion

The investigation of four commonly used tetracyclines (i.e., tetracycline, doxycycline, minocycline, and sarecycline) in the modulation of human mesenchymal stem cells' activity revealed their potential to enhance the osteogenic differentiation, as evidenced by the modulation of the actin cytoskeleton, increased osteogenic gene expression and ALP activity. Present findings indicate that TETRA and DOXY exert their effects through increased Wnt signaling, while MINO and SARE may mediate their effects through an

alternative mechanism, potentially involving increased Hedgehog signaling. It is noteworthy that MINO and SARE exhibited the highest levels of osteogenic induction, comparable to those achieved with the gold standard *in vitro* osteogenic induction using dexamethasone, ascorbic acid, and β-glycerophosphate. These outcomes could be intricately linked to variances in the chemical structure, particularly within the C7 position of the D ring, thus possibly underpinning the achieved outcomes.

The potential of TCs to promote osteogenic differentiation holds promise for targeted treatments based on specific bone-related disorders. Further investigation into the precise signaling pathways and mechanisms involved will undoubtedly contribute to the development of novel and effective regenerative therapies.

CHAPTER 5

Green Synthesis of Zn–Mg layered hydroxide nanoparticles with surface-mediated antioxidant and anti-inflammatory activity

The original article in this chapter was published as Martin V, Bettencourt AF, Fernandes MH, Alves MM, Hanafy M, Cui Z, Gomes PS, Santos CF. Green synthesis of Zn–Mg layered hydroxide nanoparticles with surface-mediated antioxidant and anti-inflammatory activity. Surf. Interfaces 2024.

DOI: 10.1016/j.surfin.2024.104037.

5.1. Introduction

Inflammation is a defensive mechanism that encompasses a variety of cellular and molecular processes related to the activation of the immune system, triggered by both external (e.g., virus, bacteria, fungi, chemical and physical agents) and internal (e.g., tissue injury and genetic disorders) sources [279]. The main objective of an inflammatory reaction is the elimination of harmful agents and/or damaged tissues, allowing proper healing and the reestablishment of homeostasis [280]. Physiologically, this process is self-limited and its resolution is currently defined by the absence of effectors within the involved site [281]. However, when this process is not completely resolved, low-grade chronic inflammation can arise, contributing to the pathogenesis of several inflammatory conditions, such as osteoarthritis, atherosclerosis, diabetes, autoimmune, and neurodegenerative diseases [279,281]. Moreover, physiological aging also contributes to a chronic inflammatory state through the increased presence of senescent cells, the accumulation of self-debris and self-molecules from aged tissues and altered gut microbiota [279,282]. Therefore, as the global population ages, there is a notable rise in the incidence and severity of these inflammatory disorders [282,283].

Currently, a variety of anti-inflammatory drugs is currently available to manage these conditions – including glucocorticoids (e.g., prednisone, dexamethasone), nonsteroidal anti-inflammatory drugs (NSAIDs, e.g., diclofenac, etoricoxib) and specific monoclonal antibodies (e.g., canakinumab, tocilizumab) [284,285]. Despite their effectiveness, long-term use is related to severe side effects, such as adrenal cortex dysfunction, cardiotoxicity, kidney injury, neutropenia, and a higher risk of opportunistic infections [284,285]. As a result, the development of viable alternative therapies for chronic inflammation with fewer adverse effects is critical.

In this context, herbal extracts and isolated phytochemicals are considered promising alternatives that may present lower incidence rates and reduced adverse effects [286]. Among the plethora of assessed specimens [287], rosehip (RH) – the pseudo fruit of the *Rosa canina* rose plant – has a composition that comprises four main groups of active compounds, namely vitamins (e.g., acid ascorbic), polyphenols (e.g., flavonoids, gallic acid), carotenoids and unsaturated fatty acids (e.g., linoleic acids). These constituents confer both anti-inflammatory and antioxidant properties [288]. Additionally, phytochemicals have demonstrated the ability to downregulate the nuclear factor kappa-light-chain-enhancer of activated B cells transcription factor (NFkB) signaling, reducing

the production of pro-inflammatory enzymes (as cyclooxygenase-1 and 2) and modulating interleukin levels (e.g., IL-1β and 6) [289]. Additionally, they can inhibit cellular nitrous oxide production and scavenge hydrogen peroxide more effectively than their synthetic counterparts, such as butylated hydroxyanisole or hydroxytoluene, providing compelling evidence of their antioxidant effectiveness [289,290].

Accordingly, RH extracts have shown beneficial effects in preclinical and clinical settings against conditions like cardiovascular diseases, osteoarthritis, and inflammatory dermatitis [288,289,291,292]. However, the oral administration of RH tea and extracts produced limited effects in clinical trials, being unable to reduce inflammation markers as C-reactive protein and adipokines [292,293]. To circumvent their partial degradation and metabolization by the hepatic portal system and gastrointestinal tract enzymes, local delivery strategies must be used to target their activity effectively [28].

Nanoparticles (NPs) have emerged as promising and versatile carrier systems for medical applications due to their large surface area, improved circulation time, and capability to overcome biological barriers [67]. Among NPs systems, layered hydroxides (LH) - defined as inorganic thin materials with anionic exchangeable properties - can act as efficient carriers for RH extract delivery [170,172]. LHs exhibit desirable physicochemical characteristics, as pH-dependent biodegradability, high swelling capacity, and remarkable adsorption capabilities [173,294]. In this context, underexplored LHs may fill a crucial gap in the realm of phytochemical carriers.

The present study devised the innovative development of a zinc-magnesium layered hydroxides (Zn-Mg LH) nanoformulation, using a straightforward co-precipitation green synthesis methodology [170,172]. Aiming to achieve synergetic effects with RH, zinc (Zn) and magnesium (Mg) were chosen to compose the LH due to their biocompatibility, antioxidant and anti-inflammatory properties [180,295]. The study comprehensively evaluates the physicochemical characteristics, such as morphology, crystallinity, and chemical composition, of the LH loaded with or without RH-derived phytochemicals. Furthermore, it details the *in vitro* cytocompatibility and investigates the antioxidant and anti-inflammatory activities of these formulations.

5.2. Methods

5.2.1. Green Synthesis of Zn-Mg LH and RH-Zn-Mg LH

The synthesis of RH-Zn-Mg LH NPs using Rosehip (RH) extract was made by the following green method. Firstly, 5 g of dried RH were added to 250 mL of deionized water and boiled for 15 min to obtain the RH extract. Then, the RH extract was diluted in dH_2O (1:1 V/V) and the 0.1 M magnesium nitrate [$Mg(NO_3)_2 \cdot 6H_2O$, Sigma] and 1 M zinc nitrate [$Zn(NO_3)_2.6H_2O$, Sigma] salts were mixed at 1:10 ratio under magnetic stirring, at room temperature. The pH value of the solution was ~2.0. RH-Zn-Mg LH NPs were precipitated after adding 25% aqueous ammonia (Merck) to a final pH value of 5.7. The attained powder was washed with deionized water and collected, using a 0.22 mm filter (Sarstedt). RH-Zn-Mg LH NPs were dried in a vacuum chamber at room temperature and sterilized using ethylene oxide. To assess the influence of phytochemicals on the green synthesis process, particles without extract (Zn-Mg LH) were produced. The experimental procedure was carried out as previously described, with the only difference being the replacement of the extract with dH_2O, while ensuring that the pH of the solution remained the same.

5.2.2. Zn-Mg LH and RH-Zn-Mg LH physicochemical characterization

Zn-Mg LH and RH-Zn-Mg LH particles' crystallinity was evaluated by X-ray diffraction (XRD) using a D8 Advance Bruker AXS (Bruker). The zinc and magnesium contents of the NPs were quantified by inductively coupled plasma spectroscopy (ICP) (ISA Jobin Yvon– JY70 Plus). The chemical characterization of the NPs was assessed with Fourier transformed infrared spectroscopy (FTIR) using a Nicolet (Thermo Electron) spectrometer with an attenuated total reflectance (ATR) apparatus. The chemical composition of the Zn-Mg LH and RH-Zn-Mg LH NPs was further assessed by X-ray photoelectron spectroscopy (XPS), using an Axis Ultra HAS equipment (Kratos). The X-ray source was equipped with an Al Monochromator and the pass energy of scans was 90 W. In addition, the charge core of the carbon peak (C1s) was adjusted to 284.8 eV due to the non-conductive nature of the NPs. Data was analyzed using CasaXPS 2.3.24PR1.0.

The zeta potential was assessed by light scattering using Zetasizer Nanoseries Nano-S/Nano-Z instruments (Malvern) in Hepes buffer, at a range of pH (4-8) and dH_2O. To determine the entire polyphenolic content, the synthesized RH-Zn-Mg LH and Zn-Mg LH were dissolved in HCl at a ratio of 50 µL HCl/mg NPs. The obtained solutions were treated with Folin-Ciocalteu reagent for the determination of the total polyphenolic content [296]. The obtained solutions were analyzed with a double-beam UV–VIS–spectrophotometer (Thermo Scientific™ 51119200) at 765 nm. They were quantified

using a calibration curve, obtained with tannic acid as a standard reference. The shape and morphology of Zn-Mg LH and RH-Zn-Mg LH NPs were analyzed by transmission electron microscopy (TEM) using a TEM-Hitachi H-9000-NA, with an acceleration voltage of 200 kV. The NPs were loaded in copper-carbon grids and coated with a fine layer of conductive gold/palladium (Polaron E-5100), prior to the observation. Additionally, Zn-Mg LH NPs were also observed by scanning electron microscopy (SEM) using a JEOL-JSM7001F apparatus (JEOL), after the analogous increase of nanoparticles' conductivity.

5.2.3. In vitro cytocompatibility assessment of Zn-Mg LH and RH-Zn-Mg LH

Cytocompatibility of Zn-Mg LH and RH-Zn-Mg LH NPs was assessed *in vitro* using human fibroblasts (HFs, ATCC® PCS-201-018™) from the 7^{th} passage, in the presence of a wide range of NPs' concentrations (1.0, 10 and 50 µg/mL). Established HFs cultures were expanded in α-MEM containing 10% (v/v) fetal bovine serum (FBS), 100 $IU.mL^{-1}$ penicillin, 100 $\mu g.mL^{-1}$ streptomycin and 2.5 $\mu g.mL^{-1}$ amphotericin B (all from Gibco). Cultures were incubated at 37 °C and 5% CO_2 in air. After reaching approx. 70% confluency, cells were trypsinized and sub-cultured at 10^4 $cells.cm^{-2}$ for subsequent assays. After 24 h, culture medium was replaced by media containing Zn-Mg LH or RH-Zn-Mg LH NPs at described concentrations. Cultures grown without NPs were used as negative control.

5.2.3.1.Metabolic activity of the cell culture

The metabolic activity of HFs incubated with the RH-Zn-Mg LH and Zn-Mg LH NPs was assessed by the MTT assay. At selected time points, a 10 % (v/v) tetrazolium dye solution (MTT, Sigma) at 5 mg/mL was added to cell cultures, which were incubated for 3 h, at 37° C. Following the incubation period, supernatant was removed and 100 µL of dimethyl sulfoxide (DMSO) were added to each well to solubilize the formazan crystals. The absorbance of the final solution was measured at 550 nm with a microplate reader (synergy HT; BioTek). Assays were conducted in quintuplicates.

5.2.3.2.Cellular morphology

The morphology of HFs and general culture organization was observed by fluorescent microscopy. After 24 and 168 h of incubation with Zn-Mg LH and RH-Zn-Mg LH NPs at 10 µg/mL, cells were fixed using formaldehyde 3.7%. Then, fixed cultures were

permeabilized using Triton-X, followed by F-actin staining using Alexa-Fluor 488-phalloidin (Molecular Probes) and nucleus counterstain using Hoechst 33342 (Enzo). Fluorescent images were obtained using a Celena S digital imaging system (Logos Biosystems) and treated with ImageJ software v.1.53k. The assay was performed in triplicate.

5.2.3.3.Cellular internalization of Zn-Mg LH and RH-Zn-Mg LH NPs

The cellular uptake of Zn-Mg LH and RH-Zn-Mg LH NPs by HFs was observed through TEM images (JEM 1400, JEOL). HF cultures were incubated with the LH NPs at 10 μg/mL, for 3 h and 24 h. After reaching the timepoints, cultures were washed, trypsinized and centrifuged for 10 min, at 300 g and 4 °C. After discarding the supernatant, the cell pellet was re-suspended in a fixation solution (2.5% glutaraldehyde + 2% formaldehyde) and stored at 4 °C. Then, samples were dehydrated using a graded ethanol series prior their inclusion in molds containing Spurr's resin. Finally, nanometric sections (35–50 nm) were cut and placed onto TEM grids for observation. The assay was performed in triplicate.

5.2.3.4.Total reactive oxygen species (ROS) – Oxidative stress evaluation

Total ROS production in HFs induced by Zn-Mg LH and RH-Zn-Mg LH NPs was evaluated using a Total ROS/Superoxide detection kit (ROS-ID® ENZ-51010, Enzo Life Sciences). Briefly, cells were seeded in 96-well plates at 3 x 10^4 cells/mL and incubated at 37 °C, until 70% confluency was reached. Then, cells were washed using ROS buffer and the negative control group was treated with N-acetyl-L-cysteine (5 mM) for 30 min, at 37 °C. Subsequently, experimental groups were incubated with various concentrations of NPs (1.0, 10 and 50 μg/mL), while the positive control was exposed to 200 μM of the ROS inducer (pyocyanin), both diluted in ROS buffer. Finally, cells were incubated with the fluorescent dye from the Total ROS detection kit (2 μM), followed by incubation at 37 °C for 1 h. Total fluorescence was measured at 488/520 nm (Excitation/Emission) using a microplate reader. Assays were conducted in quintuplicates.

The antioxidant capability of the NPs was evaluated using two distinct techniques. Firstly, HF cultures were seeded in a 96-well plate and incubated with 20 μM of 2′,7′ – dichlorofluorescin diacetate (DCFDA, Life Technologies) for 30 min and then, the culture medium was replaced with media containing distinct concentrations of NPs. Cells incubated with 1.0 mg/mL of ascorbic acid were set as negative control and cells

incubated with pure culture medium were set as positive control. Cells were incubated for 1 h at 37 °C. Subsequently, hydrogen peroxide (H_2O_2) was added in each well, obtaining a final concentration of 500 mM/well. Cells were incubated at 37°C for additional 15 min and the fluorescence was read at 485/520 nm (EX/EM) using the same microplate reader. Secondly, the free radical-scavenging ability of the NPs was evaluated through the 2,2-diphenyl-1-picrylhydrazyl (DPPH, Sigma Aldrich) assay. 10 mg of NPs were put in a 1.5 mL Epp and suspended in 425 µL of a DPPH-ethanolic solution at 0.1 mM, room temperature, under slow agitation (70 rpm). At predetermined timepoints, Epp were centrifuged, and aliquots of the supernatant (60 µL) were taken, and their absorbance was read at 517 nm using the same microplate reader. DPPH concentrations were determined using a calibration curve. Assays were conducted in quintuplicates.

5.2.4. Anti-inflammatory activity of Zn-Mg LH and RH-Zn-Mg LH NPs using an organotypic mucosal model

The anti-inflammatory activity of Zn-Mg LH and RH-Zn-Mg LH NPs was assessed using a three-dimensional mucosal model, composed of a collagenous matrix with embedded fibroblasts and an epidermal outer layer of human keratinocytes, providing an enhanced organizational complexity and higher degree of differentiation in comparison to monolayer cell cultures [297]. Briefly, a solution of collagen type I from rat tail tendon (Roche) was prepared and added in the bottom of a 24-well plate insert (Thincert transparent membrane, 0.4 µm pore size, from Greiner) to obtain an acellular layer. Then, HFs were trypsinized and set into the collagen solution to establish the mesenchyme-like layer. After the proper HFs' growth into the collagen, keratinocyte cultures were trypsinized and added over the collagen gel. Additionally, Keratinocyte Media 2 (PromoCell) culture medium was added into the insert. After 7 days, gels were exposed to the air-liquid interface by the removal of the culture medium from the insert. Finally, after a week, the mucosal model was exposed to lipopolysaccharide (LPS, from Sigma) at 1.0 µg/mL for 16 h and then, incubated with both NPs at 10 µg/mL for further 24 h (Figure 21). Moreover, to validate the structure of the mucosal model, selected gels were fixed in 4% paraformaldehyde, embedded in paraffin blocks, and cut axially in 5 µm-thick sections. Then, sections were marked with hematoxylin and eosin (H&E) staining.

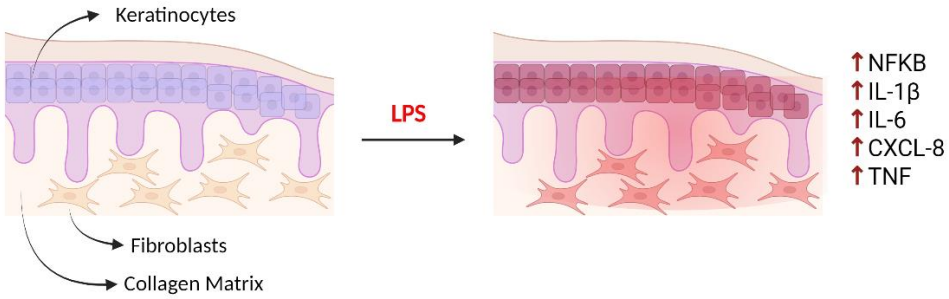

Figure 21. Schematics of the inflamed organotypic mucosal model, comprising a mesenchymal constituent (i.e., fibroblasts embedded into a collagen matrix) and a stratified epithelial outer layer of keratinocytes. *P. gingivalis*' LPS was used to trigger an inflammatory response, inducing the expression of cytokines (IL-1b, IL-6, TNF), chemokines (CXCL-8) and related transcription factors (NFKB) (data not shown).

Afterward, total RNA was isolated from the organotypic model using Trizol reagent (Ambion Life technologies) following the manufacturer's protocol. The concentration and the quality of the RNA were evaluated by absorbance reading (A260/A280) using the Take3 module (Gen5, BioTek) and a microplate reader (Synergy HT; BioTek). Quality's threshold was set between 1.9 and 2.1 for the absorbance ratio. For the conversion to cDNA, a reverse transcription system (NZY first-strand cDNA synthesis) was employed, normalizing the RNA' concentration to 250 ng/µL. Conversion' cycle was set as 10 min at 25°C, 30 min at 50°C and 5 min at 85°C and RNAse (NZY) was further added prior incubation at 37°C for 20 min.

Quantitative PCR (qPCR) analysis was performed with a CFX384 real-time PCR system (Bio-Rad), using the iTaq Universal SYBR green Supermix PCR Kit, in addition to DEPC water, pre-defined primers from Bio-Rad (Table 5) and the converted cDNA. Manufacture's protocol was followed (2 min at 95 °C; 40 cycles of 5 sec at 95 °C and 30 sec at 60 °C; melt curve, 65 – 95 °C). Wells lacking cDNA were used as negative control for each primer. Data were accessed using Bio-Rad CFX Maestro 1.1, v.4.1.24 software. Only samples with amplification between 90 and 110 and standard curve higher than 0.98 were used. The relative quantification of each target gene was normalized using the housekeeping gene (GAPDH) levels and final values were calculated via the $2^{-\Delta\Delta Ct}$ method. Five independent experiments were performed.

Table 5. Primers used for the amplification of the targeted genes.

Gene	Unique Assay ID	Gene	Unique Assay ID
GAPDH	qHsaCED0038674	CXCL8	qHsaCED0023767
IL1B	qHsaCID0022272	NFKB1	qHsaCED0002379
IL6	qHsaCED0044677	TNF	qHsaCED0037461

Abbreviations: GAPDH: Glyceraldehyde-3-Phosphate Dehydrogenase; IL1B: Interleukin 1 beta; IL6 – Interleukin 6; CXCL8 – Interleukin 8; NFKB1: Nuclear Factor Kappa B Subunit 1; TNF - Tumor Necrosis Factor.

5.2.5. Statistical analysis

Data are expressed as mean values ± standard deviation (SD). Statistical analysis was performed using the IBM® SPSS® Statistics software v.27. Data normality was assessed by the Shapiro–Wilk test. For normal datasets, one-way analysis of variance (ANOVA) was performed, followed by the post hoc Tukey test. The Kruskal–Wallis test was performed for non-parametric datasets, followed by multiple comparisons using Dunn's tests. ρ-values ≤ 0.05 were considered significant.

5.3. Results and Discussion

5.3.1. Structural and compositional characterization of Zn-Mg LH and RH-Zn-Mg LH NPs

In the present study, Zn-Mg LH NPs were successfully synthesized using dH_2O and RH extract, relying on a straightforward, rapid, scalable, and cost-effective co-precipitation method. Figure 22a shows the XRD patterns of Zn-Mg LH and RH-Zn-Mg LH NPs. It was observed that the zinc hydroxynitrate $Zn_5(NO_3)_2(OH)_8.2H_2O$ is the precipitated crystalline phase in the Zn-Mg LH NPs, as indicated by the presence of sharp, symmetric and intense reflection peaks with a basal d-spacing of 9.785 at $2\theta = 9.029$ arising from (200) plane, the (400) ($2\theta = 18.17$) at low 2θ angle, and a doublet peak at a 2θ value of 59.59º (223) and 59.81º (53-2), assigned to a monoclinic layered zinc hydroxide structure (space group C12/m1). These findings are consistent with the ICDD nº 72−0627 [181,298,299]. The presence of these strong diffraction peaks (200) and (400) clearly indicates that the nanosheets are layered zinc hydroxide nitrate.

Typically, the (200) orientation is the preferred growth direction for lamellar zinc hydroxide nitrate. Importantly, no other crystalline phase was identified. According to the literature, when NPs were synthesized in similar experimental conditions (room temperature and pH~6) without magnesium nitrate precursor, hexagonal ZnO particles were precipitated as a single crystalline phase [300,301]. Additionally, it is known that the substitution of Mg by Zn ion is possible in layered zinc hydroxide (LZH) structures.

Such substitution can cause a distortion in the octahedral interspace due to the smaller cation Mg^{2+} (0.65 Å) compared to the larger cation Zn^{2+} (0.74 Å), consequently increasing the average bond length between the two cations [302]. To evaluate the likelihood of this substitution, the lattice parameters were calculated from the XRD pattern and found to be as a = 19.47 Å, b = 6.23 Å and c = 5.52 Å for the Zn-Mg LH NPs. Remarkably, these values were smaller than the lattice parameter values reported by other authors for the $Zn_5(NO_3)_2(OH)_8.2H_2O$ structures [303–305]. Considering that the *a* parameter is dependent on the ion radius of the metal cation and, according to literature, known to decrease with decreasing zinc content, the obtained results suggest that some Mg^{2+} cations have indeed substituted Zn^{2+} cations [302]. Analogous substitutional outcomes were achieved for Co^{2+} in layered zinc hydroxide structures [303]. To validate the presence of Mg within LZH, ICP analyses were performed, and results (Figure 22b) revealed that Zn-Mg LH NPs contained approximately 0.049% of Mg, supporting the presence of these cations within the LZH structure.

Of additional relevance, the a-axis, which is perpendicular to the sheet surface, serves as the growth direction for the nanosheets. The calculated interlayer spacing of (200) is 0.979 nm, which is consistent with the literature data of 0.975 nm for hydrated LZH [305]. Based on the size of the nitrate ion (with an ionic diameter along the molecular plane of approximately 0.4 nm), and the layer thickness LZH (0.48 nm) [185], it is plausible that the nitrate anions in Zn-Mg LH could adopt a vertical orientation, allowing the interlayer to accommodate one nitrate anion within the layer (figure 22c).

In the XRD pattern of RH-Zn-Mg LH NPs (Figure 22a), the presence of broader and less intense peaks indicates a reduction in the crystallinity of the particles. This amorphization is due to the presence of phytochemicals during the synthesis. Additionally, the XRD results demonstrate a subtle rise in basal spacing, from 9.797 Å (Zn-Mg LH) to 9.805 Å (RH-Zn-Mg LH), providing evidence that the phytochemicals from the RH extract did not intercalate into the interlayer galleries of LZH. Furthermore, the presence of phytochemicals in the RH-Zn-Mg LH apparently does not condition the incorporation of magnesium into the LZH structure since an amount of 0.023% magnesium is detected in the ICP analysis (Figure 22b).

Regarding the ATR-FTIR spectra of Zn-Mg LH NPs (Figure 22d), distinctive absorption bands were identified. The presence of a sharp band at 3572 cm^{-1} indicates the stretching vibrations of OH groups, typical of hydroxide layers. The broad absorbance peak at 3448 cm^{-1} corresponds to the OH group coordinated with the nitrate group, and the band

at 1628 cm^{-1} can be attributed to the vibration absorbance band of the interlayered water molecules. The presence of characteristic asymmetric vibration (ν_3) and the asymmetric deformation (ν_2) of the interlayered nitrate (NO_3^-) was observed at 1365 cm^{-1} and 830 cm^{-1}, respectively. The Zn−OH vibration bands at 1008, 879, 764, and 632 cm^{-1} were also observed, which are in agreement with those reported in the literature for $Zn_5(NO_3)_2(OH)_8.2H_2O$ [304,306,307]. The ATR-FTIR analysis of RH-Zn-Mg LH (Figure 22d) reveals the persistence of specific characteristic bands assigned to Zn-OH and interlayer nitrate (1008, 879, 1365 cm^{-1}) from the LZH structure. Furthermore, three new broad bands were identified within the range of 1008-1076 cm^{-1}, 1575 cm^{-1}, and 3165-3450 cm^{-1}. These peaks can be attributed to the presence of bioactive compounds found in the RH extract, such as polyphenols, flavonoids, and β-carotene [308].

Figure 22e presents high-resolution XPS spectra of the chemical states of Zn, N, C, and O for both the Zn-Mg LH and RH-Zn-Mg LH NPs. In both LZH particles, the Zn $2p_{3/2}$ core level spectrum displayed two distinctive contributions with binding energies in the case of Zn-Mg LH at 1021.3 and 1022.2 eV, and for RH-Zn-Mg LH at 1020.6 and 1022.5 eV. These distinct contributions observed in the Zn $2p_{3/2}$ core are associated with the structural characteristics of the LZH, where the Zn atoms exhibit both tetrahedral and octahedral coordination in the $Zn_5(NO_3)_2(OH)_8 \cdot 2H_2O$ structure [309]. The slight deviation observed in the Zn $2p_{3/2}$ core in both LZHs when compared to reported literature values may be partly attributed to the presence of Mg^{2+} cations taking positions originally occupied by Zn^{2+} with tetrahedral coordination.

The configuration of the N1s spectra of both NPs provides further evidence that distinct chemical species are present in each NP. In the spectra of Figure 22e, corresponding to the Zn-Mg LH NPs, two-component peaks at 403.3 and 407.2 eV, were identified. These peaks are ascribed to spin-orbit characteristics of N–oxide and NO_3^-, indicating that nitrate anions, serving as compensating charges, occupy the interlayer space within LH layers. This observation confirms the presence of nitrates within the NPs. In the case of RH-Zn-Mg LH NPs, a drastic decrease in the NO_3^- signal is noted, accompanied by an extra band linked to N1s at 401.9 eV. This band is attributed to the C-NH_2 group originating from the bioactive compounds present in RH extract [310]. Additionally, XPS analysis revealed a significant decrease in the atomic nitrogen (N) percentage in RH-Zn-Mg LH nanoparticles (3.6%) in comparison to Zn-Mg LH NPs (7.6 At %). These findings demonstrate that the bioactive compounds present in the RH extract do not act as substitutes for the nitrate anions within the hydroxide layer.

The presence of carbonate ions on Zn-Mg LH NPs can be attributed to the sterilization process of the NPs with ethylene oxide (Figure 22e). Similar results were observed for other biomaterial surfaces that underwent sterilization through the same process [311,312]. Regarding the C 1s core-level spectrum, three contributions were identified at energies of 284.7, 286.4, 288.4 and 289.3 eV, associated with C–H/C-C, C-OH/C-O-C, C=O, and CO_3^{2-}, respectively. The lower binding energy value is attributed to adventitious carbon, commonly present on the surface of particles exposed to air, while the two higher binding energy values are linked to the presence of the carbonate ion.

Regarding the RH-Zn-Mg LH NPs, the C1s core level spectrum exhibited four distinct contributions upon peak fitting (Figure 22e). The chemical state observed at 286.7 eV is attributed to the carboxylate group (COO−), which engages in covalent bonding with the Zn^{2+} tetrahedral units of the layers. The pronounced peak at 288.3 eV corresponds to the presence of C–OH/C=O bonds, confirming the existence of polyphenols on the NPs. Additionally, the band positioned at 290.3 eV is associated with the carbonate anion present within the intercalation structure. Another peak at a higher binding energy of 291.1 eV is also evident in the spectrum, and this feature is linked to a shake-up characteristic consistent with aromatic structures abundant in polyphenols. Furthermore, the increase in carbon content (Figure 22f) is related to the presence of bioactive compounds in the NPs. The O 1s binding energy values were determined to be, 531.5, 532.4 and 533.1 eV, for both NPs corresponding to, hydroxide (metal(OH)x), Zn–OH and NO_3^-/ H_2O/ adsorbed O_2, respectively. The XPS results were in good agreement with FTIR results.

Regarding the surface charge (Figure 22g), Zn-Mg LH NPs presented a high zeta potential of 37 mV in dH_2O, suggesting low agglomeration and better stability of the particulate in suspension [173]. The positively charged surface might be related to the presence of Zn^{2+} ions placed in the forming layers [309]. This finding is aligned with other studies, where LZH and layered double hydroxide materials displayed zeta potential values above 20 mV [182,313,314]. However, the presence of RH extract in the synthesis produced clear changes in the surface charge, resulting in negative values (-12 mV). In fact, this observation indicates the presence of organic anions from the RH extract over the layered structure [309], corroborated by the detection of polyphenols only in the RH-Zn-Mg LH NPs. Polyphenols, such as flavonoids and gallic acid, possess hydroxyl groups that can provide a negative charge to them, allowing ionic binding interactions with positively charged structures, including proteins and LZH [315,316]. Moreover, it is documented

that the presence of organic compounds can decrease the positive surface charge of LZHs [309,317].

TEM and SEM images for both Zn-Mg LH NPs and those produced with RH extract (RH-Zn-Mg LH NPs) are shown in Figure 22h. Zn-Mg LH NPs exhibited well-defined particles with a characteristic plate-like morphology of layered metallic hydroxide particles. Some agglomeration on the basal surface was observed in the TEM micrograph (Figure 22hi). The corresponding selected area electron diffraction (SAED) pattern (Figure 22hii) showed well-defined rings corresponding to (200) and (400) planes with bright diffraction spots that revealed highly crystalline Zn-Mg LH NPs and confirmed the presence of an LH structure. In contrast, the morphology of the RH-Zn-Mg LH NPs (Figure 22hiv) showed particles with an ultrathin 2D sheet-like morphology. The diffused halo of the SAED pattern can be seen in Figure 222hv, which corroborates the poor crystallinity of the RH-Zn-Mg LH NPs, consistent with the XRD results (Figure 22a). The TEM images of both NPs are consistent with the SEM results (Figure 22hiii and hvi), depicting agglomerated nanoparticles with a heterogeneous size distribution. Additionally, the SEM images reveal that Zn-Mg LH NPs possess denser particles (figure 22hiii) compared to the RH-Zn-Mg LH NPs (Figure 22hvi). These findings distinctly highlight the influence of the RH extract in the morphological attributes of the nanoparticles.

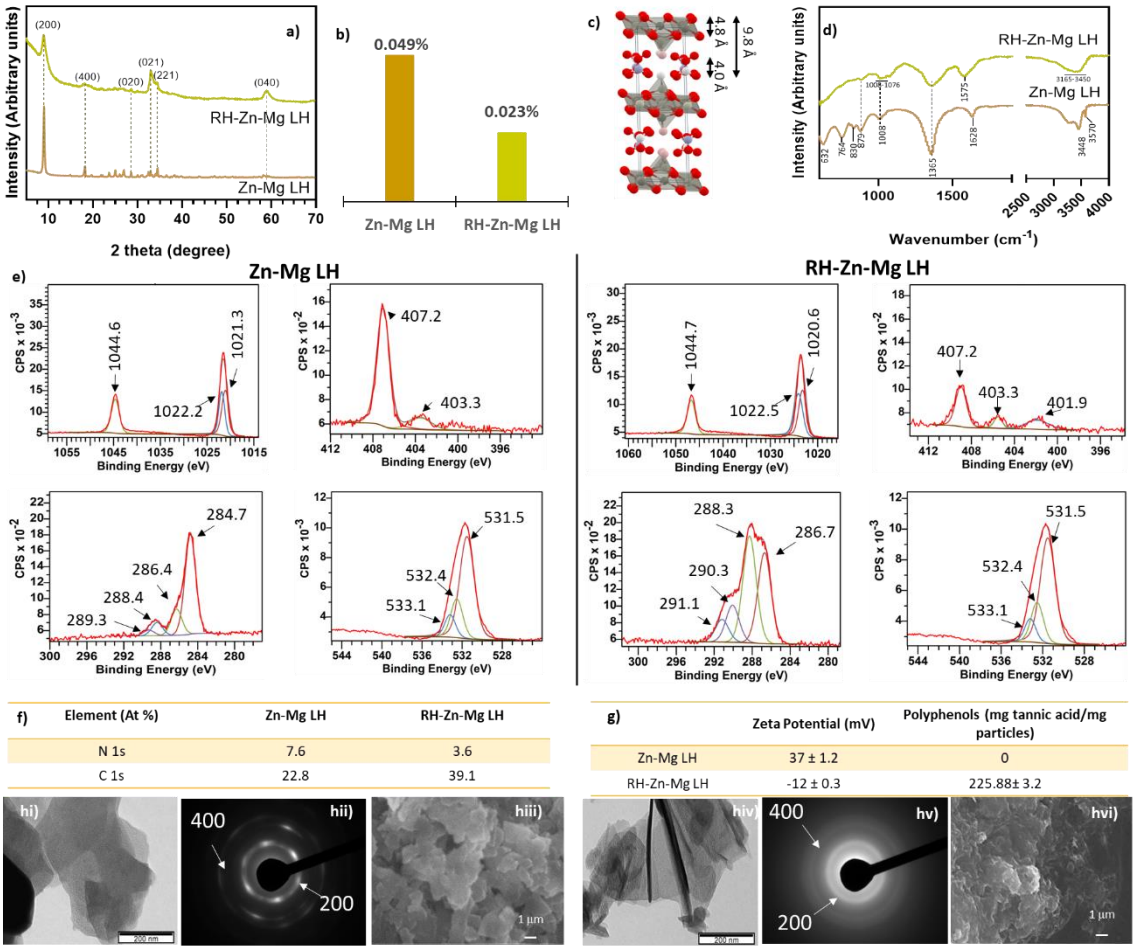

Figure 22. Physicochemical characterization of Zn-Mg LH NPs, encompassing the (a) X-ray diffraction (XRD), (b) ICP, (c) structural scheme of the LH structure, (d) FTIR/ATR, (e and f) XPS, and (g) Zeta potential analyses measured in distilled water. (hi-hiii) TEM/SEM representative images of Zn-Mg LH and (hiv-hvi) of RH-Zn-Mg LH NPs.

5.3.2. Cytocompatibility assessment of Zn-Mg LH and RH-Zn-Mg LH NPs using HFs

To assess the cytocompatibility of the synthesized NPs, as well as their antioxidant effects, human fibroblasts (HFs) were chosen as the cellular model. Control cultures presented a continuous increase in metabolic activity throughout the assay (data not shown). Both NPs presented a similar growth pattern at lower concentrations (i.e., 1.0 and 10 µg/mL), while clear cytotoxicity was observed at 50 µg/mL, in all timepoints (Figure 23a). Regarding cell morphology analysis, no significant differences were noted when compared to control cultures, confirming their cytocompatibility. HFs presented an elongated and stretched shape, prominent stress fibers, rounded and well-defined nuclei, and slender cytoplasmic extensions at day 1 (Figure 23b upper panel). At day 7, the number of cells increased significantly, and cell-to-cell contacts were unceasing, which

can be associated with the increased metabolic activity between time points (Figure 23b lower panel).

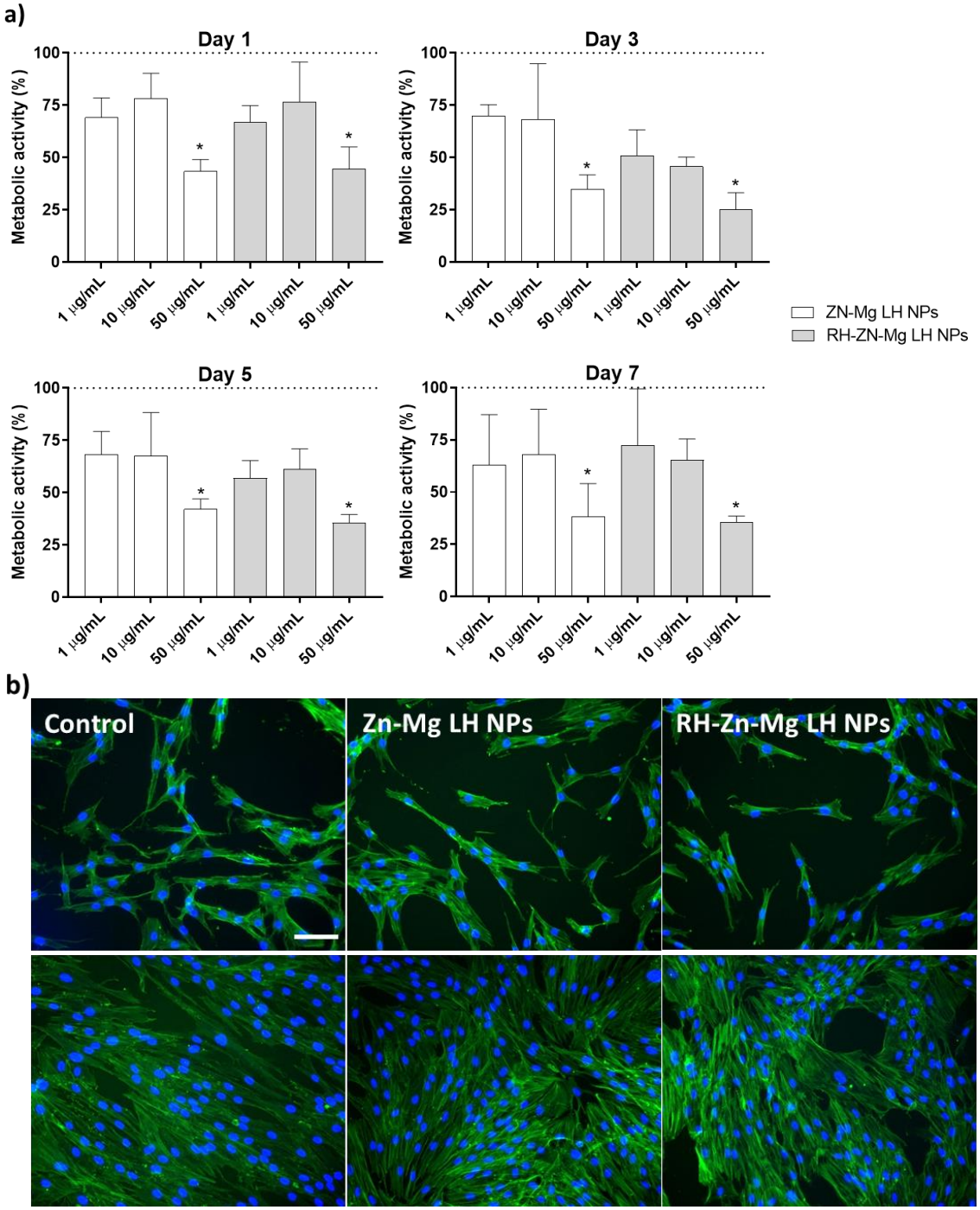

Figure 23. (a): Metabolic activity of HFs incubated with Zn-Mg LH NPs normalized by the control, represented as 100% in the graphs. (b): Representative images of the cellular morphology of HFs grown in the absence (control) or the presence of 10 µg/mL of NPs, at day 1 (upper panel) and day 7 (lower panel). Cells were stained for F-actin cytoskeleton in green and counterstained for nuclei in blue. Scale bar: 100 µm. (*) Statistically significant from control, set as 100%. $p \leq 0.05$.

Since Zn-Mg LH and RH-Zn-Mg LH NPs presented similar cytocompatible results, their surface charge was further investigated using an isotonic saline solution (Hepes buffer), at different pH values (Figure 24). Despite the observed positive zeta potential values when suspended in dH_2O (Figure 22g), Zn-Mg LH NPs have their surface charge varying from positive in acidic conditions to negative at neutral and basic pH values. This behavior was previously documented for LH systems [318], and can be due to their high positive charge, which induces the adsorption of anions from the salt solution available at high pH values, reducing their zeta potential [319]. On the other hand, the surface charge of RH-Zn-Mg LH NPs was found to be constantly negative and relatively stable regardless of the pH values or media, indicating that the polyphenols incorporated over the NPs stabilized their surface charge. This can be a major advantage to the RH-Zn-Mg LH NPs' applications, reducing their aggregation in environments with varying pH conditions [319].

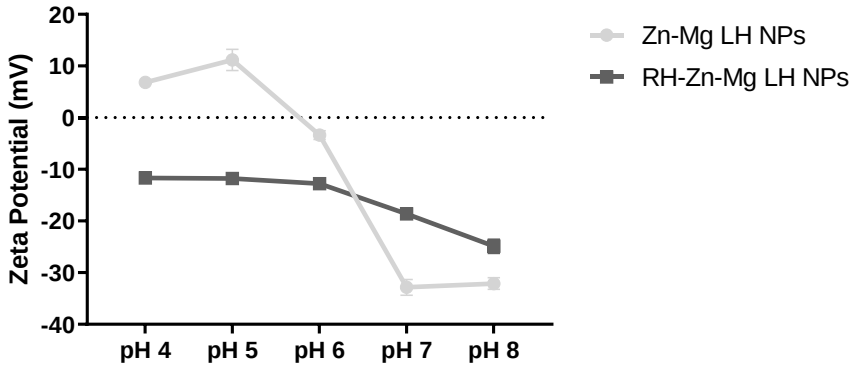

Figure 24. NPs' zeta potential measurement in an isotonic saline solution (Hepes buffer) at different pH values.

The internalization of the NPs was observed using TEM, at early and late stages of incubation (Figure 25). At a short incubation period, HF control cultures displayed smooth and short membrane protrusions, and no expressive vacuole formation within the cytosol could be observed. However, evident differences were noted when compared with experimental groups. Both Zn-Mg LH and RH-Zn-Mg LH NPs induced perturbations in the cell membrane, resulting in the formation of long and numerous protrusions and the development of multiple vacuoles at the marginal region of the cytosol.

In the late stage, the control group presented physiologic aspects, that is, an expected number of vacuoles, mitochondria, and no obvious alterations in the cell membrane. Oppositely, both Zn-Mg LH and RH-Zn-Mg LH NPs induced the formation of additional vacuoles dispersed throughout the cytosol, including membrane-bound organelles as

endosomes, amphisomes, and lysosomes located close to the nucleus. Additionally, the number and the size of mitochondria seemed to be altered, along with changes in the cell membrane, as observed in the earlier stage. Therefore, TEM images suggest that LH NPs could be internalized.

Despite established differences in physicochemical characteristics, such as crystallinity degree and chemical composition between Zn-Mg LH and RH-Zn-Mg LH NPs (Figure 22), a similar level of cytocompatibility was observed (Figure 23). This could be due to their analogous overall size and surface charge in isotonic and neutral media (Figure 24). Moreover, both NP types seemed to be equally internalized by HF cells (Figure 25), causing notable alterations in the cell membrane and cytosolic composition and organization. Correlating their fairly large size with the observed membrane protrusions, macropinocytosis is likely to be the main cellular uptake mechanism [173].

It is noteworthy that the relation between the physicochemical characteristics of inorganic NPs and their role in the biological response is still to be fully understood. Factors such as the crystallinity degree, surface charge, and shape of NPs can influence their biocompatibility. For instance, a higher crystallinity degree [320], positively charged NPs [321] and sharp-shaped particles (e.g., pyramidal, flower shapes) have been associated with lower concentrations of NPs required to reach the IC50 value of mammalian cells [320,322]. Nevertheless, the cytotoxicity of LZH systems is likely to be related to augmented intracellular concentrations of Zn^{2+} [323], which can be induced by the combination of multiple physicochemical characteristics of the particles [322].

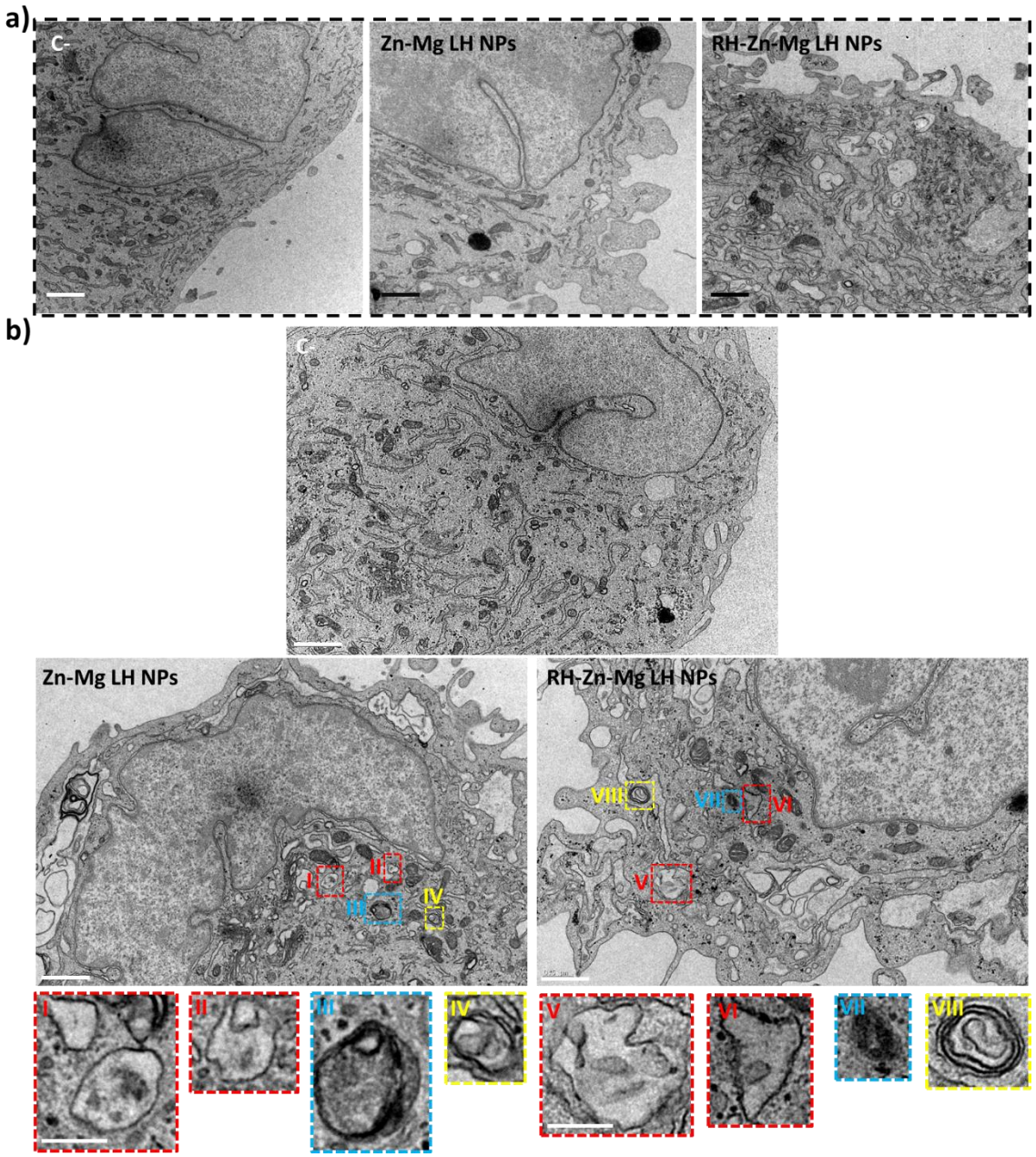

Figure 25. Representative TEM images of HF cultures incubated with Zn-Mg LH and RH-Zn-Mg LH NPs. (a) Early-stage incubation (3h), with the scale bar set at 1 µm. (b) Late-stage incubation (24h). Red squares: endosomes; Blue squares: lysosomes; Yellow squares: amphisomes. Dashed images correspond to magnified areas. Scale bar of frameless images was set at 1 µm, while the scale bar of framed images was set at 250 nm.

The generation of reactive oxygen species (ROS) by cells cultured with metallic-based NPs is another relevant factor for their biocompatibility. As displayed in Figure 26a, neither NPs' formulations induce ROS in HFs cultures, even at the high concentration of 50 µg/mL – concentration that clearly produced cytotoxic effects, suggesting that the observed cytotoxicity was not induced by ROS generation. It is important to note that zinc typically does not participate directly in radical reactions [323]. Indeed, various studies tend to state that ROS generation is more likely a consequence rather than a

primary cause of the cytotoxicity. Accordingly, free radical scavengers (methimazole), antioxidants (ascorbic acid), and catalase broadly failed to inhibit the toxic effects of Zn^{2+} in cells [323,324]. This points towards to other possible mechanisms. Supra physiological concentrations of Zn^{2+} can displace iron ions intracellularly, blocking electron transport systems, besides destabilizing lysosomes, and affecting the activity of Zn^{2+}-dependent proteins [322–324]. Therefore, these disturbances caused by Zn^{2+} can lead to mitochondrial dysfunction, ultimately resulting in oxidative stress injuries, as documented by other studies [324,325]. On the contrary, at physiological concentrations, zinc can act as an antioxidant agent by inhibiting NADPH oxidase, inducing the generation of scavenger proteins (as metallothionein), and increasing the activation of antioxidant enzymes, as glutathione and catalase [180]. Indeed, both Zn-Mg LH and RH-Zn-Mg LH NPs significantly reduced the effects of H_2O_2 in HFs, maintaining ROS levels comparable to those in untreated cells (Figure 26b). However, only RH-Zn-Mg LH NPs presented the ability to scavenge peroxides from the medium (Figure 26c), indicating that this NP type exhibits a superior antioxidant activity in comparison to Zn-Mg LH NPs, likely due to the presence of polyphenols in the formulation (Figure 22g).

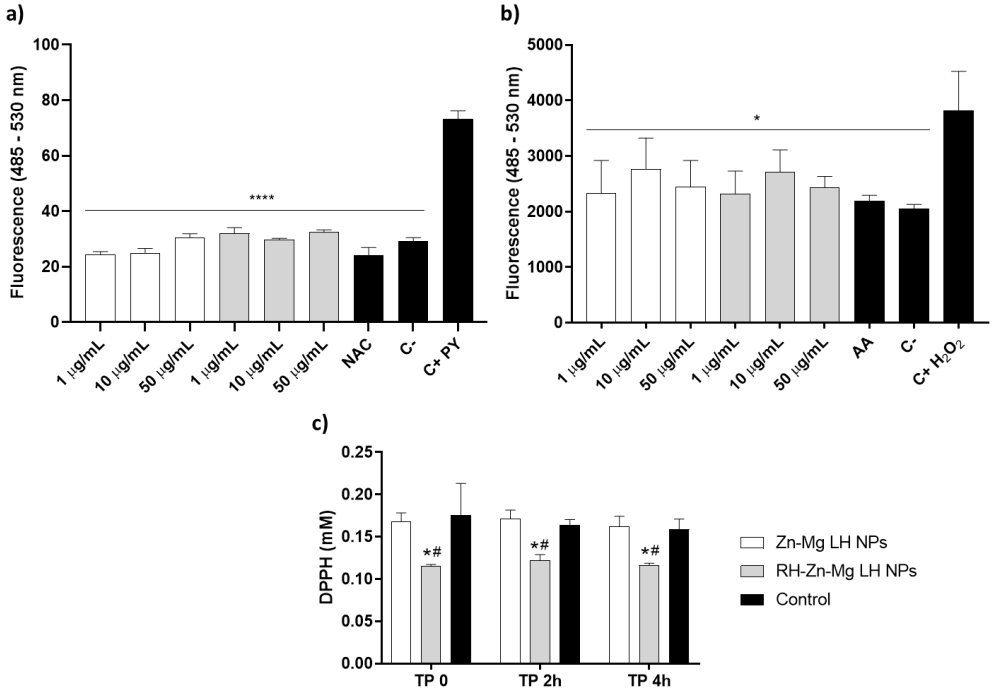

Figure 26. Reactive oxygen species (ROS) assays, using ZN-Mg LH and RH-Zn-Mg LH NPs at different concentrations. (a) Measurement of ROS generated by NPs and (b) Antioxidant activity of NPs in HF cultures. (c) ROS scavenging activity of NPs in the presence of peroxides. # significant different from other experimental samples. * Significantly different from control. * Significantly different from positive control. # Significantly different from Zn-Mg LH NPs. $p < 0.005$. **** Significantly different from positive control, $p < 0.0001$. AA corresponds to ascorbic acid; NAC corresponds to N-Acetylcysteine.

Lastly, the potential modulatory activity of Zn-Mg LH and RH-Zn-Mg LH NPs on inflammation was evaluated within an *in vitro* 3D translational model mimicking an inflamed mucosa. It is worth noting that zinc-based NPs can elicit both pro- and anti-inflammatory responses, a phenomenon likely influenced by their physicochemical properties and the specific cell type involved [180]. Since the proinflammatory induction is mostly observed in immune cell cultures (e.g., macrophages, dendritic cells) [326], both NPs were incubated with macrophages and neutrophils (supplementary figure S1 and S2) to address potential inflammatory activation. As observed, neither of the LH NP formulations induced a significant increase in IL-6 and TNF-α production, in comparison to the positive control. This reaffirms the absence of any proinflammatory activity associated with either NPs.

The anti-inflammatory potential of Zn-Mg LH and RH-Zn-Mg LH NPs was evaluated using an LPS-stimulated mucosal organotypic model. As observed in the histological section (Figure 27a), the 3D mucosal model consisted of a stratified epithelial layer of differentiated keratinocytes on a fibroblast-populated collagen matrix, resembling the native mucosa. Comparing to a monolayer system, this model possesses an increased organizational complexity, higher degree of cellular differentiation and advanced cell to cell contacts, rendering a more realistic response to external stimuli, such as LPS [297].

Exposure to LPS led to a noticeable upregulation of relevant inflammatory genes (Figure 27b). While both NP formulations induced a significant downregulation in the expression of IL-6, CXCL-8 and NFkB1 genes, RH-Zn-Mg LH NPs displayed a superior efficacy in downregulating all the assessed genes, achieving values comparable to those of untreated cells.

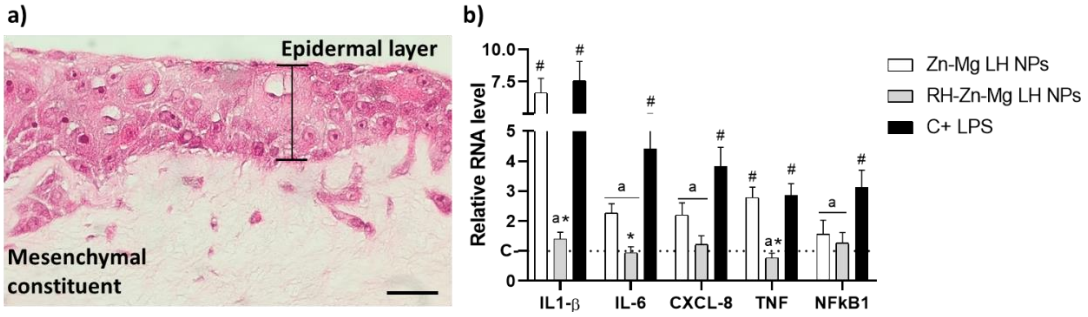

Figure 27. (a): Representative histological section of the organotypic mucosal model stained with H&E. (b): Anti-inflammatory activity of LH NPs assessed by QPCR analysis. The organotypic model was incubated with 1.0 µg/mL of LPS prior incubation with 10 µg/mL of NPs. Values were normalized by the housekeeping gene (GAPDH), set as 1.0. * Significant different from Zn-Mg LH NPs. # Significant different from negative control. (a) Significant different from C+. $p < 0.005$.

In the context of inflammatory disorders, LZH systems offer a significant advantage owing to their pH sensitivity. Inflamed tissues are known by their extracellular acidosis [327], which is reported to accelerate the dissolution of LZH, fast-forwarding the cationic release, as well as the delivery of conjugated drugs and other therapeutic molecules [171]. Additionally, the absence of aluminum in the formulation of Zn-Mg LH NPs – commonly employed in the synthesis of layered double hydroxide systems - is another benefit. Aluminum has been linked to cardiovascular and bone disorders, and possesses pro-inflammatory characteristics [328,329]. Furthermore, magnesium itself exhibits anti-inflammatory properties [295]. Despite the relatively low amounts detected in the ICP analysis (Figure 22b), magnesium may have enhanced the biological effects and facilitated the transmembrane transportation of zinc, as previously observed [330].

The anti-inflammatory effects of Zn-based NPs are acknowledged to be related to the inhibition of the expression of NFkB, TSLP and caspase-1, as well as the reduction in the number of leucocytes [180,331]. In fact, NFkB is one of the main inflammatory pathways, exerting control over the expression of IL-1β, IL-6, TNF, and CXCL-8, matrix metalloproteinases and other factors, as COX-2 [110]. Zinc modulates NFkB activation by two main pathways - blocking IkB kinase complex, which is responsible of NFkB translocation from the cytoplasm to the nucleus, targeting gene expression; and by inducing the production of zinc-dependent A20 protein, a negative modulator of the duration and activation of NFkB [332]. RH extract contains compounds can also inhibit NFkB signaling pathway, resulting in a reduced production of TNF-α, IL-1β and IL-6 [289,290,333]. Accordingly, the enhanced anti-inflammatory activity observed in RH-Zn-Mg LH NPs indicates that the detected polyphenols (Figure 22g) were functional and able to interact with cells. Besides, this improved anti-inflammatory effect signifies a conjoined action between RH's polyphenols and Zn^{2+}, which can represent an innovative approach to tackle local inflammation.

5.4. Conclusion

The present study demonstrated a feasible synthesis of an LZH-based nanomedicine designed to target local inflammatory disorders. Both Zn-Mg LH and RH-Zn-Mg LH NPs were found to be cytocompatible at 10 µg/mL and presented strong antioxidant activity when tested in human fibroblastic cultures. Moreover, these NPs demonstrated potent anti-inflammatory effects in an advanced organotypic model of an inflamed mucosa.

Notably, the addition of the RH extract during the synthesis significantly enhanced the antioxidant and anti-inflammatory effects of the NPs. All in all, these findings underscore the considerable potential of RH-Zn-Mg LH NPs as a promising alternative therapy for conditions driven by inflammation. Future investigations in advanced settings, including *in vivo* models, are warranted to further evaluate the therapeutic efficacy and translational potential of these nanoparticles.

CHAPTER 6

An Advanced Perioceutic: Layered Zinc Hydroxide Nanoparticles Loaded with Doxycycline for Targeted in Situ Release

6.1. Introduction

As described in previous chapters, periodontitis is characterized by the destruction of the tooth-supporting tissues, in a process triggered by the formation of a dysbiotic bacterial biofilm over the subgingival tooth surfaces [16,334]. The presence of pathogenic bacteria, as *Porphyromonas gingivalis* and their products (e.g., gingipains), elicit a host response. This response involves the recruitment and infiltration of leukocytes, resulting in an intensified and persistent infectious-inflammatory scenario, responsible for the detachment of junctional epithelium and, ultimately, for bone resorption [6,334].

The primary treatment of periodontitis lies on the mechanical removal of supra and subgingival calculus and plaque, aiming the reduction of bacterial load, and consequently, the resolution of the inflammatory state, reestablishing the homeostasis of the periodontium [335,336]. However, supportive treatments are frequently necessary, being the systemic antibiotic administration and the local use of antiseptic agents, the most employed ones [23,335]. These conventional methods present adverse effects and contested efficacy [23,337]. In fact, only a fraction of antibiotics administered via oral route reaches the periodontal pocket, and local antiseptic strategies (e.g., mouthwashes and toothpastes) are effective only at a supragingival level, presenting marginal effects within periodontal pockets [337,338].

To overcome these well-known limitations, the concept of in-situ drug delivery rises as a promising alternative, reducing the systemic adverse effects while providing high local concentrations of an active drug [338,339]. Given the infectious origin of PDs, antibacterial drugs as CHX, tetracyclines (TCs) and metronidazole, are often chosen for incorporation into local drug delivery systems (LDDS) for periodontitis treatment [340]. In fact, a myriad of products has been proposed, with only a few reaching commercialization, as Arestin® (TCs microparticles), Actisite® (TCs fibers), Elyzol® (metronidazole gel) and Periochip® (CHX chip) [340].

Nevertheless, despite presenting improved outcomes in relation to conventional therapy, the insertion of fibers, films, and chips can be related with challenges as a difficult insertion, mechanical irritation, and dislodging from the periodontal pocket [338]. Gels and microparticles are frequently associated with fast clearance and burst releases, raising concerns about tissue cytotoxicity and irritation [338]. Moreover, these systems, as well as most free antibacterial drugs, are generally ineffective against intracellular bacteria [21,29,30,122]. This limitation can be considered a major flaw in the overall periodontitis

therapeutic approach, since *P. gingivalis* (a key pathogen) has been shown to be internalized by gingival cells through its major fimbriae [341]. The bacteria bind to host cells' integrins, resulting in rearrangements in the cellular cytoskeleton, which promote bacterial invasion [342]. Internalized bacteria are protected from surveilling leukocytes, being able to multiplicate and disseminate to surrounding tissues, leading to a persistent infection and further tissue destruction [21].

Thus, an effective LDDS must be able to be internalized by periodontal cells to reach and act against intracellular bacterial reservoir, resolving periodontitis bacterial component, definitively. Among various LDDS, nanoparticles (NPs) are a promising option for perioceutics, which can be internalized by non-phagocytic cells [108], besides presenting enhanced mucoadhesive properties, retarding their clearance from the periodontal pocket [106]. Furthermore, an ideal drug carrier should be bioactive, providing a synergetic activity to the delivered drug, targeting an improved therapeutic outcome.

In this context, layered hydroxide (LH) NPs can meet all the requirements to serve as an efficient LDDS for periodontitis. These inorganic NPs consist of cationic layers interconnected by electrostatic interactions, possessing anionic biomolecules in-between [172,173]. Interestingly, the intermediate anionic constitution can be partially substituted with drugs, and the distance between the cationic layers can be modified along the basal axis without changing the LH structure, conferring a high drug loading capacity [170,171]. Despite these advantages, LH NPs are still unexplored for the treatment of periodontitis [343,344], clinical application that can be aided by NPs with selective degradation and high drug loading capacity [164,168,169].

Accordingly, this study describes the development and the *in vitro* physicochemical and biological characterization of an innovative perioceutic, set on zinc-magnesium layered hydroxide (Zn-Mg LH) NPs. This LDDS was loaded with doxycycline (DX), a tetracycline-antibiotic, highly effective against *P. gingivalis* and other relevant pathogens [345], which also possesses pleiotropic effects that can be useful for the PD's resolution [32,41]. Compared with other tetracyclines, DX presents improved solubility, retained activity against gram-negative bacteria and increased biosafety profile [346]. Moreover, zinc and magnesium were chosen due to their antioxidant, anti-inflammatory and bactericidal activities [180,347–349], aiming synergetic effects between them and DX for an improved therapeutic outcome.

6.2. Methods

6.2.1. Zn-Mg LH and DX-Zn-Mg LH NPs' production

The synthesis of Zn-Mg LH and DX-Zn-Mg LH NPs was set on a co-precipitation method. Briefly, magnesium nitrate ($Mg(NO_3)_2 \cdot 6H_2O$) and zinc nitrate ($Zn(NO_3)_2.6H_2O$) (all from Sigma) were added to deionized water and the corresponding solutions were obtained. Then, nitrate solutions were mixed at 1:10 ratio (0.1 M of Mg to 1 M of Zn) under magnetic stirring, at room temperature. The pH value of the solution was approx. 2.0. NPs were precipitated after the addition of 25% aqueous ammonia (Merck) that raised the pH value to approx. 6.0. The precipitate was washed with deionized water and collected, using a 0.22 um filter (Sarstedt) under vacuum. NPs were dried in a vacuum chamber at room temperature and were sterilized using ethylene oxide. For the obtention of DX-Zn-Mg LH NPs, doxycycline hydrochloride (DX, Sigma) was added to the Mg solution prior to the mixture of nitrate solutions, at a ratio of 1:320 (1 mg of DX to 320 mg of nitrates), under magnetic stirring.

6.2.2. NPs' physicochemical characterization

The morphology and size of NPs were visualized by transmission electron microscopy (TEM) using a Hitachi H-9000-NA microscope, after the dispersion of NPs in ethanol over a carbon-coated copper grid. The chemical characterization of Zn-Mg LH NPs was evaluated by Fourier transformed infrared spectroscopy (FTIR) using a Nicolet (Thermo Electron) spectrometer with an attenuated total reflectance (ATR) apparatus. The crystallinity of Zn-Mg LH NPs was assessed by X-ray diffraction (XRD) using a D8 Advance Bruker AXS (Bruker). NPs suspended in distilled water and HEPES buffer had their zeta potential values measured by light scattering using Zetasizer Nanoseries Nano-Z instruments (Malvern). The chemical composition of Zn-Mg LH and DX-Zn-Mg LH NPs was analyzed by X-ray photoelectron spectroscopy (XPS), using an Axis Ultra HAS equipment (Kratos) equipped with an Al Monochromator and the pass energy of scans was 90 W. Due to the non-conductive nature of the NPs, the charge core of the carbon peak (C1s) was adjusted to 284.8 eV. Data was analyzed using CasaXPS 2.3.24PR1.0. The quantification of Zn^{2+} and Mg^{2+} was performed by inductively coupled plasma spectroscopy (ICP) (ISA Jobin Yvon– JY70 Plus) after the dissolution of the NPs.

6.2.3. Assessment of the drug loading capacity and drug release

The drug loading capacity of DX-Zn-Mg LH NPs was assessed by dissolving 10 mg of nanoparticles in 1 mL of 0.1 N HCl solution. After the total dissolution of NPs, the absorbance of DX was quantified by spectrophotometry using a microplate reader (Synergy HT; BioTek), at 345 nm. Calibration curves (r=0.999) were obtained by DX-HCl microdilutions and were plot over a concentration range of 0.49–125 μg/mL. The drug loading capacity was determined using the following equation:

$$DL\ (\%) = \left(\frac{W_{DX}}{W_{NPs}}\right) x\ 100$$

W_{DX} is the amount (mg) of DX obtained in NPs' dissolution and W_{NPs} is the weight (mg) of dissolved NPs.

Finally, to measure the DX release from the DX-Zn-Mg LH NPs, 30 mg were added to a 15 mL Falcon tube containing 3 mL of Hepes buffer (10 mM, at pH 7.4). Tubes were incubated under constant shacking at 37 °C and, at predetermined intervals (between 1 and 312h), aliquots of the supernatant were collected for analysis and the withdrawn volume was replaced with fresh Hepes buffer. Five independent experiments were performed.

6.2.4. Evaluation of NPs' antibacterial activity

6.2.4.1.Gram-positive bacterium

Aliquots from overnight cultures of methicillin susceptible *Staphylococcus aureus* (ATCC 25923) obtained from American Type Culture Collection (ATCC) were used in the following assays.

The antibacterial susceptibility of NPs was evaluated through the Kirby-Bauer assay, performed according to Clinical and Laboratory Standards Institute (CLSI) standards [350]. Inoculum of *S. aureus* was re-suspended and further diluted in Brain-Heart Infusion media (BHI, Liofilchem) aiming to reach a 1×10^8 CFU mL^{-1} concentration at 600 nm, using a spectrophotometer (Jenway 6300). Then, the inoculum was swabbed across plates containing Mueller–Hinton Agar (MHA, Liofilchem). Finally, 5 mm filter disks containing 10 μL of NPs' solution at 10 mg/mL were placed on the agar's surface, as well as the positive control (10 μL of DX solution at 3 mg/mL), and the negative control (10 μL of distilled water). Plates were incubated (Heraeus Instruments) at 37° C for 18 h

and the inhibition zone diameter was measured using a vernier caliper. Assays were performed in five independent experiments.

The antibacterial activity of NPs was evaluated by the broth microdilution method (MIC) following the CLSI guidelines [350]. NPs' solutions at 200 µg/mL and DX solution at 8 µg/mL were diluted in Mueller–Hinton broth (MHB, Liofilchem) to produce a range of concentrations from 0.2 to 100 µg/mL and 0.008 to 4 µg/mL, respectively. Further, inoculum at 0.5×10^6 CFU mL^{-1} was placed in 96-well cell culture plates, which were incubated under static conditions at 37 °C, for 24 h. Inoculum cultured without antibiotic and sterile MHB were used as positive and negative controls. MIC was defined as the lowest antibiotic/NPs' concentration able to prevent visible bacterial growth, that is, absence of any turbidity. Five independent experiments were performed.

6.2.4.2.Gram-negative bacterium

Porphyromonas gingivalis (ATCC 33277) was incubated in anaerobic conditions until reaching exponential growth phase. Then, 20 µL of bacteria inoculum was transferred to a 96-well micro plate, at a final concentration of 10^6 CFUs mL^{-1}. After, DX-Zn-Mg LH and Zn-Mg LH NPs solutions, at final concentration of 10 µg/mL, were added, using PBS as control. Aliquots of each sample were properly diluted and seeded on blood agar medium plates (Blood Agar Oxoid No 2), supplemented with 5% (v/v) sterile horse blood (Oxoid), 5.0 mg/L hemin (Sigma) and 1.0 mg/L menadione (Merck). CFUs were counted from the agar plates after 24 h of incubation at 37 ºC in anaerobic conditions [351]. Results were expressed as the log of CFU counting or the percentage of control (NPs-free medium). Three independent experiments were performed.

6.2.5. In vitro biological assessment with human gingival fibroblasts

The cytocompatibility of DX-Zn-Mg LH and Zn-Mg LH NPs was assessed *in vitro* using human gingival fibroblasts (HGFs, ATCC® PCS-201-018™) from the 9th passage. NPs' solutions at 1.0, 10, 50 and 100 µg/mL were used. HGFs cultures were expanded in α-MEM containing 10% (v/v) fetal bovine serum (FBS), 100 $IU.mL^{-1}$ penicillin, 100 $\mu g.mL^{-1}$ streptomycin and 2.5 $\mu g.mL^{-1}$ amphotericin B (all Gibco). Incubation conditions were set as 37° C and 5% CO_2 in air. After reaching approx. 70% confluency, cells were detached and sub-cultured at 10^4 $cells.cm^{-2}$ for the following assays. The culture medium was replaced by media containing NPs at described concentrations after 24h. Negative control (C-) was set as HGF cultures grown without NPs.

To assemble the three-dimensional organotypic model of oral mucosa, HGFs were cultured and expanded in D-MEM with high glucose content (Sigma) supplemented with 10% FBS, 100 $IU.mL^{-1}$ penicillin, 100 $\mu g.mL^{-1}$ streptomycin and 2.5 $\mu g.mL^{-1}$ amphotericin B. Human oral epithelial cells (TR146 cell line, from Sigma) from the 30^{th} passage were cultured and expanded using the same D-MEM medium.

6.2.5.1.Assessment of the metabolic activity

The metabolic activity of HGFs incubated with DX-Zn-Mg LH and Zn-Mg LH NPs was assessed using the MTT assay. At 1, 5 and 7 days of culture, 10 % (v/v) of tetrazolium dye solution (MTT, Sigma) at 5 mg/mL was added to cell cultures that were further incubated for 3 h, at 37° C. Then, the supernatant was removed and 100 µL of dimethyl sulfoxide (DMSO) was added to each well to solubilize the formazan crystals. A microplate reader (Synergy HT; BioTek) was used to read the absorbance of the final solution at 550 nm with. Assays were conducted in quintuplicates.

6.2.5.2.Assessment of the cell morphology

The morphology of HGFs incubated with NPs at 10 µg/mL was observed by fluorescent microscopy. At day 1 and day 7, cells were fixed using formaldehyde 3.7%. The permeabilization of the HGF cultures was attained using Triton-X. Then, Alexa-Fluor 488-phalloidin (Molecular Probes) was employed to stain the F-actin and Hoechst 33342 (Enzo), to counterstain the nucleus. Fluorescent images were obtained using a Celena S digital imaging system (Logos Biosystems) and treated with ImageJ software v.1.53k. The assay was performed in triplicate.

6.2.5.3.Total reactive oxygen species (ROS) - Oxidative stress evaluation

The induction of ROS generation in HGFs by DX-Zn-Mg LH and Zn-Mg LH NPs was assessed using a Total ROS/Superoxide detection kit (ROS-ID® ENZ-51010, Enzo Life Sciences). Cells were seeded in 96-well plates as previous described. When cell cultures' confluence was reached, cultures were washed using ROS buffer. Additionally, besides untreated cells, a negative control group was set by the incubation of N-acetyl-L-cysteine (5 mM) for 30 min, at 37 °C. Then, experimental groups were incubated with NPs at 1.0, 10 and 50 µg/mL. 200 µM of the ROS inducer (pyocyanin) was added to the positive control. After, the fluorescent dye from the Total ROS detection kit (2 µM) was added to

HGF cultures, followed by incubation at 37 °C for 1 h. Fluorescence was measured at 488/520 nm (Excitation/Emission) using a microplate reader.

Further, the assessment of the antioxidant capabilities of the DX-Zn-Mg LH and Zn-Mg LH NPs was performed using the 2′,7′ – dichlorofluorescin diacetate (DCFDA, Life Technologies). HGF cultures were seeded and incubated in the same conditions as described before. 20 μM of DCFDA was added in each well prior 30 min of incubation. Subsequently, culture medium was removed and media containing NPs at 1.0, 10 and 50 μg/mL, were added. Negative control was set as HGFs incubated with 1 mg/mL of ascorbic acid, while the positive control was set as cells incubated with pure culture medium. HGF cultures were incubated for 1 h at 37 °C. Finally, cells were exposed to hydrogen peroxide (H_2O_2) at 500 mM/well and the fluorescence was read at 485/520 nm (EX/EM) using the same microplate reader, after 15 min of incubation at 37 °C. Five independent experiments were performed.

6.2.5.4.Cellular uptake of LH NPs and intracellular trafficking

Uptake of NPs by HGFs was evaluated using TEM images. Briefly, HGF cultures were incubated with 10 μg/mL of DX-Zn-Mg LH or Zn-Mg LH NPs. At selected timepoints, cells were washed with PBS and trypsinized prior to centrifugation at 300 g, 10 min and 4 °C. Then, supernatant was removed, and the cell pellet was re-suspended using a fixation solution (2.5% glutaraldehyde + 2% formaldehyde). Cells were stored at 4 °C and carried on to processing. Cells cultured without NPs and NPs processed without cell incubation were used as controls (data not shown). Three independent experiments were performed.

6.2.6. Evaluation of the anti-inflammatory activity of NPs using an organotypic oral mucosa model

6.2.6.1.Assemble of a three-dimensional organotypic model of oral mucosa

To assess the anti-inflammatory activity of NPs in a framework that mimics the *in vivo* environment, a three-dimensional model of oral mucosa containing epidermal and mesenchymal components was assemble as described elsewhere [297], with modifications.

Firstly, an acellular layer of collagen type I from rat tail tendon (Roche) was prepared and added in the bottom of a 24-well plate insert (Thincert transparent membrane, 0.4 μm

pore size, from Greiner). Then, HGFs were trypsinized, added into a new collagen solution and placed over the acellular layer, to form the cellular collagenous content. After collagen's curing, culture medium was added to the bottom of the well and into the insert. After 7 days, TR146 cells were trypsinized and added on the surface of the collagen gel containing the HGFs, and the culture medium of the insert (supplemented D-MEM) was changed to Keratinocyte Media 2 (PromoCell), while the bottom of the well continued to receive D-MEM. When the layer of TR146 cells was found to be confluent (5 to 7 days), the culture medium of the insert was removed, resulting in an air-liquid interface, to further differentiate the epithelial layer of the model. Culture medium of the well was changed every other day. Finally, after 7 days, the established organotypic model was stimulated with 1 μg/mL of *P. gingivalis*' lipopolysaccharide (LPS, from Sigma) for 16 h, to induce an inflammatory phenotype, and subsequently incubated with NPs at 10 μg/mL for further 24 h. Sections of fixed gels were stained with hematoxylin and eosin (H&E) to validate the structure of the mucosal model.

6.2.6.2.RNA isolation and Quantitative PCR

The total RNA was isolated from the mucosal model using Trizol reagent (Ambion, Life technologies) following the manufacturer's protocol. The isolated RNA was evaluated by absorbance reading (A260/A280) to measure its quality and concentration, using the Take3 module (Gen5, BioTek) and a microplate reader (Synergy HT; BioTek). Samples presenting quality below 1.9 and above were discarded. The conversion of RNA to cDNA was performed using a reverse transcription system (NZY first-strand cDNA synthesis), where the concentration of the RNA was normalized to 400 ng/μL. The conversion program was set to 10 min at 25°C, 30 min at 50°C and 5 min at 85°C. Then, RNAse (NZY) was added prior 20 min of incubation at 37 °C.

Quantitative PCR (qPCR) was accomplished using the CFX384 real-time PCR system (Bio-Rad). Samples were prepared by adding cDNA, iTaq Universal SYBR green Supermix PCR Kit, DEPC water and the pre-defined primers (table 5). The reaction was carried out using the manufacture's protocol (2 min at 95 °C; 40 cycles of 5 sec at 95 °C and 30 sec at 60 °C; melt curve, 65 – 95 °C). Negative control of each primer was set as samples without cDNA. The evaluation of the obtained data was done using Bio-Rad CFX Maestro 1.1, v.4.1.24 software. Parameters as amplification (90 – 110) and standard curve (>0.98) were requirements to the inclusion of each sample in the final analysis. The relative expression of each gene was obtained by their normalization to a housekeeping

gene (i.e., GAPDH) and further application of the $2^{-\Delta\Delta Ct}$ method. Five independent experiments were performed.

6.2.7. Statistical analysis

Data are expressed as mean values ± standard deviation (SD). Statistical analysis was performed using the IBM® SPSS® Statistics software v.27. Data normality was assessed by the Shapiro–Wilk test. For normal datasets, one-way analysis of variance (ANOVA) was performed, followed by the post hoc Tukey test. The Kruskal–Wallis test was performed for non-parametric datasets, followed by multiple comparisons using Dunn's tests. p-values ≤ 0.05 were considered significant.

6.3. Results

6.3.1. NPs' physicochemical characterization

The synthesis of Zn-Mg LH NPs and DX-loaded NPs (DX-Zn-Mg LH NPs) was attained through a one single step and environment-friendly method. Microscopic observation (Figure 28-A) revealed some differences between NPs' formulations – Zn-Mg LH NPs were found to be clustered, with a plate-like shape, and larger size; while DX-Zn-Mg LH NPs seemed more dispersed, with a similar shape, and slightly smaller size. Both particles presented some translucency in TEM analyses, indicating a nano-scaled thickness.

Noticeable differences between NPs can also be observed in their crystalline structure (Figure 28-B). Zn-Mg LH NPs displayed several peaks throughout the spectra, while DX NPs showed only three well-defined peaks, suggesting a reduction in the crystallinity degree due to the presence of DX in the precipitation medium. Zn-Mg LH NPs have multiple and intense reflection 2-theta (θ) peaks, including peaks at 9, 18, 34 and 59 º, indicating that zinc hydroxynitrate $Zn_5(NO_3)_2(OH)_8.2H_2O$ is the detected crystalline phase, organized in monoclinic layers [298,299]. Despite the decrease in the crystallinity degree, DX-Zn-Mg LH NPs retained these four reflection peaks, confirming the production of layered zinc hydroxide particulate.

The FTIR/ATR spectroscopy (Figure 28-C) of Zn-Mg LH NPs qualitatively confirmed the presence of hydroxyl groups in the hydroxide layers, characterized by a sharp band at 3572 cm^{-1}, with water molecules in-between, represented as a broad absorbance peak at 3448 cm^{-1} and 1628 cm^{-1}. Moreover, interlayered nitrate was noted at 1365 cm^{-1} and 830 cm^{-1}, while Zn−OH vibration bands at 1008, 879, 764, 632 cm^{-1} were observed,

corroborating the presence of zinc hydroxynitrate [304,307]. Regarding the presence of DX in the particle, the vibration band at 1359 cm^{-1} was found to be enlarged, being extended from 1311 to 1380 cm^{-1}, which can be assigned to δCO group vibrations [352]. In addition, a signal broadening between 1600-1670 cm^{-1} was also noted, which can be related to υCC vibrations in the phenyl ring [352]. Another substantial signal widening can be observed between 3300 to 3600 cm^{-1}, following the band pattern of free DX. These signal modifications qualitatively indicate the presence of DX onto DX-Zn-Mg LH NPs. Quantitatively, X-ray photoelectron spectroscopy (XPS) analysis revealed comparable amounts of oxygen, carbon, zinc, and nitrogen in both NPs (Figure 28-D). As expected, zinc layered hydroxyl (LZH) materials contain large amounts of zinc, nitrogen, and oxygen. However, in the formulation of Zn-Mg LH NPs, carbon should be absent. Its presence is likely related to the sterilization method by ethylene oxide, since a similar trend is reported in other studies [311,312]. Oppositely, chloride was found only in DX-Zn-Mg LH NPs, confirming the antibiotic's incorporation (doxycycline hydrochloride).

Moreover, Zn^{2+} and Mg^{2+} concentrations from dissolved NPs were measured by inductively coupled plasma spectroscopy (ICP), showing high amounts of Zn^{2+} content in Zn-Mg LH NPs and DX-Zn-Mg LH NPs (≈ 53%), as well as a low percentage of Mg^{2+} (below 1%), confirming the presence of magnesium in both formulations, with a reduced amount of magnesium in DX-Zn-Mg LH NPs (Figure 28-E).

The assessment of their zeta potential was performed by suspending the NPs in distilled water and HEPES buffer (Figure 28-F). NPs presented a similar behavior, being positively charge when suspended in water, while their surface charge was found to be negative in HEPES at neutral pH, with values over ±30 mV, indicating stable dispersions.

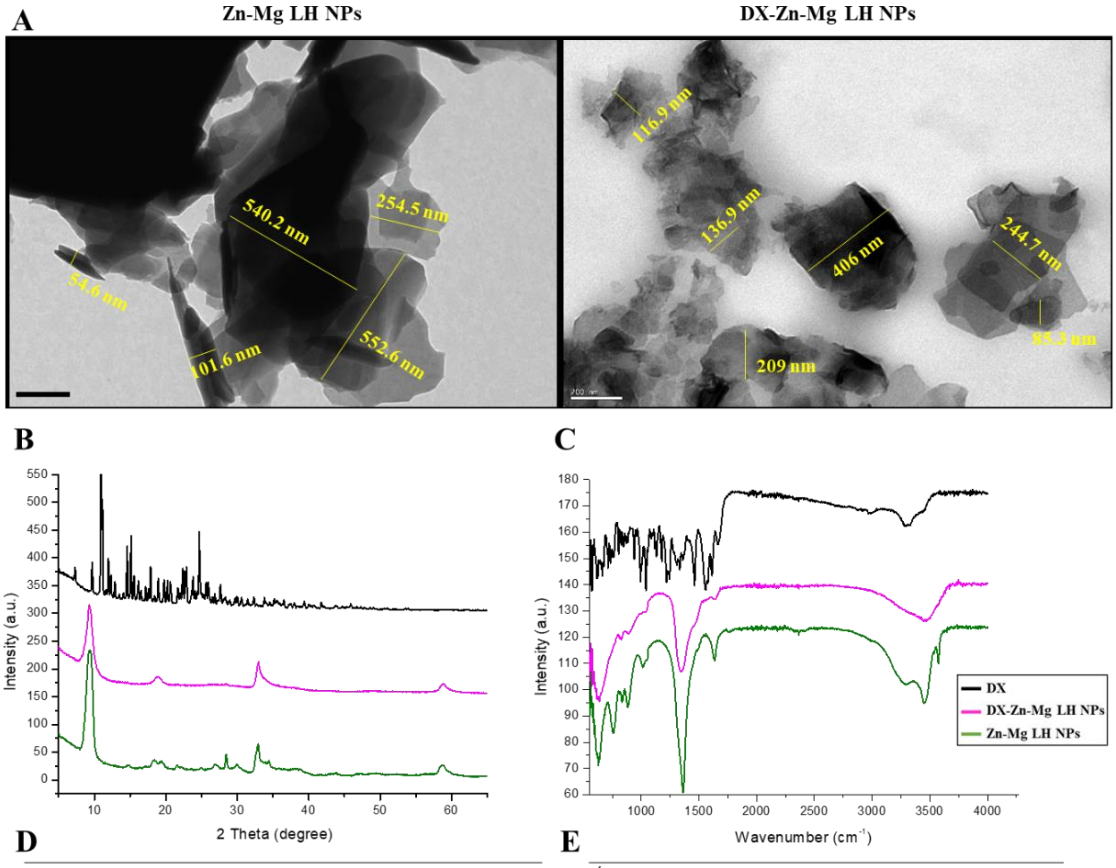

D

Element	Zn-Mg LH NPs (At%)	DX-Zn-Mg LH NPs (At%)	DX (At%)
Carbon (C 1s)	22.8	21.3	72.4
Nitrogen (N 1s)	7.6	6.4	5.7
Oxygen (O 1s)	52.2	51.0	20.2
Magnesium (Mg 1s)	0.05	N/A	N/A
Chloride Cl 2p)	N/A	0.3	1.6
Zinc (Zn $2p^3$)	17.4	21.0	N/A

E

Íon	Zn-Mg LH NPs (%)	DX-Zn-Mg LH NPs (%)
Mg	0.049	0.029
Zn	53.7	53.2

F

	dH_2O (mV ± SD)	HEPES (pH 7.0)
Zn-Mg LH NPs	37 ± 1.2	-33 ± 1.5
DX-Zn-Mg LH NPs	40 ± 0.7	-31 ± 0.2

Figure 28. Physicochemical characterization of LH NPs. A - TEM Images of Zn-Mg LH NPs and DX-Zn-Mg LH NPs. Scale bar corresponds to 200 nm. B – XRD analysis, assessing the crystallinity degree of NPs. C – FTIR/ATR results, qualitatively evaluating the composition of the NPs. D – XPS analysis and E - ICP analysis, corresponding to the quantitative analysis of NPs' composition. F – Zeta potential of NPs assessed by light scattering, using distilled water and HEPES buffer. The pH of HEPES was adjusted to 7.0.

6.3.2. Assessment of the drug loading capacity and drug release

The dissolution of 10 mg of DX-Zn-Mg LH NPs corresponded to approx. 151 µg of free DX, resulting in a 1.5% of drug loading (DL%). Regarding the drug release at physiologic pH, DX-Zn-Mg LH NPs presented a burst discharge of approx. 35% (50 µg/mL) between 1 and 2 h, followed by a slower and steady release until day 4 (Figure 29). Subsequently, between day 4 and 8, a higher discharge was observed, in addition to a continuous release extending up to day 14. Overall, NPs were successfully loaded with DX, and presented an extended drug release until day 14, releasing approx. 80% of the total DX (130 µg/mL as cumulative concentration release).

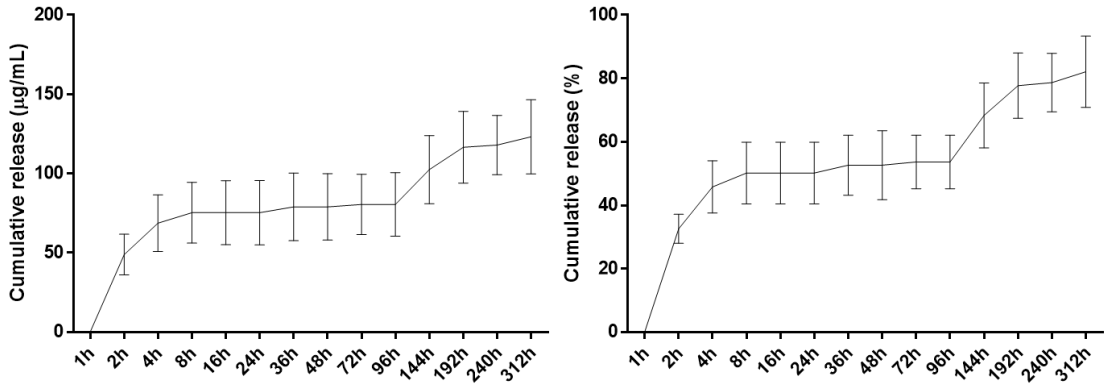

Figure 29. Concentrations of DX released from the DX-Zn-Mg LH NPs for 14 days in Hepes buffer, displayed by concentration (left graph) and percentage, using the DL% as reference for 100% (right graph).

6.3.3. Antibacterial activity of NPs

Antibacterial activity of NPs was evaluated using two bacterial strains, a gram-positive specimen (*S. aureus*) that can be associated with aggressive PD [353], and a gram-negative bacterium (*P. gingivalis*) - considered a keystone pathogen in chronic periodontal diseases [21]. As observed in figure 30, Zn-Mg LH NPs exhibit no discernible antibacterial activity against *S. aureus*, whereas DX-Zn-Mg LH NPs presented a clear inhibition zone in the agar diffusion assay (Figure 30-A), as well as a MIC of 3.12 µg/mL (Figure 30-B). These outcomes validate the antibiotic presence and functionality following the drug loading, NP's drying, and sterilization processes. Similarly, Zn-Mg LH NPs, at 10 µg/mL, were unable to significantly reduce the percentage of colony-forming unit (CFU) of *P. gingivalis*, while DX-Zn-Mg LH NPs, at the same concentration, were found to reduce in 50% the CFU of the gram-negative bacterium (Fig. 30-C).

A

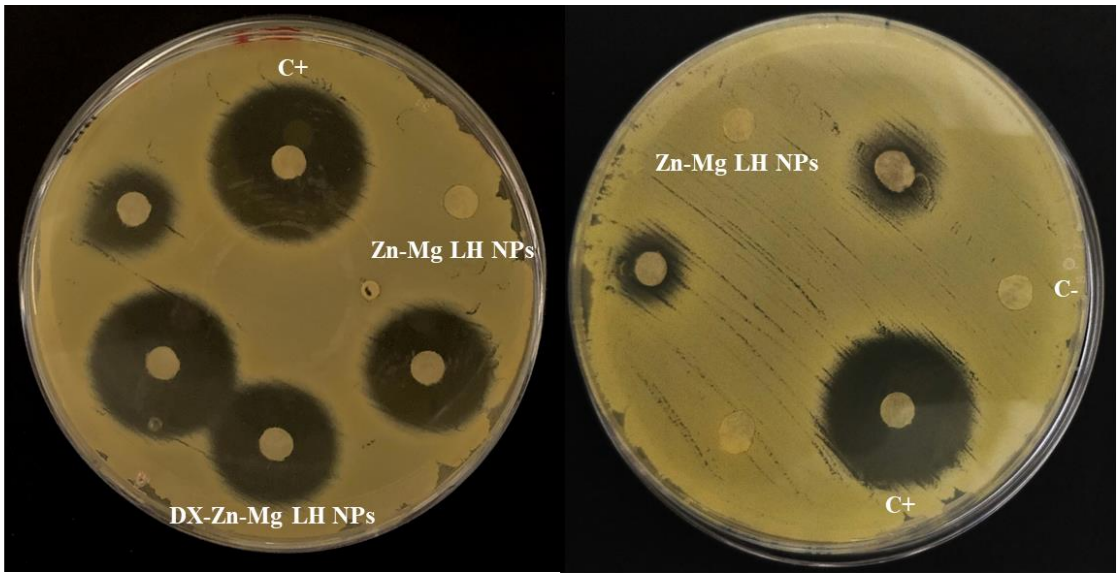

B

Disk Content	Inhibition zone diameter (mm)	MIC (µg/mL)
C- (dH_2O)	-	-
C+ (DX 30 µg)	25.3 ± 1.4	0.125
Zn-Mg LH NPs	-	-
DX-Zn-Mg LH NPs	18.89 ± 1.1	3.12

C

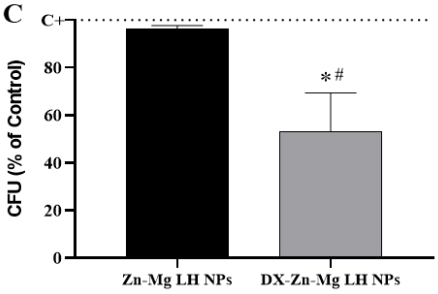

Figure 30. Antibacterial activity of Zn-Mg LH NPs and DX-Zn-Mg LH NPs against *S. aureus* (A and B) and *P. gingivalis* (C). A – Representative images of the Kirby Bauer assay. B – Inhibition zone measurements and minimum inhibitory concentration (MIC) assay of NPs against *S. aureus*. C – CFU counting of *P. gingivalis*, after 24h incubation with NPs, at 10 µg/mL. (*) Statistically different to Control. (#) Statistically different to other experimental samples.

6.3.4. Cytocompatibility assessment of NPs using HGFs

To assess the cytocompatibility of Zn-Mg LH and DX-Zn-Mg LH NPs, human gingival fibroblasts (HGFs) were chosen due to their relevance in the periodontal structures' composition. Three different concentrations of NPs, ranging from 1.0 to 50 µg/mL were chosen for the assays. Control cultures, grown in the absence of NPs, presented a continuous increase in metabolic activity throughout the assay (Figure 31). Cultures exposed to both NPs presented a similar growth pattern at lower concentrations (i.e., 1 and 10 µg/mL) and a clear reduction of the metabolic activity at 50 µg/mL, observed in all timepoints, being suggestive of cytotoxicity. Regarding cell morphology, no significant differences were noted among all the assayed groups (control and 10 µg/mL of both NPs) - HGFs presented an elongated and stretched shape, alongside stress fibers, rounded and well-defined nucleus and slender cytoplasmic extensions at day 1 (Figure

31). At day 7, the confluence of cells increased significantly, and cell-to-cell contacts were unceasing, evidencing an active cell proliferation between timepoints.

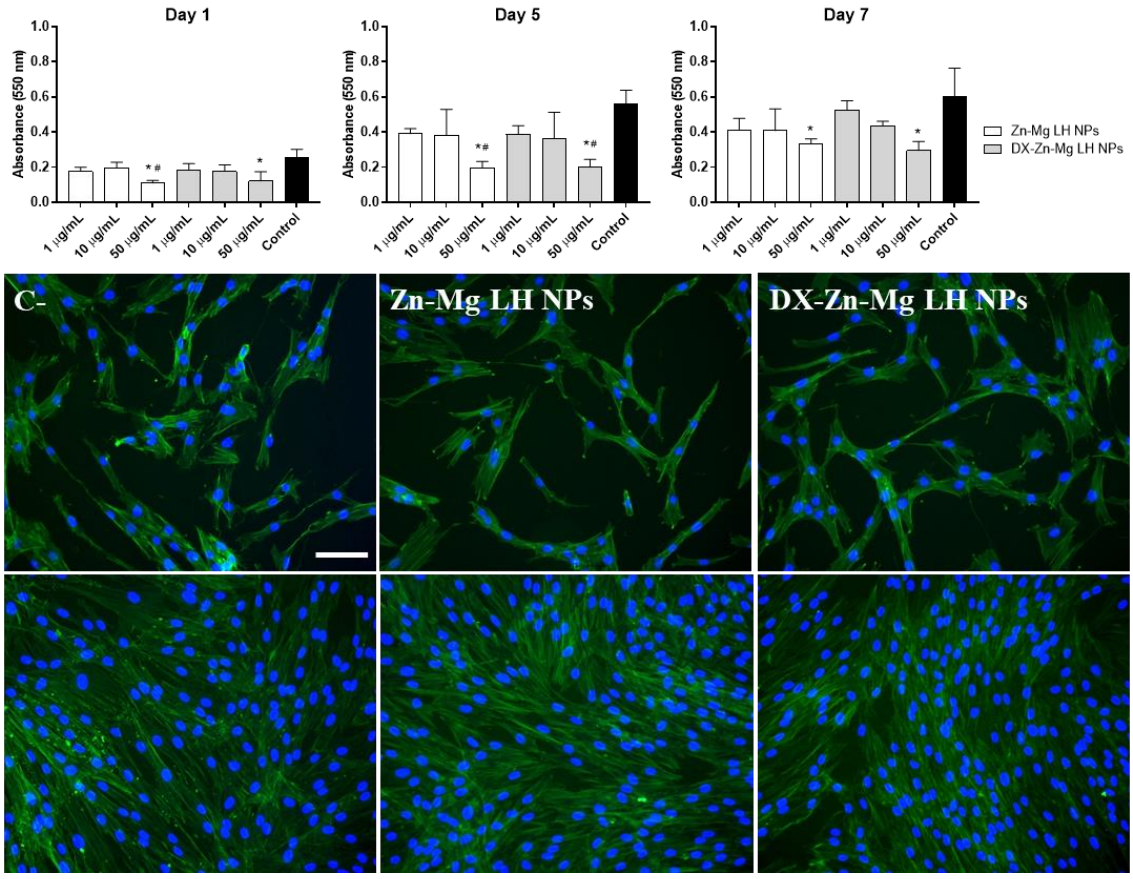

Figure 31. Upper part: Metabolic activity of HGFs incubated with and without NPs. (*) Statistically different to Control. (#) Statistically different to other experimental samples. Lower part: Representative images of cellular morphology of HGFs grown in the presence of 10 µg/mL of NPs, at day 1 and day 7. Cells were stained for F-actin cytoskeleton in green and counterstained for nuclei in blue. Scale bar: 100 µm.

The assessment of reactive oxygen species (ROS) generated by cells in contact with inorganic NPs is essential, since metallic-based materials, such as LZH, can induce ROS generation by Fenton-like reactions, ultimately leading to cell damage [354]. As displayed in figure 32-A, both NP's types did not induce ROS production in HGFs cultures, presenting values similar to untreated cells. It is worth mentioning that, at 50 µg/mL, a trend toward increase ROS levels was observed. Nevertheless, the increase was only significantly higher when compared to cells treated with N-acetylcysteine.

On the contrary, magnesium and zinc can also present antioxidant activity in mammal cells, which is observed in our findings (Figure 32-B). ROS generation was induced by H_2O_2 and the incubation with Zn-Mg LH and DX-Zn-Mg LH NPs significantly reduced the detection of ROS in cell cultures.

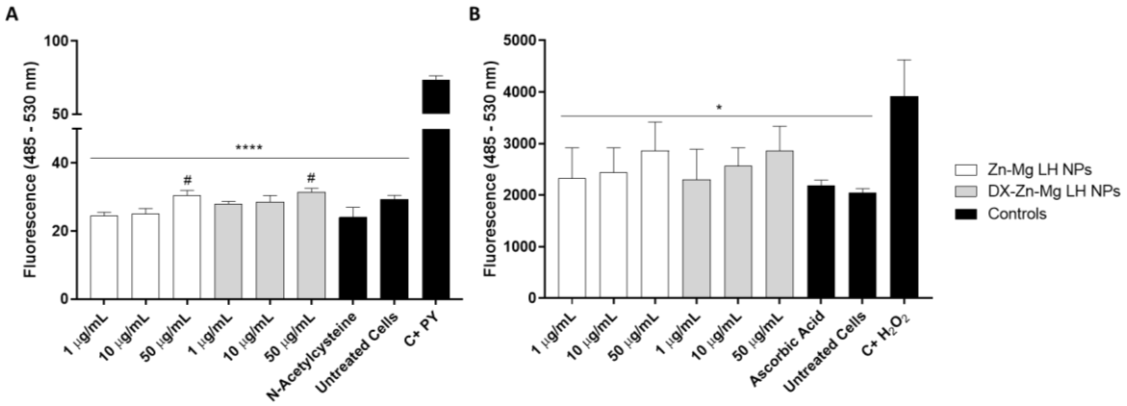

Figure 32. A - Measurement of ROS generated by Zn-Mg LH and DX-Zn-Mg LH NPs after 1 h of incubation. B - Anti-ROS activity of NPs. (#) significantly different from cells treated with N-Acetylcysteine. (*) significantly different from C+. * $p < 0.05$. **** $p < 0.0001$.

To evaluate the internalization of the NPs, HGFs were incubated with both NPs for short (3 h) and extended (24 h) periods, prior to fixation and TEM observation (Figure 33 and 34). Nonexposed cells presented no clear alterations in the cellular membrane or in the cytosol, displaying normal Golgi apparatus, mitochondria, and endoplasmic reticulum, as well as the reduced number of small vacuole formations at the periphery. Oppositely, at an early stage, HGFs exposed to Zn-Mg LH and DX-Zn-Mg LH NPs presented noticeable membrane protrusions, blebs, and perturbations, in addition to multiple vacuole formations that resemble macropinosomes, suggesting that the internalization of the NPs occurred via macropinocytosis.

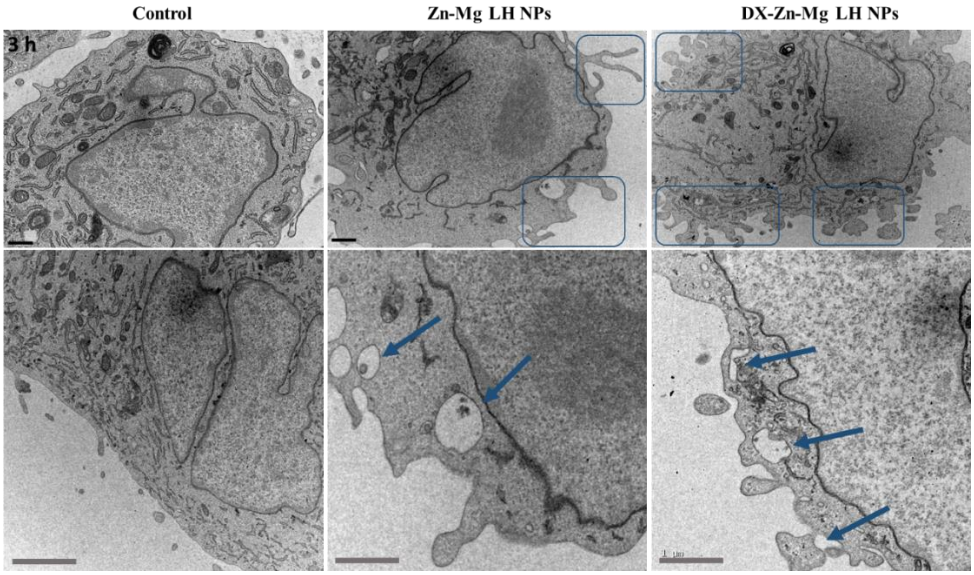

Figure 33. Representative images of NPs' uptake by HGFs after 3 h of incubation, addressed by TEM. Upper scale bar: 0.5 µm. Lower scale bar: 1 µm. Blue squares highlight membrane's protrusions and general perturbations, while blue arrows indicate areas of vacuole formations. NPs' concentration of 10 µg/mL.

Furthermore, evident alterations in the cytosol of HGFs were observed at late periods – Golgi apparatus and endoplasmic reticulum were found to be disturbed, and the number of mitochondria seems to be augmented, with some of them presenting a partial disintegration (Figure 34). Additionally, several vacuole formations (i.e., pinosomes, autophagosomes, autolysosomes) were noted, indicating an autophagic activity triggered by the presence of Zn-Mg LH and DX-Zn-Mg LH NPs inside the cells.

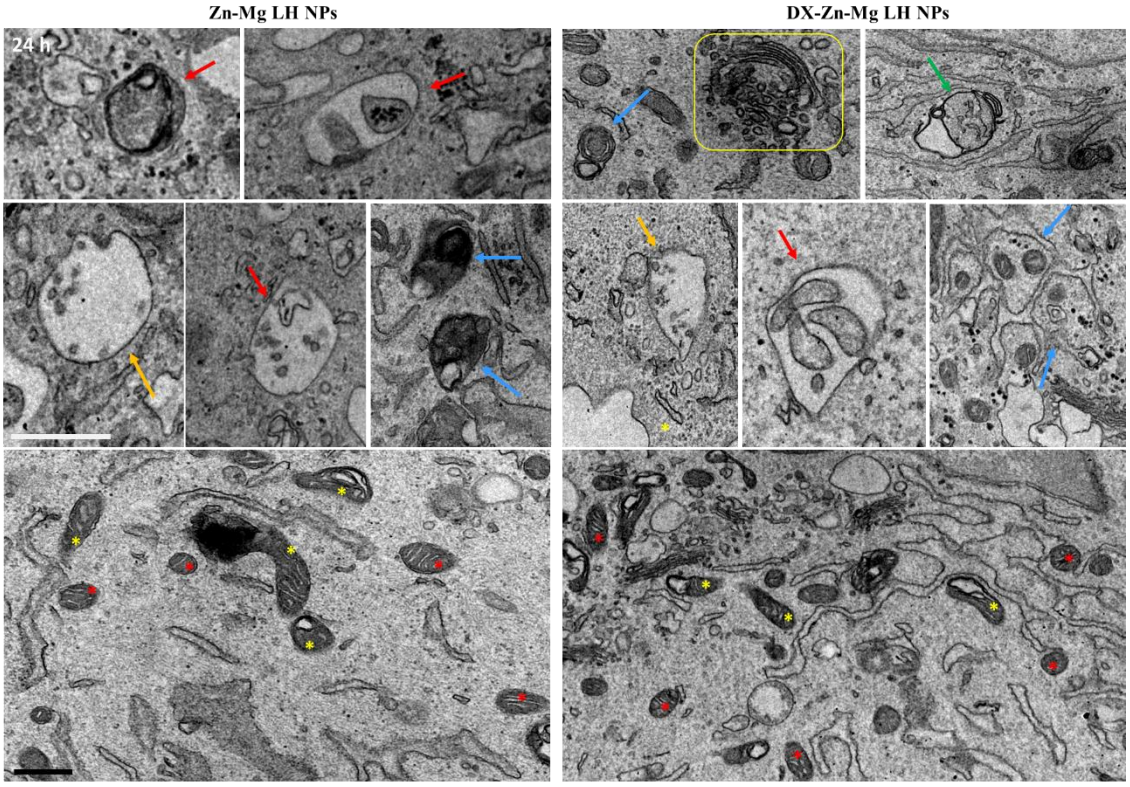

Figure 34. Representative TEM images of NPs' intracellular trafficking after 24 h of incubation. Scale bars: 0.5 µm. Yellow square: Golgi apparatus. Orange arrow: phagosomes. Red arrow: autophagosomes. Green arrow: amphisomes. Blue arrow: autolysosomes. Red asterisk: healthy mitochondria. Yellow asterisk: Damaged mitochondria. NPs' concentration of 10 µg/mL.

Lastly, the anti-inflammatory properties of Zn-Mg LH and DX-Zn-Mg LH NPs were evaluated by inflamed LPS-induced mucosal model (Figure 8). The organotypic system, in contact with LPS, presented a significant upregulation of relevant inflammatory genes, as interleukins (IL-1β, IL-6 and CXCL-8), nuclear factor kappa light chain enhancer of activated B cells (NFkB) and tumor necrosis factor (TNF). Both NPs presented undistinguishable anti-inflammatory activity. They significantly downregulated the expression of all the assayed inflammation-related genes when compared to LPS-induced conditions, effectively reducing IL-6 to levels close to those of the untreated cells.

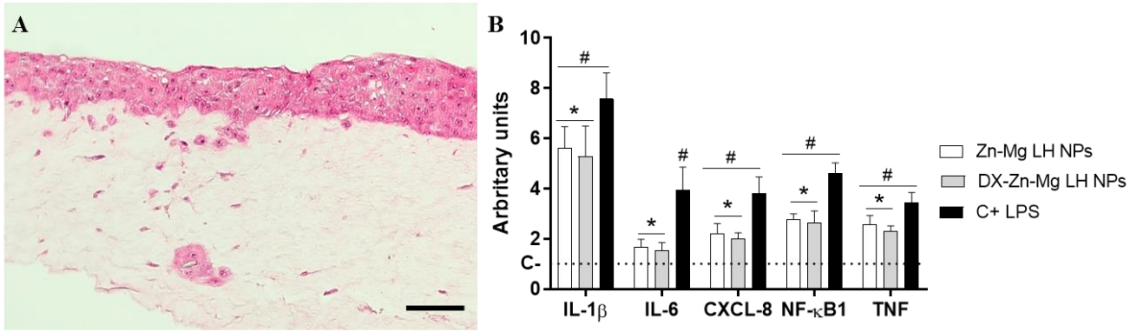

Figure 35. (A) Representative histological section of the organotypic mucosal model stained with H&E. Scale bar: 250 µm. (B) Anti-inflammatory activity of NPs assessed by QPCR. Cells were incubated with 1.0 µg/mL of LPS prior incubation with 10 µg/mL of NPs. Values were normalized by the housekeeping gene (GAPDH), set as 1.0. (*) Significantly different from C+. (#) Significantly different from C-.

6.4. Discussion

PD's etiology involves a multitude of factors, as the host immune response and environmental factors, in addition to the presence of keystone periodontal pathogens [10]. Therefore, the assessment of innovative perioceutics should ideally be set on the evaluation of their impact on the biological response of periodontal tissues, their capability to modulate local inflammation, and effectiveness against relevant bacteria.

In the present study, LH NPs were chosen as a DX carrier due to their biocompatibility, bioactive profile, and remarkable capabilities to serve as a drug carrier [171], further presenting antioxidant and anti-inflammatory effects that are expected to heighten the therapeutic effectiveness [180]. Physicochemical characteristics indicated that the developed particulates were indeed layered hydroxide NPs, which presented Zn^{2+} and Mg^{2+} cations in their composition (Figure 28). Additionally, as demonstrated by the DL% and drug release data, DX was successfully loaded into Zn-Mg LH NPs, and released with a therapeutically relevant profile (Figure 29), maintaining its antibacterial activity after the synthesis and post-processing of the NPs (Figure 30).

The incorporation of DX into LH NPs is likely related to the affinity of different anions for LHs – a higher anion charge leads to a greater binding energy to the cationic layers [355]. For both Mg- and Zn-based LHs, NO_3^- presents a decreased selectivity in comparison to other anions (e.g., OH^-, Cl^-, PO_4^{3-}, $HCOO^-$), being a suitable precursor for ionic exchange [181]. This allows DX molecules, which contain hydroxyl groups and chloride, to partially substitute the nitrates from the interlayered spaces of LH [181,355,356]. Moreover, it is documented that TCs, at pH values ranging from 4.0 – 7.0,

are mainly in their zwitterionic form (i.e., neutral charge), which enables strong electrostatic interactions with the protonated surfaces, as LH NPs [37,357,358]. Interestingly, the co-precipitation during the synthesis of DX-Zn-Mg LH NPs was attained in a pH of approx. 6.0, aligned with the literature. Furthermore, the DX was successfully released from the LH NPs, confirming their potential as LDDS. Similarly, LH NPs containing TCs displayed a burst release in the first hours [343,359,360], and a controlled release throughout long periods [343]. It is worth mentioning that the release of TCs from LH nanostructures is broadly unexplored, precluding substantiated comparisons with other NP systems.

Although the observed differences in the crystallinity degree and particle's aggregation between NP's groups, the biological response to these particles was comparable, probably due to the similar size, shape, composition, and surface charge [321,361,362]. Upon the metabolic activity evaluation of the established human fibroblastic cultures, Zn-Mg LH and DX-Zn-Mg LH NPs were found to be cytocompatible at 1.0 and 10 µg/mL. Additionally, HGFs incubated with both NPs at 10 µg/mL presented an indistinguishable morphology in comparison to control, supporting the MTT results (Figure 31). Furthermore, the cell viability was found to be reduced in approx. 50% at 50 µg/mL for experimental groups in comparison to control. The presence of DX in the NPs did not influence the metabolic activity of HGFs, probably due to the reduced amount of DX in the formulation. For instance, after a full release, 50 µg/mL of DX-Zn-Mg LH NPs would correspond to approx. 0.8 µg/mL (1.8 µM) of free DX, a concentration regarded to not interfere negatively in cell viability or functionality [190,192,193,209].

While Zn-based materials are generally considered as safe compound by the FDA [363], cytotoxicity in mammal cells is reported in the literature [363]. Two main cytotoxic mechanisms are hypothesized. First, ZN-based NPs can induce ROS generation and excessive Zn^{2+} diffusion across the cell membrane [364]. Zinc-based NPs can behave as pro-oxidant materials, causing oxidative endoplasmic-reticulum (ER) and mitochondrial stress that leads to DNA damage and imbalanced cell metabolism [365]. Second, excessive Zn^{2+} is likely to disturb the cellular homeostasis by incapacitating electron transport systems, enzymatic and mitochondrial activity, often resulting in cell cycle arrest and apoptosis [324,325,363]. Both ROS and Zn^{2+} mechanisms are likely to be associated, resulting in the activation of caspases 3 and 9 via Bax/Bcl2 signaling [365].

Our results showed that the incubation with Zn-Mg LH and DX-Zn-Mg LH NPs at 1.0 and 10 µg/mL did not induce ROS formation in HGFs (Figure 32-A), and, at a cytotoxic

concentration (50 µg/mL), a discrete ROS generation was observed. This finding indicates that the supraphysiologic Zn^{2+} levels might be an earlier cytotoxic mechanism in comparison to the ROS generation, since detected levels of ROS, at high concentrations of NPs, were comparable to those in untreated cells.

Divergently, previous studies reported a significant increase in ROS generation by cells following exposure to Zn-based NP's, particularly in the evaluation of zinc oxide particulates [325,366,367]. Ultimately, general cytotoxicity arising by ROS generation and/or acute Zn^{2+} release from zinc-based materials will be mainly related to their interaction with cells, the cell type, and NP's formulation and physicochemical characteristics [322].

Contrasting to these cytotoxic mechanisms, inorganic NPs can also present a protective effect against ROS by facilitating electron transferring of the oxygen [368]. Additionally, zinc is known as an inducer of glutathione, catalase and metallothionein, key antioxidant proteins within cells [180]. As noted, Zn-Mg LH and DX-Zn-Mg LH NPs protected HGFs cultures from the effects of exogenous hydrogen peroxide, confirming the antioxidant effect of the developed perioceutic (Figure 32-B). However, the effect was not dose-dependent – in fact, despite statistically non-significant, the peak of the antioxidant activity was observed at the lowest NP's concentration, suggesting that high concentrations of Zn-Mg LH NPs might induce pro-oxidative activity, while low concentrations can act as antioxidant agents, as described in the literature [368]. Another hypothesis is that, at lower concentrations, the antioxidant effects can compensate the ROS production induced by zinc-based NPs, while, at higher concentrations, the balance might shift towards pro-oxidant effects [366].

Tetracyclines, including DX, are also known as antioxidant molecules, being capable of increasing superoxide dismutase and catalase activity in damaged tissues [236]. Moreover, the phenolic rings of TCs can react with free radicals, resulting in a stable and not reactive molecule, ultimately leading to the reduction of nitric oxide and protein carbonylation, which are relevant oxidant markers [35,369]. Despite these features, no differences between Zn-Mg LH and DX-Zn-Mg LH NPs were observed in their pro-oxidant/antioxidant characteristics, suggesting that only the carrier's activity was observed. A credible possibility lies on the drug release rate (Figure 29), whereas the amount of released DX might not be enough to exert this pleiotropic effect in a short incubation period, as set for ROS detection assays.

Nonetheless, having an antioxidant vehicle for DX is a major clinical attribute for a perioceutic, considering that oxidative stress underlies the pathogenesis of chronic inflammatory conditions, including PD [16,370]. Due to the presence of dysbiotic biofilms, polymorphonuclear neutrophils are recruited to the periodontal pocket, leading to an overproduction of ROS. These can lead to the elimination of microorganisms, as well as cytotoxicity for host cells, leading to a proinflammatory environment. This scenario results in osteoclastogenesis and reduced collagen synthesis by affected fibroblasts, culminating in the periodontium's destruction and impaired healing [16].

Certainly, oxidative stress is not the only pro-inflammatory aspect related to PD. Lipopolysaccharides (LPS) from the cell wall of gram-negative bacteria (e.g., *P. gingivalis, A. actinomycetemcomitans*) are regarded as main pro-inflammatory compounds, which interact with cellular Toll Like Receptor-4 (TLR4), triggering the production and secretion of pro-inflammatory cytokines, as IL-1β, IL-6, TNF, and CXCL-8, via NFkB transcription factor's activation [110,371]. As displayed in figure 35, the exposure of HGFs to LPS from *P. gingivalis* resulted in an exacerbated inflammatory response, represented by the upregulation of all assessed inflammatory genes. Moreover, LPS-stimulated mucosal model incubated with either Zn-Mg LH or DX-Zn-Mg LH NPs was found to express significantly lower levels of these genes, indicating their anti-inflammatory capability. Similar results can be found in the literature, as Zn-based NPs were able to reduce inflammatory markers within *in vitro* and *in vivo* settings, corroborating our findings [347,372,373]. This anti-inflammatory activity can be attributed to Zn^{2+} release, which can downregulate the expression of proinflammatory cytokines (e.g., IL-1β, IL-6, CXCL-8) by preventing the activation of the NFKB pathway by blocking IkB kinase (IKK) and stimulating the production of negative modulators, as A20 protein [332]. By inhibiting the NFkB activation, downstream cytokines are consequently downregulated, as observed in figure 35.

TCs have also been found to produce anti-inflammatory effects via multiple routes, as suppressing NFkB activation through inhibition of IKK, in addition to downregulating p38 and MAPK pathways [234]. Moreover, even at low concentrations (0.3 µg/mL), DX was found to have significant anti-inflammatory effects on LPS-stimulated cells [374]. However, DX-Zn-Mg LH NPs did not present any additional anti-inflammatory effects in comparison to Zn-Mg LH NPs, suggesting that the anti-inflammatory capabilities of zinc and DX were not summated. Since both compounds mainly act inhibiting NFkB

signaling via IKK, it is speculated that this anti-inflammatory route was saturated, preventing any additional effects through it.

Regarding internalization, while TEM images could not clearly identify NPs within the HGFs, important intracellular alterations were noted at both assessed timepoints, implying that Zn-Mg LH and DX-Zn-Mg LH NPs were uptaken by the cells (Figure 33 and 34). In fact, it is documented that NPs' internalization is utterly influenced by their physicochemical characteristics - studies demonstrated that smaller and more dispersed NPs are internalized in higher amounts in comparison to larger and agglomerated specimens [375,376]. Moreover, smaller NPs (≤ 30 nm) tend to be internalized by clathrin-mediated endocytosis, while larger NPs (> 70 nm) are likely to be uptaken by non-specific pathways, as macropinocytosis [127,375], a process commonly observed with LH-based systems [173]. Due to the size and agglomeration of the NPs, in addition to the scarcity of clathrin-coated vesicles and the noted membrane protrusions that resulted from actin polymerization, macropinocytosis is possibly the main pathway of internalization. Additionally, the positive charge of LH-based systems plays an important role in promoting the NPs' uptake, exploiting the negatively charged cell membranes [169].

Nonetheless, regardless the uptake's via, internalized Zn-Mg LH NPs tend to be into intracellular vesicles (e.g., endosomes, lysosomes), which are highly acidic environments. This can lead to a fast NPs' dissolution, and, therefore, an acute release of Zn^{2+} and DX intracellularly [365]. Conveniently, internalized *P. gingivalis* is mainly find within these same vesicles before escaping to the cytosol or to the extracellular environment [124]. Therefore, the developed DX- Zn-Mg LH NPs can tackle intracellular bacterial reservoirs via three conjoined effects: firstly, by delivering an effective antibiotic into the same cellular compartments where *P. gingivalis* can be found; secondly, the substantial release of Zn^{2+} that can disrupt bacterial active transport, metabolism, and enzymatic activity [377]; and thirdly, by activating an autophagic profile of HGFs – trend confirmed by the presence of numerous autophagic vacuoles, increased mitochondria and associated mitochondrial damage [378,379] (Figure 34) – that might prevent intracellular bacterial proliferation and evasion [110]. Moreover, it has been described that instigating autophagy in periodontal connective tissue cells can result in the inhibition of osteoclastic activity by reducing the RANKL/OPG ratio, which can further reduce the progression of periodontitis [380].

It is worth noting that the assessment of cell metabolic activity, morphology and internalization were performed at the same concentration (10 μg/mL), and both NPs were found to be cytocompatible, with no significant alterations observed in the broad cell morphology, while triggering this functional autophagy.

Finally, besides being antioxidant and anti-inflammatory, a perioceutic should also present antibacterial activity, preferably at concentrations that is likewise cytocompatible. In the present study, Zn-Mg LH NPs did not present antibacterial activity against both assessed strains (Figure 30). The antibacterial mechanisms of Zn-Mg LH NPs are not fully understood, with reports suggesting that the antibacterial activity is mainly set on oxidative stress and Zn^{2+} release, which result in the production of H_2O_2 and changes in the pH, hampering bacterial cell wall, homeostasis, and function [381,382]. Moreover, NP's size plays a pivotal role in antibacterial activity of NPs, as in their cytocompatibility [361]. It has been demonstrated that smaller NPs exhibit enhanced bactericidal activity, due to a facilitated penetration into bacterial cells and larger surface area, mainly responsible for particle's dissolution, and, therefore, an increased release rate of Zn^{2+} and H_2O_2 generation [331,352,377,381]. As showed in figure 28, the developed NPs presented a relatively larger size, that may have hindered their bactericidal effect at assayed concentrations.

Oppositely, as displayed in figure 30, DX-Zn-Mg LH NPs were effective against *S. aureus* and *P. gingivalis* at cytocompatible concentrations, corroborating their feasibility as a local drug delivery system and their safety for medical applications. Furthermore, it is plausible that, despite not having bactericidal effect by their own, Zn-Mg LH NPs may have boosted DX's antibacterial effects. This is evident from the fact that the MIC of DX-Zn-Mg LH NPs for *S. aureus* was 3.12 μg/mL, which corresponds approx. to 0.0468 μg/mL of free DX (after the full release), accordingly to the obtained DL%. In comparison, the MIC of free DX was achieved at 0.125 μg/mL. This trend was also documented with distinct zinc-based NPs against other bacteria (e.g., *P. aeruginosa, E. coli, S. epidermidis*) [183,352,383]. Similarly, loaded LH nanocomposites were found to present an analogous antibacterial activity, similar to the free drug format (i.e., MIC) against *Mycobacterium tuberculosis* with significantly less antibiotic in their formulation [185]. This synergetic effect between antibiotics and zinc-based carriers can be related to the inhibition of bacterial' transporter proteins, biofilm formation, the reversal of antibiotic resistance mechanisms via bacteria-NP interactions, and the release of cations [183,352,383].

6.5. Conclusion

The present study demonstrated the usage of Zn-Mg LH NPs as a versatile drug carrier for the development of a novel perioceutic. The NPs' synthesis was set on a straightforward method, involving low temperatures that enabled an effective drug loading during their production.

The developed nanoparticulate presented an appropriate cytocompatibility, in addition to antioxidant and anti-inflammatory effects, confirming the carrier's bioactivity. Moreover, DX was successfully released from the NPs in a steady and long-lasting manner, enabling effective antibacterial activity against gram-positive and gram-negative bacteria. Our results suggested that Zn-Mg LH NPs were internalized by fibroblasts via macropinocytosis, which could be effective against the intracellular periodontal pathogens. Additionally, Zn-Mg LH NPs might have enhanced the antibacterial effect of DX on *S. aureus*, indicating a synergetic effect between drug and vehicle. Further studies should focus on validating these findings in more advanced settings, as *in vivo* models, and co-infection cellular cultures. All in all, DX-Zn-Mg LH NPs are a promising perioceutic and might be an effective adjutant therapy to treat recurrent periodontal diseases.

CHAPTER 7

General Conclusions and Future Perspectives

Periodontal diseases are a group of highly prevalent immuno-inflammatory conditions that affect the supporting tissues of the teeth, accountable for the aggravation of systemic chronic inflammatory conditions. The etiology is associated with dysbiosis at the gingival crevice that uplift the virulence and sustain a pro-inflammatory community, eliciting a tissue-destructive host response. Current therapies mainly rely on the mechanical removal of biofilm for the reduction of the pathogenic load, which can be ineffective for the modulation of the hosts' immune-inflammatory response. In this context, tetracyclines, antibacterial drugs with antioxidant and anti-inflammatory properties, are promising candidates to serve as adjutant therapy.

As discussed in chapter 1, micro and nanoparticles can be loaded with tetracyclines to be inserted directly in periodontal pockets, enhancing the efficacy of the therapy, and lessening the adverse effects associated with the systemic administration. Among different types of drug carriers, inorganic nanoparticles present unique characteristics that could be explored in the local delivery of tetracyclines, functioning as a local perioceutic. Despite belonging to the same antibiotic class, each tetracycline specimen possesses a unique set of characteristics that can stimulate different biological responses. For the first time, the osteogenic potential of sarecycline was assessed, being described in the chapter 3. Moreover, it was shown (chapter 4) that minocycline and sarecycline may induce osteogenic differentiation of bone-marrow stromal cells through different pathways when compared to tetracycline and doxycycline. Interestingly, these distinct mechanisms of action may be exploited for targeted treatments based on specific bone-related disorders. The development and characterization of layered zinc-magnesium hydroxide nanoparticles are reported in chapter 5 and 6. The constructs displayed adequate physicochemical characteristics and good *in vitro* biologic performance, decreasing proinflammatory markers and reactive oxygen species. The addition of doxycycline in the formulation provided a clear antibacterial activity. Overall, the developed nanoparticles demonstrated a great potential to be employed as a local perioceutic and future studies should include the assessment of their biodegradability, efficacy, and safety *in vivo*, using animal models for periodontitis-related research.

REFERENCES

[1] Trindade F, Oppenheim FG, Helmerhorst EJ, Amado F, Gomes PS, Vitorino R. Uncovering the molecular networks in periodontitis. PROTEOMICS - Clin Appl 2014;8:748–61. https://doi.org/10.1002/prca.201400028.

[2] Li X, Qi M, Li C, Dong B, Wang J, Weir MD, et al. Novel nanoparticles of cerium-doped zeolitic imidazolate frameworks with dual benefits of antibacterial and anti-inflammatory functions against periodontitis. J Mater Chem B 2019;7:6955–71. https://doi.org/10.1039/C9TB01743G.

[3] Muhammad Ashraf Nazir. Prevalence of periodontal disease, its association with systemic diseases and prevention. Int J Health Sci (Qassim) 2017;1:72–80. https://doi.org/10.1109/ISIP.2008.139.

[4] Tonetti MS, Jepsen S, Jin L, Otomo-Corgel J. Impact of the global burden of periodontal diseases on health, nutrition and wellbeing of mankind: A call for global action. J Clin Periodontol 2017;44:456–62. https://doi.org/10.1111/jcpe.12732.

[5] G. Caton J, Armitage G, Berglundh T, Chapple ILC, Jepsen S, S. Kornman K, et al. A new classification scheme for periodontal and peri-implant diseases and conditions – Introduction and key changes from the 1999 classification. J Clin Periodontol 2018;45:S1–8. https://doi.org/10.1111/jcpe.12935.

[6] Salvi GE, Roccuzzo A, Imber J, Stähli A, Klinge B, Lang NP. Clinical periodontal diagnosis. Periodontol 2000 2023:1–19. https://doi.org/10.1111/prd.12487.

[7] Cafferata EA, Alvarez C, Diaz KT, Maureira M, Monasterio G, González FE, et al. Multifunctional nanocarriers for the treatment of periodontitis: Immunomodulatory, antimicrobial, and regenerative strategies. Oral Dis 2019;25:1866–78. https://doi.org/10.1111/odi.13023.

[8] Elgreu T, Lee S, Wen S, Elghadafi R, Tangkham T, Ma Y, et al. The pathogenic mechanism of oral bacteria and treatment with inhibitors. Clin Exp Dent Res 2022;8:439–48. https://doi.org/10.1002/cre2.499.

[9] Prucsi Z, Płonczyńska A, Potempa J, Sochalska M. Uncovering the Oral Dysbiotic Microbiota as Masters of Neutrophil Responses in the Pathobiology of

Periodontitis. Front Microbiol 2021;12:1–8. https://doi.org/10.3389/fmicb.2021.729717.

[10] Sedghi LM, Bacino M, Kapila YL. Periodontal Disease: The Good, The Bad, and The Unknown. Front Cell Infect Microbiol 2021;11:1–26. https://doi.org/10.3389/fcimb.2021.766944.

[11] Van Dyke TE, Sima C. Understanding resolution of inflammation in periodontal diseases: Is chronic inflammatory periodontitis a failure to resolve? Periodontol 2000 2020;82:205–13. https://doi.org/10.1111/prd.12317.

[12] Mohanty R, Asopa S, Joseph Md, Singh B, Rajguru J, Saidath K, et al. Red complex: Polymicrobial conglomerate in oral flora: A review. J Fam Med Prim Care 2019;8:3480. https://doi.org/10.4103/jfmpc.jfmpc_759_19.

[13] Jia L, Han N, Du J, Guo L, Luo Z, Liu Y. Pathogenesis of Important Virulence Factors of Porphyromonas gingivalis via Toll-Like Receptors. Front Cell Infect Microbiol 2019;9:1–14. https://doi.org/10.3389/fcimb.2019.00262.

[14] Ganther S, Radaic A, Malone E, Kamarajan P, Chang N-YN, Tafolla C, et al. Treponema denticola dentilisin triggered TLR2/MyD88 activation upregulates a tissue destructive program involving MMPs via Sp1 in human oral cells. PLOS Pathog 2021;17:e1009311. https://doi.org/10.1371/journal.ppat.1009311.

[15] Sharma A, Inagaki S, Honma K, Sfintescu C, Baker PJ, Evans RT. Tannerella forsythia -induced Alveolar Bone Loss in Mice Involves Leucine-rich-repeat BspA Protein. J Dent Res 2005;84:462–7. https://doi.org/10.1177/154405910508400512.

[16] Sczepanik FSC, Grossi ML, Casati M, Goldberg M, Glogauer M, Fine N, et al. Periodontitis is an inflammatory disease of oxidative stress: We should treat it that way. Periodontol 2000 2020;84:45–68. https://doi.org/10.1111/prd.12342.

[17] Franco C, Patricia HR, Timo S, Claudia B, Marcela H. Matrix metalloproteinases as regulators of periodontal inflammation. Int J Mol Sci 2017;18:1–12. https://doi.org/10.3390/ijms18020440.

[18] Huang N, Dong H, Luo Y, Shao B. Th17 Cells in Periodontitis and Its Regulation by A20. Front Immunol 2021;12:1–18. https://doi.org/10.3389/fimmu.2021.742925.

[19] Figueredo CM, Lira-Junior R, Love RM. T and B Cells in Periodontal Disease: New Functions in A Complex Scenario. Int J Mol Sci 2019;20:3949. https://doi.org/10.3390/ijms20163949.

[20] Inagaki S, Kimizuka R, Kokubu E, Saito A, Ishihara K. Treponema denticola invasion into human gingival epithelial cells. Microb Pathog 2015;94:104–11. https://doi.org/10.1016/j.micpath.2016.01.010.

[21] Pan C, Liu J, Wang H, Song J, Tan L, Zhao H. Porphyromonas gingivalis can invade periodontal ligament stem cells. BMC Microbiol 2017;17:1–10. https://doi.org/10.1186/s12866-017-0950-5.

[22] Mishima E, Sharma A. Tannerella forsythia invasion in oral epithelial cells requires phosphoinositide 3-kinase activation and clathrin-mediated endocytosis. Microbiology 2011;157:2382–91. https://doi.org/10.1099/mic.0.048975-0.

[23] da Costa LFNP, Amaral C da SF, Barbirato D da S, Leão ATT, Fogacci MF. Chlorhexidine mouthwash as an adjunct to mechanical therapy in chronic periodontitis: A meta-analysis. J Am Dent Assoc 2017;148:308–18. https://doi.org/10.1016/j.adaj.2017.01.021.

[24] Sgolastra F, Petrucci A, Ciarrocchi I, Masci C, Spadaro A. Adjunctive systemic antimicrobials in the treatment of chronic periodontitis: A systematic review and network meta-analysis. J Periodontal Res 2021;56:236–48. https://doi.org/10.1111/jre.12821.

[25] Keestra JAJ, Grosjean I, Coucke W, Quirynen M, Teughels W. Non-surgical periodontal therapy with systemic antibiotics in patients with untreated aggressive periodontitis: a systematic review and meta-analysis. J Periodontal Res 2015;50:689–706. https://doi.org/10.1111/jre.12252.

[26] Keestra JAJ, Grosjean I, Coucke W, Quirynen M, Teughels W. Non-surgical periodontal therapy with systemic antibiotics in patients with untreated chronic periodontitis: a systematic review and meta-analysis. J Periodontal Res 2015;50:294–314. https://doi.org/10.1111/jre.12221.

[27] Khattri S, Kumbargere Nagraj S, Arora A, Eachempati P, Kusum CK, Bhat KG, et al. Adjunctive systemic antimicrobials for the non-surgical treatment of periodontitis. Cochrane Database Syst Rev 2020;2020. https://doi.org/10.1002/14651858.CD012568.pub2.

[28] Adepu S, Ramakrishna S. Controlled Drug Delivery Systems: Current Status and Future Directions. Molecules 2021;26:5905. https://doi.org/10.3390/molecules26195905.

[29] Misra R, Sahoo SK. Antibacterial activity of doxycycline-loaded nanoparticles. vol. 509. 1st ed. Elsevier Inc.; 2012. https://doi.org/10.1016/B978-0-12-391858-1.00004-6.

[30] Seleem MN, Jain N, Pothayee N, Ranjan A, Riffle JS, Sriranganathan N. Targeting Brucella melitensis with polymeric nanoparticles containing streptomycin and doxycycline. FEMS Microbiol Lett 2009;294:24–31. https://doi.org/10.1111/j.1574-6968.2009.01530.x.

[31] Ardila C, Bedoya-García J, Arrubla-Escobar D. Antibiotic resistance in periodontitis patients: A systematic scoping review of randomized clinical trials. Oral Dis 2022. https://doi.org/10.1111/odi.14288.

[32] Garrido-Mesa N, Zarzuelo A, Gálvez J. Minocycline: Far beyond an antibiotic. Br J Pharmacol 2013;169:337–52. https://doi.org/10.1111/bph.12139.

[33] Kurakado S, Takatori K, Sugita T. Minocycline inhibits Candida albicans budded-to-hyphal-form transition and biofilm formation. Jpn J Infect Dis 2017;70:490–4. https://doi.org/10.7883/yoken.JJID.2016.369.

[34] Chopra I, Roberts M. Tetracycline Antibiotics: Mode of Action, Applications, Molecular Biology, and Epidemiology of Bacterial Resistance. Microbiol Mol Biol Rev 2001;65:232–60. https://doi.org/10.1128/mmbr.65.2.232-260.2001.

[35] Garrido-Mesa J, Adams K, Galvez J, Garrido-Mesa N. Repurposing tetracyclines for acute respiratory distress syndrome (ARDS) and severe COVID-19: a critical discussion of recent publications. Expert Opin Investig Drugs 2022;31:475–82. https://doi.org/10.1080/13543784.2022.2054325.

[36] Nelson ML, Levy SB. The history of the tetracyclines. Ann N Y Acad Sci 2011;1241:17–32. https://doi.org/10.1111/j.1749-6632.2011.06354.x.

[37] Ramachanderan R, Schaefer B. Tetracycline antibiotics. ChemTexts 2021;7:18. https://doi.org/10.1007/s40828-021-00138-x.

[38] LaPlante KL, Dhand A, Wright K, Lauterio M. Re-establishing the utility of tetracycline-class antibiotics for current challenges with antibiotic resistance.

Ann Med 2022;54:1686–700. https://doi.org/10.1080/07853890.2022.2085881.

[39] Gallagher JC. Omadacycline: A Modernized Tetracycline. Clin Infect Dis 2019;69:S1–5. https://doi.org/10.1093/cid/ciz394.

[40] Burgos RM, Rodvold KA. Omadacycline: A novel aminomethylcycline. Infect Drug Resist 2019;12:1895–915. https://doi.org/10.2147/IDR.S171352.

[41] Martin V, Grenho L, Fernandes MH, Gomes PS. Repurposing sarecycline for osteoinductive therapies: an in vitro and ex vivo assessment. J Bone Miner Metab 2023. https://doi.org/10.1007/s00774-023-01428-9.

[42] Ramírez-Agudelo R, Scheuermann K, Gala-García A, Monteiro APF, Pinzón-García AD, Cortés ME, et al. Hybrid nanofibers based on poly-caprolactone/gelatin/hydroxyapatite nanoparticles-loaded Doxycycline: Effective anti-tumoral and antibacterial activity. Mater Sci Eng C 2018;83:25–34. https://doi.org/10.1016/j.msec.2017.08.012.

[43] Liu M, Shen S, Wen D, Li M, Li T, Chen X, et al. Hierarchical Nanoassemblies-Assisted Combinational Delivery of Cytotoxic Protein and Antibiotic for Cancer Treatment. Nano Lett 2018;18:2294–303. https://doi.org/10.1021/acs.nanolett.7b04976.

[44] Yadav M, Parle M, Sharma N, Dhingra S, Raina N, Jindal DK. Brain targeted oral delivery of doxycycline hydrochloride encapsulated tween 80 coated chitosan nanoparticles against ketamine induced psychosis: Behavioral, biochemical, neurochemical and histological alterations in mice. Drug Deliv 2017;24:1429–40. https://doi.org/10.1080/10717544.2017.1377315.

[45] Holmkvist AD, Friberg A, Nilsson UJ, Schouenborg J. Hydrophobic ion pairing of a minocycline/Ca2+/AOT complex for preparation of drug-loaded PLGA nanoparticles with improved sustained release. Int J Pharm 2016;499:351–7. https://doi.org/10.1016/j.ijpharm.2016.01.011.

[46] Jepsen K, Jepsen S. Antibiotics/antimicrobials: systemic and local administration in the therapy of mild to moderately advanced periodontitis. Periodontol 2000 2016;71:82–112. https://doi.org/10.1111/prd.12121.

[47] Baldwin H. Oral Antibiotic Treatment Options for Acne Vulgaris. J Clin Aesthet Dermatol 2020;13:26–32.

[48] Vargason AM, Anselmo AC, Mitragotri S. The evolution of commercial drug delivery technologies. Nat Biomed Eng 2021;5:951–67. https://doi.org/10.1038/s41551-021-00698-w.

[49] Trucillo P. Drug Carriers: Classification, Administration, Release Profiles, and Industrial Approach. Processes 2021;9:470. https://doi.org/10.3390/pr9030470.

[50] Yamawaki-Ogata A, Hashizume R, Satake M, Kaneko H, Mizutani S, Moritan T, et al. A doxycycline loaded, controlled-release, biodegradable fiber for the treatment of aortic aneurysms. Biomaterials 2010;31:9554–64. https://doi.org/10.1016/j.biomaterials.2010.08.069.

[51] Dhanalakshmi V, Nimal TR, Sabitha M, Biswas R, Jayakumar R. Skin and muscle permeating antibacterial nanoparticles for treating Staphylococcus aureus infected wounds. J Biomed Mater Res - Part B Appl Biomater 2016;104:797–807. https://doi.org/10.1002/jbm.b.33635.

[52] Pushpakom S, Iorio F, Eyers PA, Escott KJ, Hopper S, Wells A, et al. Drug repurposing: progress, challenges and recommendations. Nat Rev Drug Discov 2019;18:41–58. https://doi.org/10.1038/nrd.2018.168.

[53] Zheng K, Bortuzzo JA, Liu Y, Li W, Pischetsrieder M, Roether J, et al. Bio-templated bioactive glass particles with hierarchical macro–nano porous structure and drug delivery capability. Colloids Surfaces B Biointerfaces 2015;135:825–32. https://doi.org/10.1016/j.colsurfb.2015.03.038.

[54] Aydin O, Korkusuz F, Korkusuz P, Tezcaner A, Bilgic E, Yaprakci V, et al. In vitro and in vivo evaluation of doxycycline-chondroitin sulfate/PCLmicrospheres for intraarticular treatment of osteoarthritis. J Biomed Mater Res - Part B Appl Biomater 2015;103:1238–48. https://doi.org/10.1002/jbm.b.33303.

[55] Nagpal K, Singh SK, Mishra DN. Minocycline encapsulated chitosan nanoparticles for central antinociceptive activity. Int J Biol Macromol 2015;72:131–5. https://doi.org/10.1016/j.ijbiomac.2014.07.055.

[56] Nagpal K, Singh SK, Mishra D. Evaluation of safety and efficacy of brain targeted chitosan nanoparticles of minocycline. Int J Biol Macromol 2013;59:20–8. https://doi.org/10.1016/j.ijbiomac.2013.04.011.

[57] Bin S, Zhou N, Pan J, Pan F, Wu X-F, Zhou Z-H. Nano-carrier mediated co-

delivery of methyl prednisolone and minocycline for improved post-traumatic spinal cord injury conditions in rats. Drug Dev Ind Pharm 2017;43:1033–41. https://doi.org/10.1080/03639045.2017.1291669.

[58] Sivaraman B, Ramamurthi A. Multifunctional nanoparticles for doxycycline delivery towards localized elastic matrix stabilization and regenerative repair. Acta Biomater 2013;9:6511–25. https://doi.org/10.1016/j.actbio.2013.01.023.

[59] Teng SH, Lee EJ, Wang P, Jun SH, Han CM, Kim HE. Functionally gradient chitosan/hydroxyapatite composite scaffolds for controlled drug release. J Biomed Mater Res - Part B Appl Biomater 2009;90 B:275–82. https://doi.org/10.1002/jbm.b.31283.

[60] Saxena S, Ray AR, Kapil A, Pavon-Djavid G, Letourneur D, Gupta B, et al. Development of a New Polypropylene-Based Suture: Plasma Grafting, Surface Treatment, Characterization, and Biocompatibility Studies. Macromol Biosci 2011;11:373–82. https://doi.org/10.1002/mabi.201000298.

[61] Kita K, Dittrich C. Drug delivery vehicles with improved encapsulation efficiency: Taking advantage of specific drug-carrier interactions. Expert Opin Drug Deliv 2011;8:329–42. https://doi.org/10.1517/17425247.2011.553216.

[62] Martínez Rivas CJ, Tarhini M, Badri W, Miladi K, Greige-Gerges H, Nazari QA, et al. Nanoprecipitation process: From encapsulation to drug delivery. Int J Pharm 2017;532:66–81. https://doi.org/10.1016/j.ijpharm.2017.08.064.

[63] Kohane DS. Microparticles and nanoparticles for drug delivery. Biotechnol Bioeng 2007;96:203–9. https://doi.org/10.1002/bit.21301.

[64] Li Y, Kohane DS. Microparticles. Biomater. Sci. An Introd. to Mater. Med., 2020, p. 431–51. https://doi.org/10.1016/B978-0-12-816137-1.00030-1.

[65] Chen H, Xing X, Tan H, Jia Y, Zhou T, Chen Y, et al. Covalently antibacterial alginate-chitosan hydrogel dressing integrated gelatin microspheres containing tetracycline hydrochloride for wound healing. Mater Sci Eng C 2017;70:287–95. https://doi.org/10.1016/j.msec.2016.08.086.

[66] Ren B, Chen X, Du S, Ma Y, Chen H, Yuan G, et al. Injectable polysaccharide hydrogel embedded with hydroxyapatite and calcium carbonate for drug delivery and bone tissue engineering. Int J Biol Macromol 2018;118:1257–66.

https://doi.org/10.1016/j.ijbiomac.2018.06.200.

[67] Yin L, Zhong Z. Nanoparticles. Biomater. Sci., Elsevier; 2020, p. 453–83. https://doi.org/10.1016/B978-0-12-816137-1.00031-3.

[68] Haining WN, Anderson DG, Little SR, von Berwelt-Baildon MS, Cardoso AA, Alves P, et al. pH-Triggered Microparticles for Peptide Vaccination. J Immunol 2004;173:2578–85. https://doi.org/10.4049/jimmunol.173.4.2578.

[69] Kim H, Cho M, Sah H. Development of new reverse micellar microencapsulation technique to load water-soluble drug into PLGA microspheres. Arch Pharm Res 2005;28:370–5. https://doi.org/10.1007/BF02977807.

[70] Fundueanu G, Constantin M, Esposito E, Cortesi R, Nastruzzi C, Menegatti E. Cellulose acetate butyrate microcapsules containing dextran ion-exchange resins as self-propelled drug release system. Biomaterials 2005;26:4337–47. https://doi.org/10.1016/j.biomaterials.2004.10.036.

[71] M. Gillissen, R. Steendam, A. van der Laan ET. Development of doxycycline-eluting delivery systems based on SynBiosys^{TM} biodegradable multi-block copolymers. J Control Release 2006;116:90–2. https://doi.org/10.1016/j.jconrel.2006.09.065.

[72] Caroni ALPF, de Lima CRM, Pereira MR, Fonseca JLC. The kinetics of adsorption of tetracycline on chitosan particles. J Colloid Interface Sci 2009;340:182–91. https://doi.org/10.1016/j.jcis.2009.08.016.

[73] Chen Q, Liu XX, Wang D, Zheng J, Chen L, Xie Q, et al. Periodontal Inflammation-Triggered by Periodontal Ligament Stem Cell Pyroptosis Exacerbates Periodontitis. Front Cell Dev Biol 2021;9. https://doi.org/10.3389/fcell.2021.663037.

[74] Torshabi M, Nojehdehian H, Tabatabaei FS. In vitro behavior of poly-lactic-co-glycolic acid microspheres containing minocycline, metronidazole, and ciprofloxacin. J Investig Clin Dent 2017;8:1–8. https://doi.org/10.1111/jicd.12201.

[75] Van Dyke TE, Offenbacher S, Braswell L, Lessem J. Enhancing the value of scaling and root-planing: Arestin clinical trial results. J Int Acad Periodontol 2002;4:72–6.

[76] Wang J, Helder L, Shao J, Jansen JA, Yang M, Yang F. Encapsulation and release of doxycycline from electrospray-generated PLGA microspheres: Effect of polymer end groups. Int J Pharm 2019;564:1–9. https://doi.org/10.1016/j.ijpharm.2019.04.023.

[77] Mundargi RC, Srirangarajan S, Agnihotri SA, Patil SA, Ravindra S, Setty SB, et al. Development and evaluation of novel biodegradable microspheres based on poly(d,l-lactide-co-glycolide) and poly(ε-caprolactone) for controlled delivery of doxycycline in the treatment of human periodontal pocket: In vitro and in vivo studies. J Control Release 2007;119:59–68. https://doi.org/10.1016/j.jconrel.2007.01.008.

[78] Srirangarajan S, Mundargi RC, Ravindra S, Setty SB, Aminabhavi TM, Thakur S. Randomized, Controlled, Single-Masked, Clinical Study to Compare and Evaluate the Efficacy of Microspheres and Gel in Periodontal Pocket Therapy. J Periodontol 2011;82:114–21. https://doi.org/10.1902/jop.2010.100324.

[79] Liu DZ, Chen WP, Lee CP, Wu SL, Wang YC, Chung TW. Effects of alginate coated on PLGA microspheres for delivery tetracycline hydrochloride to periodontal pockets. J Microencapsul 2004;21:643–52. https://doi.org/10.1080/02652040400000512.

[80] Gjoseva S, Geskovski N, Sazdovska SD, Popeski-Dimovski R, Petruševski G, Mladenovska K, et al. Design and biological response of doxycycline loaded chitosan microparticles for periodontal disease treatment. Carbohydr Polym 2018;186:260–72. https://doi.org/10.1016/j.carbpol.2018.01.043.

[81] Victor SP, Kumar TSS. BCP ceramic microspheres as drug delivery carriers: Synthesis, characterisation and doxycycline release. J Mater Sci Mater Med 2008;19:283–90. https://doi.org/10.1007/s10856-006-0044-7.

[82] Donato L, Nasser II, Majdoub M, Drioli E. Green Chemistry and Molecularly Imprinted Membranes. Membranes (Basel) 2022;12:472. https://doi.org/10.3390/membranes12050472.

[83] Govender S, Lutchman D, Pillay V, Chetty DJ, Govender T. Enhancing drug incorporation into tetracycline-loaded chitosan microspheres for periodontal therapy. J Microencapsul 2006;23:750–61. https://doi.org/10.1080/02652040600789229.

[84] Yadav SK, Khan G, Bonde GV, Bansal M, Mishra B. Design, optimization and characterizations of chitosan fortified calcium alginate microspheres for the controlled delivery of dual drugs. Artif Cells, Nanomedicine Biotechnol 2018;46:1180–93. https://doi.org/10.1080/21691401.2017.1366331.

[85] Chiappe VB, Gomez M V, Rodriguez C, Fresolone M, Romanelli HJ. Subgingivally applied minocycline microgranules in subjects with chronic periodontitis: A randomized clinical and microbiological trial. Acta Odontol Latinoam 2015;28:122–31. https://doi.org/10.1590/S1852-48342015000200005.

[86] Rao SK, Setty S, Acharya AB, Thakur SL. Efficacy of locally-delivered doxycycline microspheres in chronic localized periodontitis and on Porphyromonas gingivalis. J Investig Clin Dent 2012;3:128–34. https://doi.org/10.1111/j.2041-1626.2011.00110.x.

[87] Song C, Huang D, Zhao C, Zhao Y. Abalone-Inspired Adhesive and Photo-Responsive Microparticle Delivery Systems for Periodontal Drug Therapy. Adv Sci 2022;9:1–9. https://doi.org/10.1002/advs.202202829.

[88] Murugan R, Ramakrishna S. Coupling of therapeutic molecules onto surface modified coralline hydroxyapatite. Biomaterials 2004;25:3073–80. https://doi.org/10.1016/j.biomaterials.2003.09.089.

[89] Calasans-Maia MD, Barboza CAB, Soriano-Souza CA, Novellino Alves ATN, De Pinheiro Uzeda MJ, Martinez-Zelaya VR, et al. Microspheres of alginate encapsulated minocycline-loaded nanocrystalline carbonated hydroxyapatite: Therapeutic potential and effects on bone regeneration. Int J Nanomedicine 2019;14:4559–71. https://doi.org/10.2147/IJN.S201631.

[90] Soriano-Souza C, Valiense H, Mavropoulos E, Martinez-Zelaya V, Costa AM, Alves AT, et al. Doxycycline containing hydroxyapatite ceramic microspheres as a bone-targeting drug delivery system. J Biomed Mater Res - Part B Appl Biomater 2020;108:1351–62. https://doi.org/10.1002/jbm.b.34484.

[91] Cruz MCP, Ravagnani SP, Brogna FMS, Campana SP, Triviño GC, Lisboa ACL, et al. Evaluation of the diffusion coefficient for controlled release of oxytetracycline from alginate/chitosan/poly(ethylene glycol) microbeads in simulated gastrointestinal environments. Biotechnol Appl Biochem 2004;40:243. https://doi.org/10.1042/ba20030216.

[92] Hejazi R, Amiji M. Stomach-specific anti-H. pylori therapy. I: Preparation and characterization of tetracyline-loaded chitosan microspheres. Int J Pharm 2002;235:87–94. https://doi.org/10.1016/S0378-5173(01)00985-1.

[93] Hejazi R, Amiji M. Stomach-specific anti-H. pylori Therapy. II. Gastric residence studies of tetracycline-loaded chitosan microspheres in gerbils. Pharm Dev Technol 2003;8:253–62. https://doi.org/10.1081/PDT-120022154.

[94] Hejazi R, Amiji M. Stomach-specific anti-H. pylori therapy. Part III: Effect of chitosan microspheres crosslinking on the gastric residence and local tetracycline concentrations in fasted gerbils. Int J Pharm 2004;272:99–108. https://doi.org/10.1016/j.ijpharm.2003.12.001.

[95] Moura LA, Ribeiro FV, Aiello TB, Duek EADR, Sallum EA, Nociti FH, et al. Characterization of the release profile of doxycycline by PLGA microspheres adjunct to non-surgical periodontal therapy. J Biomater Sci Polym Ed 2015;26:573–84. https://doi.org/10.1080/09205063.2015.1045249.

[96] Zhao J, Wei Y, Xiong J, Liu H, Lv G, Zhao J, et al. Antibacterial-Anti-Inflammatory-Bone Restoration Procedure Achieved by MIN-Loaded PLGA Microsphere for Efficient Treatment of Periodontitis. AAPS PharmSciTech 2023;24:74. https://doi.org/10.1208/s12249-023-02538-3.

[97] Fwu-Long M, Wong TB, Shyu SS. Sustained-release of oxytetracycline from chitosan microspheres prepared by interfacial acylation and spray hardening methods. J Microencapsul 1997;14:577–91. https://doi.org/10.3109/02652049709006811.

[98] Patel RS, Cho DY, Tian C, Chang A, Estrellas KM, Lavin D, et al. Doxycycline delivery from PLGA microspheres prepared by a modified solvent removal method. J Microencapsul 2012;29:344–52. https://doi.org/10.3109/02652048.2011.651499.

[99] Sousa FFO, Luzardo-Álvarez A, Blanco-Méndez J, Martín-Pastor M. NMR techniques in drug delivery: Application to zein protein complexes. Int J Pharm 2012;439:41–8. https://doi.org/10.1016/j.ijpharm.2012.09.046.

[100] Bittner B, Mäder K, Kroll C, Borchert HH, Kissel T. Tetracycline-HCl-loaded poly(DL-lactide-co-glycolide) microspheres prepared by a spray drying technique: Influence of γ-irradiation on radical formation and polymer

degradation. J Control Release 1999;59:23–32. https://doi.org/10.1016/S0168-3659(98)00170-9.

[101] Garg S, Thakur S, Gupta A, Kaur G, Pandey OP. Antibacterial and anticancerous drug loading kinetics for (10-x)CuO-xZnO-20CaO-60SiO2-10P2O5 ($2 \leq x \leq 8$) mesoporous bioactive glasses. J Mater Sci Mater Med 2017;28. https://doi.org/10.1007/s10856-016-5827-x.

[102] Trofin MA, Racovita S, Vasiliu S, Vasiliu AL, Mihai M. Porous Crosslinked Zwitterionic Microparticles Based on Glycidyl Methacrylate and N-Vinylimidazole as Possible Drug Delivery Systems. Int J Mol Sci 2022;23. https://doi.org/10.3390/ijms232314999.

[103] Hoang NH, Le Thanh T, Sangpueak R, Treekoon J, Saengchan C, Thepbandit W, et al. Chitosan Nanoparticles-Based Ionic Gelation Method: A Promising Candidate for Plant Disease Management. Polymers (Basel) 2022;14:662. https://doi.org/10.3390/polym14040662.

[104] Clogston JD, Hackley VA, Prina-Mello A, Puri S, Sonzini S, Soo PL. Sizing up the Next Generation of Nanomedicines. Pharm Res 2020;37:6. https://doi.org/10.1007/s11095-019-2736-y.

[105] Nagpal K, Singh SK, Mishra DN. Formulation, optimization, in vivo pharmacokinetic, behavioral and biochemical estimations of minocycline loaded chitosan nanoparticles for enhanced brain uptake. Chem Pharm Bull (Tokyo) 2013;61:258–72. https://doi.org/10.1248/cpb.c12-00732.

[106] Iacob AT, Lupascu FG, Apotrosoaei M, Vasincu IM, Tauser RG, Lupascu D, et al. Recent biomedical approaches for chitosan based materials as drug delivery nanocarriers. Pharmaceutics 2021;13:1–36. https://doi.org/10.3390/pharmaceutics13040587.

[107] Singh Y, Srinivas A, Gangwar M, Meher JG, Misra-Bhattacharya S, Chourasia MK. Subcutaneously Administered Ultrafine PLGA Nanoparticles Containing Doxycycline Hydrochloride Target Lymphatic Filarial Parasites. Mol Pharm 2016;13:2084–94. https://doi.org/10.1021/acs.molpharmaceut.6b00206.

[108] Tiwari SK, Agarwal S, Seth B, Yadav A, Nair S, Bhatnagar P, et al. Curcumin-Loaded Nanoparticles Potently Induce Adult Neurogenesis and Reverse Cognitive Deficits in Alzheimer's Disease Model via Canonical Wnt/β-Catenin

Pathway. ACS Nano 2014;8:76–103. https://doi.org/10.1021/nn405077y.

[109] Sousa De Almeida M, Susnik E, Drasler B, Taladriz-Blanco P, Petri-Fink A, Rothen-Rutishauser B. Understanding nanoparticle endocytosis to improve targeting strategies in nanomedicine. Chem Soc Rev 2021;50:5397–434. https://doi.org/10.1039/d0cs01127d.

[110] Martin V, Ribeiro IAC, Alves MM, Gonçalves L, Almeida AJ, Grenho L, et al. Understanding intracellular trafficking and anti-inflammatory effects of minocycline chitosan-nanoparticles in human gingival fibroblasts for periodontal disease treatment. Int J Pharm 2019;572:118821. https://doi.org/10.1016/j.ijpharm.2019.118821.

[111] Eskitoros-Togay M, Bulbul YE, Tort S, Demirtaş Korkmaz F, Acartürk F, Dilsiz N. Fabrication of doxycycline-loaded electrospun PCL/PEO membranes for a potential drug delivery system. Int J Pharm 2019;565:83–94. https://doi.org/10.1016/j.ijpharm.2019.04.073.

[112] Zhang Z, Wang Z, Nong J, Nix CA, Ji H-F, Zhong Y. Metal ion-assisted self-assembly of complexes for controlled and sustained release of minocycline for biomedical applications. Biofabrication 2015;7:015006. https://doi.org/10.1088/1758-5090/7/1/015006.

[113] Baranov M V., Kumar M, Sacanna S, Thutupalli S, van den Bogaart G. Modulation of Immune Responses by Particle Size and Shape. Front Immunol 2021;11:1–23. https://doi.org/10.3389/fimmu.2020.607945.

[114] Papa S, Caron I, Erba E, Panini N, De Paola M, Mariani A, et al. Early modulation of pro-inflammatory microglia by minocycline loaded nanoparticles confers long lasting protection after spinal cord injury. Biomaterials 2016;75:13–24. https://doi.org/10.1016/j.biomaterials.2015.10.015.

[115] Papa S, Rossi F, Ferrari R, Mariani A, De Paola M, Caron I, et al. Selective nanovector mediated treatment of activated proinflammatory microglia/macrophages in spinal cord injury. ACS Nano 2013;7:9881–95. https://doi.org/10.1021/nn4036014.

[116] Barza M, Brown RB, Shanks C, Gamble C, Weinstein L. Relation Between Lipophilicity and Pharmacological Behavior of Minocycline, Doxycycline, Tetracycline, and Oxytetracycline in Dogs. Antimicrob Agents Chemother

1975;8:713–20. https://doi.org/10.1128/AAC.8.6.713.

[117] Kim TH, Raiz A, Unni AD, Murhekar S, Donose BC, Floetenmeyer M, et al. Combating Antibiotic-Resistant Gram-Negative Bacteria Strains with Tetracycline-Conjugated Carbon Nanoparticles. Adv Biosyst 2020;4:1–9. https://doi.org/10.1002/adbi.202000074.

[118] Naimi-Shamel N, Pourali P, Dolatabadi S. Green synthesis of gold nanoparticles using Fusarium oxysporum and antibacterial activity of its tetracycline conjugant. J Mycol Med 2019;29:7–13. https://doi.org/10.1016/j.mycmed.2019.01.005.

[119] Deng H, McShan D, Zhang Y, Sinha SS, Arslan Z, Ray PC, et al. Mechanistic Study of the Synergistic Antibacterial Activity of Combined Silver Nanoparticles and Common Antibiotics. Environ Sci Technol 2016;50:8840–8. https://doi.org/10.1021/acs.est.6b00998.

[120] Das S, Vishakha K, Banerjee S, Nag D, Ganguli A. Tetracycline-loaded magnesium oxide nanoparticles with a potential bactericidal action against multidrug-resistant bacteria: In vitro and in vivo evidence. Colloids Surfaces B Biointerfaces 2022;217:112688. https://doi.org/10.1016/j.colsurfb.2022.112688.

[121] Giammarco J, Mochalin VN, Haeckel J, Gogotsi Y. The adsorption of tetracycline and vancomycin onto nanodiamond with controlled release. J Colloid Interface Sci 2016;468:253–61. https://doi.org/10.1016/j.jcis.2016.01.062.

[122] Zelmer AR, Nelson R, Richter K, Atkins GJ. Can intracellular Staphylococcus aureus in osteomyelitis be treated using current antibiotics? A systematic review and narrative synthesis. Bone Res 2022;10:1–18. https://doi.org/10.1038/s41413-022-00227-8.

[123] Alder KD, Lee I, Munger AM, Kwon HK, Morris MT, Cahill S V., et al. Intracellular Staphylococcus aureus in bone and joint infections: A mechanism of disease recurrence, inflammation, and bone and cartilage destruction. Bone 2020;141:115568. https://doi.org/10.1016/j.bone.2020.115568.

[124] Irshad M, Van Der Reijden WA, Crielaard W, Laine ML. In vitro invasion and survival of Porphyromonas gingivalis in gingival fibroblasts; Role of the capsule. Arch Immunol Ther Exp (Warsz) 2012;60:469–76. https://doi.org/10.1007/s00005-012-0196-8.

[125] Liang X, Tian H, Luo H, Wang H, Chang J. Novel quaternized chitosan and polymeric micelles with cross-linked ionic cores for prolonged release of minocycline. J Biomater Sci Polym Ed 2009;20:115–31. https://doi.org/10.1163/156856208X393536.

[126] Lee BS, Lee CC, Wang YP, Chen HJ, Lai CH, Hsieh WL, et al. Controlled-release of tetracycline and lovastatin by poly(D,L-lactide-co-glycolide acid)-chitosan nanoparticles enhances periodontal regeneration in dogs. Int J Nanomedicine 2016;11:285–97. https://doi.org/10.2147/IJN.S94270.

[127] Yao W, Xu P, Zhao J, Ling L, Li X, Zhang B, et al. RGD functionalized polymeric nanoparticles targeting periodontitis epithelial cells for the enhanced treatment of periodontitis in dogs. J Colloid Interface Sci 2015;458:14–21. https://doi.org/10.1016/j.jcis.2015.07.032.

[128] Wang H, Liu J, Tao S, Chai G, Wang J, Hu FQ, et al. Tetracycline-grafted PLGA nanoparticles as bone-targeting drug delivery system. Int J Nanomedicine 2015;10:5671–85. https://doi.org/10.2147/IJN.S88798.

[129] Lecio G, Ribeiro FV, Pimentel SP, Reis AA, da Silva RVC, Nociti-Jr F, et al. Novel 20% doxycycline-loaded PLGA nanospheres as adjunctive therapy in chronic periodontitis in type-2 diabetics: randomized clinical, immune and microbiological trial. Clin Oral Investig 2020;24:1269–79. https://doi.org/10.1007/s00784-019-03005-9.

[130] Yao W, Xu P, Pang Z, Zhao J, Chai Z, Li X, et al. Local delivery of minocycline-loaded PEG-PLA nanoparticles for the enhanced treatment of periodontitis in dogs. Int J Nanomedicine 2014;9:3963–70. https://doi.org/10.2147/IJN.S67521.

[131] Dinarvand R, Jafarzadeh Kashi T, Eskandarion, Esfandyari-Manesh, Samadi, Atyabi F, et al. Improved drug loading and antibacterial activity of minocycline-loaded PLGA nanoparticles prepared by solid/oil/water ion pairing method. Int J Nanomedicine 2012;7:221. https://doi.org/10.2147/IJN.S27709.

[132] Ignjatović NL, Ninkov P, Sabetrasekh R, Lyngstadaas SP, Uskoković DP. In vitro evaluation of a multifunctional nano drug delivery system based on tigecycline-loaded calcium-phosphate/ poly-DL-lactide-co-glycolide. Biomed Mater Eng 2014;24:1647–58. https://doi.org/10.3233/BME-140978.

[133] Sindhura Reddy N, Sowmya S, Bumgardner JD, Chennazhi KP, Biswas R,

Jayakumar R. Tetracycline nanoparticles loaded calcium sulfate composite beads for periodontal management. Biochim Biophys Acta - Gen Subj 2014;1840:2080–90. https://doi.org/10.1016/j.bbagen.2014.02.007.

[134] Madhumathi K, Rubaiya Y, Doble M, Venkateswari R, Sampath Kumar TS. Antibacterial, anti-inflammatory, and bone-regenerative dual-drug-loaded calcium phosphate nanocarriers—in vitro and in vivo studies. Drug Deliv Transl Res 2018;8:1066–77. https://doi.org/10.1007/s13346-018-0532-6.

[135] Chakrapani Venkatesan Y, Sampath Kumar TS, Raj DK, Kumary T V. Osteogenic apatite particles by sol–gel assisted electrospraying. J Biomed Mater Res - Part B Appl Biomater 2018;106:1941–54. https://doi.org/10.1002/jbm.b.34013.

[136] Madhumathi K, Sampath Kumar TS. Regenerative potential and anti-bacterial activity of tetracycline loaded apatitic nanocarriers for the treatment of periodontitis. Biomed Mater 2014;9. https://doi.org/10.1088/1748-6041/9/3/035002.

[137] Zhu H, Wen Q, Bhangu SK, Ashokkumar M, Cavalieri F. Sonosynthesis of nanobiotics with antimicrobial and antioxidant properties. Ultrason Sonochem 2022;86:106029. https://doi.org/10.1016/j.ultsonch.2022.106029.

[138] Tong F, Wang P, Chen Z, Liu Y, Wang L, Guo J, et al. Combined Ferromagnetic Nanoparticles for Effective Periodontal Biofilm Eradication in Rat Model. Int J Nanomedicine 2023;18:2371–88. https://doi.org/10.2147/IJN.S402410.

[139] Marycz K, Pazik R, Zawisza K, Wiglusz K, Maredziak M, Sobierajska P, et al. Multifunctional nanocrystalline calcium phosphates loaded with Tetracycline antibiotic combined with human adipose derived mesenchymal stromal stem cells (hASCs). Mater Sci Eng C 2016;69:17–26. https://doi.org/10.1016/j.msec.2016.06.051.

[140] Cazalbou S, Bertrand G, Drouet C. Tetracycline-loaded biomimetic apatite: An adsorption study. J Phys Chem B 2015;119:3014–24. https://doi.org/10.1021/jp5116756.

[141] Domingues ZR, Cortés ME, Gomes TA, Diniz HF, Freitas CS, Gomes JB, et al. Bioactive glass as a drug delivery system of tetracycline and tetracycline associated with β-cyclodextrin. Biomaterials 2004;25:327–33.

https://doi.org/10.1016/S0142-9612(03)00524-6.

[142] Lee JH, El-Fiqi A, Mandakhbayar N, Lee HH, Kim HW. Drug/ion co-delivery multi-functional nanocarrier to regenerate infected tissue defect. Biomaterials 2017;142:62–76. https://doi.org/10.1016/j.biomaterials.2017.07.014.

[143] Ignjatović NL, Ninkov P, Sabetrasekh R, Uskoković DP. A novel nano drug delivery system based on tigecycline-loaded calciumphosphate coated with poly-DL-lactide-co-glycolide. J Mater Sci Mater Med 2010;21:231–9. https://doi.org/10.1007/s10856-009-3854-6.

[144] Tham AY, Gandhimathi C, Praveena J, Venugopal JR, Ramakrishna S, Kumar SD. Minocycline Loaded Hybrid Composites Nanoparticles for Mesenchymal Stem Cells Differentiation into Osteogenesis. Int J Mol Sci 2016;17:1–16. https://doi.org/10.3390/ijms17081222.

[145] Lin F, Liu Y, Luo W, Liu S, Wang Y, Gu R, et al. Minocycline-Loaded Poly(α-Lipoic Acid)– Methylprednisolone Prodrug Nanoparticles for the Combined Anti-Inflammatory Treatment of Spinal Cord Injury. Int J Nanomedicine 2022;17:91–104. https://doi.org/10.2147/IJN.S344491.

[146] Marto J, Lf G, Lm G, Hm R, Aj A. Design of minocycline-containing starch nanocapsules for topical delivery. J Microencapsul 2018;0:000. https://doi.org/10.1080/02652048.2018.1487472.

[147] Cover NF, Lai-Yuen S, Parsons AK, Kumar A. Synergetic effects of doxycycline-loaded chitosan nanoparticles for improving drug delivery and efficacy. Int J Nanomedicine 2012;7:2411–9. https://doi.org/10.2147/IJN.S27328.

[148] Wang X, Xu X, Zhang S, Chen N, Sun Y, Ma K, et al. TPGS-based and S-thanatin functionalized nanorods for overcoming drug resistance in Klebsiella pneumonia. Nat Commun 2022;13. https://doi.org/10.1038/s41467-022-31500-3.

[149] Ye Z, Wang S, Xu Y, Zhang J, Yan W. Enhanced Inhibition of Drug-Resistant Escherichia coli by Tetracycline Hydrochloride-Loaded Multipore Mesoporous Silica Nanoparticles. Molecules 2022;27. https://doi.org/10.3390/molecules27041218.

[150] Alavi M, Karimi N. Antibacterial, hemoglobin/albumin-interaction, and

molecular docking properties of phytogenic AgNPs functionalized by three antibiotics of penicillin, amoxicillin, and tetracycline. Microb Pathog 2022;164:105427. https://doi.org/10.1016/j.micpath.2022.105427.

[151] Taghizadeh MT, Ashassi-Sorkhabi H, Afkari R, Kazempour A. Cross-linked chitosan in nano and bead scales as drug carriers for betamethasone and tetracycline. Int J Biol Macromol 2019;131:581–8. https://doi.org/10.1016/j.ijbiomac.2019.03.094.

[152] Zhang H, Yan D, Korale Gedara SM, Dingiri Marakkalage SSF, Kasun Methlal JG, Han Y, et al. Effects of crystallinity and surface modification of calcium phosphate nanoparticles on the loading and release of tetracycline hydro-chloride. IOP Conf Ser Mater Sci Eng 2017;182:012052. https://doi.org/10.1088/1757-899X/182/1/012052.

[153] de Lima CRM, Gomes DN, de Morais Filho JR, Pereira MR, Fonseca JLC. Anionic and cationic drug sorption on interpolyelectrolyte complexes. Colloids Surfaces B Biointerfaces 2018;170:210–8. https://doi.org/10.1016/j.colsurfb.2018.05.071.

[154] Wu S, Jiang W, Zhang X, Sun H, Zhang W, Dai J, et al. A sonochemical route for the encapsulation of drug in magnetic microspheres. J Magn Magn Mater 2012;324:124–7. https://doi.org/10.1016/j.jmmm.2011.07.038.

[155] Dougherty JA, Sucher AJ, Chahine EB, Shihadeh KC. Omadacycline: A New Tetracycline Antibiotic. Ann Pharmacother 2019;53:486–500. https://doi.org/10.1177/1060028018818094.

[156] Rusu A, Buta EL. The Development of Third-Generation Tetracycline Antibiotics and New Perspectives. Pharmaceutics 2021;13:2085. https://doi.org/10.3390/pharmaceutics13122085.

[157] Vlachopoulos A, Karlioti G, Balla E, Daniilidis V, Kalamas T, Stefanidou M, et al. Poly(Lactic Acid)-Based Microparticles for Drug Delivery Applications: An Overview of Recent Advances. Pharmaceutics 2022;14:1–37. https://doi.org/10.3390/pharmaceutics14020359.

[158] Lagreca E, Onesto V, Di Natale C, La Manna S, Netti PA, Vecchione R. Recent advances in the formulation of PLGA microparticles for controlled drug delivery. Prog Biomater 2020;9:153–74. https://doi.org/10.1007/s40204-020-00139-y.

[159] El-Alfy EA, El-Bisi MK, Taha GM, Ibrahim HM. Preparation of biocompatible chitosan nanoparticles loaded by tetracycline, gentamycin and ciprofloxacin as novel drug delivery system for improvement the antibacterial properties of cellulose based fabrics. Int J Biol Macromol 2020;161:1247–60. https://doi.org/10.1016/j.ijbiomac.2020.06.118.

[160] Rahmat D, Müller C, Barthelmes J, Shahnaz G, Martien R, Bernkop-Schnürch A. Thiolated hydroxyethyl cellulose: Design and in vitro evaluation of mucoadhesive and permeation enhancing nanoparticles. Eur J Pharm Biopharm 2013;83:149–55. https://doi.org/10.1016/j.ejpb.2012.10.008.

[161] Sahatsapan N, Ngawhirunpat T, Rojanarata T, Opanasopit P, Patrojanasophon P. Catechol-Functionalized Alginate Nanoparticles as Mucoadhesive Carriers for Intravesical Chemotherapy. AAPS PharmSciTech 2020;21:212. https://doi.org/10.1208/s12249-020-01752-7.

[162] Caswell AH, Hutchison JD. Selectivity of cation chelation to tetracyclines: Evidence for special conformation of calcium chelate. Biochem Biophys Res Commun 1971;43:625–30. https://doi.org/10.1016/0006-291X(71)90660-7.

[163] Tamimi F, Torres J, Bettini R, Ruggera F, Rueda C, López-Ponce M, et al. Doxycycline sustained release from brushite cements for the treatment of periodontal diseases. J Biomed Mater Res - Part A 2008;85:707–14. https://doi.org/10.1002/jbm.a.31610.

[164] Yang G, Phua SZF, Bindra AK, Zhao Y. Degradability and Clearance of Inorganic Nanoparticles for Biomedical Applications. Adv Mater 2019;31:1–23. https://doi.org/10.1002/adma.201805730.

[165] Mitchell MJ, Billingsley MM, Haley RM, Wechsler ME, Peppas NA, Langer R. Engineering precision nanoparticles for drug delivery. Nat Rev Drug Discov 2021;20:101–24. https://doi.org/10.1038/s41573-020-0090-8.

[166] Jiao M, Zhang P, Meng J, Li Y, Liu C, Luo X, et al. Recent advancements in biocompatible inorganic nanoparticles towards biomedical applications. Biomater Sci 2018;6:726–45. https://doi.org/10.1039/c7bm01020f.

[167] Khan ST, Al-Khedhairy AA. Metals and Metal Oxides: Important Nanomaterials With Antimicrobial Activity. Antimicrob. Nanoarchitectonics, Elsevier; 2017, p. 195–222. https://doi.org/10.1016/B978-0-323-52733-0.00008-2.

[168] Abdul Latip AF, Hussein MZ, Stanslas J, Wong CC, Adnan R. Release behavior and toxicity profiles towards A549 cell lines of ciprofloxacin from its layered zinc hydroxide intercalation compound. Chem Cent J 2013;7:1. https://doi.org/10.1186/1752-153X-7-119.

[169] Hu T, Gu Z, Williams GR, Strimaite M, Zha J, Zhou Z, et al. Layered double hydroxide-based nanomaterials for biomedical applications. Chem Soc Rev 2022;51:6126–76. https://doi.org/10.1039/d2cs00236a.

[170] Adewoyin M, Mohsin SMN, Arulselvan P, Hussein MZ, Fakurazi S. Enhanced anti-inflammatory potential of cinnamate-zinc layered hydroxide in lipopolysaccharide-stimulated RAW 264.7 macrophages. Drug Des Devel Ther 2015;9:2475–84. https://doi.org/10.2147/DDDT.S72716.

[171] Nabipour H, Hu Y. Layered zinc hydroxide as vehicle for drug delivery systems: a critical review. J Porous Mater 2022;29:341–56. https://doi.org/10.1007/s10934-021-01171-4.

[172] Khadiran NF, Hussein MZ, Ahmad R, Khadiran T, Zainal Z, Kadir WRWA, et al. Preparation and properties of zinc layered hydroxide with nitrate and phosphate as the counter anion, a novel control release fertilizer formulation. J Porous Mater 2021;28:1797–811. https://doi.org/10.1007/s10934-021-01122-z.

[173] Saha S, Ray S, Acharya R, Chatterjee TK, Chakraborty J. Magnesium, zinc and calcium aluminium layered double hydroxide-drug nanohybrids: A comprehensive study. Appl Clay Sci 2017;135:493–509. https://doi.org/10.1016/j.clay.2016.09.030.

[174] Arizaga GGC, Satyanarayana KG, Wypych F. Layered hydroxide salts: Synthesis, properties and potential applications. Solid State Ionics 2007;178:1143–62. https://doi.org/10.1016/j.ssi.2007.04.016.

[175] Arizaga GGC, Jiménez CS, Viruete A, Arratia-Quijada J. Functionalization of Surfaces in Layered Double Hydroxides and Hydroxide Salt Nanoparticles. Funct. Nanomater., InTech; 2016. https://doi.org/10.5772/66002.

[176] Nakagaki S, Machado GS, Stival JF, Henrique dos Santos E, Silva GM, Wypych F. Natural and synthetic layered hydroxide salts (LHS): Recent advances and application perspectives emphasizing catalysis. Prog Solid State Chem 2021;64. https://doi.org/10.1016/j.progsolidstchem.2021.100335.

[177] Kong L, Heydari Z, Lami GH, Saberi A, Baltatu MS, Vizureanu P. A Comprehensive Review of the Current Research Status of Biodegradable Zinc Alloys and Composites for Biomedical Applications. Materials (Basel) 2023;16:4797. https://doi.org/10.3390/ma16134797.

[178] Huat TJ, Camats-Perna J, Newcombe EA, Valmas N, Kitazawa M, Medeiros R. Metal Toxicity Links to Alzheimer's Disease and Neuroinflammation. J Mol Biol 2019;431:1843–68. https://doi.org/10.1016/j.jmb.2019.01.018.

[179] Al Alawi AM, Majoni SW, Falhammar H. Magnesium and Human Health: Perspectives and Research Directions. Int J Endocrinol 2018;2018:1–17. https://doi.org/10.1155/2018/9041694.

[180] Prasad AS. Zinc: An antioxidant and anti-inflammatory agent: Role of zinc in degenerative disorders of aging. J Trace Elem Med Biol 2014;28:364–71. https://doi.org/10.1016/j.jtemb.2014.07.019.

[181] Balcomb B, Singh M, Singh S. Synthesis and Characterization of Layered Double Hydroxides and Their Potential as Nonviral Gene Delivery Vehicles. ChemistryOpen 2015;4:137–45. https://doi.org/10.1002/open.201402074.

[182] Saifullah B, Hussein MZ, Hussein-Al-Ali SH, Arulselvan P, Fakurazi S. Sustained release formulation of an anti-tuberculosis drug based on para-amino salicylic acid-zinc layered hydroxide nanocomposite. Chem Cent J 2013;7:72. https://doi.org/10.1186/1752-153X-7-72.

[183] El-Ela FIA, Farghali AA, Mahmoud RK, Mohamed NA, Moaty SAA. New Approach in Ulcer Prevention and Wound Healing Treatment using Doxycycline and Amoxicillin/LDH Nanocomposites. Sci Rep 2019;9:6418. https://doi.org/10.1038/s41598-019-42842-2.

[184] Hesse D, Badar M, Bleich A, Smoczek A, Glage S, Kieke M, et al. Layered double hydroxides as efficient drug delivery system of ciprofloxacin in the middle ear: an animal study in rabbits. J Mater Sci Mater Med 2013;24:129–36. https://doi.org/10.1007/s10856-012-4769-1.

[185] Saifullah B, Arulselvan P, El Zowalaty ME, Fakurazi S, Webster TJ, Geilich B, et al. Development of a highly biocompatible antituberculosis nanodelivery formulation based on para-aminosalicylic acid - Zinc layered hydroxide nanocomposites. Sci World J 2014;2014. https://doi.org/10.1155/2014/401460.

[186] Wu S, Liang H, Xu B, Zhang Q, Fan H, Wang J, et al. A co-precipitation route for the preparation of eco-friendly Cu-Al-layered double hydroxides with efficient tetracycline degradation. Environ Sci Pollut Res 2023. https://doi.org/10.1007/s11356-023-29345-4.

[187] Yu Y, Chen D, Xu W, Fang J, Sun J, Liu Z, et al. Synergistic adsorption-photocatalytic degradation of different antibiotics in seawater by a porous g-C3N4/calcined-LDH and its application in synthetic mariculture wastewater. J Hazard Mater 2021;416:126183. https://doi.org/10.1016/j.jhazmat.2021.126183.

[188] El-Shahawy AAG, Abo El-Ela FI, Mohamed NA, Eldine ZE, El Rouby WMA. Synthesis and evaluation of layered double hydroxide/doxycycline and cobalt ferrite/chitosan nanohybrid efficacy on gram positive and gram negative bacteria. Mater Sci Eng C 2018;91:361–71. https://doi.org/10.1016/j.msec.2018.05.042.

[189] Weinberg MA, Bral M. Tetracycline and its analogues: A therapeutic paradigm in periodontal diseases. Crit Rev Oral Biol Med 1998;9:322–32. https://doi.org/10.1177/10454411980090030501.

[190] Gomes PS, Fernandes MH. Effect of therapeutic levels of doxycycline and minocycline in the proliferation and differentiation of human bone marrow osteoblastic cells. Arch Oral Biol 2007;52:251–9. https://doi.org/10.1016/j.archoralbio.2006.10.005.

[191] Muthukuru M, Sun J. Doxycycline counteracts bone morphogenic protein 2-induced osteogenic mediators. J Periodontol 2013;84:656–65. https://doi.org/10.1902/jop.2012.120338.

[192] Park J-B. Effects of Doxycycline, Minocycline, and Tetracycline on Cell Proliferation, Differentiation, and Protein Expression in Osteoprecursor Cells. J Craniofac Surg 2011;22:1839–42. https://doi.org/10.1097/SCS.0b013e31822e8216.

[193] Suzuki A, Yagisawa J, Kumakura S, Tsutsui T. Effects of minocycline and doxycycline on cell survival and gene expression in human gingival and periodontal ligament cells. J Periodontal Res 2006;41:124–31. https://doi.org/10.1111/j.1600-0765.2005.00843.x.

[194] Haidari W, Bruinsma R, Cardenas-de la Garza JA, Feldman SR. Sarecycline Review. Ann Pharmacother 2019:106002801987311.

https://doi.org/10.1177/1060028019873111.

[195] Zhanel G, Critchley I, Lin LY, Alvandi N. Microbiological profile of sarecycline, a novel targeted spectrum tetracycline for the treatment of acne vulgaris. Antimicrob Agents Chemother 2019;63:1–15. https://doi.org/10.1128/AAC.01297-18.

[196] Bunick CG, Keri J, Tanaka SK, Furey N, Damiani G, Johnson JL, et al. Antibacterial mechanisms and efficacy of sarecycline in animal models of infection and inflammation. Antibiotics 2021;10:1–12. https://doi.org/10.3390/antibiotics10040439.

[197] Martin V, Garcia M, Montemor M de F, Fernandes JCS, Gomes PS, Fernandes MH. Simulating In Vitro the Bone Healing Potential of a Degradable and Tailored Multifunctional Mg-Based Alloy Platform. Bioengineering 2022;9:255. https://doi.org/10.3390/bioengineering9060255.

[198] Garbieri TF, Martin V, dos Santos CF, Gomes PDS, Fernandes MH. The Embryonic Chick Femur Organotypic Model as a Tool to Analyze the Angiotensin II Axis on Bone Tissue. Pharmaceuticals 2021;14:469. https://doi.org/10.3390/ph14050469.

[199] Araújo R, Martin V, Ferreira R, Fernandes MH, Gomes PS. A new ex vivo model of the bone tissue response to the hyperglycemic environment – The embryonic chicken femur organotypic culture in high glucose conditions. Bone 2022;158:116355. https://doi.org/10.1016/j.bone.2022.116355.

[200] Kanczler JM, Smith EL, Roberts CA, Oreffo ROC. A Novel Approach for Studying the Temporal Modulation of Embryonic Skeletal Development Using Organotypic Bone Cultures and Microcomputed Tomography. Tissue Eng Part C Methods 2012;18:747–60. https://doi.org/10.1089/ten.tec.2012.0033.

[201] Ding DC, Shyu WC, Lin SZ. Mesenchymal stem cells. Cell Transplant 2011;20:5–14. https://doi.org/10.3727/096368910X.

[202] Shen LC, Chen YK, Lin LM, Shaw SY. Anti-invasion and anti-tumor growth effect of doxycycline treatment for human oral squamous-cell carcinoma - In vitro and in vivo studies. Oral Oncol 2010;46:178–84. https://doi.org/10.1016/j.oraloncology.2009.11.013.

[203] Onoda T, Ono T, Dhar DK, Yamanoi A, Fujii T, Nagasue N. Doxycycline inhibits cell proliferation and invasive potential: Combination therapy with cyclooxygenase-2 inhibitor in human colorectal cancer cells. J Lab Clin Med 2004;143:207–16. https://doi.org/10.1016/j.lab.2003.12.012.

[204] Garrido-Mesa N, Zarzuelo A, Gálvez J. What is behind the non-antibiotic properties of minocycline? Pharmacol Res 2013;67:18–30. https://doi.org/10.1016/j.phrs.2012.10.006.

[205] Sagar J, Sales K, Seifalian A, Winslet M. Doxycycline in Mitochondrial Mediated Pathway of Apoptosis: A Systematic Review. Anticancer Agents Med Chem 2010;10:556–63. https://doi.org/10.2174/187152010793498645.

[206] Chen M, Ona VO, Li M, Ferrante RJ, Fink KB, Zhu S, et al. Minocycline inhibits caspase-1 and caspase-3 expression and delays mortality in a transgenic mouse model of Huntington disease. Nat Med 2000;6:797–801. https://doi.org/10.1038/77528.

[207] Walters B, Uynuk-Ool T, Rothdiener M, Palm J, Hart ML, Stegemann JP, et al. Engineering the geometrical shape of mesenchymal stromal cells through defined cyclic stretch regimens. Sci Rep 2017;7:6640. https://doi.org/10.1038/s41598-017-06794-9.

[208] Jhala D, Rather H, Vasita R. Polycaprolactone-chitosan nanofibers influence cell morphology to induce early osteogenic differentiation. Biomater Sci 2016;4:1584–95. https://doi.org/10.1039/c6bm00492j.

[209] Almazin SM, Dziak R, Andreana S, Ciancio SG. The effect of doxycycline hyclate, chlorhexidine gluconate, and minocycline hydrochloride on osteoblastic proliferation and differentiation in vitro. J Periodontol 2009;80:999–1005. https://doi.org/10.1902/jop.2009.080574.

[210] Martin V, Ribeiro IA, Alves MM, Gonçalves L, Claudio RA, Grenho L, et al. Engineering a multifunctional 3D-printed PLA-collagen-minocycline-nanoHydroxyapatite scaffold with combined antimicrobial and osteogenic effects for bone regeneration. Mater Sci Eng C 2019;101:15–26. https://doi.org/10.1016/j.msec.2019.03.056.

[211] Kim YY-HY, Kim J, Lee H, Shin W-R, Lee S, Lee J, et al. Tetracycline Analogs Inhibit Osteoclast Differentiation by Suppressing MMP-9-Mediated Histone H3

Cleavage. Int J Mol Sci 2019;20:4038. https://doi.org/10.3390/ijms20164038.

[212] Lattanzi W, Bernardini C. Genes and Molecular Pathways of the Osteogenic Process. Osteogenesis 2012. https://doi.org/10.5772/34022.

[213] Song L. Calcium and Bone Metabolism Indices. vol. 82. 1st ed. Elsevier Inc.; 2017. https://doi.org/10.1016/bs.acc.2017.06.005.

[214] Rosset EM, Bradshaw AD. SPARC/osteonectin in mineralized tissue. Matrix Biol 2016;52–54:78–87. https://doi.org/10.1016/j.matbio.2016.02.001.

[215] Hosseini S, Naderi-Manesh H, Vali H, Baghaban Eslaminejad M, Azam Sayahpour F, Sheibani S, et al. Contribution of osteocalcin-mimetic peptide enhances osteogenic activity and extracellular matrix mineralization of human osteoblast-like cells. Colloids Surfaces B Biointerfaces 2019;173:662–71. https://doi.org/10.1016/j.colsurfb.2018.10.035.

[216] Santibanez JF, Obradović H, Kukolj T, Krstić J. Transforming growth factor-β, matrix metalloproteinases, and urokinase-type plasminogen activator interaction in the cancer epithelial to mesenchymal transition. Dev Dyn 2018;247:382–95. https://doi.org/10.1002/dvdy.24554.

[217] Kuwahara ST, Liu S, Chareunsouk A, Serowoky M, Mariani F V. On the horizon: Hedgehog signaling to heal broken bones. Bone Res 2022;10:13. https://doi.org/10.1038/s41413-021-00184-8.

[218] Miao D, Liu H, Plut P, Niu M, Huo R, Goltzman D, et al. Impaired endochondral bone development and osteopenia in Gli2-deficient mice. Exp Cell Res 2004;294:210–22. https://doi.org/10.1016/j.yexcr.2003.10.021.

[219] Shimoyama A, Wada M, Ikeda F, Hata K, Matsubara T, Nifuji A, et al. Ihh/Gli2 Signaling Promotes Osteoblast Differentiation by Regulating Runx2 Expression and Function. Mol Biol Cell 2007;18:2411–8. https://doi.org/10.1091/mbc.e06-08-0743.

[220] Bagheri L, Pellati A, Rizzo P, Aquila G, Massari L, De Mattei M, et al. Notch pathway is active during osteogenic differentiation of human bone marrow mesenchymal stem cells induced by pulsed electromagnetic fields. J Tissue Eng Regen Med 2018;12:304–15. https://doi.org/10.1002/term.2455.

[221] Suh JH, Lee HW, Lee JW, Kim JB. Hes1 stimulates transcriptional activity of

Runx2 by increasing protein stabilization during osteoblast differentiation. Biochem Biophys Res Commun 2008;367:97–102. https://doi.org/10.1016/j.bbrc.2007.12.100.

[222] Zamurovic N, Cappellen D, Rohner D, Susa M. Coordinated activation of Notch, Wnt, and transforming growth factor-β signaling pathways in bone morphogenic protein 2-induced osteogenesis: Notch target gene Hey1 inhibits mineralization and Runx2 transcriptional activity. J Biol Chem 2004;279:37704–15. https://doi.org/10.1074/jbc.M403813200.

[223] Qin Y, Zhang Q, Lee S, Zhong W long, Liu Y rong, Liu H juan, et al. Doxycycline reverses epithelial-to-mesenchymal transition and suppresses the proliferation and metastasis of lung cancer cells. Oncotarget 2015;6:40667–79. https://doi.org/10.18632/oncotarget.5842.

[224] Bonner C, Farrelly AM, Concannon CG, Dussmann H, Baquie M, Virard I, et al. Bone morphogenetic protein 3 controls insulin gene expression and is down-regulated in INS-1 cells inducibly expressing a hepatocyte nuclear factor 1A-maturity-onset diabetes of the young mutation. J Biol Chem 2011;286:25719–28. https://doi.org/10.1074/jbc.M110.215525.

[225] Di Pietro L, Barba M, Prampolini C, Ceccariglia S, Frassanito P, Vita A, et al. Gli1 and axin2 are distinctive markers of human calvarial mesenchymal stromal cells in nonsyndromic craniosynostosis. Int J Mol Sci 2020;21:1–19. https://doi.org/10.3390/ijms21124356.

[226] Smith EL EL, Kanczler JMJ, Oreffo RROC. A new take on an old story: chick limb organ culture for skeletal niche development and regenerative medicine evaluation. Eur Cells Mater 2013;26:91–106. https://doi.org/10.22203/eCM.v026a07.

[227] Cole AA, Chubinskaya S, Luchene LJ, Chlebek K, Orth MW, Greenwald RA, et al. Doxycycline disrupts chondrocyte differentiation and inhibits cartilage matrix degradation. Arthritis Rheum 1994;37:1727–34. https://doi.org/10.1002/art.1780371204.

[228] Gomes PS, Santos JD, Fernandes MH. Cell-induced response by tetracyclines on human bone marrow colonized hydroxyapatite and Bonelike®. Acta Biomater 2008;4:630–7. https://doi.org/10.1016/j.actbio.2007.12.006.

[229] Silva T, Silva JC, Colaco B, Gama A, Duarte-Araújo M, Fernandes MH, et al. In vivo tissue response and antibacterial efficacy of minocycline delivery system based on polymethylmethacrylate bone cement. J Biomater Appl 2018;33:380–91. https://doi.org/10.1177/0885328218795290.

[230] Nelson ML, Ismail MY. The Antibiotic and Nonantibiotic Tetracyclines. Compr. Med. Chem. II, Elsevier; 2007, p. 597–628. https://doi.org/10.1016/B0-08-045044-X/00221-2.

[231] Bryskier A. Antibiotics and Antibacterial Agents: Classifications and Structure-Activity Relationship. Antimicrob. Agents, Washington, DC, USA: ASM Press; 2014, p. 13–38. https://doi.org/10.1128/9781555815929.ch2.

[232] Nguyen F, Starosta AL, Arenz S, Sohmen D, Dönhöfer A, Wilson DN. Tetracycline antibiotics and resistance mechanisms. Biol Chem 2014;395:559–75. https://doi.org/10.1515/hsz-2013-0292.

[233] Fuoco D. Classification Framework and Chemical Biology of Tetracycline-Structure-Based Drugs. Antibiotics 2012;1:1–13. https://doi.org/10.3390/antibiotics1010001.

[234] Al-kuraishy HM, Al-Gareeb AI, Alqarni M, Cruz-Martins N, El-Saber Batiha G. Pleiotropic Effects of Tetracyclines in the Management of COVID-19: Emerging Perspectives. Front Pharmacol 2021;12:1–7. https://doi.org/10.3389/fphar.2021.642822.

[235] Yang C, Gao J, Wu B, Yan N, Li H, Ren Y, et al. Minocycline attenuates the development of diabetic neuropathy by inhibiting spinal cord Notch signaling in rat. Biomed Pharmacother 2017;94:380–5. https://doi.org/10.1016/j.biopha.2017.07.078.

[236] Golub LM, Elburki MS, Walker C, Ryan M, Sorsa T, Tenenbaum H, et al. Non-antibacterial tetracycline formulations: Host-modulators in the treatment of periodontitis and relevant systemic diseases. Int Dent J 2016;66:127–35. https://doi.org/10.1111/idj.12221.

[237] Li H, Jiao S, Li X, Banu H, Hamal S, Wang X. Therapeutic effects of antibiotic drug tigecycline against cervical squamous cell carcinoma by inhibiting Wnt/β-catenin signaling. Biochem Biophys Res Commun 2015;467:14–20. https://doi.org/10.1016/j.bbrc.2015.09.140.

[238] Hirohashi Y, Kamijo S, Khan M, Ikeda M, Oki M, Matin K, et al. Tetracycline, an Appropriate Reagent for Measuring Bone-Formation Activity in the Murine Model of the Streptococcus mutans-Induced Bone Loss. Front Cell Infect Microbiol 2021;11:1–12. https://doi.org/10.3389/fcimb.2021.714366.

[239] Macri-Pellizzeri L, De Melo N, Ahmed I, Grant D, Scammell B, Sottile V. Live Quantitative Monitoring of Mineral Deposition in Stem Cells Using Tetracycline Hydrochloride. Tissue Eng - Part C Methods 2018;24:171–8. https://doi.org/10.1089/ten.tec.2017.0400.

[240] Zegre M, Barros J, Ribeiro IAC, Santos C, Caetano LA, Gonçalves L, et al. Poly(DL-lactic acid) scaffolds as a bone targeting platform for the co-delivery of antimicrobial agents against S. aureus-C.albicans mixed biofilms. Int J Pharm 2022;622:121832. https://doi.org/10.1016/j.ijpharm.2022.121832.

[241] Silva T, Grenho L, Barros J, Silva J, Pinto R, Matos A, et al. Minocycline-releasing PMMA system as a space maintainer for staged bone reconstructions – in vitro antibacterial, cytocompatibility and anti-inflammatory characterization. Biomed Mater 2017;12:35009. https://doi.org/10.1088/1748-605X/aa68b8.

[242] Rifkin BR, Vernillo AT, Golub LM. Blocking Periodontal Disease Progression by Inhibiting Tissue-Destructive Enzymes: A Potential Therapeutic Role for Tetracyclines and Their Chemically-Modified Analogs. J Periodontol 1993;64:819–27. https://doi.org/10.1902/jop.1993.64.8s.819.

[243] Bettany J., Peet N., Wolowacz R., Skerry T., Grabowski P. Tetracyclines induce apoptosis in osteoclasts. Bone 2000;27:75–80. https://doi.org/10.1016/S8756-3282(00)00297-0.

[244] Zhou X, Zhang P, Zhang C, An B, Zhu Z. Tetracyclines Inhibit Rat Osteoclast Formation and Activity In Vitro and Affect Bone Turnover in Young Rats In Vivo. Calcif Tissue Int 2010;86:163–71. https://doi.org/10.1007/s00223-009-9328-5.

[245] Kinugawa S, Koide M, Kobayashi Y, Mizoguchi T, Ninomiya T, Muto A, et al. Tetracyclines Convert the Osteoclastic-Differentiation Pathway of Progenitor Cells To Produce Dendritic Cell-like Cells. J Immunol 2012;188:1772–81. https://doi.org/10.4049/jimmunol.1101174.

[246] Agwuh KN, MacGowan A. Pharmacokinetics and pharmacodynamics of the

tetracyclines including glycylcyclines. J Antimicrob Chemother 2006;58:256–65. https://doi.org/10.1093/jac/dkl224.

[247] Del Rosso JQ. SARECYCLINE AND THE NARROW-SPECTRUM TETRACYCLINE CONCEPT: Currently Available Data and Potential Clinical Relevance in Dermatology. J Clin Aesthet Dermatol 2020;13:45–8.

[248] Monk E, Shalita A, Siegel DM. Clinical applications of non-antimicrobial tetracyclines in dermatology. Pharmacol Res 2011;63:130–45. https://doi.org/10.1016/j.phrs.2010.10.007.

[249] Caton J, Ryan ME. Clinical studies on the management of periodontal diseases utilizing subantimicrobial dose doxycycline (SDD). Pharmacol Res 2011;63:114–20. https://doi.org/10.1016/j.phrs.2010.12.003.

[250] Mohamed-Ahmed S, Fristad I, Lie SA, Suliman S, Mustafa K, Vindenes H, et al. Adipose-derived and bone marrow mesenchymal stem cells: a donor-matched comparison. Stem Cell Res Ther 2018;9:168. https://doi.org/10.1186/s13287-018-0914-1.

[251] Xu L, Liu Y, Sun Y, Wang B, Xiong Y, Lin W, et al. Tissue source determines the differentiation potentials of mesenchymal stem cells: a comparative study of human mesenchymal stem cells from bone marrow and adipose tissue. Stem Cell Res Ther 2017;8:275. https://doi.org/10.1186/s13287-017-0716-x.

[252] Langenbach F, Handschel J. Effects of dexamethasone, ascorbic acid and β-glycerophosphate on the osteogenic differentiation of stem cells in vitro. Stem Cell Res Ther 2013;4:117. https://doi.org/10.1186/scrt328.

[253] Coelho M., Fernandes M. Human bone cell cultures in biocompatibility testing. Part II: effect of ascorbic acid, β-glycerophosphate and dexamethasone on osteoblastic differentiation. Biomaterials 2000;21:1095–102. https://doi.org/10.1016/S0142-9612(99)00192-1.

[254] Thomas S, Jaganathan BG. Signaling network regulating osteogenesis in mesenchymal stem cells. J Cell Commun Signal 2022;16:47–61. https://doi.org/10.1007/s12079-021-00635-1.

[255] Griffin MO, Fricovsky E, Ceballos G, Villarreal F. Tetracyclines: a pleitropic family of compounds with promising therapeutic properties. Review of the

literature. Am J Physiol Physiol 2010;299:C539–48. https://doi.org/10.1152/ajpcell.00047.2010.

[256] Griffin MO, Ceballos G, Villarreal FJ. Tetracycline compounds with non-antimicrobial organ protective properties: Possible mechanisms of action. Pharmacol Res 2011;63:102–7. https://doi.org/10.1016/j.phrs.2010.10.004.

[257] Bettany JT, Wolowacz RG. Tetracycline Derivatives Induce Apoptosis Selectively in Cultured Monocytes and Macrophages but not in Mesenchymal Cells. Adv Dent Res 1998;12:136–43. https://doi.org/10.1177/08959374980120010901.

[258] Malaval L, Liu F, Roche P, Aubin JE. Kinetics of osteoprogenitor proliferation and osteoblast differentiation in vitro. J Cell Biochem 1999;74:616–27.

[259] Frank O, Heim M, Jakob M, Barbero A, Schäfer D, Bendik I, et al. Real-time quantitative RT-PCR analysis of human bone marrow stromal cells during osteogenic differentiation in vitro. J Cell Biochem 2002;85:737–46. https://doi.org/10.1002/jcb.10174.

[260] Kartsogiannis V, Ng KW. Cell lines and primary cell cultures in the study of bone cell biology. Mol Cell Endocrinol 2004;228:79–102. https://doi.org/10.1016/j.mce.2003.06.002.

[261] Song H, Fares M, Maguire KR, Sidén Å, Potácová Z. Cytotoxic Effects of Tetracycline Analogues (Doxycycline, Minocycline and COL-3) in Acute Myeloid Leukemia HL-60 Cells. PLoS One 2014;9:e114457. https://doi.org/10.1371/journal.pone.0114457.

[262] Pablo Rodríguez J, González M, Ríos S, Cambiazo V. Cytoskeletal organization of human mesenchymal stem cells (MSC) changes during their osteogenic differentiation. J Cell Biochem 2004;93:721–31. https://doi.org/10.1002/jcb.20234.

[263] Wu H, Whitfield TW, Gordon JAR, Dobson JR, Tai PWL, van Wijnen AJ, et al. Genomic occupancy of Runx2 with global expression profiling identifies a novel dimension to control of osteoblastogenesis. Genome Biol 2014;15:R52. https://doi.org/10.1186/gb-2014-15-3-r52.

[264] Wang JS, Tokavanich N, Wein MN. SP7: from Bone Development to Skeletal

Disease. Curr Osteoporos Rep 2023;21:241–52. https://doi.org/10.1007/s11914-023-00778-7.

[265] Komori T. Whole Aspect of Runx2 Functions in Skeletal Development. Int J Mol Sci 2022;23. https://doi.org/10.3390/ijms23105776.

[266] Ballhause TM, Jiang S, Baranowsky A, Brandt S, Mertens PR, Frosch K-H, et al. Relevance of Notch Signaling for Bone Metabolism and Regeneration. Int J Mol Sci 2021;22:1325. https://doi.org/10.3390/ijms22031325.

[267] Luo Z, Shang X, Zhang H, Wang G, Massey PA, Barton SR, et al. Notch Signaling in Osteogenesis, Osteoclastogenesis, and Angiogenesis. Am J Pathol 2019;189:1495–500. https://doi.org/10.1016/j.ajpath.2019.05.005.

[268] Dao DY, Yang X, Flick LM, Chen D, Hilton MJ, O'Keefe RJ. Axin2 regulates chondrocyte maturation and axial skeletal development. J Orthop Res 2009:n/a-n/a. https://doi.org/10.1002/jor.20954.

[269] Goodnough LH, Chang AT, Treloar C, Yang J, Scacheri PC, Atit RP. Twist1 mediates repression of chondrogenesis by β-catenin to promote cranial bone progenitor specification. Development 2012;139:4428–38. https://doi.org/10.1242/dev.081679.

[270] Galli C, Piemontese M, Lumetti S, Manfredi E, Macaluso G, Passeri G. The importance of WNT pathways for bone metabolism and their regulation by implant topography. Eur Cells Mater 2012;24:46–59. https://doi.org/10.22203/eCM.v024a04.

[271] Gomes PS, Resende M, Fernandes MH. Doxycycline restores the impaired osteogenic commitment of diabetic-derived bone marrow mesenchymal stromal cells by increasing the canonical WNT signaling. Mol Cell Endocrinol 2020;518:110975. https://doi.org/10.1016/j.mce.2020.110975.

[272] Gomes N, Paula A, Nunes N, Góes P, Dutra P. Doxycycline induces bone repair and changes in Wnt signalling. Int J Oral Sci 2017;9:158–66. https://doi.org/10.1038/ijos.2017.28.

[273] Baht GS, Silkstone D, Nadesan P, Whetstone H, Alman BA. Activation of hedgehog signaling during fracture repair enhances osteoblastic-dependent matrix formation. J Orthop Res 2014;32:581–6.

https://doi.org/10.1002/jor.22562.

[274] Luo M, Huang H-X, Huang H, Li Z-T, Lai Y-Y. [Hedgehog signaling pathway and osteoporosis]. Zhongguo Gu Shang 2014;27:169–72.

[275] Nakamura T, Naruse M, Chiba Y, Komori T, Sasaki K, Iwamoto M, et al. Novel Hedgehog Agonists Promote Osteoblast Differentiation in Mesenchymal Stem Cells. J Cell Physiol 2015;230:922–9. https://doi.org/10.1002/jcp.24823.

[276] Kwon Y, Park C, Lee J, Park DH, Jeong S, Yun C-H, et al. Regulation of Bone Cell Differentiation and Activation by Microbe-Associated Molecular Patterns. Int J Mol Sci 2021;22:5805. https://doi.org/10.3390/ijms22115805.

[277] Chen L, Jiang W, Huang J, He B-C, Zuo G-W, Zhang W, et al. Insulin-like growth factor 2 (IGF-2) potentiates BMP-9-induced osteogenic differentiation and bone formation. J Bone Miner Res 2010;25:2447–59. https://doi.org/10.1002/jbmr.133.

[278] Lai S-W, Chen J-H, Lin H-Y, Liu Y-S, Tsai C-F, Chang P-C, et al. Regulatory Effects of Neuroinflammatory Responses Through Brain-Derived Neurotrophic Factor Signaling in Microglial Cells. Mol Neurobiol 2018;55:7487–99. https://doi.org/10.1007/s12035-018-0933-z.

[279] Neves J, Sousa-Victor P. Regulation of inflammation as an anti-aging intervention. FEBS J 2020;287:43–52. https://doi.org/10.1111/febs.15061.

[280] Panigrahy D, Gilligan MM, Serhan CN, Kashfi K. Resolution of inflammation: An organizing principle in biology and medicine. Pharmacol Ther 2021;227:107879. https://doi.org/10.1016/j.pharmthera.2021.107879.

[281] Duarte LRF, Pinho V, Rezende BM, Teixeira MM. Resolution of Inflammation in Acute Graft-Versus-Host-Disease: Advances and Perspectives. Biomolecules 2022;12:75. https://doi.org/10.3390/biom12010075.

[282] Greene MA, Loeser RF. Aging-related inflammation in osteoarthritis. Osteoarthr Cartil 2015;23:1966–71. https://doi.org/10.1016/j.joca.2015.01.008.

[283] Barbu E, Popescu M-R, Popescu A-C, Balanescu S-M. Inflammation as A Precursor of Atherothrombosis, Diabetes and Early Vascular Aging. Int J Mol Sci 2022;23:963. https://doi.org/10.3390/ijms23020963.

[284] Hafiane A, Daskalopoulou SS. Targeting the residual cardiovascular risk by

specific anti-inflammatory interventions as a therapeutic strategy in atherosclerosis. Pharmacol Res 2022;178:106157. https://doi.org/10.1016/j.phrs.2022.106157.

[285] Preshaw PM. Host modulation therapy with anti-inflammatory agents. Periodontol 2000 2018;76:131–49. https://doi.org/10.1111/prd.12148.

[286] Soeken KL. Herbal medicines for the treatment of rheumatoid arthritis: a systematic review. Rheumatology 2003;42:652–9. https://doi.org/10.1093/rheumatology/keg183.

[287] Zhu F, Du B, Xu B. Anti-inflammatory effects of phytochemicals from fruits, vegetables, and food legumes: A review. Crit Rev Food Sci Nutr 2018;58:1260–70. https://doi.org/10.1080/10408398.2016.1251390.

[288] Lin T-K, Zhong L, Santiago J. Anti-Inflammatory and Skin Barrier Repair Effects of Topical Application of Some Plant Oils. Int J Mol Sci 2017;19:70. https://doi.org/10.3390/ijms19010070.

[289] Ayati Z, Amiri MS, Ramezani M, Delshad E, Sahebkar A, Emami SA. Phytochemistry, Traditional Uses and Pharmacological Profile of Rose Hip: A Review. Curr Pharm Des 2019;24:4101–24. https://doi.org/10.2174/1381612824666181010151849.

[290] Schwager J, Hoeller U, Wolfram S, Richard N. Rose hip and its constituent galactolipids confer cartilage protection by modulating cytokine, and chemokine expression. BMC Complement Altern Med 2011;11:1–14. https://doi.org/10.1186/1472-6882-11-105.

[291] Ramos PT, Pedra NS, Soares MSP, da Silveira EF, Oliveira PS, Grecco FB, et al. Ketoprofen-loaded rose hip oil nanocapsules attenuate chronic inflammatory response in a pre-clinical trial in mice. Mater Sci Eng C 2019;103:109742. https://doi.org/10.1016/j.msec.2019.109742.

[292] Andersson U, Berger K, Högberg A, Landin-Olsson M, Holm C. Effects of rose hip intake on risk markers of type 2 diabetes and cardiovascular disease: a randomized, double-blind, cross-over investigation in obese persons. Eur J Clin Nutr 2012;66:585–90. https://doi.org/10.1038/ejcn.2011.203.

[293] Kirkeskov B, Christensen R, Bügel S, Bliddal H, Danneskiold-Samsøe B,

Christensen LP, et al. The effects of rose hip (Rosa canina) on plasma antioxidative activity and C-reactive protein in patients with rheumatoid arthritis and normal controls: A prospective cohort study. Phytomedicine 2011;18:953–8. https://doi.org/10.1016/j.phymed.2011.02.008.

[294] Sirajudheen P, Karthikeyan P, Meenakshi S. Mechanistic performance of organic pollutants removal from water using Zn/Al layered double hydroxides imprinted carbon composite. Surfaces and Interfaces 2020;20:100581. https://doi.org/10.1016/j.surfin.2020.100581.

[295] Veronese N, Pizzol D, Smith L, Dominguez LJ, Barbagallo M. Effect of Magnesium Supplementation on Inflammatory Parameters: A Meta-Analysis of Randomized Controlled Trials. Nutrients 2022;14:679. https://doi.org/10.3390/nu14030679.

[296] İlbay Z, Şahin S, Kirbaşlar Ş. Investigation of Polyhenolic Content of Rose Hip (Rosa canina L.) Tea Extracts: A Comparative Study. Foods 2013;2:43–52. https://doi.org/10.3390/foods2010043.

[297] Dongari-Bagtzoglou A, Kashleva H. Development of a highly reproducible three-dimensional organotypic model of the oral mucosa. Nat Protoc 2006;1:2012–8. https://doi.org/10.1038/nprot.2006.323.

[298] Demel J, Hynek J, Kovář P, Dai Y, Taviot-Guého C, Demel O, et al. Insight into the Structure of Layered Zinc Hydroxide Salts Intercalated with Dodecyl Sulfate Anions. J Phys Chem C 2014;118:27131–41. https://doi.org/10.1021/jp508499g.

[299] Newman SP, Jones W. Comparative Study of Some Layered Hydroxide Salts Containing Exchangeable Interlayer Anions. J Solid State Chem 1999;148:26–40. https://doi.org/10.1006/jssc.1999.8330.

[300] Wahab R, Kim YS, Shin HS. Synthesis, characterization and effect of pH variation on zinc oxide nanostructures. Mater Trans 2009;50:2092–7. https://doi.org/10.2320/matertrans.M2009099.

[301] Wahab R, Ansari SG, Kim YS, Song M, Shin HS. The role of pH variation on the growth of zinc oxide nanostructures. Appl Surf Sci 2009;255:4891–6. https://doi.org/10.1016/j.apsusc.2008.12.037.

[302] Sakr AAE, Zaki T, Elgabry O, Ebiad MA, El-Sabagh SM, Emara MM. Mg-Zn-

Al LDH: Influence of intercalated anions on CO2 removal from natural gas. Appl Clay Sci 2018;160:263–9. https://doi.org/10.1016/j.clay.2018.02.043.

[303] Ramesh TN, Madhu TL. Thermal Decomposition Studies of Layered Metal Hydroxynitrates (Metal: Cu, Zn, Cu/Co, and Zn/Co). Int J Inorg Chem 2015;2015:1–11. https://doi.org/10.1155/2015/536470.

[304] Shinagawa T, Watanabe M, Mori T, Tani JI, Chigane M, Izaki M. Oriented Transformation from Layered Zinc Hydroxides to Nanoporous ZnO: A Comparative Study of Different Anion Types. Inorg Chem 2018;57:13137–49. https://doi.org/10.1021/acs.inorgchem.8b01242.

[305] Ruiz C V., Rodríguez-Castellón E, Giraldo O. Structural Analysis and Conduction Mechanisms in Polycrystalline Zinc Hydroxide Nitrate. Inorg Chem 2018;57:9067–78. https://doi.org/10.1021/acs.inorgchem.8b01074.

[306] Ming Z, Jiehu C, Jie Z, Li P, Du X, Li C. TEA-assisted hydro-thermal synthesis of layered Zn hydroxide nitrate adsorbent and its rapid adsorption for MO. Inorg Nano-Metal Chem 2021:1–9. https://doi.org/10.1080/24701556.2021.1891101.

[307] Li P, Xu ZP, Hampton MA, Vu DT, Huang L, Rudolph V, et al. Control Preparation of Zinc Hydroxide Nitrate Nanocrystals and Examination of the Chemical and Structural Stability. J Phys Chem C 2012;116:10325–32. https://doi.org/10.1021/jp300045u.

[308] Alves MM, Batista C, Mil-Homens D, Grenho L, Fernandes MH, Santos CF. Enhanced antibacterial activity of Rosehip extract-functionalized Mg(OH)2 nanoparticles: An in vitro and in vivo study. Colloids Surfaces B Biointerfaces 2022;217:112643. https://doi.org/10.1016/j.colsurfb.2022.112643.

[309] Ruiz C V., Becerra ME, Giraldo O. Structural, Thermal, and Release Properties of Hybrid Materials Based on Layered Zinc Hydroxide and Caffeic Acid. Nanomaterials 2020;10:163. https://doi.org/10.3390/nano10010163.

[310] Şenol AM, Bozkurt E. A green “off–on” fluorescent sensor to detect Fe3+ and ATP using synthesized carbon dots from Rosehip. Res Chem Intermed 2023;49:2175–89. https://doi.org/10.1007/s11164-023-04960-5.

[311] Vezeau P., Koorbusch G., Draughn R., Keller J. Effects of multiple sterilization on surface characteristics and in vitro biologic responses to titanium. J Oral

Maxillofac Surg 1996;54:738–46. https://doi.org/10.1016/S0278-2391(96)90694-1.

[312] Brétagnol F, Rauscher H, Hasiwa M, Kylián O, Ceccone G, Hazell L, et al. The effect of sterilization processes on the bioadhesive properties and surface chemistry of a plasma-polymerized polyethylene glycol film: XPS characterization and L929 cell proliferation tests. Acta Biomater 2008;4:1745–51. https://doi.org/10.1016/j.actbio.2008.06.013.

[313] Nabipour H, Batool S, Hu Y. Pectin-Coated Baclofen-Layered Zinc Hydroxide Nanohybrid as a Bio-Based Nanocomposite Carrier for Oral Delivery. IEEE Trans Nanobioscience 2023;22:63–70. https://doi.org/10.1109/TNB.2022.3155785.

[314] Janani FZ, Taoufik N, Khiar H, Boumya W, Elhalil A, Sadiq M, et al. Nanostructured layered double hydroxides based photocatalysts: Insight on synthesis methods, application in water decontamination/splitting and antibacterial activity. Surfaces and Interfaces 2021;25:101263. https://doi.org/10.1016/j.surfin.2021.101263.

[315] Li M, Ritzoulis C, Du Q, Liu Y, Ding Y, Liu W, et al. Recent Progress on Protein-Polyphenol Complexes: Effect on Stability and Nutrients Delivery of Oil-in-Water Emulsion System. Front Nutr 2021;8. https://doi.org/10.3389/fnut.2021.765589.

[316] Shahidi F, Dissanayaka CS. Phenolic-protein interactions: insight from in-silico analyses – a review. Food Prod Process Nutr 2023;5:2. https://doi.org/10.1186/s43014-022-00121-0.

[317] Mohammed AN, Radi AM, Khaled R, Abo El-Ela FI, Kotp AA. Exploitation of new approach to control of environmental pathogenic bacteria causing bovine clinical mastitis using novel anti-biofilm nanocomposite. Environ Sci Pollut Res 2020;27:42791–805. https://doi.org/10.1007/s11356-020-10054-1.

[318] Lu H, Lu T, Zhang H, Qiu Y, Yin D, Zhu Z. Enhanced adsorption performance of aspartic acid intercalated Mg-Zn-Fe-LDH materials for arsenite. Dalt Trans 2018;47:4994–5004. https://doi.org/10.1039/c8dt00199e.

[319] Minnelli C, Laudadio E, Galeazzi R, Barucca G, Notarstefano V, Cantarini M, et al. Encapsulation of a Neutral Molecule into a Cationic Clay Material: Structural

Insight and Cytotoxicity of Resveratrol/Layered Double Hydroxide/BSA Nanocomposites. Nanomaterials 2019;10:33. https://doi.org/10.3390/nano10010033.

[320] Selim AA, Al-Sunaidi A, Tabet N. Effect of the surface texture and crystallinity of ZnO nanoparticles on their toxicity. Mater Sci Eng C 2012;32:2356–60. https://doi.org/10.1016/j.msec.2012.07.007.

[321] An SSA, Kim C-S, Nguyen H-D, Ignacio RM, Kim J-H, Cho H, et al. Immunotoxicity of zinc oxide nanoparticles with different size and electrostatic charge. Int J Nanomedicine 2014:195. https://doi.org/10.2147/IJN.S57935.

[322] Alves MM, Andrade SM, Grenho L, Fernandes MH, Santos C, Montemor MF. Influence of apple phytochemicals in ZnO nanoparticles formation, photoluminescence and biocompatibility for biomedical applications. Mater Sci Eng C 2019;101:76–87. https://doi.org/10.1016/j.msec.2019.03.084.

[323] Borovanský J, Riley PA. Cytotoxicity of zinc in vitro. Chem Biol Interact 1989;69:279–91. https://doi.org/10.1016/0009-2797(89)90085-9.

[324] Shen C, James SA, de Jonge MD, Turney TW, Wright PFA, Feltis BN. Relating Cytotoxicity, Zinc Ions, and Reactive Oxygen in ZnO Nanoparticle–Exposed Human Immune Cells. Toxicol Sci 2013;136:120–30. https://doi.org/10.1093/toxsci/kft187.

[325] Chang M-C, Tang C, Lin Y-H, Liu H, Wang T, Lan W, et al. Toxic mechanisms of Roth801, Canals, microparticles and nanoparticles of ZnO on MG-63 osteoblasts. Mater Sci Eng C 2021;119:111635. https://doi.org/10.1016/j.msec.2020.111635.

[326] Czyżowska A, Barbasz A. Cytotoxicity of zinc oxide nanoparticles to innate and adaptive human immune cells. J Appl Toxicol 2021;41:1425–37. https://doi.org/10.1002/jat.4133.

[327] Erra Díaz F, Dantas E, Geffner J. Unravelling the Interplay between Extracellular Acidosis and Immune Cells. Mediators Inflamm 2018;2018:1–11. https://doi.org/10.1155/2018/1218297.

[328] Feng R, Fan Y, Chen L, Ge Q, Xu J, Yang M, et al. Based on 16 S rRNA sequencing and metabonomics to reveal the new mechanism of aluminum

potassium sulfate induced inflammation and abnormal lipid metabolism in mice. Ecotoxicol Environ Saf 2022;247:114214. https://doi.org/10.1016/j.ecoenv.2022.114214.

[329] Carbonara CEM, Roza NA V., Quadros KRS, França RA, Esteves ABA, Pavan CR, et al. Effect of aluminum accumulation on bone and cardiovascular risk in the current era. PLoS One 2023;18:e0284123. https://doi.org/10.1371/journal.pone.0284123.

[330] Yang F, Xue Y, Wang F, Guo D, He Y, Zhao X, et al. Sustained release of magnesium and zinc ions synergistically accelerates wound healing. Bioact Mater 2023;26:88–101. https://doi.org/10.1016/j.bioactmat.2023.02.019.

[331] Mandal AK, Katuwal S, Tettey F, Gupta A, Bhattarai S, Jaisi S, et al. Current Research on Zinc Oxide Nanoparticles: Synthesis, Characterization, and Biomedical Applications. Nanomaterials 2022;12. https://doi.org/10.3390/nano12173066.

[332] Jarosz M, Olbert M, Wyszogrodzka G, Młyniec K, Librowski T. Antioxidant and anti-inflammatory effects of zinc. Zinc-dependent NF-κB signaling. Inflammopharmacology 2017;25:11–24. https://doi.org/10.1007/s10787-017-0309-4.

[333] Winther K, Campbell-Tofte J, Vinther Hansen AS. Bioactive ingredients of rose hips (Rosa canina L) with special reference to antioxidative and anti-inflammatory properties: in vitro studies. Bot Targets Ther 2016:11. https://doi.org/10.2147/btat.s91385.

[334] Bosshardt DD. The periodontal pocket: pathogenesis, histopathology and consequences. Periodontol 2000 2018;76:43–50. https://doi.org/10.1111/prd.12153.

[335] Hardan L, Bourgi R, Cuevas-Suárez CE, Flores-Rodríguez M, Omaña-Covarrubias A, Nicastro M, et al. The Use of Probiotics as Adjuvant Therapy of Periodontal Treatment: A Systematic Review and Meta-Analysis of Clinical Trials. Pharmaceutics 2022;14:1017. https://doi.org/10.3390/pharmaceutics14051017.

[336] Assunção M, Carneiro VMA, Stefani CM, de Lima CL. Clinical efficacy of subgingivally delivered propolis as an adjuvant to nonsurgical periodontal

treatment of periodontitis: A systematic review and meta-analysis. Phyther Res 2021;35:5584–95. https://doi.org/10.1002/ptr.7193.

[337] James P, Worthington H V, Parnell C, Harding M, Lamont T, Cheung A, et al. Chlorhexidine mouthrinse as an adjunctive treatment for gingival health. Cochrane Database Syst Rev 2017;2021. https://doi.org/10.1002/14651858.CD008676.pub2.

[338] Dubar M, Lizambard M, Delcourt-Debruyne E, Batool F, Huck O, Siepmann F, et al. In-situ forming drug-delivery systems for periodontal treatment: Current knowledge and perspectives. Biomed Mater 2021;16. https://doi.org/10.1088/1748-605X/ac254c.

[339] Basudan AM. Nanoparticle based periodontal drug delivery – A review on current trends and future perspectives. Saudi Dent J 2022;34:669–80. https://doi.org/10.1016/j.sdentj.2022.09.006.

[340] Tan OL, Safii SH, Razali M. Commercial Local Pharmacotherapeutics and Adjunctive Agents for Nonsurgical Treatment of Periodontitis: A Contemporary Review of Clinical Efficacies and Challenges. Antibiotics 2019;9:11. https://doi.org/10.3390/antibiotics9010011.

[341] Yilmaz O, Verbeke P, Lamont RJ, Ojcius DM. Intercellular Spreading of Porphyromonas gingivalis Infection in Primary Gingival Epithelial Cells. Infect Immun 2006;74:703–10. https://doi.org/10.1128/IAI.74.1.703-710.2006.

[342] Bostanci N, Belibasakis GN. Porphyromonas gingivalis: An invasive and evasive opportunistic oral pathogen. FEMS Microbiol Lett 2012;333:1–9. https://doi.org/10.1111/j.1574-6968.2012.02579.x.

[343] Chakraborti M, Jackson JK, Plackett D, Gilchrist SE, Burt HM. The application of layered double hydroxide clay (LDH)-poly(lactide-co- glycolic acid) (PLGA) film composites for the controlled release of antibiotics. J Mater Sci Mater Med 2012;23:1705–13. https://doi.org/10.1007/s10856-012-4638-y.

[344] Chakraborti M, Jackson JK, Plackett D, Brunette DM, Burt HM. Drug intercalation in layered double hydroxide clay: Application in the development of a nanocomposite film for guided tissue regeneration. Int J Pharm 2011;416:305–13. https://doi.org/10.1016/j.ijpharm.2011.06.016.

[345] Conrads G, Klomp T, Deng D, Wenzler JS, Braun A, Abdelbary MMH. The Antimicrobial Susceptibility of Porphyromonas gingivalis: Genetic Repertoire, Global Phenotype, and Review of the Literature. Antibiotics 2021;10. https://doi.org/10.3390/antibiotics10121438.

[346] Warner AJ, Hathaway-Schrader JD, Lubker R, Davies C, Novince CM. Tetracyclines and bone: Unclear actions with potentially lasting effects. Bone 2022;159:116377. https://doi.org/10.1016/j.bone.2022.116377.

[347] Lee J-H, Lee H, Kim K-N, Kim K. Cytotoxicity and anti-inflammatory effects of zinc ions and eugenol during setting of ZOE in immortalized human oral keratinocytes grown as three-dimensional spheroids. Dent Mater 2016;32:e93–104. https://doi.org/10.1016/j.dental.2016.01.003.

[348] Muzammil S, Hayat S, Fakhar-e-Alam M, Aslam B, Siddique MH, Nisar MA, et al. Nanoantibiotics: Future nanotechnologies to combat antibiotic resistance. Front Biosci - Elit 2018;10:352–74. https://doi.org/10.2741/e827.

[349] Shahid S, Ejaz A, Javed M, Mansoor S, Iqbal S, Elkaeed EB, et al. The Anti-Inflammatory and Free Radical Scavenging Activities of Bio-Inspired Nano Magnesium Oxide. Front Mater 2022;9. https://doi.org/10.3389/fmats.2022.875163.

[350] CLSI_M100-S27. M100-S27 Performance standards for antimicrobial susceptibility testing. 2017.

[351] Alonso-Español A, Bravo E, Ribeiro-Vidal H, Virto L, Herrera D, Alonso B, et al. The Antimicrobial Activity of Curcumin and Xanthohumol on Bacterial Biofilms Developed over Dental Implant Surfaces. Int J Mol Sci 2023;24:2335. https://doi.org/10.3390/ijms24032335.

[352] Rogowska A, Railean-plugaru V, Pomastowski P, Walczak-skierska J, Król-górniak A, Gołębiowski A, et al. The study on molecular profile changes of pathogens via zinc nanocomposites immobilization approach. Int J Mol Sci 2021;22. https://doi.org/10.3390/ijms22105395.

[353] Passariello C, Lucchese A, Virga A, Pera F, Gigola P. Isolation of Staphylococcus aureus and progression of periodontal lesions in aggressive periodontitis. Eur J Inflamm 2012;10:501–13. https://doi.org/10.1177/1721727X1201000326.

[354] Li Q, Wei G, Yang Y, Li Z, Zhang L, Shao L, et al. Insight into the enhanced catalytic activity of a red mud based Fe 2 O 3 /Zn–Al layered double hydroxide in the photo-Fenton reaction. Catal Sci Technol 2020;10:7365–77. https://doi.org/10.1039/D0CY01539C.

[355] Zhao X-J, Zhu Y-Q, Xu S-M, Liu H-M, Yin P, Feng Y-L, et al. Anion exchange behavior of M II Al layered double hydroxides: a molecular dynamics and DFT study. Phys Chem Chem Phys 2020;22:19758–68. https://doi.org/10.1039/D0CP02537B.

[356] Hibino T. Anion Selectivity of Layered Double Hydroxides: Effects of Crystallinity and Charge Density. Eur J Inorg Chem 2018;2018:722–30. https://doi.org/10.1002/ejic.201701067.

[357] Debnath B, Majumdar M, Bhowmik M, Bhowmik KL, Debnath A, Roy DN. The effective adsorption of tetracycline onto zirconia nanoparticles synthesized by novel microbial green technology. J Environ Manage 2020;261:110235. https://doi.org/10.1016/j.jenvman.2020.110235.

[358] Gopal G, Sankar H, Natarajan C, Mukherjee A. Tetracycline removal using green synthesized bimetallic nZVI-Cu and bentonite supported green nZVI-Cu nanocomposite: A comparative study. J Environ Manage 2020;254:109812. https://doi.org/10.1016/j.jenvman.2019.109812.

[359] Chahardahmasoumi S, Sarvi MN, Jalali SAH. Modified montmorillonite nanosheets as a nanocarrier with smart pH-responsive control on the antimicrobial activity of tetracycline upon release. Appl Clay Sci 2019;178:105135. https://doi.org/10.1016/j.clay.2019.105135.

[360] Bouaziz Z, Soussan L, Janot J-M, Jaber M, Ben Haj Amara A, Balme S. Dual role of layered double hydroxide nanocomposites on antibacterial activity and degradation of tetracycline and oxytetracyline. Chemosphere 2018;206:175–83. https://doi.org/10.1016/j.chemosphere.2018.05.003.

[361] Babayevska N, Przysiecka Ł, Iatsunskyi I, Nowaczyk G, Jarek M, Janiszewska E, et al. ZnO size and shape effect on antibacterial activity and cytotoxicity profile. Sci Rep 2022;12:8148. https://doi.org/10.1038/s41598-022-12134-3.

[362] Vasile OR, Serdaru I, Andronescu E, Truşcă R, Surdu VA, Oprea O, et al. Influence of the size and the morphology of ZnO nanoparticles on cell viability.

Comptes Rendus Chim 2015;18:1335–43. https://doi.org/10.1016/j.crci.2015.08.005.

[363] Król A, Pomastowski P, Rafińska K, Railean-Plugaru V, Buszewski B. Zinc oxide nanoparticles: Synthesis, antiseptic activity and toxicity mechanism. Adv Colloid Interface Sci 2017;249:37–52. https://doi.org/10.1016/j.cis.2017.07.033.

[364] Kim I, Viswanathan K, Kasi G, Thanakkasaranee S, Sadeghi K, Seo J. ZnO Nanostructures in Active Antibacterial Food Packaging: Preparation Methods, Antimicrobial Mechanisms, Safety Issues, Future Prospects, and Challenges. Food Rev Int 2022;38:537–65. https://doi.org/10.1080/87559129.2020.1737709.

[365] Liao C, Jin Y, Li Y, Tjong SC. Interactions of Zinc Oxide Nanostructures with Mammalian Cells: Cytotoxicity and Photocatalytic Toxicity. Int J Mol Sci 2020;21:6305. https://doi.org/10.3390/ijms21176305.

[366] Şeker Ş, Elçin AE, Yumak T, Sinağ A, Elçin YM. In vitro cytotoxicity of hydrothermally synthesized ZnO nanoparticles on human periodontal ligament fibroblast and mouse dermal fibroblast cells. Toxicol Vitr 2014;28:1349–58. https://doi.org/10.1016/j.tiv.2014.06.016.

[367] Sharma V, Anderson D, Dhawan A. Zinc oxide nanoparticles induce oxidative DNA damage and ROS-triggered mitochondria mediated apoptosis in human liver cells (HepG2). Apoptosis 2012;17:852–70. https://doi.org/10.1007/s10495-012-0705-6.

[368] Król-Górniak A, Rafińska K, Monedeiro F, Pomastowski P, Buszewski B. Comparison study of cytotoxicity of bare and functionalized zinc oxide nanoparticles. Int J Mol Sci 2021;22. https://doi.org/10.3390/ijms22179529.

[369] Altoé LS, Alves RS, Miranda LL, Sarandy MM, Bastos DSS, Gonçalves-Santos E, et al. Doxycycline Hyclate Modulates Antioxidant Defenses, Matrix Metalloproteinases, and COX-2 Activity Accelerating Skin Wound Healing by Secondary Intention in Rats. Oxid Med Cell Longev 2021;2021. https://doi.org/10.1155/2021/4681041.

[370] Zhao X, Yang Y, Yu J, Ding R, Pei D, Zhang Y, et al. Injectable hydrogels with high drug loading through B–N coordination and ROS-triggered drug release for efficient treatment of chronic periodontitis in diabetic rats. Biomaterials 2022;282:121387. https://doi.org/10.1016/j.biomaterials.2022.121387.

[371] Nativel B, Couret D, Giraud P, Meilhac O, D'Hellencourt CL, Viranaïcken W, et al. Porphyromonas gingivalis lipopolysaccharides act exclusively through TLR4 with a resilience between mouse and human. Sci Rep 2017;7:1–12. https://doi.org/10.1038/s41598-017-16190-y.

[372] Gad SS, Fayez AM, Abdelaziz M, Abou El-ezz D. Amelioration of autoimmunity and inflammation by zinc oxide nanoparticles in experimental rheumatoid arthritis. Naunyn Schmiedebergs Arch Pharmacol 2021;394:1975–81. https://doi.org/10.1007/s00210-021-02105-2.

[373] Hasannasab M, Nourmohammadi J, Dehghan MM, Ghaee A. Immobilization of bromelain and ZnO nanoparticles on silk fibroin nanofibers as an antibacterial and anti-inflammatory burn dressing. Int J Pharm 2021;610:121227. https://doi.org/10.1016/j.ijpharm.2021.121227.

[374] Di Caprio R, Lembo S, Di Costanzo L, Balato A, Monfrecola G, Caprio R Di, et al. Anti-inflammatory properties of low and high doxycycline doses: An in vitro study. Mediators Inflamm 2015;2015:1–10. https://doi.org/10.1155/2015/329418.

[375] Kim KM, Kim MK, Paek HJ, Choi SJ, Oh JM. Stable fluorescence conjugation of ZnO nanoparticles and their size dependent cellular uptake. Colloids Surfaces B Biointerfaces 2016;145:870–7. https://doi.org/10.1016/j.colsurfb.2016.06.006.

[376] Abdelmonem AM, Pelaz B, Kantner K, Bigall NC, Del Pino P, Parak WJ. Charge and agglomeration dependent in vitro uptake and cytotoxicity of zinc oxide nanoparticles. J Inorg Biochem 2015;153:334–8. https://doi.org/10.1016/j.jinorgbio.2015.08.029.

[377] Sirelkhatim A, Mahmud S, Seeni A, Kaus NHM, Ann LC, Bakhori SKM, et al. Review on zinc oxide nanoparticles: Antibacterial activity and toxicity mechanism. Nano-Micro Lett 2015;7:219–42. https://doi.org/10.1007/s40820-015-0040-x.

[378] Mittag A, Hoera C, Kämpfe A, Westermann M, Kuckelkorn J, Schneider T, et al. Cellular Uptake and Toxicological Effects of Differently Sized Zinc Oxide Nanoparticles in Intestinal Cells. Toxics 2021;9:96. https://doi.org/10.3390/toxics9050096.

[379] Mendoza-Milla C, Macías Macías FI, Velázquez Delgado KA, Herrera Rodríguez MA, Colín-Val Z, Ramos-Godinez M del P, et al. Zinc Oxide

Nanoparticles Induce Toxicity in H9c2 Rat Cardiomyoblasts. Int J Mol Sci 2022;23:12940. https://doi.org/10.3390/ijms232112940.

[380] Chen L, Mo S, Hua Y. Compressive force-induced autophagy in periodontal ligament cells downregulates osteoclastogenesis during tooth movement. J Periodontol 2019;90:1170–81. https://doi.org/10.1002/JPER.19-0049.

[381] Nair S, Sasidharan A, Divya Rani V V., Menon D, Nair S, Manzoor K, et al. Role of size scale of ZnO nanoparticles and microparticles on toxicity toward bacteria and osteoblast cancer cells. J Mater Sci Mater Med 2009;20:235–41. https://doi.org/10.1007/s10856-008-3548-5.

[382] Parham S, Wicaksono DHB, Bagherbaigi S, Lee SL, Nur H. Antimicrobial Treatment of Different Metal Oxide Nanoparticles: A Critical Review. J Chinese Chem Soc 2016;63:385–93. https://doi.org/10.1002/jccs.201500446.

[383] Pandey P, Sahoo R, Singh K, Pati S, Mathew J, Pandey AC, et al. Drug resistance reversal potential of nanoparticles/ nanocomposites via antibiotic's potentiation in multi drug resistant p. Aeruginosa. Nanomaterials 2022;12. https://doi.org/10.3390/nano12010117.

SUPPLEMENTARY MATERIAL

Methods

Proinflammatory activity of Zn-Mg LH and RH-Zn-Mg LH NPs on MPRO murine bone marrow derived neutrophils

Mouse MPRO cell line from the American Type Culture Collection (Manassas, VA) was grown in Iscove's modified Dulbecco's medium (IMDM) supplemented with 20% (v/v) horse serum, 10 ng/mL, Granulocyte macrophage colony stimulating factor (GM-CSF), and 1% penicillin/streptomycin, all from Gibco (Grand Island, NY). MPRO suspension cells were seeded in 96-well plate at a density 10,000 cells/well. After one-hour of incubation, Zn-Mg LH and RH-Zn-Mg LH NPs were added into each well to reach a final concentration of 100 µg/mL and the cells were incubated for 4 or 8 additional hours in 5% CO_2, 37°C. Cells that were stimulated with LPS were considered a positive control, while cells that were untreated were the negative control. After the incubation, the cell culture medium was collected. IL-6 and TNF-α contents in the medium were quantified using IL-6 and TNF-a ELISA kits (Thermofischer, Waltham, MA).

Proinflammatory activity of Zn-Mg LH and RH-Zn-Mg LH NPs on J774A.1 murine bone marrow derived macrophages

Mouse J774A.1 macrophage cell line from the American Type Culture Collection (Manassas, VA) were grown in Dulbecco's Modified Eagle Media (DMEM) supplemented with 10% (v/v) fetal bovine serum and penicillin/streptomycin, all from Gibco (Grand Island, NY). J774A.1 cells were seeded in 96-well plate in complete DMEM at a density 20,000 cells/well. After overnight incubation, the medium was removed and Zn-Mg LH and RH-Zn-Mg LH NPs were added in each well to reach nanoparticles final concentration of 30 µg/mL, and the cells were incubated for 4 or 8 h. Cells that were stimulated with LPS were considered a positive control, while cells that were untreated were the negative control. After incubation, cell culture medium was collected and IL-6 and TNF-α contents in the medium were quantified using IL-6 and TNF-a ELISA kits as mentioned above.

Results

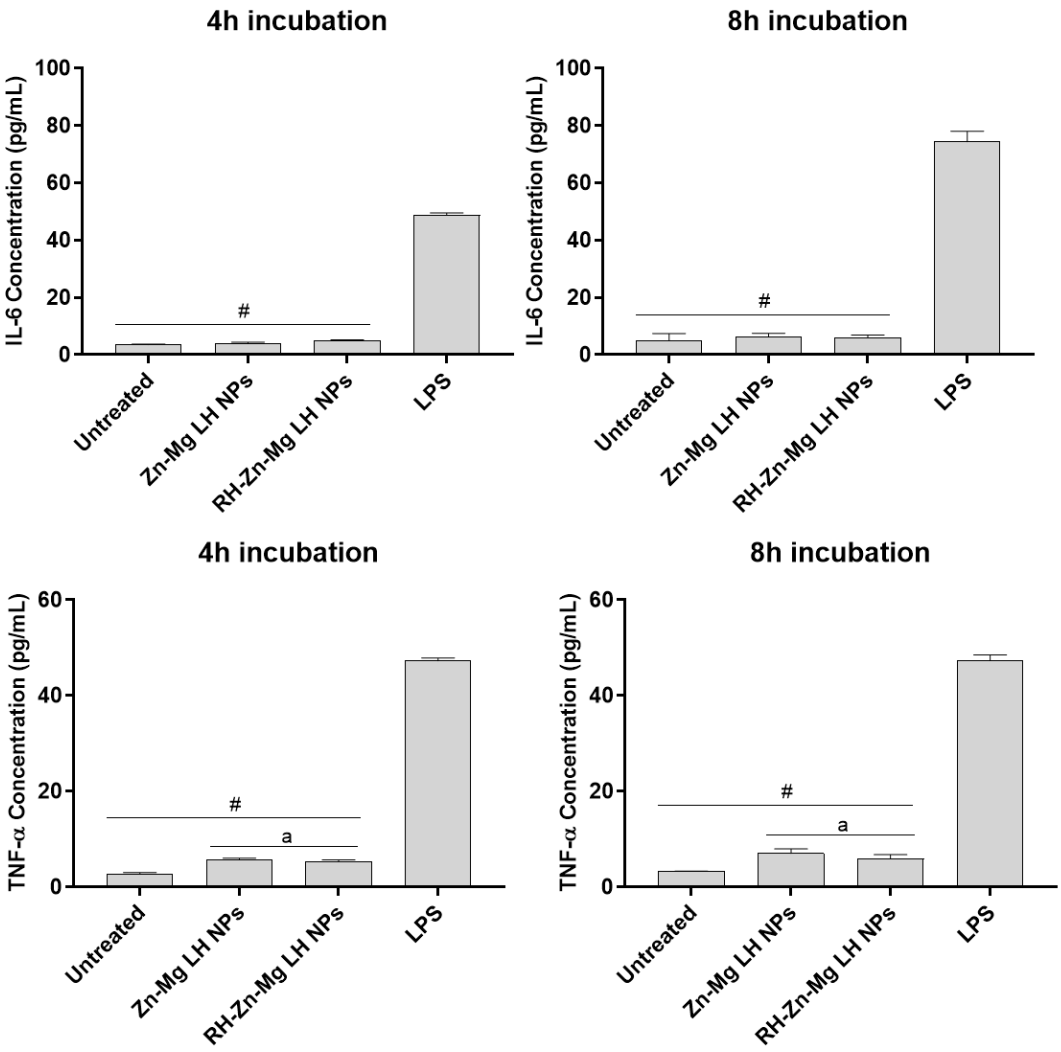

Figure S1: IL-6 and TNF- α production by MPRO cells after 4 h or 8 h of treatment with the NPs. Data are mean ± S.D., (n = 5). (#, $p < 0.05$ vs. LPS; a $p < 0.05$ vs. Untreated).

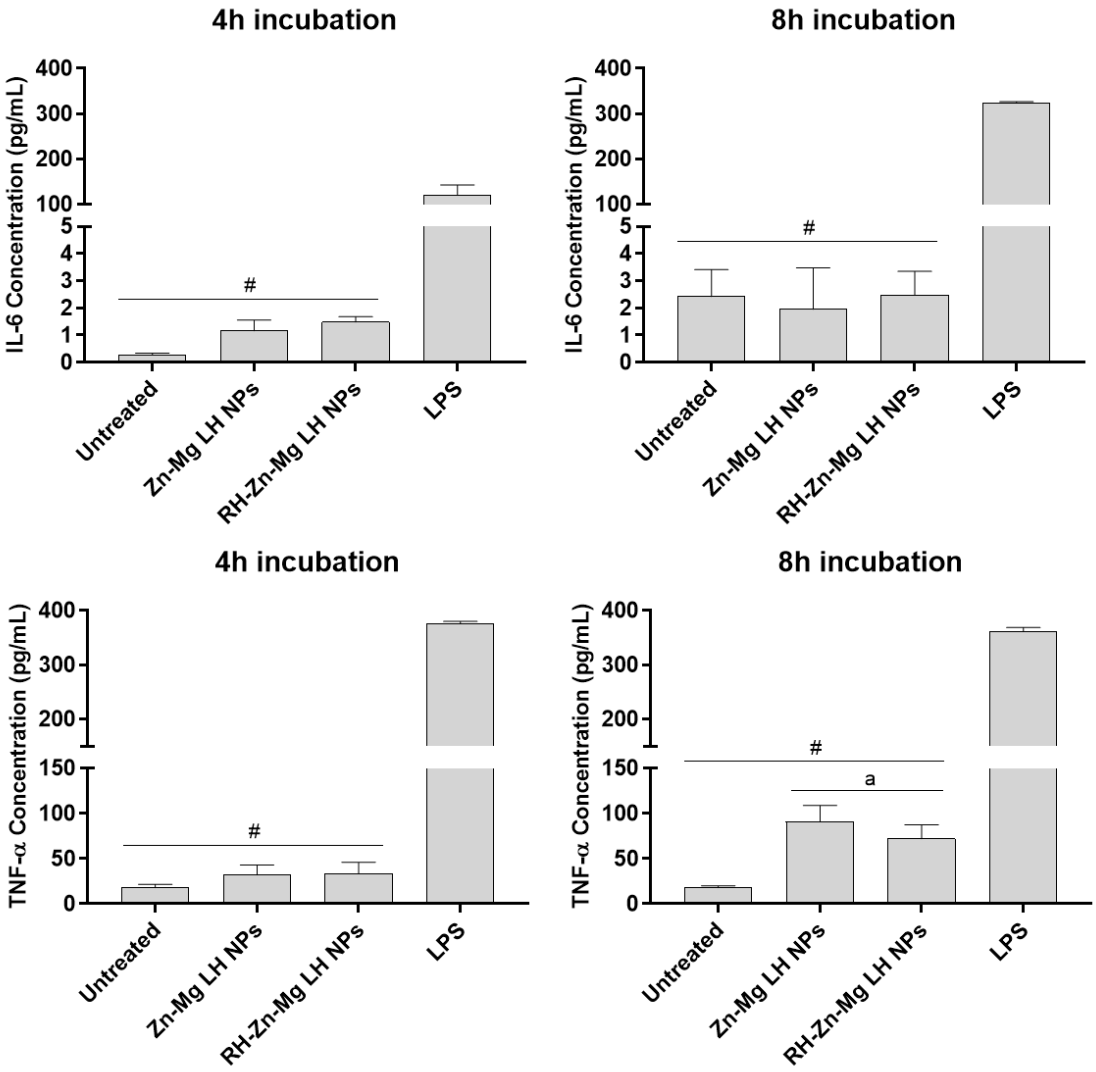

Figure S2: IL-6 and TNF- α production by J774A.1 cells after 4 h or 8 h of treatment with the NPs. Data are mean ± S.D., (n = 5). (#, $p < 0.05$ vs. LPS; a $p < 0.05$ vs. Untreated).